Title	PREPARATION AND PROPERTIES OF THE CONPOUNDS OF GALLIUM WITH THE GROUP V ELEMENTS AND AN INDIUM-SELENIDE COMPOUND(Dissertation_全文)
Author(s)	Osamura, Kozo
Citation	Kyoto University (京都大学)
Issue Date	1970-11-24
URL	http://dx.doi.org/10.14989/doctor.k1049
Right	
Type	Thesis or Dissertation
Textversion	author

PREPARATION AND PROPERTIES
OF
THE COMPOUNDS OF GALLIUM WITH THE GROUP V ELEMENTS
AND
AN INDIUM-SELENIDE COMPOUND

by

KOZO OSAMURA

Submitted to Kyoto University
in June, 1970
in Partial Fulfilment of the Requirements for
the Degree of Doctor of Engineering

CONTENTS

Chapter I

Introduction

The first of the III-V compounds to be reported was InP, prepared over sixty years ago by Thiel and Koelsch.1) Huggins2) pointed out in 1926 that binary compounds formed between group IIIb and group Vb elements should crystallize in a form similar to the diamond structure taken up by the group IV semiconductors, and this was confirmed by the experiments of Goldschmidt.3) The fact that one of the compounds, InSb, is a simiconductor akin to germanium and grey tin, was reported in 1950 by Blum et al,4) and by Goryunova et al.5) Welker,6) however, appears to have been the first to appreciate the importance of the III-V compounds as a new family of semiconductors, when in 1952 he described the semiconducting properties of several of these compounds and drew attention to some of their special properties, such as the very high electron mobility and small energy gap of indium antimonide. Work on III-V compounds has given us much information about those physical processes which cannot be studied on germanium and silicon. The particular features that attracted interest were the low effective mass, which revealed itself by a very high electron mobility, and the ionic component in the crystal binding. After the first exploratory research, nearly all of the work was limited to InSb, partly because this was an almost ideal vehicle for such studies, but also because it was easy to grow InSb single crystals. As a result the technology of InSb advanced to the stage that the best material made a year or so ago compared well in impurity content with the purest germanium and silicon. The technology of the other compounds fell far behind this, for the purification was very difficult and there was no great incentive to work in this field.

The invention of the semiconductor laser and the discovery of the Gunn effect have caused a marked change in this situation. There is now an increased prospect of industrial application of these materials, and we may expect a growing interest in GaAs, GaP, and compounds or alloys of compounds which can emit visible or microwave radiation. It is useful at this stage to assess our present knowledge, and to point out areas where the evidence is insufficient or confliciting. These tasks are attempted in the thesis, with a number of articles giving detailed treatments of specific aspects of the subject. Especially, phenomena in substitutional solid solutions of III-V compounds is an important object in this thesis.

This introductory article serves a rather qualitative purpose. It is more general in scope, and more speculative in its approach. It deals with three of the most important features which have led to our interest in III-V compounds, that is, details of conduction bands, effective charges and crystal binding, and phenomena in solid solutions.

As the interest in compounds shifts toward the variation of band structure in substitutional solid solution, a knowledge of band structure becomes more important. The family of III-V compounds has some members with a direct band gap and some with an indirect gap, and in order to predict the band structure of alloys of compounds it is necessary to know not only the energy of the lowest conduction bands minimum, but also the energies of the higher minima. Fortunately we can derive much of the required information by combining the results of various experiments. The energies of two of the three important vertical transitions, $X_5 - X_1$, and $L_3 - L_1$, can be measured or estimated by ultraviolet reflectivity, and determinations of these energies have now been made for all the better known compounds.7) The energy difference between $\Gamma_{15} - \Gamma_1$ can also be found by optical techniques. Moreover, some inter-conduction band transitions from the lowest minimum to the higher minima, that is, $\Gamma_1 - X_1$ and $\Gamma_1 - L_1$ and be studied by the infrared transmission measurement and by the Hall effect measurement.

In a compound like GaP, where the lowest energy transition between the conduction and valence bands is the indirect one from $\Gamma_1 - X_1$, we can deduce the relative positions of Γ_1 and X_1 from optical transmission or from the spectral response of the photosensitive barrier at a metal-semiconductor interface. We cannot find the position of L_1 in the same way. In the direct gap materials, GaAs and GaSb, the minima at X and L are not much higher than Γ_1 and their position can be determined by Hall effect measurements and by a study of the pressure dependence of resistivity. The powerful method determining the band structures is the reflectivity and transmission measurement in the region of visible light to infrared one.

As an example we take the band structure of the three gallium compounds. The direct transitions have been established with good accuracy by a number of workers. The conduction band structure of GaAs has been studied by Sagar an Miller,8) and by Becker et al.9) and the two sets of results are in good agreement.

In the present work, the transition of conduction electron from the Γ_1 lowest minimum to the L_1 one has been established from the Hall effect measurements in fairly pure n-GaSb. A recent investigation by Zallen and Paul[10] on the optical properties of GaP has given the Γ_{15}-X_1 and Γ_{15}-Γ_1 energies with good accuracy, and the results agree will with those of Nelson et al.[11]

The direct transition $\Gamma_{15} - \Gamma_1$ in GaAs has been established by the transmission measurements of Sturge.[12] Ehrenreich[13] has calculated the energy difference between Γ_1 and X_1 from the high temperature behavior of the Hall coefficient, and he finds this to be 0.36 eV at low temperature. Spitzer and Mead[14] give a slightly smaller value, 0.28 eV at 300 °K.

Optical properties of $GaAs_{1-x}P_x$ solid solutions near the intrinsic absorption edge were studied by many authors as shown in Fig. 1. The dependence of energy gap on composition might be represented in the form of two straight lines intersecting near $x=0.4$. It is understanding that the experimental data can be devided into the two types, that is, of the direct transition and of the indirect one.

The interconduction band transition from Γ_1 minimum to X_1 minima has been observed in some III-V compounds by many authors.[15] In GaAs, the energy separation between Γ_1 minimum and X_1 ones was determined to be 0.36 eV in the infrared optical measurement. It has been found for n-type $GaAs_{1-x}P_x$ solid solutions with GaAs rich composition that the additional infrared absorption arises from the transition of conduction electron from the Γ_1 minimum to the X_1 ones. The linear dependence of the threshold energy on composition has been confirmed and this

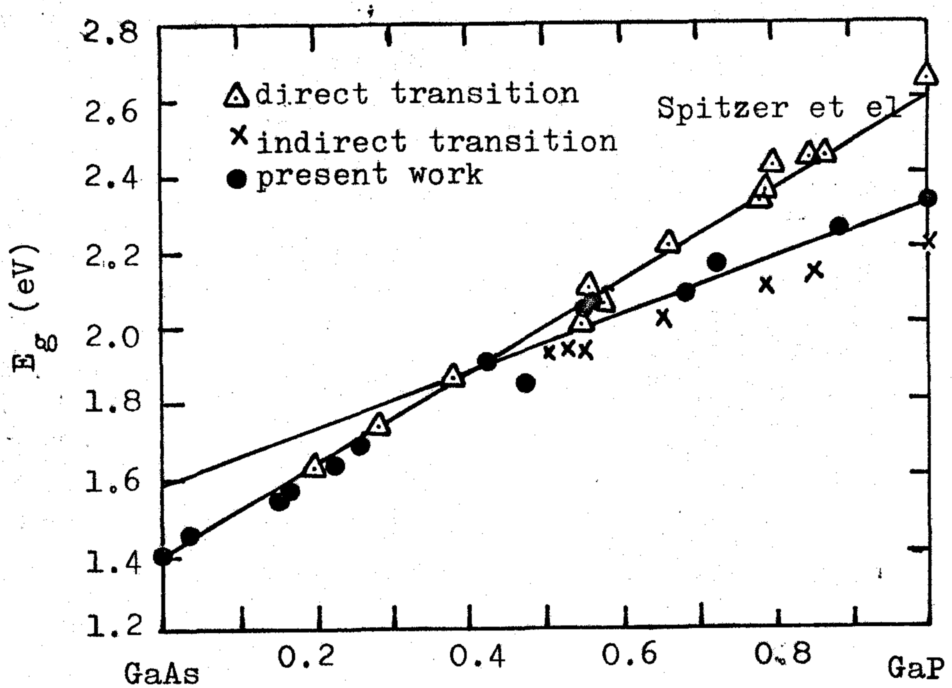

Mole Fraction of GaP

Fig. 1 Dependence of thresholds for direct and indirect transitions on composition x in $GaAs_{1-x}P_x$

is relating to the linear change of band structure in $GaAs_{1-x}P_x$ solid solutions as expected from the observation of the fundamental absorption edge.

The absorption spectra for $GaAs_{1-x}P_x$ solid solutions have been studied in detail in the infrared region as described in chapter IV, along with the electronic transition from the impurity level to the conduction band, the optical absorption due to lattice vibrations and the free carrier absorption.

It can be seen from the periodic table that group IIIb atoms have three electrons with an s^2p^1-configuration outside a core of closed shells, and that group Vb atoms have five electrons in a s^2p^3-configuration. Between them, therefore, the III and V atoms have an average of four valence electrons per atom available for binding. III-V compounds with the zinc-blende structure do indeed have properties rather like those of the group IV crystals, diamonds, silicon, germanium, and grey tin, in which covalent bonds are formed between tetrahedral sp^3-hybrid orbitals.

In III-V compounds, three idealized possibilities for the crystal bonding may be considered; covalent binding, ionic binding and neutral binding. For covalent binding each V atom donates an electronto a III atom, so that V^+ and III^- ions are formed, each with four valence electrons. These combine into sp^3-hybrids and tetrahedral bonds are formed, as in diamond. There will, however, be an additional electrostatic attraction between the charged ions. For pure ionic binding we may suppose that the III atoms donate three electrons to the V atoms, forming III^{3+} and V^{3-} ions, each with spherically symmetrical closed-shell configuration. These ions would be held together in the crystal by purely electrostatic forces. In the neutral bond,16) the III atoms retain three electrons and the V atoms five so that there is no charge difference between the atoms. These three bonding schemes represent simplified ideal cases and the actual bonding will not correspond exactly to any one of them. It appears that the bonding in III-V zinc-blende structure crystals is near to the neutral bonding scheme but with a varying degree of charge difference between the III and V atoms in the different compounds. It is not immediately obvious, however, whether electrons will tend to be transferred from the III to the V atoms or vice versa. In the thesis, some of the evidence on the partially ionic scheme of the crystal bonding will be described in chapter IV.

Generally, the wave function of the valence electrons in a III-V crystal may be represented by means of a linear combination of the wave functions of the idealized covalent and ionic structures.17) As an ionic component increases relative to a covalent one of the wave function, the bonds become polarrized towards the V atom, and a certain value of the proportion of ionic component to the covalent one will correspond to a neutral bond. The other value of its proportion will result in a charge difference between the III and V atoms. Then the effective charge, e^* might be defined as the total charge within the III atom sphere. Therefore ideally e^* would be zero for neutral binding, $-e$ for covalent binding, and $+3e$ for ionic binding.

The simplest method of measuring effective charge uses far infrared reflectivity. The shape and position of the reflectivity maximum give the low frequency and high frequency dielectric constants and the transverse optical mode frequency. The square of the effective charge can then be calculated.18) Also the X-ray diffraction experiment19) gives both the magnitude and sign of the effective charge. In chapter IV, the precise measurements of X-ray intensity on the $GaAs_{1-x}P_x$ solid solution will be reported and the advanced method of the determination of effective charge will be discussed.

If there is a transfer of charge between the atoms in III-V compounds, we may expect this to be related to the electronegativity of the two kinds of atom. Electronegativity is the power of an atom in a compound to attract electrons to itself, and electrons will tend to be transferred from atoms with low electronegativity values to those having higher ones. There is no general scale of electronegativity, because the electronegativity of an atom depends on the kind of bond. For a given type of bond, however, it should be possible to construct a self-consistent electronegativity scale[20] as shown in Table 2. We can see that the V atoms, P, As and Sb are all more electronegative than the III atoms, Al, Ga and In. Hence, in compounds between these elements we may expect a tendency for electrons to transfer from the III to the V atoms.

Table 2 Scale of electronegativity value

B 2.0	C 2.5	N 3.0
Al 1.5	Si 1.8	P 2.1
Ga 1.6	Ge 1.7	As 2.0
In I III 1.5 1.9	Pb 1.7	Sb III V 1.8 2.1
Tl I III 1.5 1.9		Bi 1.8

In the preceding paragraphs we have examined some of the evidence for the degree of charge transfer in the III-V compounds and this seems to agree qualitatively with the electronegativity values of the atoms. If we take the values of the effective charge, e*, to be a measure of the charge transfer between the atoms, we see that this implies the following sequence of electronegativities:

$$P > As > Sb > Ga > In > Al \ , \qquad (1)$$

ane this is in approximate agreement with the order of decreasing electronegativity values. This implies that in the following series of compounds there is a progressive decrease from left to right in the charge transferred from the III to the V atoms:

AlP, AlAs, InP, GaP, InAs, AlSb, GaAs, InSb, GaSb (2)

It is apparent that further work needs to be done in order to decide the nature of the bonding in III-V crystals with zinc-blende structure. The evidence of the preceding paragraph, however, suggests that the bonding scheme may be described as essentially of the neutral form but with some degree of electron transfer from the III to the V atoms, the amount of negative charge transferred decreasing with the various compounds according to the sequence (2). We may think of each III-V bond as basically a two-electron covalent bond but with some polarization towards the V atom. The degree of polarization is such that the contribution from the four bonds puts a net negative charge on the V atoms, leaving an equivalent positive charge on the III atoms. The polarization of the bonds will increase with the difference in electronegativity of the III and V atoms, giving rise to the sequence (2) of relative charge transfer in the different compounds.

As above mentioned, it is seen that the effective charge is greatly related to the electronegativity. This conception is more important to describe the formation of substitutional solid solutions of III-V compounds. As suggested by O. G. Folberth,[21)] the polarization effect is connected with the formation of solid solutions. Instead of the parameter given by

O. G. Folberth, it is assumed that the quasi-chemical interchange energy, Ω , can explain some peculiarities which are connected with the formation of solid solutions as following. Let us consider two kinds of III-V compounds, that is, $A^{III}B^{V}$ and $D^{III}E^{V}$. Since the amount of charge transfer varies from compound to compound and the differences in the electrostatic attraction alters the bond length. Thus the change of the internal energy in the quasi-binary compound seems to be caused mainly from the electrostatic part of crystal bonding. In the similar manner for the quasi-binary system, the interchange energy may be related to the difference of the electronegativities between III-V compounds by the equation,

Table 3 List of η and $(\Delta a)_{max}$

	AlP	AlAs	AlSb	GaP	GaAs	GaSb	InP	InAs	InSb
AlP		4.27	12.9	0.37	4.11	12.2	8.08	11.5	19.3
AlAs	18.1		8.35	3.88	0.15	7.65	3.64	7.00	14.4
AlSb	113	40.0		12.5	8.52	0.65	4.54	1.27	5.59
GaP	0.02	17.4	110		3.72	11.8	7.67	11.1	18.8
GaAs	20.1	0.02	38.0	18.7		7.81	3.80	7.16	14.5
GaSb	116	42.0	0.02	113	40.0		3.86	0.61	6.28
InP	0.90	27.8	134	1.22	29.5	138		3.23	10.3
InAs	11.4	0.90	52.9	10.4	1.22	55.2	18.7		6.93
InSb	94.2	28.9	0.90	91.2	27.2	1.22	113	40.0	

$(\Delta a)_{max}$ (%)

$\eta \times 10^3$

$$\Delta\Omega = P_{AB\cdot DE}\left[H_{AB\cdot DE} - \tfrac{1}{2}(H_{AB\cdot AB} + H_{DE\cdot DE})\right]$$

$$\equiv A\eta \quad , \tag{3}$$

and

$$\eta = [(\kappa_A - \kappa_B) - (\kappa_D - \kappa_E)]^2 \quad , \tag{4}$$

where A is the constant. Table 3 shows the value of η for each quasi-binary system. The quasi-binary system with the smaller value of η is easily expected to have a tendency forming solid solution. The advanced treatment will be discussed in chapter II.

In thesis, the terms of "mixed crystal", "substitutional solid solution" and "solid solution" have been used in the same meaning.

References

1) A. Thiel and H. Koelsch; Z. anorg. Chem. 65-66(1910)288

2) M. L. Huggins; Phy. Rev. 27(1926)286

3) V. M. Goldschmidt; Trans. Faraday Soc. 25(1929)253

4) A. N. Blum, N. P. Mokrovski and A. R. Regel; Seventh All-Union Conference on the Properties of Semiconductors, Kiev (1950)

5) N. A. Goryunova and A. P. Obukhov; Seventh All-Union Conference on the Properties of Semiconductors, Kiev (1950)

6) M. Welker; Z. Natur forsch. 11(1952)744

7) M. Cardona; J. Phys. Chem. Solids 24(1963)24

8) A. Sagar and R. C. Miller; J. Appl. Phys. Suppl. 32(1961) 2073

9) W. M. Becker, A. K. Ramdas and H. Y. Fan; J. Appl. Phys. Suppl. 32(1961)2094

10) R. Zallen and W. Paul.; Phys. Rev. 134(1964)A1628

11) R. F. Nelson, L. F. Johnson and M. Gershenzon; Bull. Am. Phys. Soc. 9(1964)236

12) M. D. Steerge; Phys. Rev. 127(1962)768

13) H. Ehrenreich; Phys. Rev. 120(1960)1951

14) W. G. Spitzer and C. A. Mead; Phys. Rev. 133(1964)872

15) E. Haga and H. Kimura; J. Phys. Soc. Japan 19(1964)1596

16) J. C. Slater and G. F. Koster; Phys. Rev. 94(1954)1499

17) L. Pauling; The Nature of the Chemical Bond, Oxford Univ. Press, London (1940)

18) B. Szigeti; Trans. Faraday Soc. 45(1949)155

19) N. N. Sirota; Semiconductors and Semimetals, Academic Press, vol.4 (1968) 36

20) O. G. Folberth; Z. Naturforsch. 13a(1958)856

21) O. G. Folberth; J. Phys. Chem. Solids 8(1959)14

Chapter II

Phase Diagrams of the Quasi-Binary Systems containing III-V Compounds

1. Quasi-binary phase diagram of III-V compounds

1-1) Introduction

A number of the III-V quasi-binary systems has been studied previously, since it is very important to give careful considerration to the phase equilibria. Solid solutions of these compounds in each other would provide semiconductors with a continuous range of properties such as energy gap and carrier mobility. In addition, knowledge of the solubility limits, when a complete mutual solid solubility is not realized, is very important to investigate on the nature of the chemical bond.

The first work, carried out in 1953, showed the absence of solid solutions in the system InAs-InSb.1) On the other hand, the formation of substitutional solid solutions over the entire concentration range of this system was reported in 1958.2) Similarly, studies were followed by many authors which established the phase diagram of these quasi-binary system. This work contains the experimental determinations of the quasi-binary phase diagrams of GaAs-GaP and GaAs-GaSb system.

However there have not been any considerations whether a continuous solid solution exists in the quasi-binary system. The thermodynamic properties for these systems are discussed and the resulting expression is applied to the GaAs-GaP, GaAs-GaSb, and other quasi-binary system.

1-2) Theoretical Background

It is well known that the binding energy between the III and V atoms is very strong and two kinds of atoms form a stoichiometric compound. Additively, in the quasi-binary system of these III-V compounds, the third species of atoms can be only substituted for the same group of atoms, that is, the quasi-binary compounds, $A^{III}(B^{V}_{1-x}C^{V}_{x})$, are stoichiometrically formed. Vieland's regular solution method of treating the equilibrium between a liquid and a binary compound of virtually invariant composition can be generalized to ternary systems of sub-regular solutions. The liquidus becomes a surface and the solid phase field, a line in the binary system, becomes a plane. The equilibrium treated is between the liquid and III-V mixed crystal solid solution, AB-AC in the quasi-binary section. The chemical potentials in the solid phase$^{3)}$ are

$$\mu^{s}_{AB} = \mu^{so}_{AB} + RT \ln \gamma_{AB} X^{s} , \qquad (1)$$

$$\mu^{s}_{AC} = \mu^{so}_{AC} + RT \ln \gamma_{AC} (1-X^{s}), \qquad (2)$$

where X^{s} is the mole fraction of AB in the solid solution. In this case, it is assumed that each of A-B or A-C atoms pair is a molecule, B or C, respectively. Hereafter the approximation may be called as a molecular-like pair model (MLP model). The chemical potentials in the liquid phase may be expressed as:

$$\mu^{\ell}_{i} = \mu^{\ell o}_{i} + RT \ln \gamma_{i} N_{i} , \quad i = A, B, C \qquad (3)$$

where μ_i^{10} is the chemical potential in the standard state of $N_i=1$ and γ_i is the activity coefficient of component i. At equilibrium,

$$\mu_{AB}^{s} = \mu_A^{l} + \mu_B^{l} \quad , \qquad (4)$$

$$\mu_{AC}^{s} = \mu_A^{l} + \mu_C^{l} \quad . \qquad (5)$$

The integral molar free energy of liquid is given by

$$G^{l} = N_A\mu_A^{l} + N_B\mu_B^{l} + N_C\mu_C^{l} \, . \qquad (6)$$

In the quasi-binary section, always assuming that N_A is 0.5 and $N_B+N_C=0.5$, the integral molar free energy may be expressed as:

$$G^{l} = N_B[\mu_A^{l} + \mu_B^{l}] + N_C[\mu_A^{l} + \mu_C^{l}] \, . \qquad (7)$$

Then the composition changes only in the section of $N_A=0.5$, and the free energy is given as an uni-variable function of composition. The above equation is assumed to be written by the compositive chemical potentials, μ_{AB}^{1} and μ_{AC}^{1} as

$$G^{l} = X^{l}\mu_{AB}^{l} + (1-X^{l})\mu_{AC}^{l} \qquad (8)$$

where X^1 is the mole fraction of the composite, AB and

$$\mu_{AB}^{l} = \mu_A^{l} + \mu_B^{l} \qquad (9)$$

$$\mu_{AC}^{l} = \mu_A^{l} + \mu_C^{l} \qquad (10)$$

As above discussed, the equilibrium of liquid and solid in the quasi-binary section can be treated similarly to a AB-AC binary system (hereafter B-C binary system). In fact, the assumption seems to be reasonable in the system containing III-V compounds.

Assuming that the solution constituted by two components, B and C, is regular, the chemical potential of each component is expressed by

$$\mu_B = \mu_B^\circ + RT\ln X_B + (1-X_B)^2\Omega \ , \qquad (11)$$

$$\mu_C = \mu_C^\circ + RT\ln X_C + (1-X_C)^2\Omega \ , \qquad (12)$$

where X_B is the mole fraction of B, Ω is the quasi-chemical interchange energy and μ_i° is the chemical potential in the standard state of $X_i=1$.

The change in the free energy on fusion can be approximately written as:

$$\Delta G_{fi} = \Delta H_{fi}\,(1 - T/T_{m.p.i}) \qquad (13)$$

where

$$\Delta H_{fi} = T_{m.p.i}\,\Delta S_{fi} \qquad (14)$$

and ΔH_{fi} and ΔS_{fi} are the enthalpy and entropy of fusion respectively, and $T_{m.p.i}$ is the melting point of pure substance, i. An estimate of the entropy of fusion of GaAs can be obtained by a comparison with the entropy of fusion of Ge. The entropy of fusion of GaAs would be expected to be approximately twice the entropy of fusion of Ge(6.7 e.u.) plus a mixing entropy term of R ln 4; about 16.2 e.u. as shown by the equation,

$$\Delta S_f(GaAs) = 2\Delta S_f(Ge) + R\ln 4 \qquad (15)$$

Similarly, the values of the entropy of fusion for the other III-V compounds can be obtained as shown in Table 1, where the other data reported by previous authors are listed.

Table 1 Values of entropy and enthalpy of fusion

Compound	Melting Point $T_{m.p.}$ (°C)	ΔS_f (e.u.)			H_f (kcal/gmole)	
		Value estimated		Literature value	Value estimated	Literature value
AlP	2000	$2\Delta S_f(Si) + R\ln 4$	17.03		48.64	
AlAs	1600	$\Delta S_f(Si)+\Delta S_f(Ge)+R\ln 4$	16.25		30.44	
AlSb	1080	$\Delta S_f(Si)+\Delta S_f(Sn)+R\ln 4$	15.08		20.40	14.2 [20]
GaP	1540	$\Delta S_f(Si)+\Delta S_f(Ge)+R\ln 4$	16.25		29.45	
GaAs	1238	$2\Delta S_f(Ge)+R\ln 4$	15.47	14.7 [3] 13.9 [21] 15.3 [22] 16.64 [23]	23.38	21 [20]
GaSb	712	$\Delta S_f(Ge)+\Delta S_f(Sn)+R\ln 4$	14.30		14.10	12 [20]
InP	1060	$\Delta S_f(Si)+\Delta S_f(Sn)+R\ln 4$	15.08		20.10	12 [20]
InAs	942	$\Delta S_f(Ge)+\Delta S_f(Sn)+R\ln 4$	14.30	14.7 [3] 21.4 [21] 10.4 [22] 11.5 [24]	17.38	26 [20]
InSb	530	$2\Delta S_f(Sn)+R\ln 4$	13.12	12.2 [26] 11.3 [21] 13.3 [3] 11.9 [22] 14.1 [25] 14.4 [24]	10.53	12.2 [20] 9.3 [20]

Applying the MLP model in the quasi-binary system, the calculation of phase diagram can be performed in two ways. One is that both liquid and solid solution are ideal. Then the liquidus and solidus can be given as a function of temperature by

$$X_B^\ell = \left\{ \exp\left[\frac{\Delta H_{fC}}{R}\left(\frac{1}{T} - \frac{1}{T_{m.p.C}} \right) \right] \right\} \Big/ \left\{ \exp\left[\frac{\Delta H_{fC}}{R}\left(\frac{1}{T} - \frac{1}{T_{m.p.C}} \right) \right] - \exp\left[\frac{\Delta H_{fB}}{R}\left(\frac{1}{T} - \frac{1}{T_{m.p.B}} \right) \right] \right\}, \quad (16)$$

$$X_B^S = X_B^\ell \exp\left[\frac{\Delta H_{fB}}{R}\left(\frac{1}{T} - \frac{1}{T_{m.p.B}} \right) \right] . \quad (17)$$

It is apparent that the difference of compositions between solidus and liquidus rises from the change in the free energy on fusion.

On the other hand, under an assumption of regular solution, the condition which means that chemical potentials must be equal for the two phases is represented as follows.

$$RT \ln X_B^\ell + (1 - X_B^\ell)^2 \Omega_\ell + \Delta G_{fB} = RT \ln X_B^S + (1 - X_B^S)^2 \Omega_S , \quad (18)$$

$$RT \ln X_C^\ell + (1 - X_C^\ell)^2 \Omega_\ell + \Delta G_{fC} = RT \ln X_C^S + (1 - X_C^S)^2 \Omega_S , \quad (19)$$

These equations cannot be solved analytically, but can be solved numerically on the computer for given temperature.

1-3) Experiments and results

a) GaAs-GaP system

As is well known already, continious solid solutions are formed in the GaAs-GaP system, and the change of their lattice parameters with composition obeys Vegard's law.$^{4)}$ This fact proves that its solid solution behaves like an ideal one. This work is concerned with the phase diagram of this system, and its thermodynamic properties will be discussed.

Specimens of GaAs-GaP alloys were prepared by the two temperatures method,5) and all of compositions over the system were obtained, where these compositions were determined by powder X-ray method. Melting points (m.ps.) of these alloys were determined using the apparatus reported by Mori et al.6) as shown in Fig. 1.

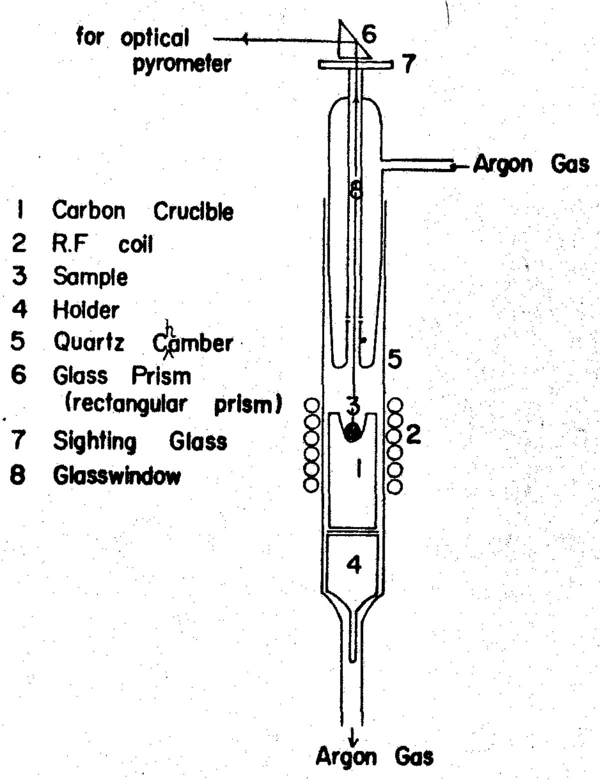

Fig. 1 The apparatus for measuring melting points

It consists of a RF coil and a chamber charged with graphite boat. The sample is heated in argon atomospher of about one atm. The measurement of m.P. was taken on the two color eye optical pyrometer and its value corrected with respect to the influence of sublimation of volatile components. The results are shown in Fig. 2, in which dotted lines are theoretical solidus and liquidus.

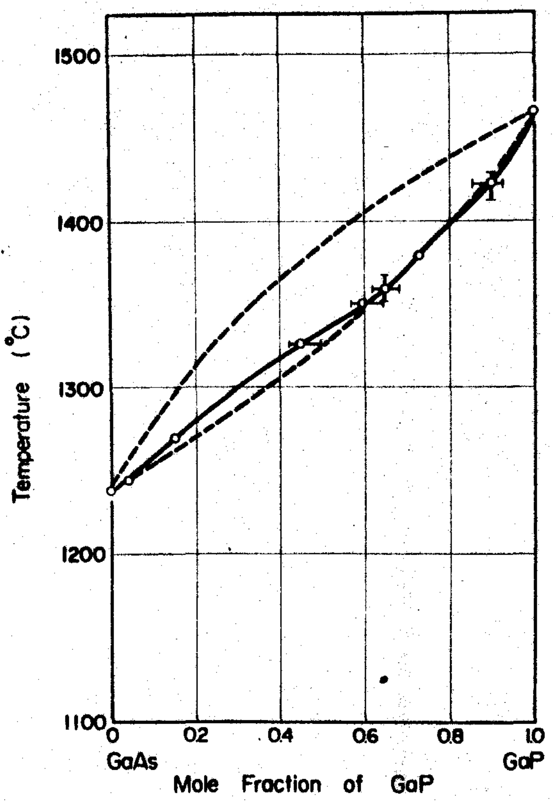

Fig. 2 Phase diagram of GaAs-GaP quasi-binary system. Solid and dotted lines show the experimental data and theoretical curves, respectively.

Assuming that, in GaAs-GaP quasi-binary system, each of Ga-As or Ga-P atoms pair is a molecule, B or C, respectively, and these molecules form an ideal solution, the equilibrium relation of reaction between liquid and solid phase can be calculated as the similar manner discussed in the previous section. The entropies of fusion of GaAs and GaP have not been measured. An estimate of these entropies can be obtained by a comparison with entropies of IV-group elements as same as done by Thurmond,[7)] but whose values are employed from the table of Kubaschewski.[8)] The entropy of fusion of GaAs would be expected to be approximately twice the entropy of Ge (6.4 e.u.) plus a mixing entropy term of R ln 4: about 15.5 e.u.. Similarly the entropy of GaP is estimated to be 16.3 e.u.. Using these values, Equs.(16) and (17) would be actually calculated as shown in Fig. 2. The experimental values can be explained well by the theoretical solidus line except a small deviation. Although we can not definitely conclude the thermodynamic properties of this system, it appears to be the proof that our molecular-like pair model of Ga-As or Ga-P atoms is a good approximation for such covalent quasi-binary compounds.

b) GaAs-GaSb system

O. G. Folberth[9)] has denied the existence of a complete range of solid solutions in GaAs-GaSb system. Recently, R. B. Clough and J. J. Tietjen[10)] have grown alloys of $GaAs_{1-x}Sb_x$ with compositions ranging from 1 to 80 mole pct GaAs, as well as GaSb by using a vapor-phase epitaxial growth technique.

The purpose of this paper is to clarify these disagreements[11)] in the phase equilibria of a GaAs-GaSb system by means of differential thermal analysis, microscopic observation, and measurements of lattice constants by X-ray method.

b-i) Experimental

(i) Differential thermal analysis

We have found it convenient to empoly differential thermal analysis to determine liquidus and eutectic temperatures. Ga, As and Sb with purities better than 99.999% pct were used in this work. The required amounts of GaAs and GaSb which were prepared previously were weighed and sealed under vacuum into fused silica capsules (11.5 ϕx34 mm) with a hole for the thermocouple with the shape shown in Fig. 3 (a). Fused silica capsules were previously immersed in HF solution for 20 minutes and washed by water and then dried. The differntial thermal analysis cell was placed in a inconel block (350 ϕx560 mm in length) with two holes for the differential thermocouples inside a resistance furnace. The inconel block was provided with a cover of the same material to ensure temperature homogenization as shown in Fig. 3 (b). Pt-Pt 13%Rh thermocouple was used for temperature measurement. The furnace, and thus the inconel block and the thermal analysis cell were heated to 1270 °C in order to melt together completely since the

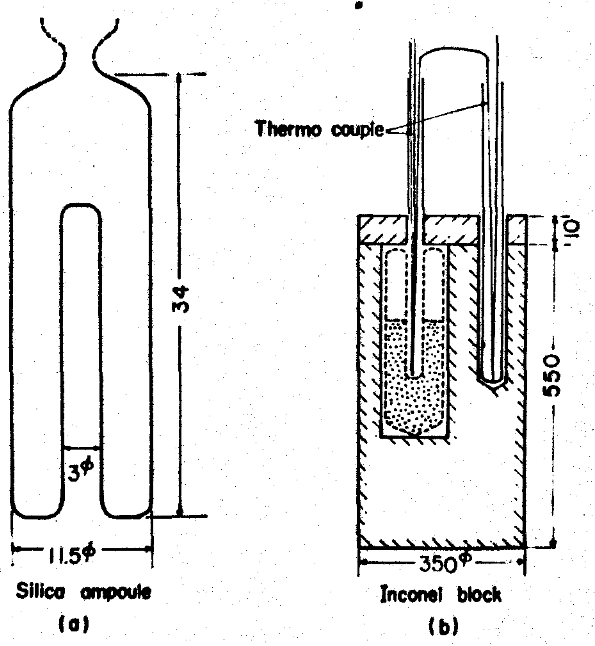

Silica ampoule
(a)

Inconel block
(b)

Fig. 3 The apparatus for differential thermal analysis melting temperature for GaAs compound is 1238 °C, (although that for GaSb 712 °C). After holding at the temperature for 30 min., the furnace power was reduced gradually to maintain a constant cooling rate of 1.5 °C per minutes. The difference between a specimen and the inconel block was amplified by about 30 times and then noted by a X-Y recorder. The transformation temperatures were determined from inflection points, which appeared in every cooling curve thus obtained. These inflection points, and thus the transformation temperatures seem to be reasonably accurate since the temperature difference between a specimen and the inconel block was very small within several degree centigrade, and its amplification was very well regulated. The chemical compositions of the specimens were considered to be indentical to the weighed amounts of the component elements, which were shown in Table 2.

Table 2 Compositions of alloys and results of thermal analysis

Composition of solutions (mol% GaAs)	1.00	10.0	20.0	35.0	50.0	70.0
Liquidus temperature (T°C)	773	919	959	1067	1101	1163
Eutectic temperature (T°C)	703	708	702	708	705	703

(ii) Microscopic observation

Microscopic observation was carried out to determine whether the two compounds are mutually soluble in all portions or miscibility in the solid state is limited. Very slow cooling rate and very long time homogenization of the specimens for microscopic observation were adopted to realize the conditions near equilibrium. The specimens were carefully polished on the final cloth after preliminary grinding by fine emery papers. Etching was not needed, since structural details was revealed immediately after polishing because of the difference in hardness among constituents.

(iii) Determination of lattice constants

Lattice constants of the specimens used for thermal analysis were determined by Debye-Scherrer method by using Norelco diffrectometer. The diffraction angles were determined within the accuracy of about 0.008^{0} from the X-ray peaks calibrated by the standard angles of Si powder. The accuracy seemed to be sufficient to precise determination of lattice constants when compositions of compounds changed very slightly.

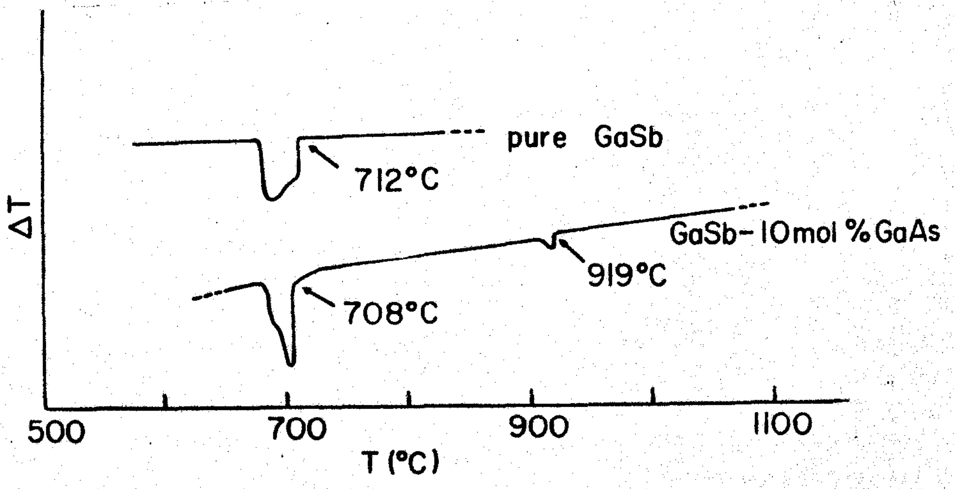

Fig. 4 Typical cooling curves

b-ii) Results and discussion

The typical cooling curves are shown in Fig. 4. Two distinct deflection points are observed for a GaSb-10 mol% GaAs specimen. Table 1 shows results of thermal analysis, together with compositions of alloys. From the results, eutectic type diagram with eutectic temperature at 708 °C was obtained as shown Fig. 5.

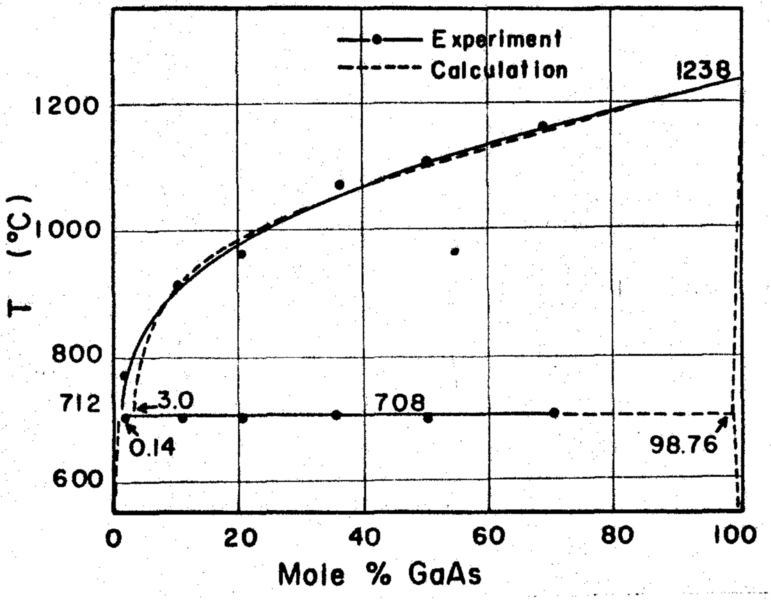

Fig. 5 GaAs-GaSb phase diagram

Photo. 1 and 2 are the typical photomicrographs. A GaSb-50 mol% GaAs specimen in Photo. 1 was melt together at 1255 °C, held for 1 hr. and cooled very solwly down to 740 °C, and then held at this temperature for 2 hrs and cooled in the furnace. Moreover, the specimen was homogenized for long time at 630 °C, and then quenched into water. This microphotograph indicates the location of the primary GaAs black crystals and a eutectic mixture of GaAs and GaSb crystals. Photo. 2 shows the microphotograph of GaSb-70 mol% GaAs specimens used for thermal analysis, where a larger quantity of the primary GaAs than the other specimen are recognized. From the results of microscopic observations, it appears very likely that this quasi-binary system is eutectic type, and not complete solid solution type.

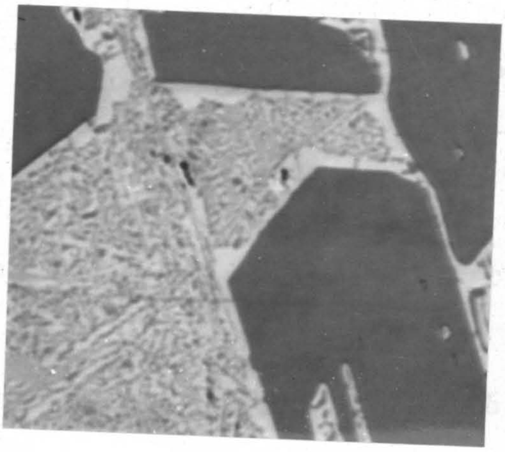

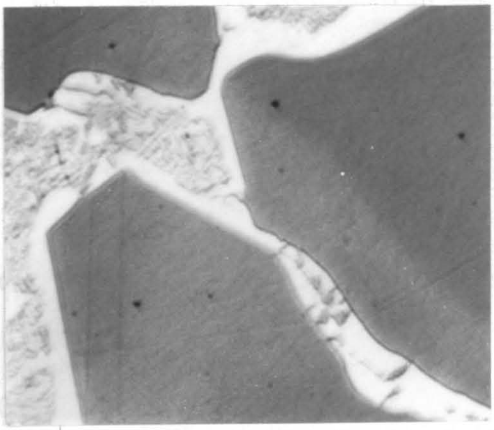

Photo. 1 Microphotograph of GaSb-50 mol% GaAs alloy

Photo. 2 Microphotograph of GaSb-70 mol% GaAs alloy

The following further definite evidence is found to confirm a limited miscibility in the solid state for the quasi-binary system. Fig. 6 shows X-ray diffraction curves for GaAs, GaSb and GaSb-70 mol% GaAs specimen which are shown in dotted, dashed and solid line respectively. The X-ray diffraction profile for GaSb-70 mol% GaAs specimen is clearly shown to be consisted of GaAs and GaSb phases, whose lattice constants are slightly different from those of stoichiometric compounds. The peaks corresponding to GaAs and GaSb phases shift slightly toward ones for GaSb and GaAs respectively. These lattice constants calculated

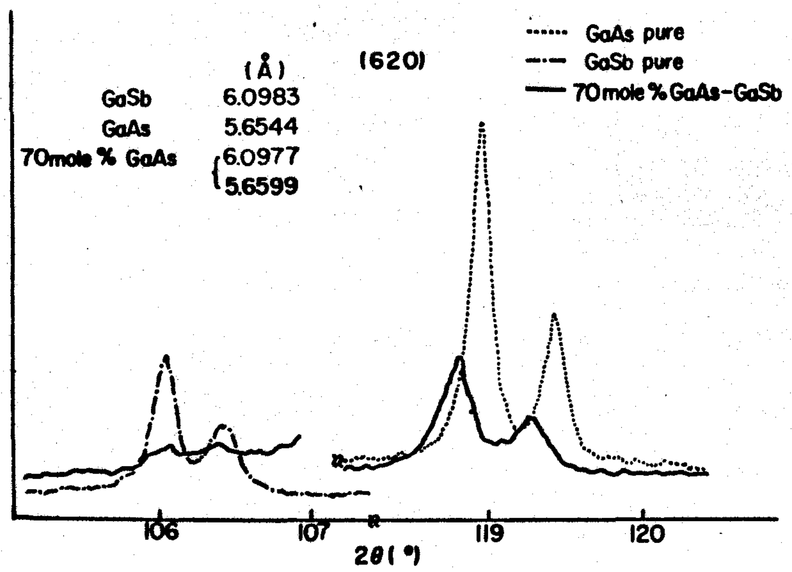

Fig. 6 Intensity distribution of (620) diffraction line

from present measurements are 6.0983 Å for GaSb, 5.6544 Å for GaAs and, then 6.0977 and 5.6599 Å for two phases in the specimen respectively. Differences between the two stoichiometric compounds and the two phases corresponding to each compounds are 1.24 mol% (GaAs phase) and 0.14 mol% (GaSb phase) respectively. From above results it is apparent that a miscibility gap occurs in the quasi-binary system, whose compound components have small solid solubility.

In the next place, some thermodynamic calculations will be carried out by using some present data to discuss a solid solubility and an eutectic composition. As discussed in section 1-2), under an assumption of regular solution, the condition which means that chemical potentials must be equal for the two phases is represented as given in equations (18) and (19).

Similarly, the condition of equilibrium between solid and solid phase is represented as follows.

$$RT\ln X^{\alpha} + (1-X^{\alpha})^2\{D+2X^{\alpha}E\} = RT\ln X^{\beta} + (1-X^{\beta})^2\{D+2X^{\beta}E\}, \quad (20)$$

$$RT\ln(1-X^{\alpha}) + (X^{\alpha})^2\{D+(2X^{\alpha}-1)E\} = RT\ln(1-X^{\beta}) + (X^{\beta})^2\{D+(2X^{\beta}-1)E\}. \quad (21)$$

In above equations, concentration dependence for solid phase is considered as $\Omega_s = D+E_x$, where x is concentration and D and E constants. We have calculated $\Omega_s = 8{,}670 + 4{,}230x$ cal/mole by using the experimental data of 1.24 and 0.14 mol% for each mutual solubility between GaAs and GaSb phases, and equations (20) and (21). The composition of eutectic point and interaction energy for liquid phase can be calculated from equations (18) and (19) to be 3.0 mol% GaAs and -1,470 cal/mole respectively. The results obtained from the calculation from equation (18) and (19) by using the parameters mentioned above are shown in both Table 3 and Fig. 5.

Table 3 Calculated values for x and x_s

Temperature (°K)	x_ℓ (mol%)	x_s (mol%)
1192	10.0	99.37
1374	50.0	99.78
1436	70.0	99.90

Since stoichiometric compounds are easily formed between III and V elements because of their large binding energy, the molecular pair model[12)] is assumed to be applied to GaAs and GaSb compounds, and thus the binary solution is taken to be regular. There seems the good agreement between the experimental and the binary regular liquidus curves except near the eutectic temperature. As for the equilibrium between a liquid and solid, for example, calculated values for compositions of a liquid and solid in equlibrium at 1163 °C are 70.0 mol% GaAs and 99.90 mol% GaAs respectively. The results described above are verified by the experimental fact that the crystallized GaAs has only a very little solubility for GaSb. On the other hand, as for solid-solid equilibrium, solid solubility of GaAs in GaSb at 600 °C is calculated to be 0.092 mol% GaAs. It may be necessary to take into account of vibrational entropy for the more exact estimation.

b-iii) Summary

The quasi-binary diagram of GaAs and GaSb have been investigated by means of differential thermal analysis, microscopic observations and X-ray measurements of lattice constants. Thermodynamic calculations were also carried out by using some present data.

From these results it was concluded that this quasi-binary system is simple eutectic type, whose eutectic point occurs at 3.0 mol% GaAs at 708 °C. Solid solubilities in both GaAs and GaSb terminal solutions are found to be about 0.2 mol%.

c) Other quasi-binary system of III-V compounds

Many phase diagram of III-V compounds reported by other authors can be examined using the mathematical method described previously. In this section, the applicability of the MLP model to some quasi-binary systems can be tested by comparing the available experimental phase diagram data with the calculated results.

c-i) InSb-InAs system

The system was first studied in reference (1) and then in reference (13); in both studies, no solid solutions were found in the system. In 1958 the formation of substitutional solid solutions over the entire concentration range of this system was reported in reference (2). The phase diagram is shown in Fig. 7, where the dotted lines have been calculated by an ideal approximation, and the solid lines correspond to the regular approximation. The interaction parameter was determined by fitting one calculated solidus point to the experimental value, the good agreement between calculation and experiment for the liquidus and solidus across the entire diagram is valid evidence in support of the model.

c-ii) InAs-GaAs

The system was first studied by X-ray diffraction,13) and was later studied in more detail with a larger number alloys.3) The change in lattice spacings with composition showed a very close agreement with Vegard's law. The interaction parameters of Ω_s and Ω_l determined by curve fitting have been 2,445 and 467 cal/mole. The phase diagram is shown in Fig. 8.

c-iii) InSb-GaSb system

The formation of solid solutions in this system was first established by X-ray diffraction.13) The phase diagram was established by the authors28),29),30) as shown in Fig. 9. In the figure, the solid lines have been calculated, assumed that $\Delta\Omega_\ell$ and $\Delta\Omega_s$ are 0 and 1,500 cal/mole respectively.

c-iv) AlSb-GaSb system

The existence of solubility was predicted in this system31) despite the data where no solid solutions were observed.28) In a number of subsequent works32),33),34) the formation of solid solutions was confirmed as shown in Fig. 10, where solid lines have been calculated, assumed that both $\Delta\Omega_\ell$ and $\Delta\Omega_s$ is -5,000 cal/mole.

c-v) InSb-AlSb system

Preliminary investigations enabled the authors31) to state that this system contains a continuous series of substitutional solid solutions. Later35),36),37) homogeneous samples of the alloys were obtained. The interaction parameters of $\Delta\Omega_s$ and $\Delta\Omega_\ell$ determined by curve fitting have been 37 and -80 cal/mole respectively.

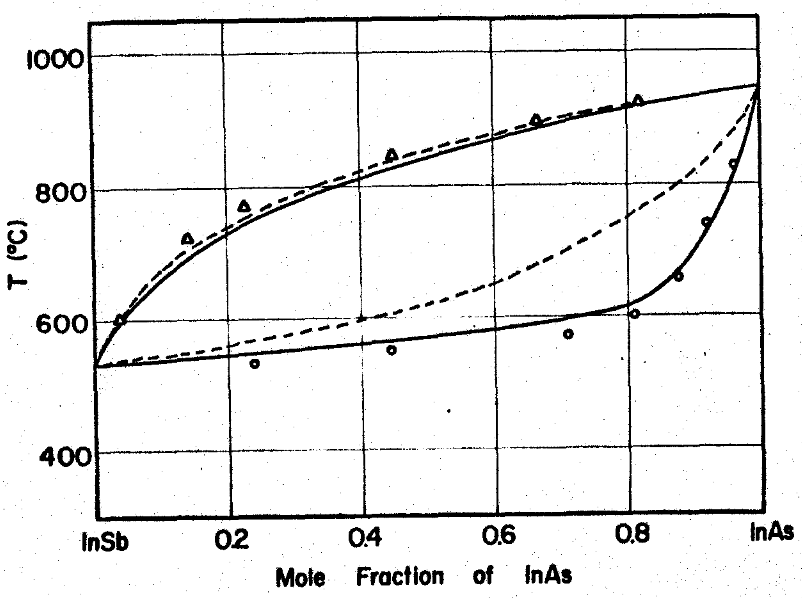

Fig. 7 InSb-InAs phase diagram

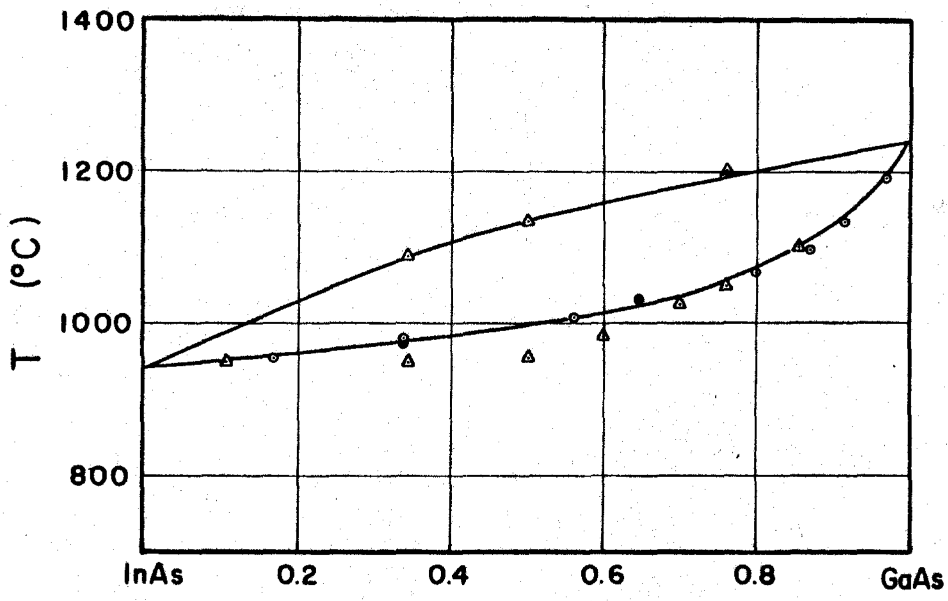

Fig. 8 The InAs-GaAs quasi-binary phase diagram

Solid lines were calculated; △ Van Hook and Lenker [14]; ⊙ Woolley and Smith [2]; ● Hockings et al. [15]

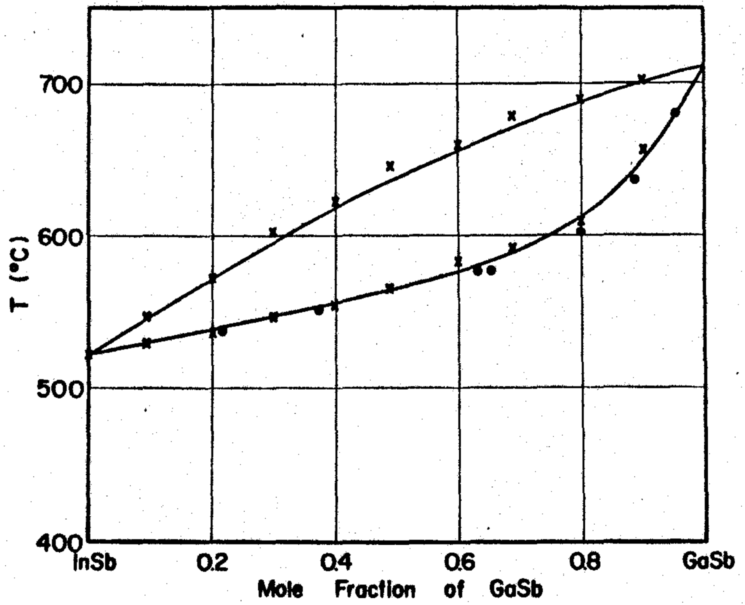

Fig. 9 InSb-GaSb phase diagram

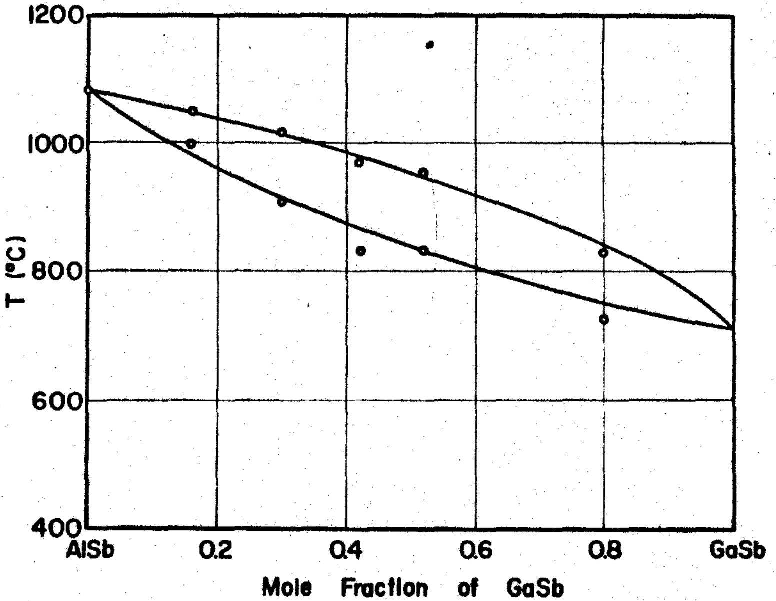

Fig. 10 AlSb-GaSb phase diagram

Observed data (o) given by A. S. Borchchevskii et al.[34] and solid lines calculated

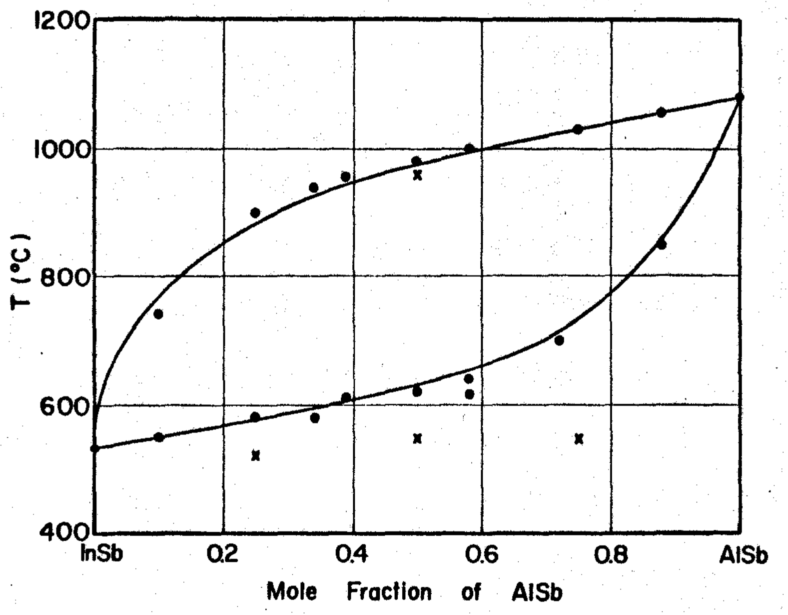

Fig. 11 InSb-AlSb phase diagram

Experimental values given by D. Effer[37)] and solid lines calculated.

1-4) Discussion

If we consider the various groups of semiconducting materials, we find some general rules governing the variation of the energy gap and the thermodynamic property. Thus it is well known that the energy gap decreases with increasing atomic number; for instance, the energy gap of the elements of group IV of the periodic system decreases from diamond to gray tin. A similar rule exists also for the semiconducting $A^{III}B^{V}$ compounds. Furthermore the $A^{III}B^{V}$ compounds all have higher energy gaps than the corresponding isoelectronic elements of group IV. These rules were set forth by Welker[16)] in 1952, on the basis of binding theory. The essential basis of the argument was that for the $A^{III}B^{V}$

compounds there exist a small additional ionic bond which arises from the inequality between the two kinds of atoms, namely the A^{III} and the B^{V} atoms. The covalent bond and the ionic bond come to resonance according to Pauling17) and the result is a larger total binding strength and from this a larger energy gap. However, it is not possible to explain by this concept alone the differences between the energy gaps of $A^{III}B^{V}$ compounds with the same mean atomic weight, the so-called isoelectronic compounds. Therefore a further factor must exist, whose effect is greater than that of the binding strength. Folberth18) proposed a model for the interpretation of the characteristic properties of the $A^{III}B^{V}$ compounds. To a first approximation all $A^{III}B^{V}$ compounds have the same difference between the potential valleys at the sites of the A^{III} and B^{V} atoms. In this approximation it is assumed that every B^{V} atom gives one valence electron to an A^{III} atom, so that all atoms now share equally four valence electrons. These charged atoms could now build up a crystal having a tetrahedral structure like the elements of group IV. The resulting structure has the ZnS lattice. In this approximation the difference in charge between the B^{V} and the A^{III} sites amounts to two electronic charges uniformly for all $A^{III}B^{V}$ compounds.

For a better approximation it is still necessary to consider the deformation of the electronic structure caused by the abovementioned charge difference, namely the polarization of the valence and the inner-shell electrons in the direction towards the B^{V} atoms. This polarization differs for the various $A^{III}B^{V}$ compounds; it increases with increasing difference in electronegativity between the B^{V} and A^{III} atoms, and therefore it increases with increasing ionic bond. It increases also with the atomic weight. If the polarization is very small, the valence electrons are almost equally distributed over the valence bridges in the same manner as in the elements of group IV. So the potential is essentially determined by the difference of charge between B^{V} and A^{III} sites. By making certain assumptions it is possible to estimate the polarization in arbitrary units by the following formula;

$$J = \frac{E_{ion}}{E_{cov}} (Z^{III} + Z^{V})^{3/2} \qquad (22)$$

where E_{ion} is the ionic extra energy according to Pauling, E_{cov} is the covalent binding energy, and Z^{III} and Z^{V} are the atomic numbers of the elements A^{III} and B^{V}, respectively. The concept of electronegativity of the component elements is often used for the determination of the ionic component of interaction energy in III-V compounds. According to Pauling,19) the ionic component of bond energy is equal to the squared difference of electronegativities of each component:

$$E_{ion} = const.\, (K_A - K_B)^2 \qquad (23)$$

Also the covalent component of the interaction energy may be estimated in comparison with the bonding energies of group IV atoms. These results are shown in Table 4, where the total energy, $E_F = E_{cov} + E_{ion}$, is listed in coulmn 5th. Thus the total energy of III-V compound constituted almost from the covalent term is greatly larger than the interchange energy of the III-V

Table 4 Binding energies and polarization factor

$A^{III}B^{V}$	Electronegativity 27)	E_{ion} kcal/mole	E_{cov}^{III-V} kcal/mole	E_F kcal/mole	$\frac{E_{ion}}{E_{cov}}$ (%)	J
AlP	Al 1.05 P 1.862	60.8				
GaP	Ga 1.055 P 1.862	60.07	273.85	332.15	17.5	66.7
InP	In 1.02 P 1.862	65.4	258.45	323.95	20.2	130.0
AlAs	Al 1.05 As 1.725	42.0				
GaAs	Ga 1.055 As 1.725	41.4	270.45	311.95	13.3	78.6
InAs	In 1.02 As 1.725	45.8	256.1	302.1	15.2	133.5
AlSb	Al 1.05 Sb 1.525	20.8	280.8	301.6	6.9	38.0
GaSb	Ga 1.055 Sb 1.525	20.4	268.85	289.35	7.1	56.6
InSb	In 1.02 Sb 1.525	23.5	255.2	278.8	8.47	92.5

Table 5 Peculiarity in the quasi-binary system of III-V compounds

System	$(\Delta a)_{max}$	ΔJ	ζ	Ω_S (cal/mole)		Nature of interaction
				from MLP model	Literature value	
InAs-InP	3.23%	3.5	0.018769	0		Solid solutions over the entire concentration
GaAs-GaP	3.72	11.9	0.018769	0, (5,000*)		ditto
InSb-GaSb	6.28	35.9	0.001225	1500		ditto
InSb-AlSb	5.59	54.5	0.000900	37		ditto
GaSb-AlSb	0.65	18.6	0.000025	-5000		ditto
InAs-GaAs	7.16	54.9	0.001225	2445	2800 [3]	ditto
InSb-InAs	6.93	41	0.040000	2090	2900 [3]	ditto
InSb-InP	10.3	37.5	0.113569			
GaSb-GaAs	7.81	22	0.040000	8670+4230x		Phase separation
InP-GaP	7.67	63.3	0.001225			
GaSb-GaP	11.8	10.1	0.113569			

* See the chapter III.

quasi-binary energy, even though the interchange energy is an important factor to present whether the continious solid solution in a given quasi-binary system is formed or not.

The polarization effect may also explain some peculiarities which are connected with the formation of solid solution. From metallic alloy systems it is known that a continuous solid solution exists if the two components crystallize in the same crystal system and if the lattice constants do not differ by more than approximately 10 per cent. These conditions also apply in semiconducting systems, but they are not always sufficient. A study of the quasi-binary systems between $A^{III}B^{V}$ compounds shows that in some of these systems continuous solid solutions do not form or form only to a limited extent. This is the case even though the lattice constants satisfy the above-mentioned conditions well. These facts may be explained in the following way. If the polarization values of the two compounds differ too greatly, a considerable distortion of the electronic structure results. Consequently the internal energy is raised and decomposition is favoured, since the system then passes into a state with lower energy. In Table 5 the relative disparity between the lattice constants and the difference in the polarization values are listed for various quasi-binary systems Evidently a continuous solid solution exists only in those systems for which the polarization values and the lattice constants do not differ very markedly. For the same reason, continuous solid solutions do not exist between $A^{III}B^{V}$ compounds and elements of group IV. For example, GaAs and germanium do not mix together over a wide range in spite of having almost equal lattice constants. By the same reasoning it follows that continuous solution between a $A^{III}B^{V}$ compound and a $A^{III}B^{V}$ compound is not possible. However, when the average value of melting points of two terminal compounds is defined as $\langle T \rangle$ and the interchange energy, Ω_s divided by $R\langle T \rangle$ has been considered for various quasi-binary systems, a correlation has been found between $\Omega_s/R\langle T \rangle$ and η.

Near the ends of the quasi-binary systems, the formation of solid solutions is favoured by the increased influence of the entropy in there regions. In these cases solid solutions may exist even if the above-mentioned rules are not satisfied.

1-5) Conclusion

In this section, the following contents could be concluded:

(1) The thermodynamic properties for III-V quasi-binary systems have been concerned and the molecular like pair model could be established to be applicable to these systems.

(2) The quasi-binary phase diagrams of GaAs-GaP and GaAs-GaSb system have been determined in the present work.

(3) The applicability of the MLP model to some quasi-binary systems could be tested by comparing the available experimental phase diagram data with the calculated results.

(4) The interaction parameters obtained by curve fitting for experimental data in these systems seemed to have the same tendency with the expected effect from the crystal binding theory.

2. Calculation of binary phase diagram

2-1) Introduction

A method of calculating the phase diagrams is extremely desirable because the experimetnal determination of the diagrams including liquidus and solidus curves requires many times and introduce the large degree of uncertainty in the results. The calculation of the phase diagrams is worthy to examine the thermodynamic properties of any multicomponent system. However, the general functions representing the equilibrium relation are difficult to be solved analytically, but can be solved numerically on a computer. In the work, the computations of the binary phase diagrams have been performed for the ideal, regular and athermal solutions. For the present purpose, it is conveniently assumed that the solution is the binary system and two constituent substances are designated by A and B.

2-2) Theoretical background

The relative partial molar free energy (also called partial molar free energy of mixing) is the change in total free energy upon mixing 1 mole of pure substance i with an infinite quantity of a solution of given composition for fixed values of P and T,

$$G_i^M = \bar{G}_i - G_i^\circ \quad . \qquad (24)$$

In accordance with Scatchard,1) the deviation of the relative partial molar free energy, G_i^M, from that for an ideal solution, $RT\ln x_i$, may be called the excess partial molar free energy of component i is and designated by the symbol G_i^{xs},

$$G_i^{xs} = G_i^M - RT\ln X_i = RT\ln \gamma_i \quad (25)$$

Accordingly, the excess integral molar free energy G^{xs} of a solution is defined as the deviation of the relative integral molar free energy, G^M, from that for an ideal solution, $RT(x_A \ln x_A + x_B \ln x_B)$:

$$G^{xs} = G^M - RT(X_A \ln X_A + X_B \ln X_B) = RT(X_A \ln \gamma_A + X_B \ln \gamma_B) . \quad (26)$$

Also the excess value for enthalpy, H^{xs}, identical with the corresponding relative quantity, H^M, since the relative quantity referring to enthalpy vanishes for an ideal solution. The excess integral molar entropy, S^{xs}, equals

$$S^{xs} = S^M + R(X_A \ln X_A + X_B \ln X_B) . \quad (27)$$

Accordingly, the excess molar entropy and enthalpy are connected to the excess integral molar free energy as follows:

$$G^{xs} = H^{xs} - TS^{xs} . \quad (28)$$

Some thermodynamic relations for the excess values are easily shown as

$$S^{xs} = -\frac{\partial G^{xs}}{\partial T} , \quad (29)$$

$$H^{xs} = -T^2 \frac{\partial (G^{xs}/T)}{\partial T} , \quad (30)$$

$$\ln \gamma_i = \frac{1}{RT}\left(\frac{\partial G^{xs}}{\partial N_i}\right) . \quad (31)$$

Discussing the thermodynamic properties of solutions, it is conventional to define the solution in three ways. One is an ideal solution which obeys Rault's law over all temperatures and pressures at which it is capable of existing. The other solutions are the regular and the athermal solution as following.

Regular Solution

Regular solution is characterized by

$$S^{xs} = 0, \text{ and } H^{xs} \neq 0 \ . \tag{32}$$

Therefore, the relation of Eq.(31) using Eq.(26) is reduced to

$$\frac{\partial G^{xs}}{\partial T} = R \sum_i x_i \left\{ \ln \gamma_i + T \frac{\partial \ln x_i}{\partial T} \right\} = 0 \tag{33}$$

Always being $S^{xs}=0$ over all composition range, $\frac{\partial S^{xs}}{\partial x_i}$ equals to zero, accordingly

$$\frac{\partial RT \ln \gamma_i}{\partial T} = 0 \ . \tag{34}$$

Thus the excess integral molar free energy and the excess partial molar enthalpy in the binary system are given by

$$G^{xs} = \alpha x_1 x_2 \tag{35}$$

and

$$H_i^{xs} = \alpha (1 - x_i)^2 \ , \quad i = A, B \tag{36}$$

where α is the parameter independent of temperature and is called the quasi-chemical interchange energy as discussed later.

Athermal solution

The solution is defined as

$$H^{xs} = 0, \text{ and } S^{xs} \neq 0, \tag{37}$$

and additively

$$\frac{\partial \ln \gamma_i}{\partial T} = 0. \qquad (38)$$

The logarithmic activity coefficient is independent of temperature as shown in Eq.(38) and may be expressed as a function of composition by

$$R \ln \gamma_i = \beta (1 - X_i)^2 , \quad i = A, B \qquad (39)$$

In the binary system, the excess integral molar free energy and the excess partial molar entropy are obtained as

$$G^{xs} = - T\beta \, X_A X_B , \qquad (40)$$

$$S_i^{xs} = - T\beta (1 - X_i)^2 , \quad i = A, B \qquad (41)$$

where β is the constant. Here, the physical meanings of constants, α and β, should be understood from the aspects of the statistical mechanics as mentioned later.

For the binary system at equilibrium, the essential concept is that the chemical potential of any component is identical in all phases. It follows that

$$\mu_A^{I} = \mu_A^{II}, \quad \mu_B^{I} = \mu_B^{II} , \qquad (42)$$

where the superscripts, I and II, are referred to two phases, respectively.

2-3) Computation of phase diagram

As mentioned above, the phase equilibria can be computed from the condition of Eqs.(42). For the present purpose, it is conveniently assumed that the melting points of two constituent substances, $T_{m.p.A}$ and $T_{m.p.B}$ are put into 1,000 °K and 1,500 °K, and also both entropies of fusion of A and B obey Richard's law, that is, ΔS_{fA} and ΔS_{fB} equal to 2 e.u.. In such a binary system of A and B, the phase relations will be examined using of the computer (HITAC-5020 and FACOM-230-60).

a) Ideal solution

The phase equilibria are simply represented, because the excess values are only reduced to the mixing term, $RT(x_A \ln x_B + x_B \ln x_B)$. The liquidus and solidus can be given as a function of temperature as shown in Eqs.(16) and (17). The result is shown in Fig. 12, and the entropy of mixing is shown in Fig. 13 as a function of composition.

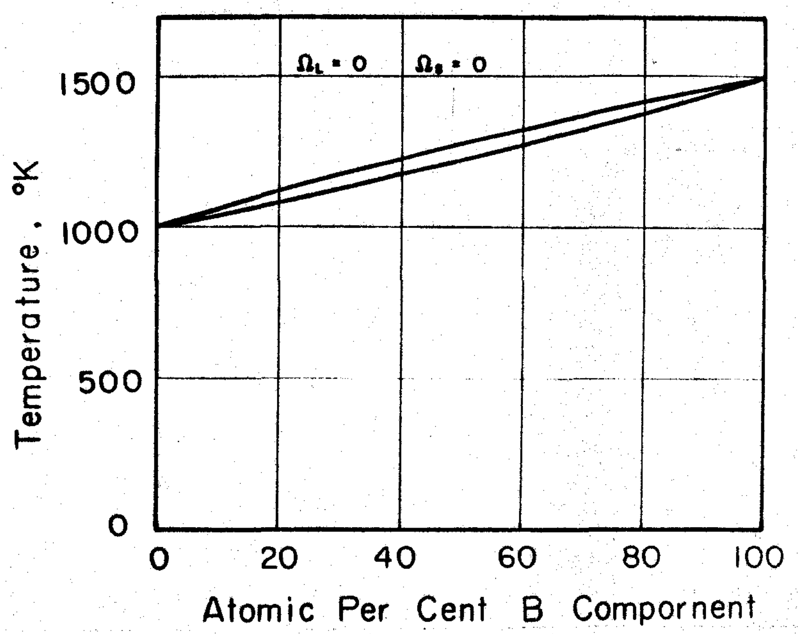

Fig. 12 Phase diagram constituted by ideal solutions

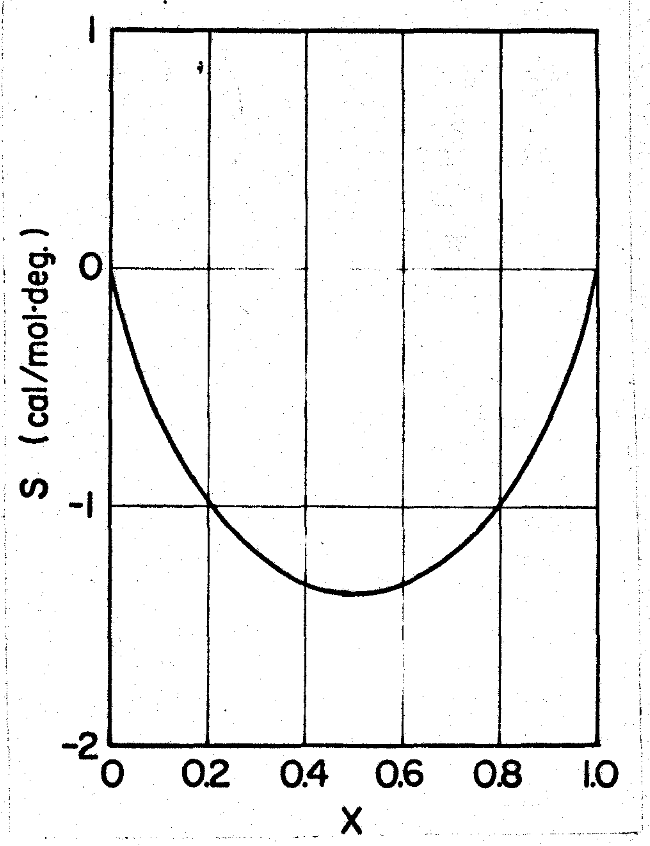

Fig. 13 Entropy of mixing

b) Regular solution

Under an assumption of regular solution, the condition which means that chemical potentials must be identical the two phases is represented as follows, for the liquid-solid equilibrium,

$$RT\ln X_A^l + (1-X_A^l)^2\alpha_l + \Delta G_{fA} = RT\ln X_A^S + (1-X_A^S)^2\alpha_S , \qquad (43)$$

$$RT\ln X_B^l + (1-X_B^l)^2\alpha_l + \Delta G_{fB} = RT\ln X_B^S + (1-X_B^S)^2\alpha_S . \qquad (44)$$

These equations cannot be solved analytically, but can be solved numerically on the computer for a given temperature. On the other hand, the condition for the equilibrium between a and b solid phases is given by

$$RT\ln X_A^a + (1-X_A^a)^2\alpha_a = RT\ln X_A^b + (1-X_A^b)^2\alpha_b \ , \qquad (45)$$

$$RT\ln X^a + (1-X_B^a)^2\alpha_a = RT\ln X_B^b + (1-X_B^b)^2\alpha_b \ . \qquad (46)$$

Assuming that $\alpha_a = \alpha_b$, the functions of Eqs.(45) and (46) are deduced as

$$RT\ln\frac{X_A}{1-X_A} + (1-2X_A)\alpha_s = 0 \ , \qquad (47)$$

and the free energy curve shows a central symmetry at $X_A = X_B = 0.5$. Moreover, at X=0.5, the following differential relations are satisfied:

$$\frac{\partial G^{xs}}{\partial X} = 0 \ , \quad \frac{\partial^2 G^{xs}}{\partial X^2} = 0 \ , \qquad (48)$$

and the critical temperature, T_c, is defined by

$$T_c = \alpha_s/2R \ . \qquad (49)$$

Then the symmetrical equation of Eq.(47) can be rewritten in a characterized form as

$$\ln\frac{X}{1-X} + \frac{2}{(T/T_c)}(1-2X) = 0 \ . \qquad (50)$$

It means that, T/T_c holding constant, the solutions with different values of α_s behave in the same manner. Fig. 14 shows the phase separation, that is, the solid solibility curve as a function of T/T_c.

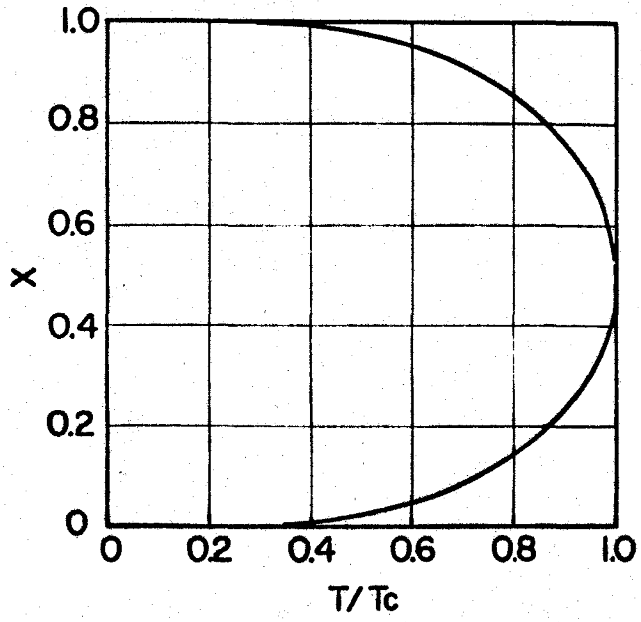

Fig. 14 Solid solubility curve as a function of T/T_c

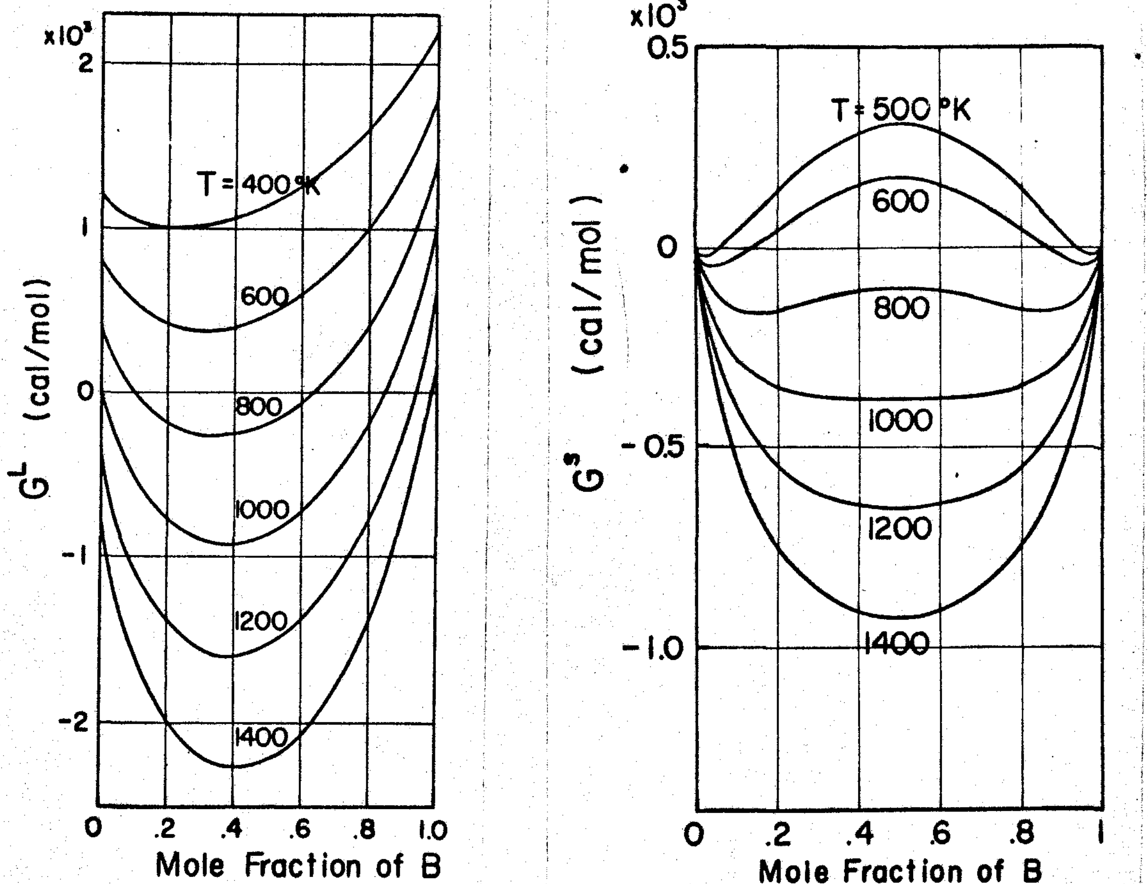

Fig. 15 The free energy of mixing of liquid,
(a), and solid, (b)

As well known, the parameter, α_s and α_ℓ, in the regular solution is called the quasi-chemical interchange energy as defined by

$$\alpha = N_0 Z \left(E_{AB} - \frac{1}{2}(E_{AA} + E_{BB}) \right), \qquad (51)$$

where E_{AB}, E_{AA} and E_{BB} represent the binding energy of the A and B atom, the A and A atom, and the B and B atom respectively. On general thermodynamic grounds we know that for positive values of α this system must segregate at low temperatures into an A-rich and a B-rich phase. In a similar way we arrive at the conclusion that for negative values of α the equilibrium state at low temperature must involve the formation of an ordered-phase AB. The Figs. 15 show the free energy of mixing of liquid and solid solution for various temperatures, assuming that $\alpha_\ell = 0$ and $\alpha_s = 4000.0$. The computing phase diagrams are shown for various values of α_s and α_ℓ in Figs. 16.

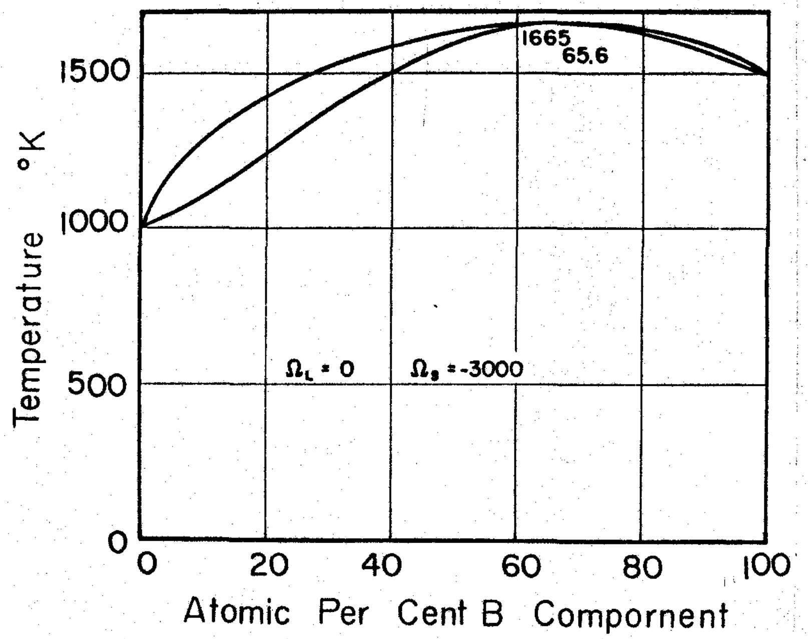

(a)

Fig. 16 Calculating binary phase diagrams under the approximation of regular solution

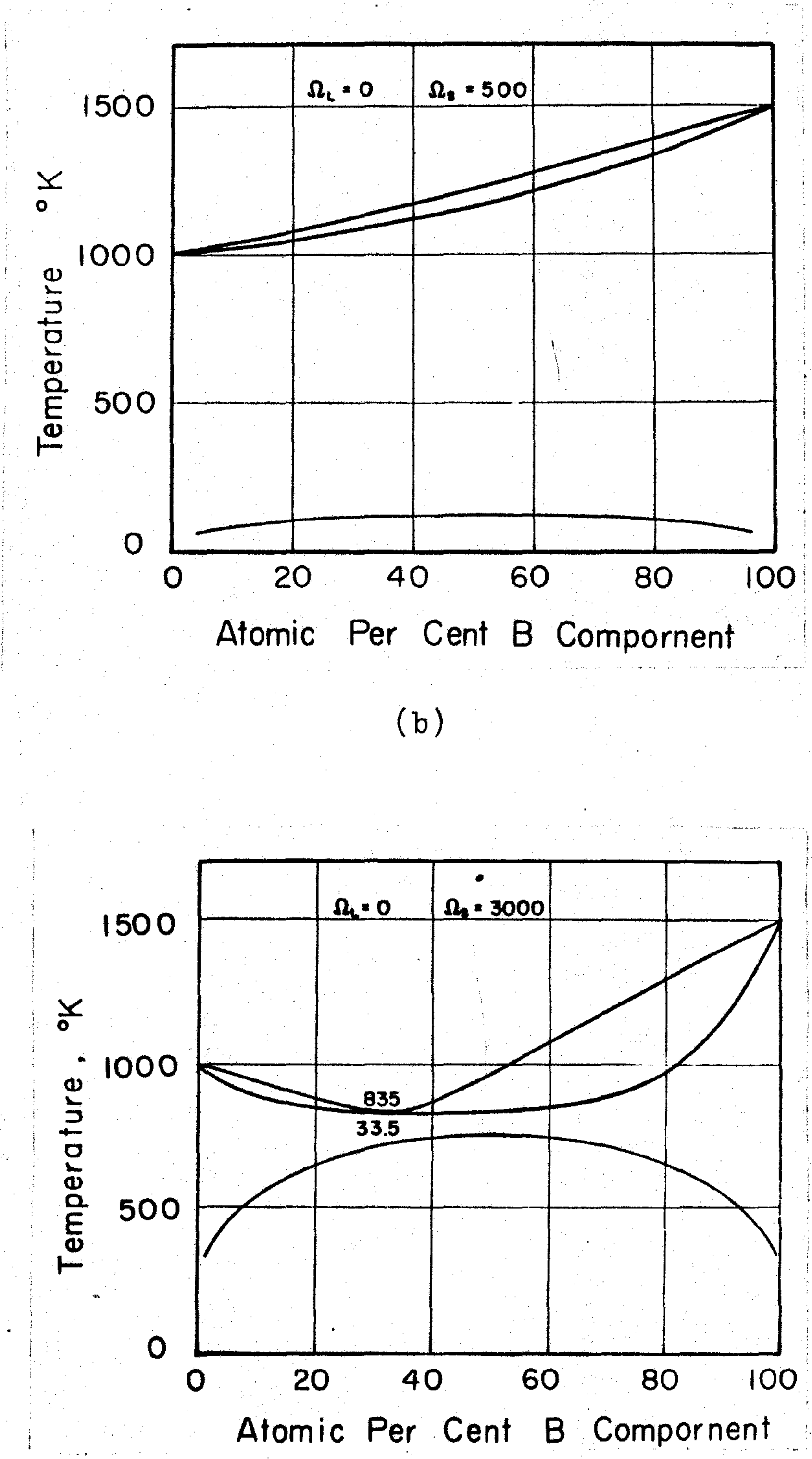

(b)

(c)

Fig. 16 Calculating binary phase diagrams under the approximation of regular solution

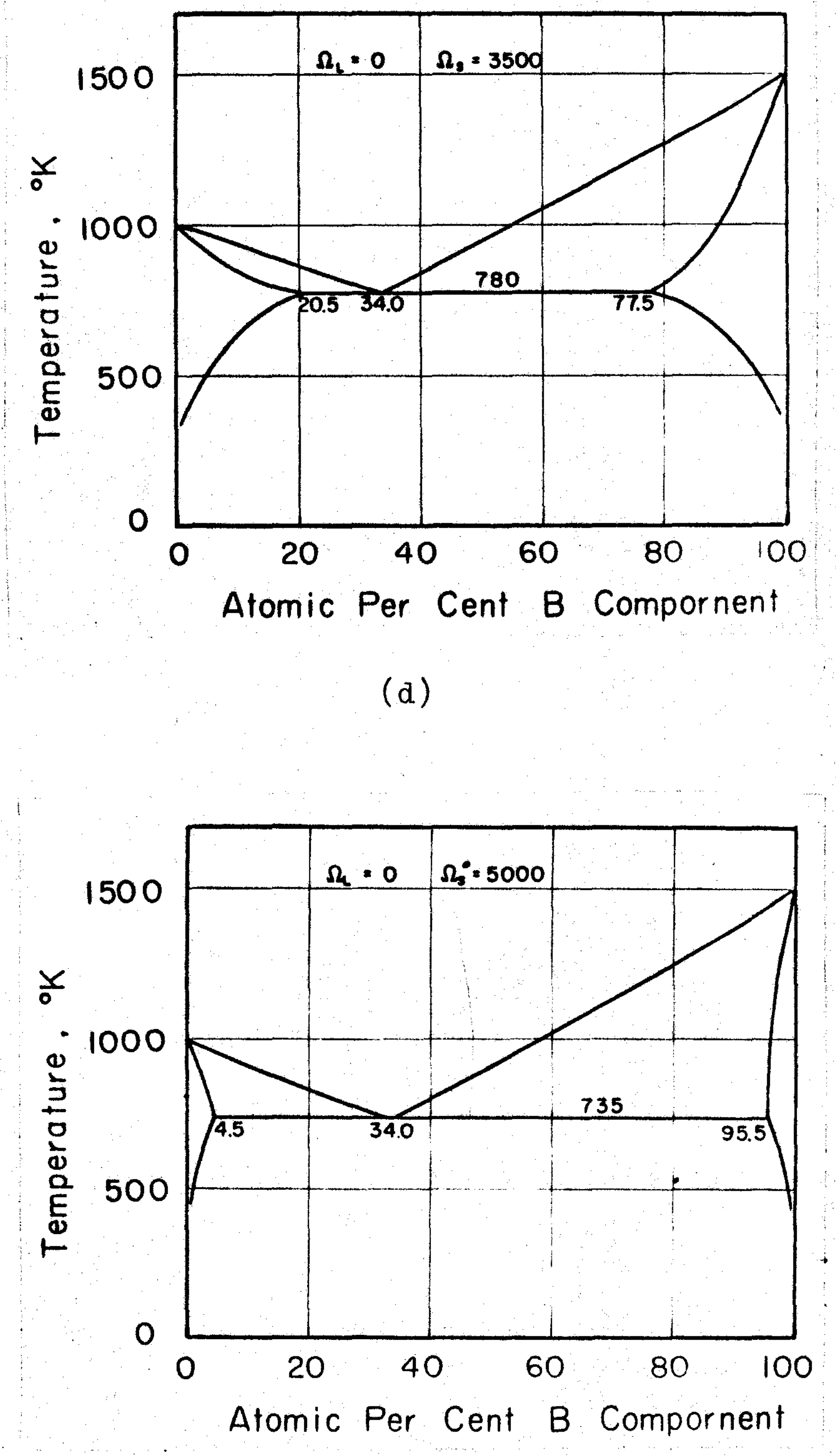

(d)

(e)

Fig. 16 Calculating binary phase diagrams under the approximation of regular solution

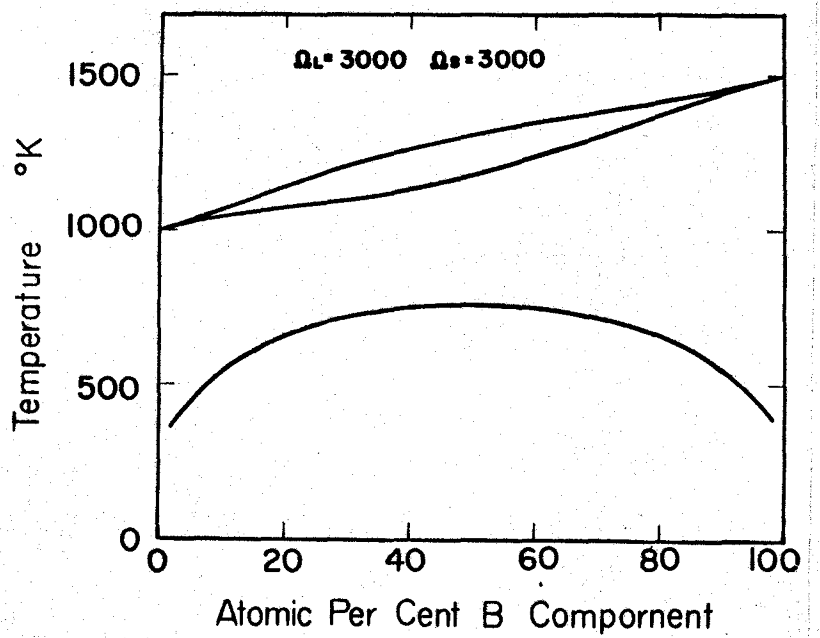

(f)

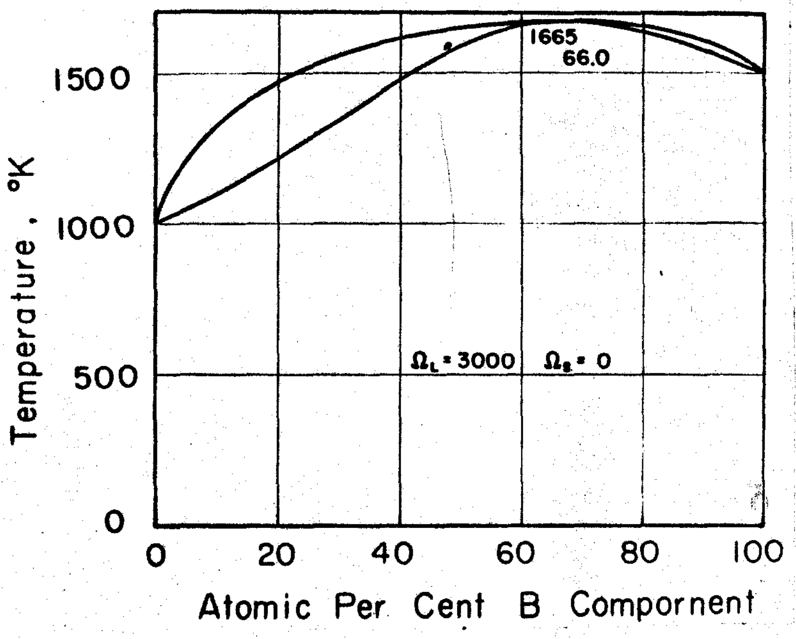

(g)

Fig. 16 Calculating binary phase diagrams under the approximation of regular solution

c) Athermal solution

Similarly as above discussed, the conditions of phase equilibria for the athermal solution can be expressed as follows; for the liquid-solid equilibrium,

$$RT\ln X_A^l + (1-X_A^l)^2\beta_l T + \Delta G_{fA} = RT\ln X_A^s + (1-X_A^s)^2\beta_s T, \qquad (52)$$

$$RT\ln X_B^l + (1-X_B^l)^2\beta_l T + \Delta G_{fB} = RT\ln X_B^s + (1-X_B^s)^2\beta_s T, \qquad (53)$$

where β_l and β_s are the constant mentioned in Eq.(41). For the solid-solid equilibrium, the conditions are

$$R\ln X_A^a + (1-X_A^a)^2\beta_a = R\ln X_A^b + (1-X_A^b)^2\beta_b, \qquad (54)$$

$$R\ln X_B^a + (1-X_B^a)^2\beta_a = R\ln X_B^b + (1-X_B^b)^2\beta_b. \qquad (55)$$

Assuming that $\beta_a = \beta_b$, the above equations are reduced as

$$\ln\frac{X}{1-X} + (1-2X)\frac{\beta}{R} = 0, \qquad (56)$$

and the value of free energy of mixing shows a central symmetry at $X_A = X_B = 0.5$. The athermal solution is very different from the regular one, especially the expression for the solid-solid equilibrium does not contain the temperature term. The situation is interpreted in Fig. 17, which is seen to be in contrast with Fig. 15. Thus the magnitude of phase separation in solid state is independent of temperature. Fig. 18 shows the relation between the parameter, β , and the equilibrium composition, X. Fig. 19 shows the binary phase diagrams of athermal solutions.

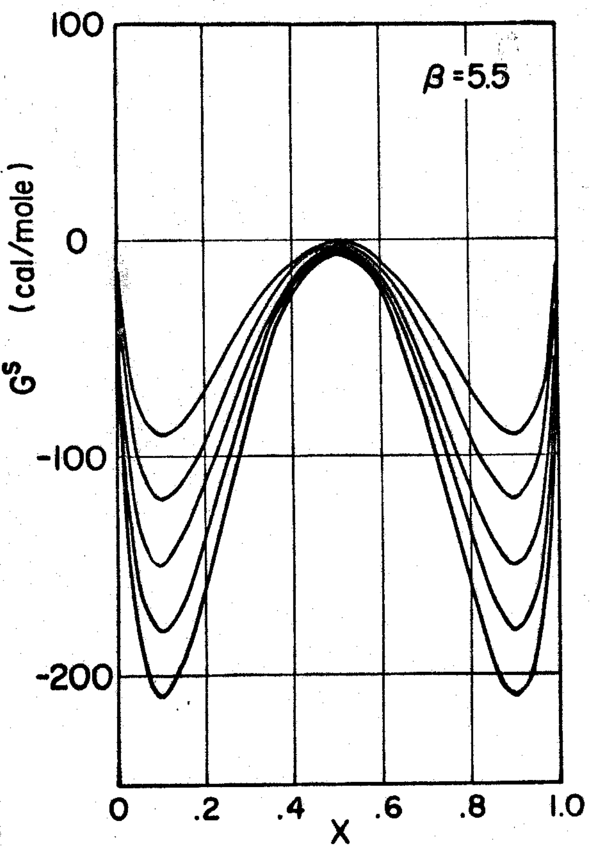

Fig. 17 The free energy of mixing assuming that the solid solution is athermal.

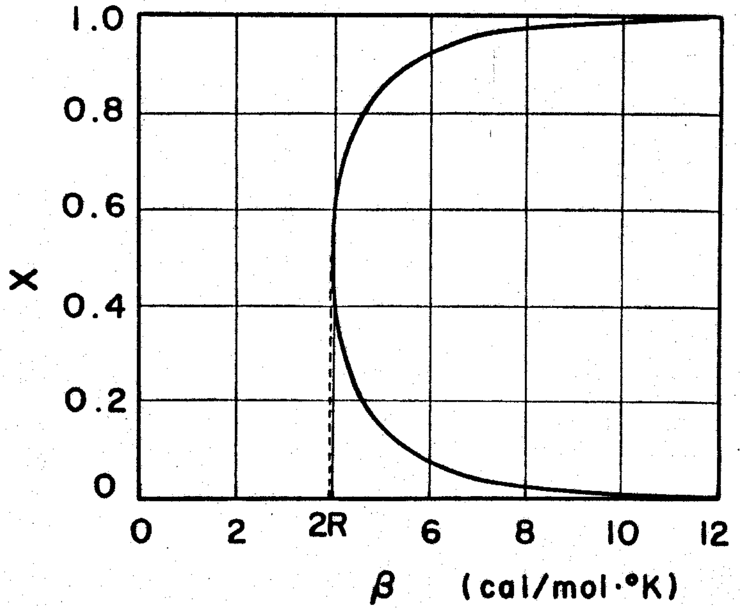

Fig. 18 Solubility limit in the athermal solid solution as a function of β.

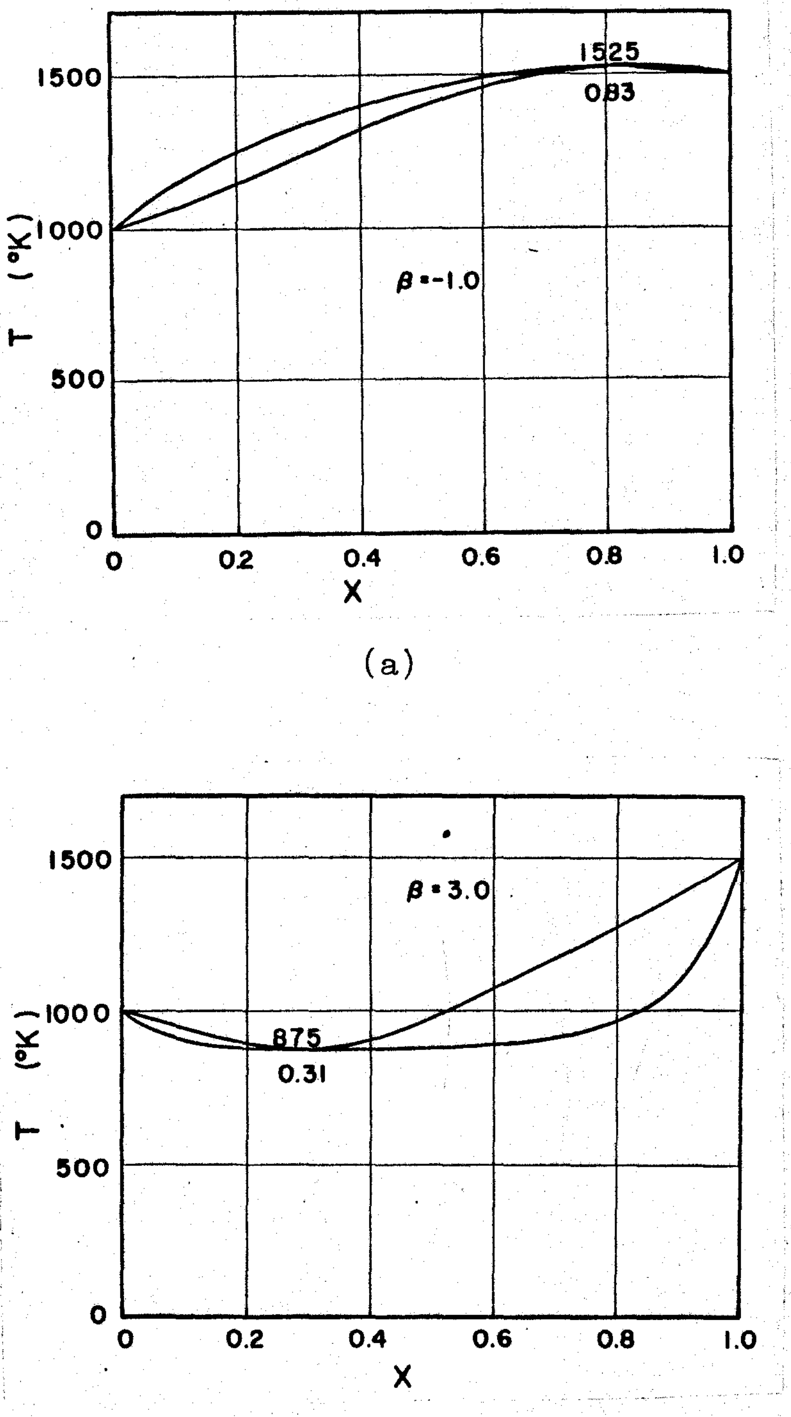

(a)

(b)

Fig. 19 Calculated phase diagram among athermal solutions

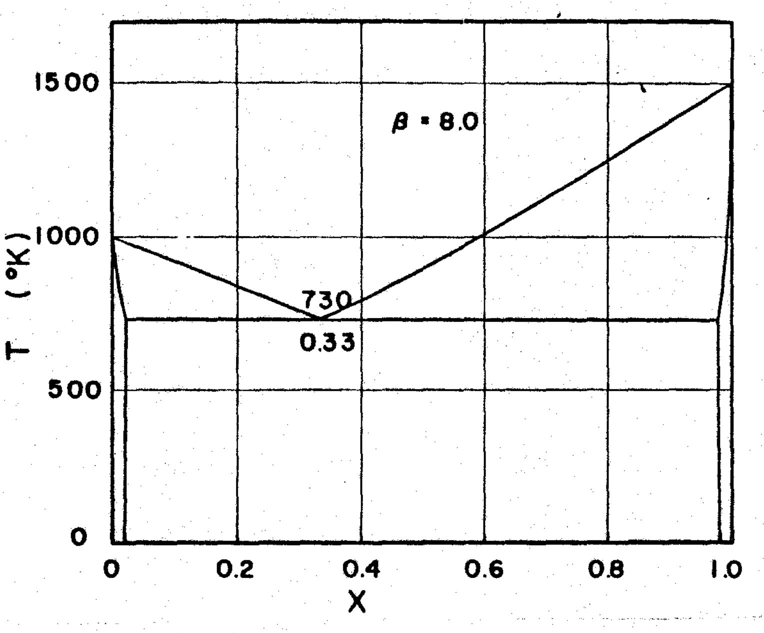

(c)

Fig. 19 Calculated phase diagram among athermal solutions

d) More complicated solution

The activity coefficient of one element is knowm to be affected by the presence of other elements present in solution. Wagner proposed a power series expansion in term of the mole fractions of the various elements present that is expected to hold approximately for the dilute solution case. A quadratic formalism or α -parameter approach proposed and studied by Darken is a much more suitable procedure for evaluating the concentration dependence of activity coefficients for alloys of appreciable solute content. In the present investigation, some solutions have been defined in sec. 2-2), and the quantity of ln $\gamma_i/(1-x_i)^2$ equals to α/RT for the regular solution and to β/R for the athermal solution. Then a parameter Ω is used differing only by a factor of 2.303 from that of Darken; i.e.

$$\Omega = \frac{\ln \gamma_i}{(1-X_i)^2} \qquad (57).$$

where the equation is a consequence of the Margules expansion for the excess partial molar free enrgy in a binary system .
In the Margules power series of $(1-n_i)^N$, the n=0 terms must be absent in order to satisfy Raoult's law and the n=1 term must be absent in order to satisy the Gibbs-Duhem equation. The series therefore reduced to

$$\begin{aligned} \Delta S_i^{XS} &= A_2 R(1-X_A)^2 + A_3 R(1-X_A)^3 + \cdots \\ \Delta H_i^{XS} &= B_2 R(1-X_A)^2 + B_3 R(1-X_A)^3 + \cdots \end{aligned} \qquad (58)$$

Therefore, Ω is given for a binary system by

$$\Omega = -A_2 - A_3 X_B + \frac{1}{T}[B_2 + B_3 X_B] \cdots \qquad (59)$$

As a simplifing approximation for this work, the higher power terms will be negelcted and the terms of α and β will be rewritten as

$$\alpha = R(B_2 + B_3 X_B) \qquad (60)$$

$$\beta = -R(A_2 + A_3 X_B) \qquad (61)$$

Then the corresponding solutions are recognized to add the concentration dependent term to the previously discussed sclutions.

In general, it is convenient that the composite solution has the excess free energy as defined by the equation,

$$\begin{aligned} G^{xs} &= \alpha X_A X_B + \beta T X_A X_B \\ &= R(B_2 + B_3 X_B - A_2 T - A_3 T X_B) \;. \end{aligned} \qquad (62)$$

The form of the excess value can be often applied to many real solid solutions. For example, the Al-Zn binary system had been analyzed using the form of (62).42)

2-4) Analytical expression of some characteristic relations

a) The azeotropic transformation

The azeotropic transformation may be simply defined as the phase transformation without the composition change. In the binary system, the transformation between the solid and liquid phase can be represented by the following conditions, since $x_A=x_A^S$, and $x_B=x_B^S$,

$$\ln\frac{\gamma_A^{\ell}}{\gamma_A^{s}} = -\frac{\Delta G_{fA}}{RT_z}\,,\qquad \ln\frac{\gamma_B^{\ell}}{\gamma_B^{s}} = -\frac{\Delta G_{fB}}{RT_z}\,, \tag{63}$$

where T_z is the temperature of the azeotropic transformation. For the case of the regular solution, the above relations are reduced to

$$(1-X_{Az})^2(\alpha_s-\alpha_\ell) = \Delta G_{fA} \tag{64}$$

$$(X_{Az})^2(\alpha_s-\alpha_\ell) = \Delta G_{fB} \tag{65}$$

where X_{AZ} is the composition of component A at the azeotropic point. Therefore, from the equations, (64) and (65), the azeotropic point areexpressed as

$$X_{AZ} = \frac{1}{1-\delta} \pm\sqrt{\frac{\delta}{(1-\delta)^2} - \frac{1}{\Delta\alpha}\,\frac{\Delta H_{fA}\delta-\Delta H_{fB}}{1-\delta}} \tag{66}$$

$$T_Z = \frac{2\Delta\alpha}{\Delta S_{fA}-\Delta S_{fB}}\left\{\frac{1+\delta}{2(1-\delta)} + \frac{\Delta H_{fA}-\Delta H_{fB}}{2\Delta\alpha} \pm\sqrt{\frac{\delta}{(1-\delta)^2} - \frac{1}{\Delta\alpha}\,\frac{\Delta H_{fA}\delta-\Delta H_{fB}}{1-\delta}}\right\} \tag{67}$$

where $\Delta\alpha = \alpha_s - \alpha_\ell$, $\delta = \Delta S_{fB}/\Delta S_{fA}$.
Also assuming that $\Delta S_{fA} = \Delta S_{fB}$, the point is given by

$$T_z = T_{m.p.B} - \frac{[\Delta\alpha - \Delta S_f(T_{m.p.A} - T_{m.p.B})]^2}{4\Delta S_f \Delta\alpha}, \tag{68}$$

$$X_{AZ} = \frac{1}{2}\left\{1 + \frac{\Delta S_f(T_{m.p.A} - T_{m.p.B})}{\Delta\alpha}\right\} \tag{69}$$

In the previous section, some diagrams computed in the assumption of regular solution show such an azeotropic point. Here the influence of α-parameters on the azeotropic phase-transformation can be analitically measured using above expressions. Assuming that the entropy of fusion obeys Richard's law, and the melting points of pure substance, $T_{m.p.A}$ and $T_{m.p.B}$, are 1;000 $^{\circ}$K and 1,500 $^{\circ}$K respectively, the interesting results are obtained as shown in Fig. 21. These points can be classified in two kinds: one may be called the positive azeotropic phase transformation which is characterized by some conditions of $T_z \geq T_{m.p.B}$, $\Delta\alpha < -10^3$ and $0.5 > X_{AZ}$, the another may be called the negative one which exists in the conditions of $T_z \leq T_{m.p.c}$, $\Delta\alpha > 10^3$ and $X_{AZ} > 0.5$. Accordingly, the conditions that the azeotropic point can exist are described as follows; (1) the absolute difference of α-parameters between solid and liquid, $|\Delta\alpha|$, is larger than $\Delta G_{fB} - \Delta G_{fC}$, (2) the azeotropic temperature can not exist in the range between melting points of two terminal substances.

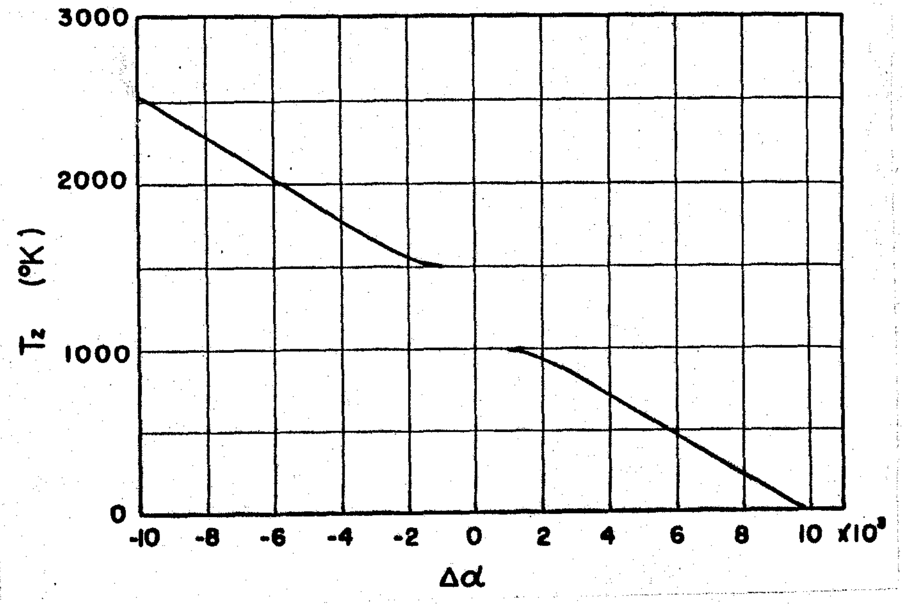

(a)

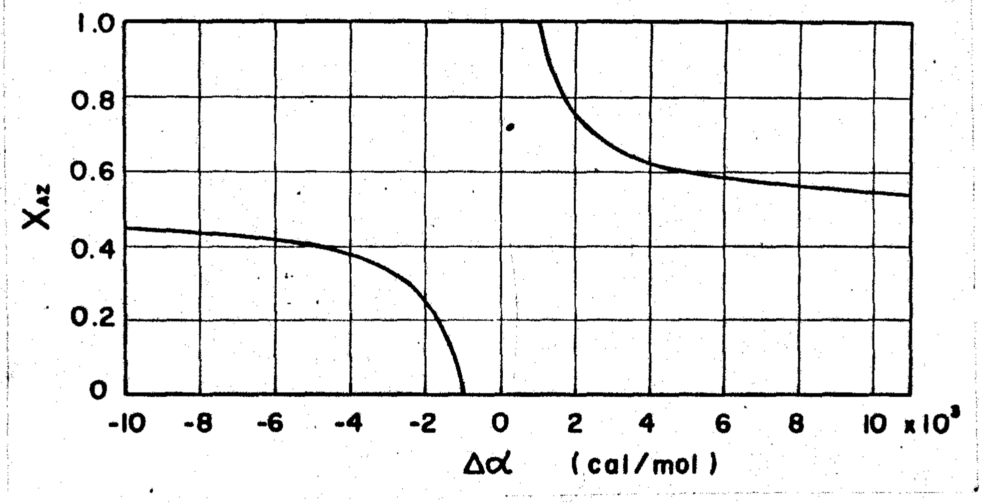

(b)

Fig. 21 Azeotropic temperature, T_z, and composition, X_{AZ} as a function of $\Delta\alpha$

b) Eutectic point

When the liquid coexists with two solid solution of α and β phase at the eutectic temperature, T_e, the condition may be expressed as

$$\ln a_A^l + \Delta G_{fA}/RT_e = \ln a_A^\alpha = \ln a_A^\beta , \qquad (70)$$

$$\ln a_B^l + \Delta G_{fB}/RT_e = \ln a_B^\alpha = \ln a_B^\beta , \qquad (71)$$

where a_i^j is the activity of component i in the corresponding phase j. Assuming that both the solid and liquid phase are regular, the chemical potential is represented by a central symmetric function, that is, $X_A^\alpha + X_A^\beta = 1$, and equations, (70) and (71) are reduced to

$$T_e = \frac{(\Delta H_{fA} - \Delta H_{fB}) + (2X_e^l - 1)\alpha_l}{R\ln X_e^l/1-X_e^l + (\Delta S_{fA} - \Delta S_{fB})} , \qquad (72)$$

$$T_e = \frac{(2X_A^s - 1)\alpha_s}{R\ln X_A^s/1-X_A^s} . \qquad (73)$$

The above two equations with respect to T_e can be simultaneously solved by using the computer as functions of two compositions, X_A^s and X_e^l

2-5) Conclusion

The computation of the binary phase diagrams has been performed for the ideal, regular and athermal solutions. The numerical method might be expected to make progress for the more complicated phase diagram and should be believed to be available for the metallography.

References

1) C. Shih and E.A. Peretti; J. Amer. Chem. Soc. 75(1953)608

2) J. C. Wolley and B. A. Smith; Proc. Phys. Soc. 72(1958)214

3) G. B. Stringfellow and P. E, Greene; J. Phys. Chem. Solids 30(1969)1779

4) M. E. Straumains et al.; J. Electrochem. Soc. 114(1967)640

5) K. Osamura and Y. Murakami; Abstract 2, Sring Meeting of Phys. Soc. of Japan at Osaka (April,1968)147

6) T. Mori and K. Fujita and S. Iwasaki; Suiyokai-shi 16(1968)

7) C. D. Thurmond; J. Phys. Chem. Solids 26(1965)785

8) O. Kubaschewski et al.; Metall. Thermochem. 1958

9) O. G. Folberth; J. Phys. Chem. Solids, 8(1959)14

10) R. B. Clough and J. J. Tietjien; Trans. AIME 245(1969)583

11) E. K. Müller amd L. J. Richards; J. Appl. Phys. 35(1964)1233

12) K. Osamura and Y. Murakami; Japan J. Appl. Phys. 8(1969)967

13) N. A. Goryunova and N. N. Fedorova; Zh. tekh. fiz. 25 (1955)1339

14) H. J. Van Hook and E. S. Lenker; Trans. Metal. Soc. AIME 227(1963)220

15) E. F. Hockings, I. Kudman, T. E. Seidel, C.M. Schmelz and E. F. Steigmeier; J. Appl. Phys. 37(1966)2879

16) H. Welker; Z. Naturf. 7a(1952)744

17) L. Pauling; The Nature of the Chemical Bond, Oxford Univ. Press (1950)

18) O. G. Folberth and H. Welker; J. Phys. Chem. Solids 8(1959)14

19) L. Pauling; Nature of the Chemical Bond, Cornell Univ. Press, Ithaca, New York, 3rd ed. (1960)

20) N. N. Sirota; Semiconductors and Semimetals, Academic Press 4(1968)121

21) D. Richman and E. F. Hocking; J. Elecrochem. Soc. 112(1965)461

22) V. M. Glazov, A. N. Krestovnikov and G. L. Malyntina; Dokl. Akad. Nauk. SSSR 175(1967)631

23) J. R. Arthur; J. Phys. Chem. Solids 28(1967)2257

24) C. E. Ludin, M. J. Pool and R. V. Sullivan; Final Report, Contract No. AF 19(604)7222 University of Dember (1963)

25) N. H. Nachtrieb and N. Clementi; J. Phys. Chem. 62(1958)876

26) W. F. Schottky and M. B. Bever; Acta. Metall. 6(1958)320

27) O. G. Folberth; Z. Naturforsch. 13a(1958)856

28) W. Köster and B. Thoma; Z. Metallkunde 46(1955)293

29) J. C. Wolley, B. A. Smith and D. G. Lees; Proc. Phys. Soc. 69(1956)1339

30) W. Köster and W. Ulrich; Z. Metallkunde 49(1958)7

31) I. E. Gorshkov and N. A. Goryunova; Zh. nauch. Khim. 3(1958) 668

32) N. A. Goryunova and I. I. Burdiyan; Dokl. Akad. Nauk. SSSR, 120(1958)1031

33) I. I. Burdiyan and A. S. Borshchevskii; Zh. tekh. fiz. 28 (1958)2684

34) A. S. Borchchevskii et al.; Zh. nauch. Klim., 4(1959)2824

35) N. A. Goryunova and B. V. Baranov; Dokl. Akad. Nauk. SSSR, 129(1959)4

36) B. V. Baranov and N. A. Goryunova; Fiz. tverd. tela. 2(1960) 284

37) D. Effer; J. Electrochem. Soc. 108(1961)357

38) G. Scatchard; Chem. Rev. 44(1949)7

39) C. Wagner; Thermodynamics of Alloys Addison-Wesley, New York, (1952)

40) L. S. Darken; Trans. AIME 239(1967)80: ibid. 239(1967)90

41) E. T. Turkdogan and L. S. Darken; Trans. AIME 242(1968)1997

42) J. Lašek; Czech. J. Phys. B15(1965)848

Chapter III

Preparation of III-V Compound Semiconductors

The main method of preparing the compounds is from a melt including equal atomic proportions of the elements (stoichiometric melt). For the gallium antimonide, the crystal has been grown horizontally by the Bridgman technique, in which the molten material is contained in a boat, and is frozen directionally by being drawn through a steep temperature gradient. For the gallium arsenide, a vapour pressure control furnace is added. If the cooling is slow and carefully controlled, so that the crystallization progresses from one end, solid ingots may be formed. The pressure required for preparing the gallium phosphide and their alloys with gallium arsenide from a stoichiometric melt is rather high. The method of growth under such a condition has been developed in the present work.

1. Preparation of GaAs compound

The horizontal Bridgman technique is suitable for the crystal growth of GaAs. The apparatus is shown in Fig. 1, where the left resistance furnace is used for the vapour pressure control, the central furnace is required for zone refining. The temperature distribution for preparing GaAs crystal is shown in this figure. The reaction tube is evacuated and sealed after excess arsenic is added to create the required vapour pressure. Single crystal or ingots including large grains have been grown in silica boats when the molten ingot does not stick to the boat. To prevent sticking the inner surface of the silica boat is roughened with a fine sand paper. The tube

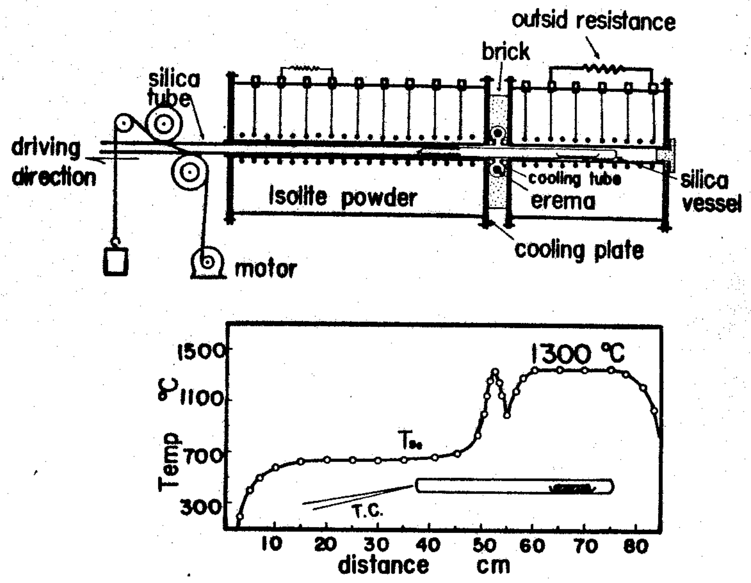

Fig. 1 Apparatus for growth of GaAs and its temperature gradient.

is placed in the furnaces in the position shown in the diagram, and then the mullite tube supporting the container is pulled to the left at the rate of 2-5 cm per hr. The left resistance furnace has maintained the ambient temperature at just above 600 ^{o}C. Many ingots prepared in this way have been supplied for the X-ray, the infrared, and the electric measurements.

2. Preparation of GaSb compound

The ingots of GaSb have been prepared using the same apparatus as described in the previous section (III-1). However, the equilibrium vapor pressures of constituent components, Ga and Sb are negligible small, and then the left furnace in Fig. 1

is unnecessary to be controlled. Photo. 1 shows the ingot grown from the melt. The nondoped crystals prepared in this way are always p type with a hole concentration near 1.2×10^{16} cm^{-3} and a room temperature mobility of 826 $cm^2/Vsec$ and a mobility at 77 ^{o}K of 2710 cm^2/sec. To examine the electrical properties of n-type material, Te doped ingots were prepared. Electrical properties of the ingots prepared in this way are listed in Table 1.

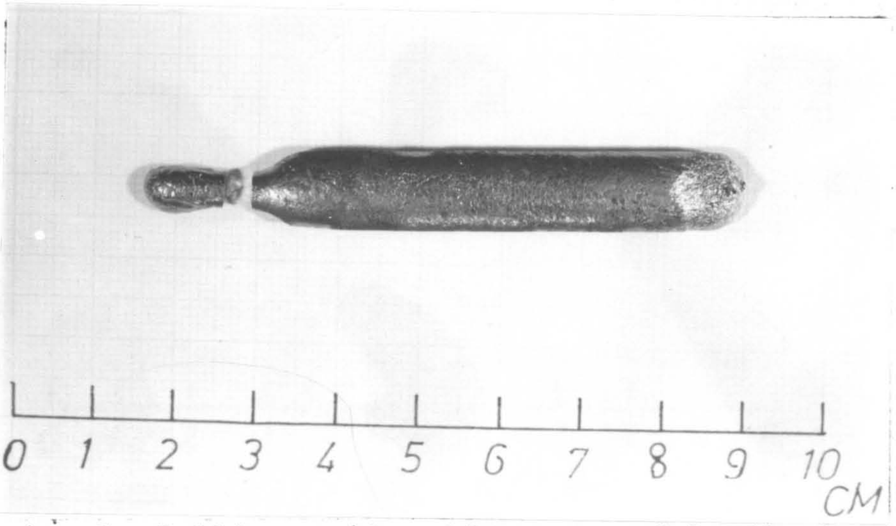

Photo. 1 Gallium antimonide prepared by the horizontal Bridgeman furnace

Table 1 Electrical properties of GaSb prepared in the present work

Sample Number	Type	dopant	carrier concentration (cm^{-3})		mobility ($cm^2/Vsec$)	
			R.T.	L.N.T.	R.T.	L.N.T.
B918‴-2	p	-	1.73×10^{17}	0.37×10^{17}	711	2054
B919-1	p	-	1.20	0.23	826	2670
B001-4	n	0.5 wt%Te	15.5	19.3	1750	2920
B003-1	n	0.005wt%Te	2.3	4.2	1790	2510
B008-5	n	0.003wt%Te	0.69	1.13	3198	2926
B005-5	p	0.001wt%Te	1.74	0.48	660	1017

3. Phase equilibrium in the Ga-As-P system and preparation of $GaAs_{1-x}P_x$ compounds

3-1) Introduction

Compounds of the III-V elements have been grown from the melt, from gaseous phases, and from liquid metal solutions. These compounds are of considerable interest in the semiconductor field because of their electrical characteristics. Crystalline solid solutions of III-V compounds which contain As and P are of particular interest because their energy gaps are large and change continuously with the As/P ratio.

The preparation from the melt of the crystalline solid solutions $A^{III}As_{1-x}P_x$ has not been studied to any great extent, mainly because As and P have high equilibrium vapor pressures at the high temperatures required. Except for the preparation 1)-3) from the melt of $InAs_{1-x}P_x$, the conditions for controlling the composition of these compounds have not been studied. Thus, the authors have considered a general method for preparing such compounds from the melt. $GaAs_{1-x}P_x$ has been prepared successfully by this method, as described in the first part of this paper.

In the next section, the concept of pseudo-equilibrium in a heterogeneous system containing two different temperatures is described. A general method of preparing $A^{III}As_{1-x}P_x$ from the melt by controlling pressures is also presented.

3-2) Experimental

The crystalline solid solutions of $GaAs_{1-x}P_x$ have been grown in our laboratory from the melt under controlled pressures of As and P. The total pressure at the melting point ranged from

1 atm$^{4)}$ to a maximum of about 25 atm$^{5)}$, as will be discussed later in section 4. These high pressures made neccessary modifications in the usual techniques of preparing GaAs crystals; consequently, the apparatus was modified to permit operation at pressures up to about 10 atm.

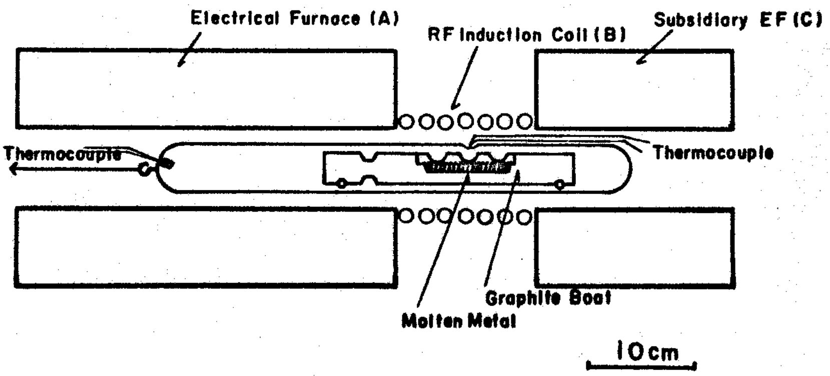

Fig. 2 Apparatus for the preparation of $GaAs_{1-x}P_x$ compound.

The modified apparatus that was used is shown in Fig. 2. It consists of (A) an electric furnace which was used to control pressures, (B) a RF induction coil with an 18 kw generator tuned to about 30 kHz, and (C) a subsidiary electric furnace. The reaction vessel for preparing the compound is located within the furnace as shown in Fig. 2. It consists of a 40cm long fused silica tube with an internal diameter of 35 mm. This length is sufficient to keep part of the tube in one of the lower temperature zones throughout the preparation of the ingot. The highest temperature which the fused silica reaches is 1000 °C, or less. The reaction vessel, containing Ga (in a graphite boat), As and P, was evacuated. With the reaction vessel in place, the middle furnace (B) was slowly heated to the reaction temperature T_h, then the electric furnace (A) was heated to the temperature, T_c, required to hold the desired pressure which was calculated as described in the following section. The temperature of the subsidiary furnace (C) was held at the intermediate temperature between T_h and T_c. After sufficient time passes, an As-P solid solution was formed in the end of the reaction vessel at T_c, and liquid and solid solutions of Ga, As and P were formed in the graphite boat at T_h. When the pseudo-equilibrium in the system was established, the sample boat was then moved through the RF coil.

The effect of variables such as temperatures, T_c and T_h, travelling rate, and the amounts of Ga, As and P were investigated to develop a suitable technique for producing uniform ingots of the crystalline solid solution of $GaAs_{1-x}P_x$.

The best control over the composition of the grown crystals can be obtained when the amounts Ga, As and P in the vessel correspond rigorously to the proportion calculated by the concept of the pseudo-equilibrium. When the negligible small amount of the crystalline solid solution is formed, the necessary numericals to be determined are as follows: At T_h, molar quantities of N_{As}^{lh}, N_P^{lh} and N_{Ga}^{lh}, and mole fractions of X_P^{lh} and X_{As}^{lh}, where $X_P^{lh}=N_P^{lh}/(N_{Ga}^{lh}+N_{As}^{lh}+N_P^{lh})$, $X_{As}^{lh}=N_{As}^{lh}/(N_{As}^{lh}+N_{Ga}^{lh}+N_P^{lh})$, $N_{As}^{lh}+N_P^{lh}=N_{Ga}^{lh}$, and where the superscript lh refers to the ternary liquid in the quasi-binary section; at T_c, similar quantities of N_{As}^{sc}, N_P^{sc}, X_{As}^{sc} and X_P^{sc}, where $X_{As}^{sc}=N_{As}^{sc}/(N_{As}^{sc}+N_P^{sc})$ and $X_P^{sc}=N_P^{sc}/(N_{As}^{sc}+N_P^{sc})$, and where super-subscript sc refers to the solid solution of As and P; also, total mloar quantities of As, P and Ga, $N_{As}=N_{As}^{sc}+N_{As}^{lh}$, $N_P=N_P^{sc}+N_P^{lh}$ and $N_{Ga}=N_{Ga}^{lh}$.

The relative amounts of Ga, As and P were used in conjunction with Eq.(14) in order to obtain the mole fraction X_P^{lh} for $GaAs_{1-x}P_x$ compound. Then the value of X_P^{sc} in the left side of the apparatus shown in Fig. 2 for the values of X_P^{lh} and T_h in the right side can be calculated. After N_{Ga} and N_{As} moles of Ga and As were weighed out, the total amount N_P of P required was determined from the following equation which has been derived from the above definitions,

$$N_P = 2N_{Ga}X_P^{lh} + [N_{As} - N_{Ga}(1-2X_P^{lh})]X_P^{sc}/(1-X_P^{sc}) \quad . \qquad (1)$$

The amounts of each element were initially weighed to correspond to the mole fractions, X_P^{sc} and $2X_P^{lh}$, listed in Table 2. In addition, the ratio of $N_{As}+N_P$ to N_{Ga} is listed in the fifth column of Table 2.

In the next place, the temperatures of T_h and T_c must be determined. The solidus temperature, T_h corresponding to the desired compound is known from the quasi-binary diagram of GaAs-GaP. T_c and X_P^{sc} which correspond to T_h can be calculated from the condition of pseudo-equilibrium described later in section 3. These calculated values are shown in Table 2.

T_h was determined preliminarily for the empty vessel by both thermocouple and optical pyrometer. The effect of RF heating on the molten metal was neglected because of the large heat capacity of graphite boat, and the temperature of the molten metal was considered to be very near the temperature determined preliminarily.

Table 1 Preparing conditions

T_h^{cal} means the liquidus point at the composition X_P^{sh} and T_c^{exp} shows the maximum value in the boat without the molten material

	Starting Material				Theoretical values					Experimental values		
Sample Number	N_{Ga} ($x10^3$ mole)	N_{As}	N_P	$\frac{N_{As}+N_P}{N_{Ga}}$	X_P^{sc}	$2X_P^{lh}$	$2X_P^{sh}$	T_h^{cal} (^oK)	T_c^{cal} (^oK)	$2X_P^{sh}$ (ingot)	T_h^{exp} (^oK)	T_c^{exp} (^oK)
1	80.00	120.00	-	1.50	0.0	0.0	0.0	1518	885	0	1530	888
2	73.12	138.69	5.09	1.97	0.040	0.040	0.114	1535	877	0.110	1540	888
3	105.88	105.88	6.16	1.06	0.051	0.054	0.152	1541	875	0.150	1553	878
4	119.52	121.50	6.78	1.07	0.051	0.054	0.152	1541	875	0.042	1553	883
5	112.36	198.11	22.47	1.96	0.087	0.082	0.220	1552	873	0.324	1563	868
6	77.84	135.83	10.85	1.88	0.083	0.082	0.220	1552	873	0.130	1563	878
7	73.61	121.00	16.47	1.87	0.102	0.138	0.340	1572	859	0.390	1593	853
8	92.53	173.90	45.34	2.37	0.181	0.242	0.500	1603	847	0.506	1623	833
9	75.35	74.38	25.17	1.32	0.205	0.270	0.532	1610	848	0.500	1623	843
10	81.95	67.62	34.88	1.25	0.318	0.248	0.618	1629	837	0.660	1653	813
11	77.25	57.29	48.05	1.36	0.482	0.448	0.706	1650	836	0.720	1673	808
12	86.14	31.08	61.11	1.07	0.787	0.654	0.840	1688	858	0.900	1713	723
13	113.33	24.46	219.99	2.16	0.908	0.876	0.950	1722	868	0.954	1723	723
14	80.00	-	120.00	1.50	1.0	-	-	1738		1.00	1723	723

The temperature profile of T_h over the molten metal was found to have a temperature gradient of about 10 $^oC/cm$, while T_c was found to be essentially uniform. In the present work, T_c was set empirically to a temperature shown in the sixth column of Table 2. These temperatures were determined to be in the neighbourhood of the calculated value with respect to X_P^{sc}. When the vapor pressure increases over several atomosphers, the temperatures were necessarily made slightly lower for safty. The thermocouple which was inserted into the RF coil (see Fig. 2) was used only as a monitor. The travelling rate of the boat was kept about 1.0 cm/hr. throughout the procedure.

Photo. 2 Ingot of $GaAs_{1-x}P_x$ compound

In these experiments, all ingots consisted of small crystals of grain size 5 mm or less. Photo. 2 shows a typical ingot of $GaAs_{1-x}P_x$. The ingot was cut into pieces about 5 mm in length. The average composition of each sample was determined by a powder X-ray method. It was assumed that the lattice constant changes linearly with composition$^{6)}$. The average composition of typical samples as a function of their position in the ingot is shown in Fig. 3. The composition was also estimated in another way. The intensity of the K_α-X-ray

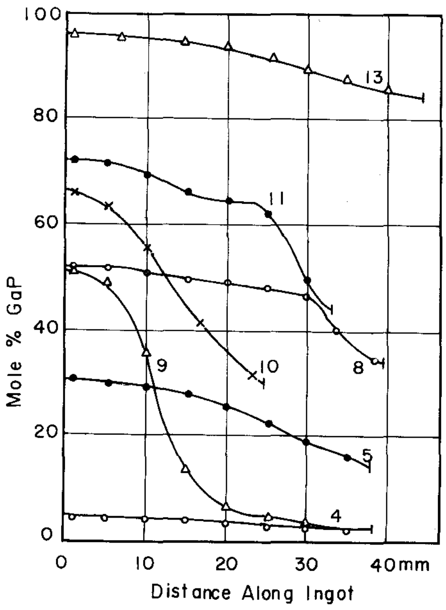

Fig. 3 Distribution of the $GaAs_{1-x}P_x$ alloy composition along the ingot.

emission lines of P and As were measured by using an electron microanalyzer. Analysis of these emission lines provided a suitable method for determining a change in composition from one grain to another. In spite of the fact that the ingot cross section contained many small grains it was found that in all ingots, regardless of initial composition the change of composition in the cross section perpendicular to the growth direction was small in comparison with the change of composition in the growth direction.

The composition of the crystalline solid solution was taken as the composition of the initially solidified part of the ingot. This composition, written as X_p^{sh} (ingot), is determined by the intercept of the mole% GaP curves with the vertical axis (see Fig. 3). The relation between X_P^{sh}(ingot) and T_c is shown in Fig.6. The value of X_P^{sc} has not been determined experimentally, but has been assumed to be indentical with the calculated one shown in Table 2. Immediately after initial growth of the compound from the melt, a change of the relative proportion of As, P and Ga distributed between two sides under the steady state condition, would be thought to be so small that it could be neglected. The solid line in Fig.7 indicate the relation between X_P^{sc} and $X_P^{\ell h}$ (ingot).

X_P^{sh} at the top of ingot was also estimated from methods based on the measurement of certain optical properties of the quasi-binary compound. The first method[7),8)] involved the measurement of the lattice vibrations. It is based on the fact that the integral absorption, $\int \alpha\, d\lambda$ for the 700 cm^{-1} absorption band is proportional to the composition. The other method[9)] involved the measurement of the electrical fundamental edges. All dimensions of the specimens which were cut from the initially solidified part of the ingot, were about 1.0 x 0.5 cm^2. X_P^{sh} values determined by these methods have been described in Chap. I and V.

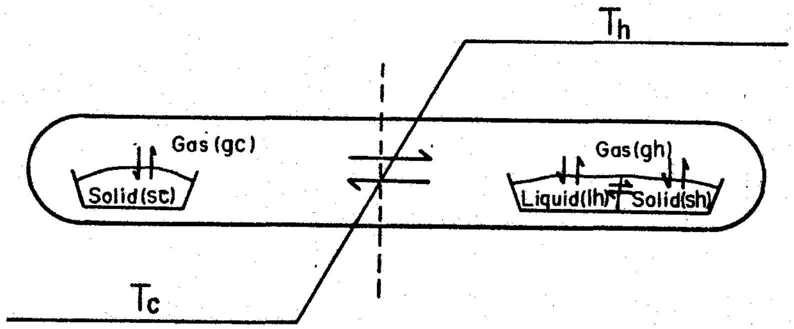

Fig. 4 Schematic representation of the present procedure. The closed system includes four phases as shown in the figure: (sc), binary solid solution of As and P; (gc) and (gh), gas phase; (lh), ternary solution of Ga, As and P; (sh), crystalline solid solution of $GaAs_{1-x}P_x$

3-3) Theoretical Background

Presentation

Fig.4 is a schematic diagram of the apparatus used in preparing $GaAs_{1-x}P_x$. Known quantities of As and P placed in the left side of the apparatus are maintained at a temperature T_c. T_c is always lower than T_h, the temperature of the right side of the apparatus. The phases present in the left side are known from the results reported by Krebs$^{10)}$. The thermodynamic parameters for As and P are determined by assuming that the solid solutions of As and P are regular as will be described below. In the right side of the apparatus, the three components, As, P, and Ga, coexist in the solid, liquid and gas phases. The partial pressure of Ga is assumed to be negligible compared with those of As and P.

In applying the phase rule to the system it is found that there are two degrees of freedom for each side of the apparatus considered independently. Hence, the equation of state for each phase can be determined if the temperature and pressure are fixed. The relation between the mass density and partial pressure of vapor phase species, assuming ideal gas conditions, is given by

$$n = MP/RT \qquad (2)$$

where n and M are mass density and molecular weight respectively. It is reasonable to consider the mass density rather than the corresponding partial pressure of each element in the gas phase.

The components in the gas phase, assumed to be As and P, can exist as various molecular species. The possible stable molecular species in the temperature range from $600^{\circ}K$ to $1,800^{\circ}K$ appears to include As_2, As_4, P_2, P_4, AsP and four-atom molecules formed by various combination of As and P. Although it has been known[11)] that some solid substances may be transported through the vapor phase in the presence of a reactive gas such as a halogen or a hydrogen halide, the gas phase in the present system does not contain any transporting agent, and the mass transport does not seem to be important.

In the present experiment above mentioned, when each furnace reaches the constant temperature and is held for sufficient time, a steady state will be set up. Consider the hypothetical interface at the boundary between the T_c and T_h parts. Then the total mass flux passing through its interface from the T_c part is represented by the term, $\sum_{i\lambda} n_{i\lambda c} v_{i\lambda c}$, where $n_{i\lambda c}$ and $v_{i\lambda c}$ are the mass density and mean molecular speed of molecular species $i\lambda$. The condition that there is no net flow of atoms in either direction between T_c and T_h parts is related to the fact that the total mass flux from the T_c part is equal to that from the T_h part at the interface. In the present case, we restrict As_2, As_4, P_2, and P_4 as molecular species in the gas phase. Here, remembering that mass flow of a molecular species is written as nv/4, where v is a mean molecular speed, then from equation (2) the following relation is obtained, nv/4 = SP. We could consider that the tube has a "pumping speed" $S_{i\lambda}$, a function of molecular weight M, which is shown to be $S = \sqrt{M/2\pi RT}$ using a simple mass flow theory. At steady state where no net atom flow occurs, the condition for balance is written as follows.

$$\sum_{\lambda} \left(S_{i\lambda H} P_{i\lambda H} - S_{i\lambda c} P_{i\lambda c} \right) = 0 , \quad i = As, P \qquad (3)$$

where λ refers to number of moleculs of each species, and i to the kind of species respectively.

The system described in the previous paragraphs is in a state which might be described as a sort of pseudo-equilibrium. If the pseudo-equilibrium is realized between the left side and the right side of the apparatus, the conditions for equilibrium can be thermodynamically developed. Here it is assumed that the binary solution of As and P is regular, that the liquid and solid solution of Ga, As and P is regular, and that the gas phase is ideal. The theory of regular solution is now applied to the present system.

Consider the thermodynamic properties of As and P located in the left hand side of the apparatus. The integral molar free energy of mixing of the solid solution F_M containing the two components may be expressed$^{12)}$ by

$$F_M(\text{As-P Binary}) = RT\sum_i \ln a_i^{sc} \tag{4}$$

$$= X_{As}^{sc}X_P^{sc}\Omega_{AsP} + RT(X_{As}^{sc}\ln X_{As}^{sc} + X_P^{sc}\ln X_P^{sc}),$$

where x and a are the mole fraction and activity of the components, Ω_{As-P} is the quasi-chemical interchange energy per gr-atom between As and P, R is the gas constant, and T is the absolute temperature. By applying the Duhem's differential relation to Eq. (4), the activities a_{As}^{sc} and a_P^{sc} may be expressed by

$$\ln a_{As}^{sc} = \ln X_{As}^{sc} + (1-X_{As}^{sc})^2\Omega_{AsP}/RT, \tag{5-a}$$

$$\ln a_P^{sc} = \ln X_P^{sc} + (1-X_P^{sc})^2\Omega_{AsP}/RT, \tag{5-b}$$

where the supersubscripts sc and gc refer to the condensed phase and the gas phase respectively in the left side. Supersubscripts gh, lh and sh, which will be used later, refer to the gas, liquid and solid phase in the right side of the apparatus, respectively. Defining the activity coefficient as $\gamma_i = a_i/x_i$, the second term of Eqs. (5) become $\ln\gamma_i$.

When the gas and solid phases coexist in equilibrium at temperature T_c, the congruent chemical potential of each component may be expressed as follows:

$$\mu_i^{sc}(\text{As-P Binary}, T_c) = \mu_i^{gc}(\text{Gas}, T_c), \quad i = \text{As}, \text{P} \tag{6}$$

Then activities of each component in the solid solution can be represented in terms of the corresponding partial pressure of some molecular species in the gas phase.

$$a_{As}^{sc} = [P_{As_4}(T_c)/P^{\circ}_{As_4}(T_c)]^{1/4} = [P_{As_2}(T_c)/P^{\circ}_{As_2}(T_c)]^{1/2} , \quad (7\text{-}a)$$

$$a_{P}^{sc} = [P_{P_4}(T_c)/P^{\circ}_{P_4}(T_c)]^{1/4} = [P_{P_2}(T_c)/P^{\circ}_{P_2}(T_c)]^{1/2} , \quad (7\text{-}b)$$

where P is the partial pressure above the saturated solution and P^{o} is the pressure above the pure substance.

In a similar way, the thermodynamic properties of the components located in the right side of the apparatus may be derived by assuming that chemical equilibrium among the three phases is established. It follows that the ternary integral molar energy of mixing may be given as follows:

$$F_M(\text{Ternary Liquid}) = X_{Ga}^{\ell h} X_{As}^{\ell h} \Delta\Omega_{GaAs}^{\ell} + X_{Ga}^{\ell h} X_{P}^{\ell h} \Delta\Omega_{GaP}^{\ell} + X_{As}^{\ell h} X_{P}^{\ell h} \Delta\Omega_{AsP}^{\ell}$$
$$+ RT(X_{Ga}^{\ell h} \ln X_{Ga}^{\ell h} + X_{As}^{\ell h} \ln X_{As}^{\ell h} + X_{P}^{\ell h} \ln X_{P}^{\ell h}) . \quad (8)$$

The activities a_{Ga}^{lh}, a_{As}^{lh}, and a_{P}^{lh} may be expressed by(II-3)

$$\ln a_{Ga}^{\ell h} = \ln X_{Ga}^{\ell h} + [(X_{As}^{\ell h}\Delta\Omega_{GaAs}^{\ell} + X_{P}^{\ell h}\Delta\Omega_{GaP}^{\ell})(X_{As}^{\ell h} + X_{P}^{\ell h}) - X_{As}^{\ell h} X_{P}^{\ell h}\Delta\Omega_{AsP}^{\ell}]/RT, \quad (9\text{-}a)$$

$$\ln a_{As}^{\ell h} = \ln X_{As}^{\ell h} + [(X_{Ga}^{\ell h}\Delta\Omega_{GaAs}^{\ell} + X_{P}^{\ell h}\Delta\Omega_{AsP}^{\ell})(X_{Ga}^{\ell h} + X_{P}^{\ell h}) - X_{Ga}^{\ell h} X_{P}^{\ell h}\Delta\Omega_{GaP}^{\ell}]/RT, \quad (9\text{-}b)$$

$$\ln a_{P}^{\ell h} = \ln X_{P}^{\ell h} + [(X_{Ga}^{\ell h}\Delta\Omega_{GaP}^{\ell h} + X_{As}^{\ell h}\Delta\Omega_{AsP}^{\ell})(X_{Ga}^{\ell h} + X_{As}^{\ell h}) - X_{Ga}^{\ell h} X_{As}^{\ell h}\Delta\Omega_{GaAs}^{\ell}]/RT . \quad (9\text{-}c)$$

The condition for the chemical equilibrium at temperature T_h between liquid and gas phases is found to be

$$\mu_i^{\ell h}(\text{Ternary Liquid}, T_h) = \mu_i^{gh}(\text{Gas}, T_h) , \quad i = Ga, As, P . \quad (10)$$

Neglecting the partial pressure of Ga, the partial pressures of As_2, As_4, P_2 and P_4 are related to the activities of As and P by

$$a_{As}^{\ell h} = [P_{As4}(T_h)/P^{\circ}_{As4}(T_h)]^{1/4} = [P_{As2}(T_h)/P^{\circ}_{As2}(T_h)]^{1/2} , \qquad (11\text{-}a)$$

$$a_{P}^{\ell h} = [P_{P4}(T_h)/P^{\circ}_{P4}(T_h)]^{1/4} = [P_{P2}(T_h)/P^{\circ}_{P2}(T_h)]^{1/2} . \qquad (11\text{-}b)$$

The chemical potentials in the solid phase$^{(II-3)}$ are

$$\mu_{GaAs}^{sh} = \mu_{GaAs}^{sho} + RT_h \ln \gamma_{GaAs}(1-X) , \qquad (12\text{-}a)$$

$$\mu_{GaP}^{sh} = \mu_{GaP}^{sho} + RT_h \ln \gamma_{GaP} X , \qquad (13\text{-}b)$$

where X is the mole fraction of GaP in the crystalline solid solution and here X equals to $2X_P^{sh}$. The another representation for the chemical potential in the solid phase has been described in Appendix, but the similar forms to the above equations(12) have been resulted.

The condition of the equilibrium between liquid and solid phase is given by the equations(II-4) and (II-5). Under the regular approximation, its condition could be reduced to the equations,

$$\ln(1-X) + X^2 \Delta\Omega_s/RT_h = \ln(1-2X_P^{\ell h}) + (2X_P^{\ell h})^2 \Delta\Omega_{AsP}^{\ell}/2RT_h + \Delta G_{fGaAs} , \qquad (14\text{-}a)$$

$$\ln X + (1-X)^2 \Delta\Omega_s/RT_h = \ln(2X_P^{\ell h}) + (1-2X_P^{\ell h})^2 \Delta\Omega_{AsP}^{\ell}/2RT_h + \Delta G_{fGaP} , \qquad (14\text{-}b)$$

Therefore we can find numerically the equilibrium condition.

On the other hand, for the reactions of $2As_2=As_4$ and $2P_2 =P_4$, the equilibrium constants, K_{As} and K_P may be defined as

$$K_{As} = P_{As4}/[P_{As2}]^2 , \qquad (15\text{-}a)$$

$$K_P = P_{P4}/[P_{P2}]^2 , \qquad (15\text{-}b)$$

Upon substituting Eqs.(7) and (11) into Eq.(3), one obtains

$$\ln \frac{P^{\circ}_{As_4T}(T_c)}{P^{\circ}_{As_4T}(T_h)} + 4 \ln \frac{a^{sc}_{As}}{a^{lh}_{As}} + \ln \frac{S_{As_4}(T_c)\,\omega(As, sc, T_c)}{S_{As_4}(T_h)\,\omega(As, lh, T_h)} = 0 \,, \qquad (16\text{-}a)$$

$$\ln \frac{P^{\circ}_{P_4T}(T_c)}{P^{\circ}_{P_4T}(T_h)} + 4 \ln \frac{a^{sc}_{P}}{a^{lh}_{P}} + \ln \frac{S_{P_4}(T_c)\,\omega(P, sc, T_c)}{S_{P_4}(T_h)\,\omega(P, lh, T_h)} = 0 \,, \qquad (16\text{-}b)$$

where

$$\omega(i, m, T) = 1 + \frac{P^{\circ}_{i_2}(T)}{P^{\circ}_{i_T}(T)} \, \frac{S_{i_2}(T) - S_{i_4}(T)\{a^{m}_{i}(T)\}^2}{S_{i_4}(T)\{a^{m}_{i}(T)\}^2} \,.$$

Eqs.(16-a) and (16-b) represent the fundamental relations for the pseudo-equilibrium between the binary solid phase at the T_c part and the ternary liquid phase at the T_h part.

From the results obtained above, the mole fraction of the binary solid solution, X^{sc}_{P} and the temperature T_c in the left hand side of the apparatus can be calculated using the relations (14) and (16), and provided, (a) the mole fraction of the crystalline solid solution X^{sh}_{P} and its formation temperature T_h are given, and (b) parameters Ω_i and each partial pressure of the pure component are known.

3-4) Numerical Analysis

In order to analyze numerically the above pseudo-equilibrium, it is necessary to know their parameters. The data on the vapour pressure over the pure elements of Table 3 is used to analyze the pseudo-equilibrium state. The molecular species of the pure elements listed in Table 3 are thought to consist of four atoms

Table 3 Vapor Pressure over Pure Elements, log P (atm)

The parentheses and brackets denote the pressure over the solid and liquid phase, respectively

Element	Literature	Adopted
(As_4)	-6872/T + 7.766[13] -6570/T + 7.373[14] -7357/T + 8.279[15]	-7357/T + 8.279
[As_4]	-2450/T + 3.800[15] -1286.5/T + 2.547[14]	-2450/T + 3.800
(P_4)	-6322/T + 8.958[13] -7240/T + 9.969[16] -5600/T + 8.119[16]	-6322/T + 8.958
[P_4]	-2740/T + 4.959[16] -2757.5/T + 5.073[15]	-2757.5/T + 5.073

Table 4 Equilibrium Constants, log K

Reaction	Literature	Adopted
$2As_2 = As_4$	15360/T - 8.29[17] 14955/T - 8.67[18]	15360/T - 8.29
$2P_2 = P_4$	7518/T - 4.938[15] 8400/T - 6.68[17]	7518/T - 4.938

As indicated by various authors reporting on the low temperature measurements. Since the condenced systems investigated on the present study are solid and liquid, the data for the solid and liquid phases listed in

Table 5 Quasi-Chemical Interchange Energy
(cal/gr-mole)

System	Literature	Adopted
Ga - As	$9969 - 11.15T$[14] $-3.7T$[19]	$9969 - 11.15T$
Ga - P	$7900 - 7.00T$[14]	$7900 - 7.00T$
As - P	2000	2000

Table 3 are used. Table 4 lists the values of equilibrium constants for reactions $2As_2 = As_4$ and $2P_2 = P_4$ over compounds. Partial pressures of the di-atomic species, As_2 and P_2, then can be computed from the data on the tera-atomic species by use of the equilibrium constants.

In the binary solid solution of As and P, Ω^{s}_{As-P} has been calculated from the phase diagram[10] to be approximately 2000 cal/gr-mole.

In general, Ω is independent of composition and temperature in a regular solid solution. However it is dependent on temperature in real binary liquids such as Ga-As and Ga-P as shown in Table 4. Such solutions are defined by $\Omega = \alpha - \beta T$. For binary systems similar to the III-V systems, the composition of liquid state corresponds to that of the solid state at the melting point. For this point the activity coefficient of component i in solid solution can be written as $\ln \gamma_i^{sh} = \Delta G_{fi} + \ln \gamma_i^{\ell h}$. ΔG_{fi} is the molar free energy of fusion of component i. The activity coefficient is related to the quasi-chemical interchange energy by the relation $\ln \gamma_i = \Omega/4RT$. Hence the data reported by C. D. Thurmond[14)] and J. R. Arthur[19)] may be used near the melting point as the interchange energy in the binary liquid phase.

The GaAs-GaP quasi-binary phase diagram[20)] is shown in Fig. 2 of chapter II. The dotted curves indicate the ideal solidus and liquidus lines calculated on the assumption of the molecular-like model of Ga-As or Ga-P atoms pair. In the diagram, the experimental values, indicated by the open circles, are in good agreement with the calculated solidus line. In addition it is known[6)] that the change in lattice parameter vs. composition for the GaAs-GaP system obeys Vegards law. Thus it can be said that the solid solution behaves like an ideal one. As a result, $_s$ might be taken to be approximately zero.

Using the values discussed in the previous paragraphs, various thermodynamic parameters of the system in pseudo-equilibrium can be computed from Eqs.(16). Fig. 6 shows the temperature T_c, the temperature in the left hand side of the apparatus, required to hold the composition X_P^{sh} and the temperature T_h on the experimental solidus line of the quasi-binary phase diagram. Fig. 7 shows the composition X_P^{sc} as a function of composition X_P^{lh}. The partition of relative molar quantities of Ga, As, and P for the two parts with different temperature is shown. Moreover the composition, X_P^{sh} of crystalline solid solution corresponding to X_P^{lh} could be found from the equation(14). Fig. 8 indicates the equilibrium partial and total pressures of As and P on the liquidus line.

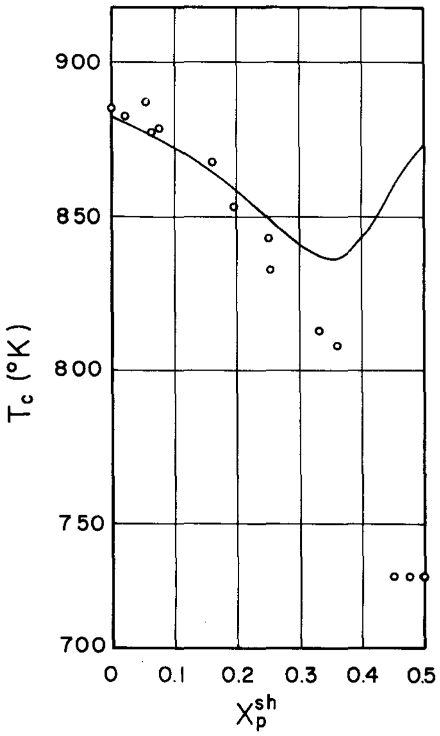

Fig. 6 Temperature in the T_c part required to obtain the crystalline solid solution of mole fraction X_P. The solid lines show the theoretical curves. Open circles are the values obtained experimentally.

It is possible from the above discussion to apply the concept of pseudo-equilibrium to the preparation of the ternary compound containing two volatile components, for example, the crystalline solid solution of the type $A^{III}As_{1-x}P_x$, where A^{III} may be a low volatility element such as Al, Ga and In. When the left side of the apparatus is kept in a suitable state which is characterized by X_P^{sc} and T_c, the crystalline solid solution can be produced in the right side. The method of preparation of the $GaAs_{1-x}P_x$ compound can be developed according to this conception. The details of experimental method had been described in the previous section 2.

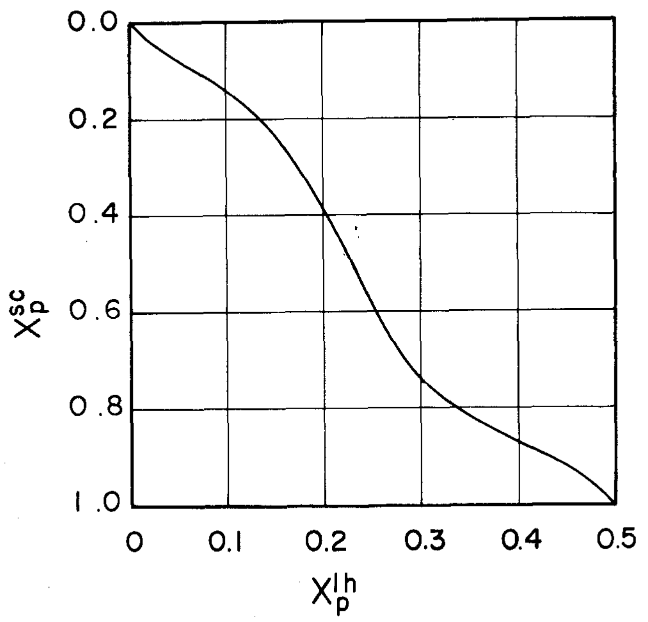

Fig. 7 Distribution of P in two phases (sc) and (sh) necessary to hold the pseudo-equilibrium. The solid lines show the theoretical curves. Open circules are the values obtained experimentally.

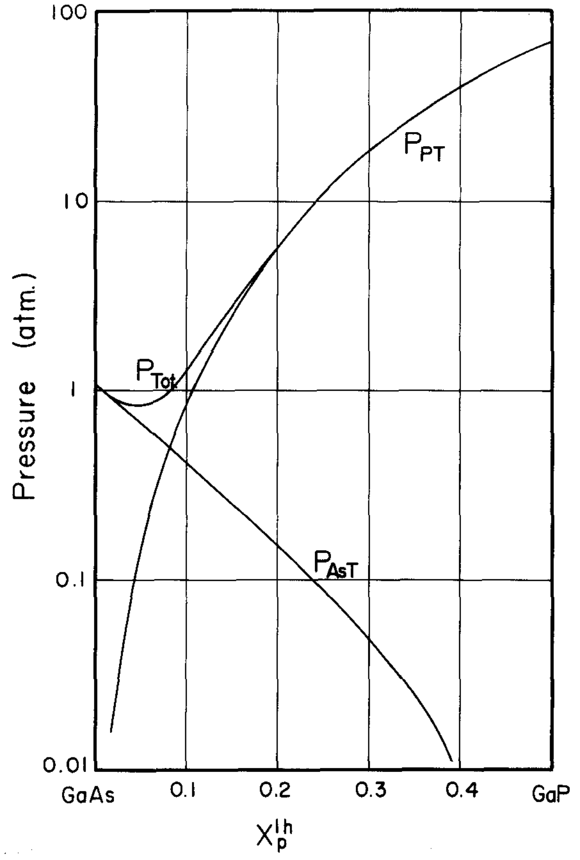

Fig. 8 Theoretical equilibrium partial and total pressures of As and P at the melting point of the crystalline solid solutions. The solid and dotted lines are labeled A and B, respectively (see in the text).

4. Discussion

In the present work, the method for the preparation of the crystalline solid solution of $GaAs_{1-x}P_x$ from the melt has been developed by controlling vapour pressure of As and P. The compounds of $GaAs_{1-x}P_x$ in the whole composition range of GaAs and GaP could be obtained by the method. The crystal structure and lattice parameters were confirmed and determined by powder X-ray method. Compounds thus obtained have exhibited a high degree of homogeneity in their Ga-As-P ratio perpendicular to the growth direction. The composition along the length of crystals remains constant or varies gradually depending upon the condition of the preparation. Several important points to obtain a homogeneous ingot with desired composition by the present technique will now be discussed as follows.

When the relative molar amounts of Ga, As and P were weighed out and put into the vessel, the composition of ingot prepared in the present method is mainly dependent on the temperature T_c in the left side of the apparatus. It is found that the higher value of T_c results in the lower value of the composition $2X_p^{sh}$(ingot) of ingot. These tendencies were known in Table 2, for example, when sample number 3 and 4, or 5 and 6 were compared with each other.

The change of composition along the ingot in Fig. 3 is closely related to the fact that after the initial solidification occurs, the relative amounts of the composition change in each phase. This change of composition could be estimated from the phase relations as indicated in Figs. II-2 and 7. The quasi-binary phase diagram of GaAs and GaP compounds suggests that the relative amount of phosphorous along the ingot decreases from the top to the tail. However the change in composition can be reduced to some extent by putting sufficiently large amounts of As and P to the left side of the apparatus. It is confirmed from the experimental results that the larger the ratio of $N_{As}+N_P$ to N_{Ga} becomes, the smaller change of composition along the ingot. As shown in Fig. 3, some ingots have exhibited a high degree of homogeneity in the portion around the top of ingot.

Fig. 9 shows the relation between X_P^{sh}(ingot) and X_P^{sh} which was initially determined, where the solid line means the coincidence of the theoretical consideration with the experiments. It could be seen that the experimental data are located around the the solid line. The pseudo-equilibrium was based on the assumption that there is no net flow of atoms in either direction between T_c and T_h parts of the apparatus. Its equilibrium has been

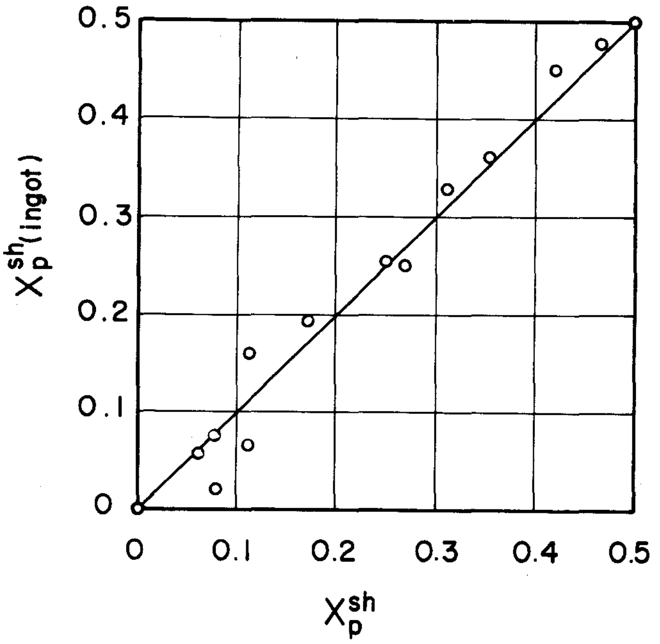

Fig. 9 Coincidence between the composition X_P^{sh}(ingot) and the initially weighed value X_P^{sh}.

concluded to exist between the Ga-As-P ternary system and the As-P binary system under the suitable conditions.

5. Summary

(1) A two temperatures method has been developed for the preparation of the crystalline solid solution of $GaAs_{1-x}P_x$. As seen in Table 2, the $GaAs_{1-x}P_x$ compounds with various compositions were obtained in the present work.

(2) Solid solutions obtained have exhibited a high degree of homogeneity in their Ga-As-P ratio in the section perpendicular to the growth direction. The composition along the length of ingots remains constant or varies gradually depending upon the condition of the preparation.

(3) The theoretical formulae were derived in order to calculate the pseudo-equilibrium in a heterogeneous system consisting of two parts with different temperatures. Its equilibrium was based on the assumption that there is no net flow of atoms in either direction between T_c and T_h parts. The equilibrium has been concluded to exist between the Ga-As-P ternary system and the As-P binary system under the suitable conditions.

Appendix

The thermodynamic values for the enthalpy, entropy and free energy of solution are related by the Gibbs-Helmholtz equation,

$$F_M = H_M - TS_M. \qquad (A-1)$$

Assuming that all condensed phases are taken to be regular, the value for entropy which coincides with one of ideal solution, is given by

$$S_M = R\,(X_{Ga} \ln X_{Ga} + X_{As} \ln X_{As} + X_P \ln X_P)\,. \qquad (A-2)$$

The molar enthalpy of solution is calculated as follows. The GaAs-GaP compound with a zinc-blende type structure is represented in Fig. 10. Here the middle-points of each dumb-bell pair consisting of either Ga-As or Ga-P have a fcc symmetry. Representing each of Ga-As or Ga-P pair as a molecule B or C, respectively, the excess molar enthalpy of the crystalline solid solution could be calculated by Giggenheims quasi-chemical method used in binary solutions. The total entropy of the solutions is

$$H_M = \tfrac{1}{2} Z N_B H_{BB} + \tfrac{1}{2} Z N_C H_{CC} + P_{BC}\left[H_{BC} - \tfrac{1}{2}(H_{BB} + H_{CC})\right]. \qquad (A-3)$$

For convenience, the value Ω_S is defined as follows:

$$P_{BC}\left[H_{BC} - \tfrac{1}{2}(H_{BB} + H_{CC})\right] \equiv X_{As} X_P \Omega_s\,, \qquad (A-4)$$

where P_{BC} is the total number of bonds between unlike molecules, Z is the coordination number, and $2(N_B + N_C) = N_o$ is the number of atoms per one gr-atom where N_o is Avogadros number. H_{BB}, H_{CC} and H_{BC} are the corresponding bonding energies for the individual combinations. The excess molar enthalpy of $2N_B$ atoms in the

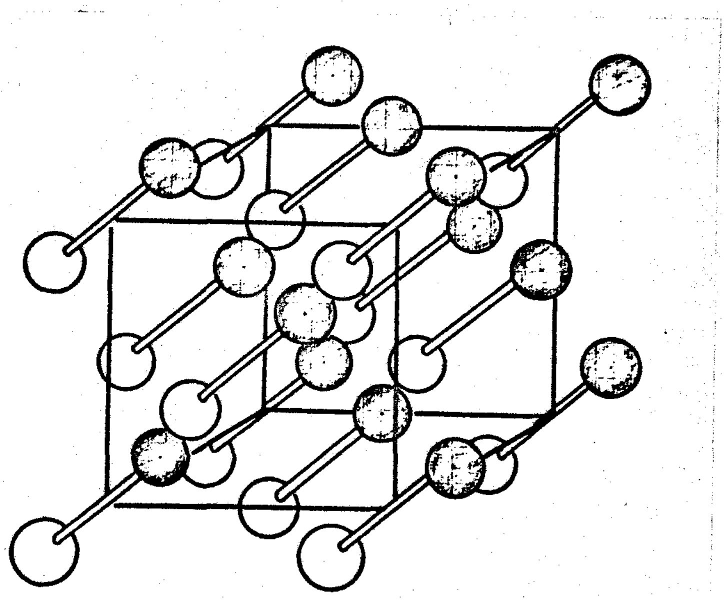

Fig. 10 Structure of $GaAs_{1-x}P_x$ compound: a dumb-bell indicates a pair of Ga-As or Ga-P, where a white ball shows the Ga atom and a grey one the As or P.

Ga-As binary system is equal to $1/2ZN_BH_{BB}$. This may be written as $1/2N_B/N_o\Delta\Omega_{Ga-As}$ where $1/4\Delta\Omega_{Ga-As}$ is the excess value per one gr-atom. Correspondingly the enthalpy of $2N_C$ atoms in the pure Ga-P binary system is equal to $1/2N_c/N_o\Delta\Omega_{Ga-P}$. The integral molar enthalpy of mixing is given by

$$H_M = \tfrac{1}{2} X_{As}\Delta\Omega_{GaAs} + \tfrac{1}{2} X_P\Delta\Omega_{GaP} + X_{As}X_P\Delta\Omega_s \,. \qquad (A-5)$$

Thus the relative partial molar free energy and activities can be obtained directly with the aid of the general thermodynamic differential equations with the added conditions, $X_{Ga} = 1/2$ and $X_{As} + X_P = 1/2$, one obtains

$$\bar{F}_{M,Ga} = RT\ln a_{Ga} = RT\ln\tfrac{1}{2} + \tfrac{1}{2}X_{As}\Delta\Omega_{GaAs} + \tfrac{1}{2}X_{P}\Delta\Omega_{GaP} + X_{As}X_{P}\Delta\Omega_{s}, \tag{A-6-a}$$

$$\bar{F}_{M,As} = RT\ln a_{As} = RT\ln X_{As} + \tfrac{1}{4}\Delta\Omega_{GaAs} + \tfrac{1}{4}(1-2X_{As})^{2}\Delta\Omega_{s}, \tag{A-6-b}$$

$$\bar{F}_{M,P} = RT\ln a_{P} = RT\ln X_{P} + \tfrac{1}{4}\Delta\Omega_{GaP} + \tfrac{1}{4}(1-2X_{P})^{2}\Delta\Omega_{s}. \tag{A-6-c}$$

References

1) O. G. Folberth; Z. Naturf. 10(1955)502

2) W. Köster and W. Ulrich; Z. Metallk., 49(1958)365

3) O. V. Bogorodskii, and A. Yanashel'skii and V. Z. Ostrovskaya ;Soviet Phys. Crystallography 6(1961)95

4) D. Richman; J. Phys. Chem. Solids 24(1963)1131

5) C. J. Frosch and L. Derick; J. Electrochem. Soc. 108(1961)251

6) M. E. Straumains, J.-P. Krumme and M. Rubenstein; J. Electrochem. Soc. 114(1967)640

7) Y. S. Chen, W. Shockley and G. L. Pearson; 151(1968)648

8) W. G. Spitzer; J. Phys. Chem. Solids; 28(1968)33

9) T. K. Bergstresser, M. L. Cohen and E. W. Williams; Phys. Rev. Letters 15(1965)662

10) H. Krebs, W. Holz and K. H. Worms; Chem. Ber. 90(1958)1031

11) R. R. Fergusson and T. Gabor; J. Electrochem. Soc. 111(1964)589

12) R. A. Swalin; Thermodynamics of Solids, John Wiley and Sons , New York, 1963

13) R. E. Honig; RCA Review, 1962, p567

14) C. D. Thurmond; J. Phys. Chem. Solids 26(1966)785

15) A. N. Nesmeyanov; Vapor Pressure of the Chemical Elements, Elsevier Publishing Company, 1963

16) O. Kubaschewski and E. LL. Evans; Metallurgical Thermochemistry, Pergamon Press, 1958

17) J. Drowart and P. Goldfinger; J. Shim. Phys. 55(1958)721

18) P. Goldfinger; Advances in Mass Spectrometry, Pergamon Press, London, 1959, p534

19) J. R. Atthur; J. Phys. Chem. Solids 28(1967)2257

20) K. Osamura and Y. Murakami; J. Appl. Phys. Japan 8(1957)967

Chapter IV

X-Ray Studies on Structure and Properties of Compound Semiconductors

1. Relative integrated intensity and effective charge in $GaAs_{1-x}P_x$ compounds.

1-1) Introduction

Precise measurements of X-ray intensity diffracted from crystals seem to become more and more important for the investigation of electron distributions in crystals with known structures and for any kind of other quantitative works with X-rays.

An accuracy of 1-2% in the absolute values of the atomic scattering and structure factors may be considered in some cases as sufficient for solving a number of quantum-chemical and quantum-mechanical problems.1) Quantitative calculation of certain properties of crystals is already possible from the atomic scattering or structure factor values with an accuracy comparable with a direct experimental determination. We shall enumerate some opportunities which are now open in terms of the experimentally determined structure factors. They are as follows: qualitative classification of crystals according to the type of the chemical bond, including a calculation of the number of quasi-free electrons in metals; determination of dia- and paramagnetic components (Langevin and van Vleck part) of magnetic susceptibility in semiconductor crystals of elements and the simplest compounds, for example with a sphalerite structure; definition of the effective ionic charges in ionic and covalent crystals; semi-quantitative estimation of the energy of the chemical bond in crystals; calculation of the zone structure in semiconductors; calculation of the elastic constants and phonon spectra in crystals, using maps of the electron density distribution or directly using structure and atomic scattering factors.

One of the fundamental differences between the III-V compounds and the elemental semiconductors is the crystal binding. We are mainly interested in establishing the charge difference between the III atom with its surrounding electron cloud and the V atom with its cloud. The simple picture we can use, say for GaAs, starts with the Ga^{3+} atom and its three valence electrons in proximity to the As^{5+} atom and five valence electrons. If no charge transfer took place the bonding would be neutral. The eight valence electrons could, however, all congregate around the As atom, forming Ga^{3+} and As^{3-} ions. The crystal would be ionic. A third possibility is for one electron to pass from the As atom to the Ga atom. Tetrahedral bonds could be formed as in germanium, and we would say the crystal binding was covalent. It is important to realize that covalence of the bond does not imply neutrality of the atoms. A charge transfer of one electron is large, and such a covalent compound would behave in a number of ways exactly like a strongly ionic crystal. We can give a semivalence of a numerical scale to the charge transfer by postulating that we can arbitrarily divide the crystal, with each III atom and an electron cloud in a sphere, and the V atom and an electron cloud in a neighboring sphere. We can then define an effective charge e^*, as the total charge within the III atom sphere.

The X-ray diffraction measurement gives both the magnitude and sign of e^*, and many authors2),3),4) have calculated it for III-V compounds.

The object of the present work is mainly to investigate the variation of the effective charge in GaAs-GaP quasi-binary system.

1-2) Experimentals

(a) Samples

Specimens of GaAs-GaP alloys for the present work were prepared by the two temperatures method. Polycrystalline ingots were grown from melts with various compositions. Fine powders were collected by sedimentation in xylene. The particle size was less than about 7μ . The homogeneity and alloy composition of specimens were tested by powder X-ray diffractometer. It was assumed that the change of their lattice parameters with composition obeys Vegard's law.

(b) Apparatus

Relative intensities of diffracted X-rays were measured by a diffractometer with CuKα. The measurement was carried out with a Geiger-Müller counter, and with a monochromator consisting of a curve crystal of quartz set in front of the counter.

(c) Measurements

The intensity measurements were performed by two techniques. In the measurements of the intensities of ordinary diffraction lines, the counter was scanned at a constant speed of 1/4 or 1/8 degree per minute, and background intensity for each reflection was subtracted from total counts. Intensities of the background were measured by counting for more than 10 minutes at positions sufficiently apart from the diffraction line concerned. Intensities of the background at the positions of the line were determined by interpolation. On the other hand, the intensities of (200), (222), and (422) diffraction lines are relatively weak. Intensities for these weak lines were measured at the fixed angle so long time that the statistical error would be counted out, and the operation was performed at intervals of $\theta = 0.025^\circ$ around the maximum diffraction angle. At the same time, the strong diffraction line was measured as a reference line and the integrated intensity was compared with the former one obtained by the scanning method.

1-3) Evaluation of the scale factor

The relative values of the structure factors, $F_{exp}(hk\ell)$, were obtained from the relative intensities, $I(hk\ell)$, by the following relation,

$$[F_{exp}(hk\ell)]^2 = \frac{k v^2 \mu}{j} K^2 I(hk\ell) , \qquad (1)$$

where K^2 is given by

$$K^2 = \frac{\sin^2\theta \cos\theta}{1 + \cos^2 2\theta_M \cos^2 2\theta} , \qquad (2)$$

when the monochromator was used, and by

$$K^2 = \frac{\sin^2\theta \cos\theta}{1 + \cos^2 2\theta} \qquad (3)$$

when it was not used, where θ_M is the Bragg angle for monochromating crystal, j is the multiplicity factor, v is the volume of a unit cell, μ is the linear absorption coefficient, and k is a constant to bring $F_{exp}(hk\ell)$ to convenient magnitude. The absolute values of the structure factors were obtained from the relative values by the procedure described in the following.

Table 1 Atomic scattering factor and anormalous dispersion

Atomic scattering factor, f^o

	0.00	0.05	0.10	0.15	0.20	0.25	0.30	0.35
P	15.00	14.47	13.17	11.66	10.34	9.33	8.59	8.02
Ga	31.00	30.30	28.65	26.76	24.92	23.16	21.47	19.84
As	33.00	32.27	30.47	28.29	26.20	24.34	22.69	21.15

	0.40	0.50	0.60	0.70
P	7.54	6.67	5.83	5.02
Ga	18.26	15.38	12.95	11.02
As	19.69	16.95	14.48	12.37

Anormalous dispersion, f' and f'' for CuKα radiation

	P	Ga	As
f'	0.27	-1.45	-1.17
f''	0.46	0.98	1.17

The theoretical structure factors without the anomalous dispersion were calculated from the theoretical atomic scattering factors of Ga, As and P, where atoms are neutral. The correction for the anomalous dispersion was made by using the values tabulated by D. T. Cromer[5)] as shown in Table 1.

The theoretical structure factors taking account of the anomalous dispersion were given by

$$F_T(hkl) = \exp(-\langle B\rangle \sin^2\theta/\lambda^2)\, F_0(hkl) \quad , \qquad (4)$$

$$F_0(hkl) = \begin{cases} 4\left[(f_{\mathrm{III}}^{0} + f_{\mathrm{V}}^{0} + f_{\mathrm{III}}' + f_{\mathrm{V}}')^2 + (f_{\mathrm{II}}'' + f_{\mathrm{V}}'')^2\right]^{1/2} \\ \quad \text{for } (220), (400), (422), \text{ and } (620) \text{ line} \\ 4\left[(f_{\mathrm{III}}^{0} - f_{\mathrm{V}}^{0} + f_{\mathrm{III}}' - f_{\mathrm{V}}')^2 + (f_{\mathrm{III}}'' - f_{\mathrm{V}}'')\right]^{1/2} \\ \quad \text{for } (200), (222), \text{ and } 422 \text{ line} \\ 4\left[(f_{\mathrm{III}}^{0} + f_{\mathrm{III}}' \pm f_{\mathrm{V}}'')^2 + (f_{\mathrm{V}}^{0} + f_{\mathrm{V}}' \pm f_{\mathrm{V}}^{\mathrm{III}})\right]^{1/2} \\ \quad \text{for } (111), (311), (333), (511), (533), (531) \\ \quad \text{and } (551) \text{ line} \end{cases}$$

where f_{III}^{0} and f_{V}^{0} are atomic scattering factors of the III-atom and the V-atom respectively, and f' and f'' are real and imaginary part of the anomalous dispersion term, $\langle B\rangle$ is the average temperature factor which is determined by the procedure shown later.

In the alloy system, it was assumed that both As and P atoms substitute each other in the V-atom site. Then the atomic scattering factors in the alloy system were given by the equation,

$$f_{\mathrm{III}} = f_{Ga} ,$$
$$f_{\mathrm{V}} = x f_P + (1-x) f_{As} , \qquad (6)$$

where x is the mole fraction of GaP. The relation between the theoretical and experimental structure factor was combined by the scale factor k_0 as shown in the equation;

$$F_{exp}(hkl)/F_0(hkl) = k_0 \exp(-\langle B\rangle \sin^2\theta/\lambda^2) . \qquad (7)$$

The average temperature factor and the scale factor, k_o, were estimated from the gradient of log (F_{exp}/F_o) plotted against $\sin^2\theta / \lambda^2$ by using the square mean least method. At the same time, in the alloy system, the alloy composition was checked by using the condition that the R-factor defined by $\left\{\sum_{\mathbb{h}} |F_{exp}(\mathbb{h})|^2 - |F_T(\mathbb{h})|^2\right\} / \sum_{\mathbb{h}} |F_{exp}(\mathbb{h})|^2$ is minimum. In this estimation, the data for (200), (222), and (422) were omitted, because F_o for these reflections might deviate from the real one due to the partially ionicity of constituent atoms.

1-4) Temperature factors of individual atoms

The square mean least method is used for determining the temperature factors of individual atoms of a crystal having the zinc-blende type structure as defined by the equation.

$$R_s = \sum_q \omega(\mathbb{h}) \left\{ \sum_j \frac{\partial F_T(\mathbb{h}; u_j)}{\partial u_j} \Delta u_j - \left[|F_{exp}(\mathbb{h})| - |F_T(\mathbb{h})| \right]^2 \right\}, \tag{8}$$

$$\partial R_s / \partial u_i = 0 , \tag{9}$$

where the theoretical structure factor, $F_T(\mathbb{h})$ may be written in the convenient form instead of the equation(4),

$$F_T(hk\ell) = 4 \Big\{ \big[f_{III} \exp(-B_{III}\xi) + (f_V \cos\tfrac{\pi}{2}(h+k+\ell) - f'_V \sin\tfrac{\pi}{2}(h+k+\ell)) \exp(-B_V\xi) \big]^2$$
$$+ \big[f'_{III} \exp(-B_{III}\xi) + (f_V \sin\tfrac{\pi}{2}(h+k+\ell) + f'_V \cos\tfrac{\pi}{2}(h+k+\ell)) \exp(-B_V\xi) \big]^2 \Big\}^{1/2}$$

where f_{III} or f_V is the real part of atomic scattering factor containing the anomalous dispersion term for the atom of III or

V site, respectively, and f'_{III} or f''_{V} is the imaginary one for each atom, ξ is $\sin^2\theta / \lambda^2$ and B_{III} and B_{V} are the temperature factors of the III- and V-atom, respectively. When the individual temperature factor for each atom is different to a small extent from the average temperature factor, $\langle B \rangle$, the following representations are allowable.

$$B_{\mathrm{III}} = \langle B \rangle + \Delta B_{\mathrm{III}} ,$$
$$B_{\mathrm{V}} = \langle B \rangle + \Delta B_{\mathrm{V}} . \tag{10}$$

Thus, the condition described by the equation(8) is explicitly given by the equations.

$$\partial R_s / \partial \Delta B_{\mathrm{III}} = 0, \quad \partial R_s / \partial \Delta B_{\mathrm{V}} = 0 . \tag{11}$$

Assuming that $\Delta B_{\mathrm{III}} / \langle B \rangle \ll 1$ and $\Delta B_{\mathrm{V}} / \langle B \rangle \ll 1$, the following approximate equations were obtained.

$$\sum_{\mathbf{h}} w(\mathbf{h}) \left[\frac{\partial F_T(\mathbf{h})}{\partial \Delta B_{\mathrm{III}}} \right]^2 \Delta B_{\mathrm{III}} + \sum_{\mathbf{h}} w(\mathbf{h}) \left[\frac{\partial F_T(\mathbf{h})}{\partial \Delta B_{\mathrm{III}}} \frac{\partial F_T(\mathbf{h})}{\partial \Delta B_{\mathrm{V}}} \right] \Delta B_{\mathrm{V}} = \frac{1}{2} \sum_{\mathbf{h}} w(\mathbf{h}) \left[|F_{exp}(\mathbf{h})| - |F_T^A(\mathbf{h})| \right] \frac{\partial F_T(\mathbf{h})}{\partial \Delta B_{\mathrm{III}}},$$

$$\sum_{\mathbf{h}} w(\mathbf{h}) \left[\frac{\partial F_T(\mathbf{h})}{\partial \Delta B_{\mathrm{III}}} \frac{\partial F_T(\mathbf{h})}{\partial \Delta B_{\mathrm{V}}} \right] \Delta B_{\mathrm{III}} + \sum_{\mathbf{h}} w(\mathbf{h}) \left[\frac{\partial F_T(\mathbf{h})}{\partial \Delta B_{\mathrm{V}}} \right]^2 \Delta B_{\mathrm{V}} = \frac{1}{2} \sum_{\mathbf{h}} w(\mathbf{h}) \left[|F_{exp}(\mathbf{h})| - |F_T^A(\mathbf{h})| \right] \frac{\partial F_T(\mathbf{h})}{\partial \Delta B_{\mathrm{V}}}, \tag{12}$$

where

$$A_r = f_{\mathrm{III}} + f_{\mathrm{V}} \cos\frac{\pi}{2}(h+k+\ell) - f'_{\mathrm{V}} \sin\frac{\pi}{2}(h+k+\ell) , \tag{13}$$

$$A_i = f'_{\mathrm{III}} + f_{\mathrm{V}} \sin\frac{\pi}{2}(h+k+\ell) + f'_{\mathrm{V}} \cos\frac{\pi}{2}(h+k+\ell) , \tag{14}$$

$$F_T(\mathbf{h}) = F_T^A(\mathbf{h}) + \frac{\partial F_T(\mathbf{h})}{\partial \Delta B_{\mathrm{III}}} \Delta B_{\mathrm{III}} + \frac{\partial F_T(\mathbf{h})}{\partial \Delta B_{\mathrm{V}}} \Delta B_{\mathrm{V}} , \tag{15}$$

$$F_T^A(\mathbb{h}) = 4\exp(-\langle B\rangle\xi)\left[A_r^2 + A_i^2\right]^{1/2} \qquad (16)$$

$$\frac{\partial F_T(\mathbb{h})}{\partial \Delta B_{\text{III}}} = -\xi\exp(-2\langle B\rangle\xi)\left[f_{\text{III}}A_r + f'_{\text{III}}A_i\right]/F_T^A(\mathbb{h}), \qquad (17)$$

$$\frac{\partial F_T(\mathbb{h})}{\partial \Delta B_{\text{V}}} = -\xi\exp(-2\langle B\rangle\xi)\Big\{\left[f_{\text{V}}\cos\tfrac{\pi}{2}(h+k+\ell) - f'_{\text{V}}\sin\tfrac{\pi}{2}(h+k+\ell)\right]A_r$$
$$+\left[f_{\text{V}}\sin\tfrac{\pi}{2}(h+k+\ell) + f'_{\text{V}}\cos\tfrac{\pi}{2}(h+k+\ell)\right]A_i\Big\}/F_T^A(\mathbb{h}). \qquad (18)$$

From (11) the values of ΔB_{III} and ΔB_{V} and therefore, of B_{III} and B_{V} would be determined.

1-5) Results

Table 2 shows the sample number used here and its alloy composition, along with the lattice constant at room temperature. The lattice constant of GaAs obtained, 5.6530±0.0005 Å, is in agreement with the reported ones$^{6),7)}$. Also that of GaP obtained, 5.4506±0.0005 Å, agrees quite well with G. Giesecke's data$^{6)}$, but disagree with Straumanis′ one$^{8)}$.

The log arithmetic plots of F_{exp}/F_o against $\sin^2\theta / \lambda^2$ are shown in Fig. 1.

The absolute values of structure factors determined by the method discussed above are listed in Tables 3, along with the theoretical structure factors, $F_T(\mathbb{h})$, and the average temperature factor, $\langle B\rangle$.

The temperature factors of the two atoms, B_{III} and B_{V}, were determined by the least mean square method. The value of $F_T(\mathbb{h})$ was obtained with the above temperature factors and is listed in

Table 2 Sample number, lattice constant and alloy composition

Sample No.	a (Å)	x	Remark
GaAs	5.6530 ± 0.0005	0	GaAs
X13	5.627 ± 0.001	0.13	A802P-1
X34	5.583 ± 0.001	0.343	RF805-2
X53	5.543 ± 0.001	0.535	RF902-1
X75	5.502 ± 0.001	0.749	Rf808-2
GaP	5.4506 ± 0.0005	1.000	GaP

Tables 4, along with $F_{exp}(\mathbb{h})$ and $\Delta F(\mathbb{h})$, where $\Delta F(\mathbb{h})$ is given by $F_{exp}(\mathbb{h}) - F_T(\mathbb{h})$.

In the above analysis, the reflections of (200), (222) and (422) lines were omitted, because these intensities are relatively weak. Also the atomic scattering factors used were referred to neutral states, but the actual electron distribution around each atom has no spherical symmetry and would be expected that negative charge is being passed from the V atom to the III atom. Their situations will directly influence the intensities of (200), (222), and (422) lines having the structure factor given by the difference of atomic scattering factors between the III and the V atom. Values of these experimental structure factors were put to be the intensities multiplied by the scale factor. These theoretical values, however, were refferred to neutral states.

Fig. 2 shows the scale factor, k_o as a function of alloy composition corresponding to the term of $(kv^2\mu)^{-1/2}$ in the equation. The linear absorption coefficient is represented by

$$\mu = \frac{\rho}{M} \sum_i (\mu/\rho)_i n_i A_i \ , \qquad (19)$$

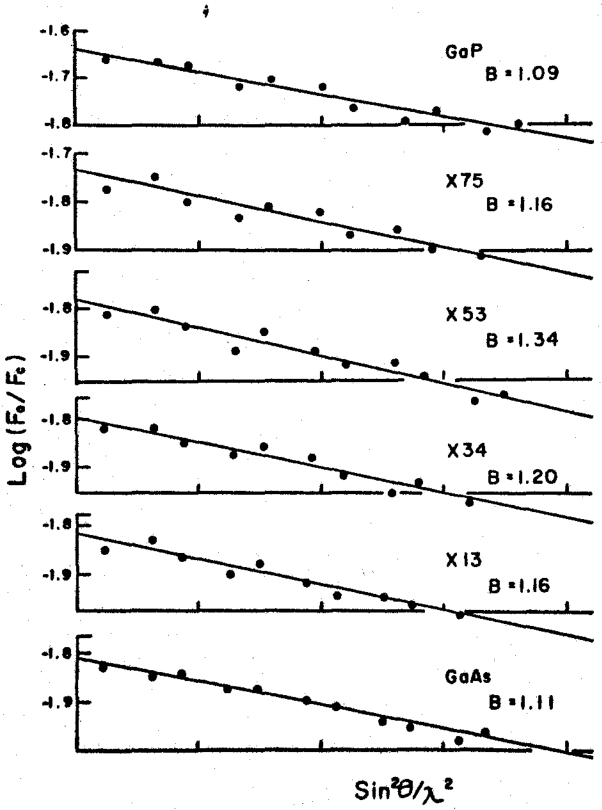

Fig. 1 $\log(F_{obs}/F_{cal})$ v.s. $\sin^2\theta / \lambda^2$

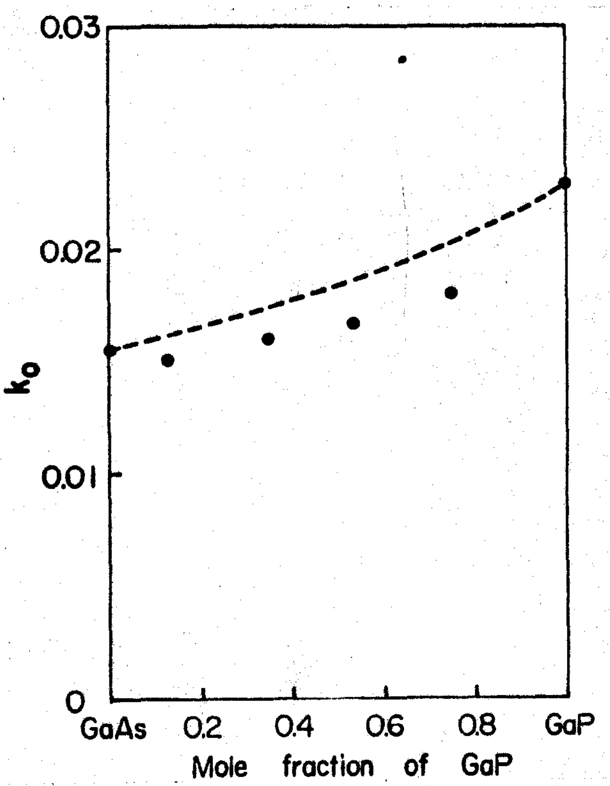

Fig. 2 The variation of scale factor, k_o as a function of alloy composition

Table 3a The absolute values of the structure factors

	GaP			X75			X53		
hkl	F_{obs}	F_{cal}	ΔF	F_{obs}	F_{cal}	ΔF	F_{obs}	F_{cal}	ΔF
111	104.41	107.31	-2.90	110.95	115.73	-4.78	116.93	121.70	-4.77
200	47.16	51.08	-3.88	32.60	34.70	-2.10	18.85	22.60	-3.75
220	116.68	114.48	2.20	138.10	129.07	9.03	143.53	137.52	6.01
311	80.79	78.45	2.34	82.47	84.37	-1.90	87.88	88.14	-0.26
222	37.60	38.66	-1.05	25.92	26.04	-0.12	-	-	-
400	86.50	89.94	-3.44	94.68	100.64	-5.96	101.20	106.43	-5.23
331	64.76	62.43	2.33	69.91	67.25	2.66	73.03	69.64	3.39
420	30.75	28.94	1.81	-	-	-	-	-	-
422	76.41	73.20	3.21	86.45	81.71	4.74	87.25	85.29	1.96
333 511	48.99	50.75	-1.76	52.82	54.62	-1.80	54.74	56.01	-1.27
440	57.08	60.43	-3.35	70.62	67.24	3.38	73.04	69.50	3.54
531	42.95	42.14	0.81	43.59	45.01	-1.42	45.75	45.71	0.04
620	48.84	50.40	-1.56	55.01	55.90	-0.89	53.50	57.10	-3.60
533	36.48	34.92	1.56	37.38	37.53	-0.15	38.60	37.91	0.69
	$B = 1.09$ Å^2 $k = 0.0229$, $R = 0.063$ $a = 5.4506 \pm 0.0005$ Å			$B = 1.16$ Å^2 $k = 0.0180$, $R = 0.095$ $a = 5.502 \pm 0.001$ Å			$B = 1.34$ Å^2 $k = 0.0166$, $R = 0.073$ $a = 5.543 \pm 0.001$ Å		

Table 3b The absolute values of the structure factors

	X34			X13			GaAs		
hkl	F_{obs}	F_{cal}	ΔF	F_{obs}	F_{cal}	ΔF	F_{obs}	F_{cal}	ΔF
111	124.82	129.13	-4.31	133.62	139.23	-5.61	141.44	144.15	-2.71
200	11.70	13.83	-2.13	6.58	0.74	5.84	8.08	6.95	1.13
220	152.95	148.15	4.80	168.71	161.28	7.43	164.26	167.32	-3.06
311	93.28	95.05	-1.77	103.86	103,09	0.77	110.52	107.50	3.02
222	-	-	-	-	-	-	-	-	-
400	113.66	115.97	-2.31	122.65	127.03	-4.38	132.23	132.57	-0.34
331	79.18	75.92	3.26	86.97	83.01	3.96	88.75	86.79	1.96
420	-	-	-	-	-	-	-	-	-
422	98.09	93.72	4.37	103.46	102.92	0.54	109.44	107.88	1.56
333 511	61.10	61.66	-0.56	65.75	67.75	-2.00	72.05	71.05	1.00
440	73.01	77.44	-4.43	85.75	85.54	0.21	88.60	90.12	-1.52
531	53.38	50.90	2.48	56.38	56.36	0.02	58.23	59.36	-1.13
620	62.79	64.42	-1.45	71.58	71.34	0.24	72.84	75.46	-2.62
533	42.66	42.68	-0.02	47.21	47.41	-0.20	51.96	50.27	1.69
	$B = 1.20$ Å^2 $k = 0.0160$, $R = 0.063$ $a = 5.583 \pm 0.001$ Å			$B = 1.16$ Å^2 $k = 0.0151$, $R = 0.056$ $a = 5.627 \pm 0.001$ Å			$B = 1.11$ Å^2 $k = 0.0154$, $R = 0.035$ $a = 5.6530 \pm 0.0005$ Å		

Table 4a Experimental structure factors and calculated structure factors

	GaP				X75			
hkl	F_{obs}	F_{cal}	ΔF	r	F_{obs}	F_{cal}	ΔF	r
111	104.40	107.54	-3.13	-0.060	110.95	115.27	-4.32	-0.079
200	47.16	51.06	-3.90	-0.152	32.60	34.75	-2.15	-0.123
220	116.67	114.73	1.94	0.033	138.10	127.90	10.19	0.142
311	80.78	79.14	1.63	0.040	82.47	83.13	-0.66	-0.161
222	37.60	38.70	-1.10	-0.056	25.92	25.88	0.03	0.002
400	86.49	90.28	-3.78	-0.089	94.68	98.89	-4.20	-0.090
331	64.75	63.33	1.42	0.043	69.91	65.63	4.27	0.118
420	30.75	28.97	1.77	0.122	-	-	-	-
422	76.40	73.56	2.83	0.072	86.45	79.70	6.74	0.150
333 511	48.99	51.73	-2.74	-0.115	52.82	52.88	-0.06	-0.002
440	57.07	60.81	-3.73	-0.135	70.62	65.13	5.47	0.149
531	42.95	43.09	-0.13	-0.006	43.59	43.24	0.34	0.015
620	48.83	50.74	-1.90	-0.079	55.01	53.82	1.19	0.042
533	36.47	35.94	0.53	0.028	37.38	35.79	1.58	0.083
	$B_{Ga} = 0.927$ Å^2 $B_P = 1.363$ Å^2 $R = 0.060$				$B_{Ga} = 1.394$ Å^2 $B_{As} = 1.510$ Å^2, $B_P = 0.813$ Å^2 $R = 0.093$			

Table 4b Experimental structure factors and calculated structure factors

	X53				X34			
hkl	F_{obs}	F_{cal}	ΔF	r	F_{obs}	F_{cal}	ΔF	r
111	116.93	121.05	-4.11	-0.071	124.82	129.00	-4.17	-0.067
200	18.85	23.05	-4.20	-0.355	11.70	13.85	-2.15	-0.310
220	143.53	135.60	7.93	0.107	152.95	147.62	5.33	0.068
311	87.88	86.40	1.48	0.033	93.28	94.72	-1.43	-0.030
222	-	-	-	-	-	-	-	-
400	101.20	103.54	-2.34	-0.046	113.66	115.11	-1.45	-0.025
331	73.03	67.34	5.69	0.149	79.18	75.42	3.75	0.092
420	-	-	-	-	-	-	-	-
422	87.25	81.96	5.28	0.117	98.09	92.68	5.41	0.107
333 511	54.74	53.49	1.24	0.044	61.10	61.07	0.028	0.001
440	73.04	65.97	7.07	0.184	73.01	76.27	-3.26	-0.091
531	45.75	43.13	2.62	0.111	53.38	50.24	3.14	0.114
620	53.50	53.58	-0.08	-0.003	62.79	63.19	-0.40	-0.012
533	38.60	35.34	3.26	0.161	42.66	41.98	0.67	0.031
	$B_{Ga} = 1.616$ Å^2 $B_{As} = 1.751$ Å^2, $B_P = 0.942$ Å^2 $R = 0.072$				$B_{Ga} = 1.081$ Å^2 $B_{As} = 1.502$ Å^2, $B_P = 1.321$ Å^2 $R = 0.061$			

Table 4c Experimental structure factors and calculated structure factors

	X13				GaAs			
hkl	F_{obs}	F_{cal}	ΔF	r	F_{obs}	F_{cal}	ΔF	r
111	133.62	139.27	-5.64	-0.086	141.44	144.09	-2.64	-0.037
200	6.58	0.74	5.84	0.987	8.08	6.94	1.14	0.262
220	168.71	161.40	7.30	0.084	164.26	167.08	-2.81	-0.034
311	103.86	103.20	0.66	0.012	110.51	107.35	3.16	0.056
222	-	-	-	-	-	-	-	-
400	122.65	127.21	-4.56	-0.075	132.22	132.22	0.00	0.000
331	86.97	83.15	3.81	0.085	88.75	86.63	2.11	0.047
420	-	-	-	-	-	-	-	-
422	103.46	103.15	0.30	0.006	109.44	107.49	1.95	0.035
333 511	65.75	67.90	-2.15	-0.066	72.05	70.91	1.13	0.031
440	85.75	85.78	-0.03	-0.001	88.60	89.73	-1.13	-0.025
531	56.38	56.49	-0.11	-0.004	58.22	59.29	-1.06	-0.031
620	71.58	71.57	0.01	0.0002	72.84	75.10	-2.26	-0.063
533	47.21	47.53	-0.32	-0.013	51.96	50.26	1.69	0.064
	B_{Ga} = 0.992 Å^2 B_{As} = 1.342 Å^2, B_P = 0.875 Å^2 R = 0.055				B_{Ga} = 1.286 Å^2 B_{As} = 1.006 Å^2 R = 0.034			

where ρ is the density, M the molecular weight per chemical unit, and A_i, n_i and $(\mu/\rho)_i$ is the atomic weight, the number and the mass absorption coefficient of the i-th atom respectively. The absorption coefficients of GaAs and GaP are reported to be 353.9[7)] and 297.3[1)] respectively. Assuming that the density changes linearly with alloy composition, the term of $(v^2\mu)^{-1/2}$ was calculated and shown by the dotted curve in Fig. 2, where the common scale factor k was estimated to be 1.62×10^{-4} for the best fitting between the above terms and the experimental scale factors.

Fig. 3 illustrates the temperature factors obtained by the two procedures described above. The average temperature factors of GaAs and GaP are larger than the reported ones.[7),1)] Also the average values in the alloy were seemed to change systematically with alloy composition. However, the individual

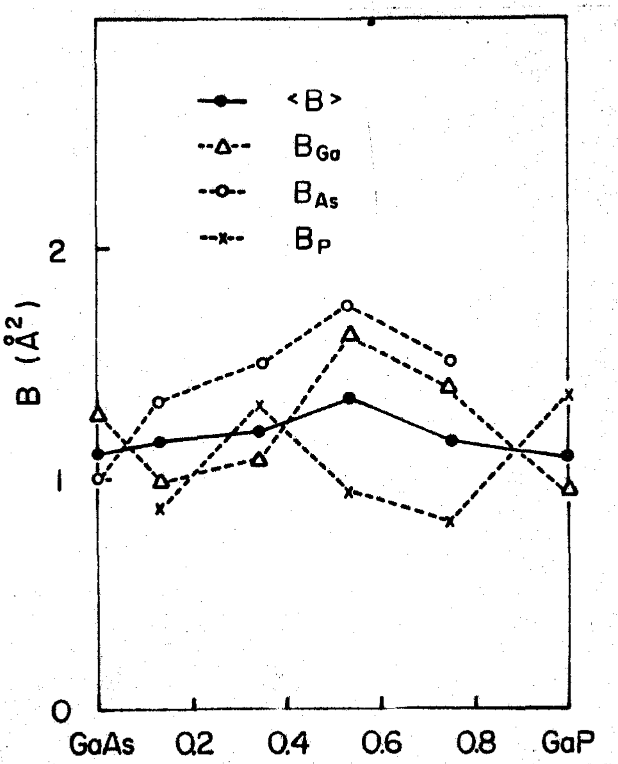

Fig. 3 Temperature factors in GaAs, GaP and their alloys

temperature factors of the III and V atom indicated the large composition dependence. This behavior is very interesting, but it is difficult to interpret it using the simple lattice model.

The temperature factor in the monoatomic lattice could be calculated in the system of harmonic oscillators by the Debye approximation. The result is represented by

$$B = \frac{6h^2}{mk\Theta_M} \frac{1}{x} \left\{ \Phi(x) + \frac{x}{4} \right\}, \qquad (20)$$

where

$$\Phi(x) = \frac{1}{x} \int_0^x \frac{\xi}{e^\xi - 1} d\xi \quad , \qquad (21)$$

and Θ_M is the characteristic temperature, h the Planck constant, k the Boltzman constant, and m the mass of an oscillator.

In the present case having the diatomic lattice, it was assumed that m is referred to the reduced mass. Then, the temperature factors for GaAs and GaP at 300 °K are given by

$$B = \begin{cases} 0.954 \times 10^{-11}/\Theta_M^2 \quad (\mathring{A}^2) \quad \text{for GaAs,} \\ 1.607 \times 10^{-11}/\Theta_M^2 \quad (\mathring{A}^2) \quad \text{for GaP,} \end{cases} \qquad (22)$$

Using the avarage temperature factor $\langle B \rangle$, the characteristic temperature were estimated from the above relation(22) as shown in Table 5. However, the corresponding representation interpreting the difference between individual temperature factors has not been developed.

On the other hand, the Einstein model might be applied to the lattice vibration, at relatively high temperature. The model assumes that all atoms are vibrating at constant frequency, ν. Then the temperature factor is represented by

Table 5 Characteristic temperature according to the Debye approximation

	$\langle B \rangle$	Θ_M	
GaAs	1.11 $Å^2$	297 °K	206 cm^{-1}
GaP	1.09	384	266

$$B = 8\pi^2 \langle u^2 \rangle = \frac{2\hbar^2 T}{m k \Theta_E^2} , \qquad (23)$$

where Θ_E is the characteristic temperature of the Einstein oscillator. Also its temperature is connected with the expression for the heat capacity of one gram atom at constant volume:

$$C_v = 3R(\Theta_E/T)^2 \exp(\Theta_E/T)[\exp(\Theta_E/T) - 1]^{-2} . \qquad (24)$$

Here the characteristic temperature, Θ_E could be estimated from the equation(23) using the experimental temperature factors. The results are shown in Table 6, where the heat capacity given by the equation(24) is listed in the sixth column. The corresponding characteristic temperatures between different atoms have the same value in the crystal. The calculated heat capacities are in agreement with the experimental ones. Therefore the model may be adopted in the present analysis. Then the large difference between individual temperature factors in GaP can be deduced to rise from the mass difference.

Table 6. Analysis of temperature factor and specific heat

	Oscillator	atomic weight	B ($\mathring{A}^2$)	Θ_E (^oK)	C_V^{cal}	C_V^{exp}
GaAs	Ga	69.72	1.17	118	0.0815	0.0760
	As	74.92	1.12	117	0.0815	
	pair	33.54	1.11	174	-	
GaP	Ga	69.72	0.870	137	0.116	0.124
	P	30.97	1.74	145	0.116	
	pair	20.51	1.09	226	-	

The experimental and theoretical structure factors as a function of alloy composition were shown in Fig. 4. The experimental values of (111) and (400) lines were smaller than the theoretical ones, and oppositely the experimental (220), (422), and (311) difraction lines had larger values than the theoretical ones over all alloy compositions. However, it has been not understood why the experimental intensity of (220) line is largely differ with the theoretical one.

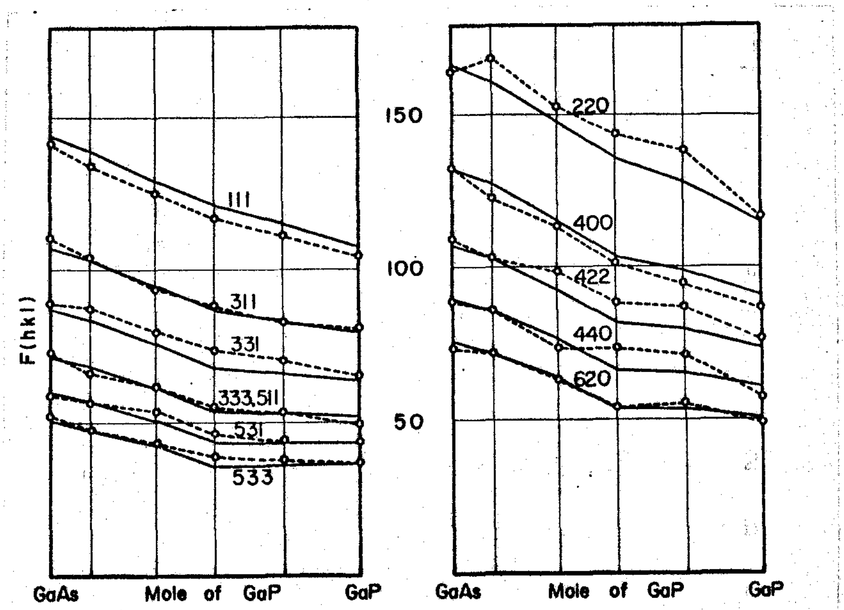

Fig. 4 Comparison between F_{exp} and F_{cal}

1-6) Discussion

(a) The difference between the squared theoretical and experimental structure factor, $r(\mathbf{h})$.

The parameter, $r(\mathbf{h})$ may be defined by the equation

$$r(\mathbf{h}) = [\,|F_{exp}(\mathbf{h})|^2 - |F_T(\mathbf{h})|^2\,] / |F_T(\mathbf{h})|^2 \, . \qquad (25)$$

Then the F-factor described before corresponds to the sum of $r(\mathbf{h})$, $\sum r(\mathbf{h})$. Fig. 5 shows the $r(\mathbf{h})$ as a function of $\sin\theta/\lambda$. It is interesting that the value of $r(\mathbf{h})$ means the difference of these two structure factors on the point with the radius $\sin\theta/\lambda$ in the reciprocal lattice space. The broken lines for GaAs and GaP were similar to the results reported by other authors.$^{1),7)}$ The sign of r(200) is possitive for GaAs, but negative for GaP. It seems that the behavior for the broken lines of the alloys had always the same tendency with the terminal ones, and the sign of r(200) changed around the sample of X13 with alloy composition, 0.13 mole fraction of GaP. Thus such a broken line as a function of $\sin\theta/\lambda$ would be considered to have some physical meanings; how electric state has been referred as the atomic scattering factor, and whether the electron distribusion is isotropic in the space.

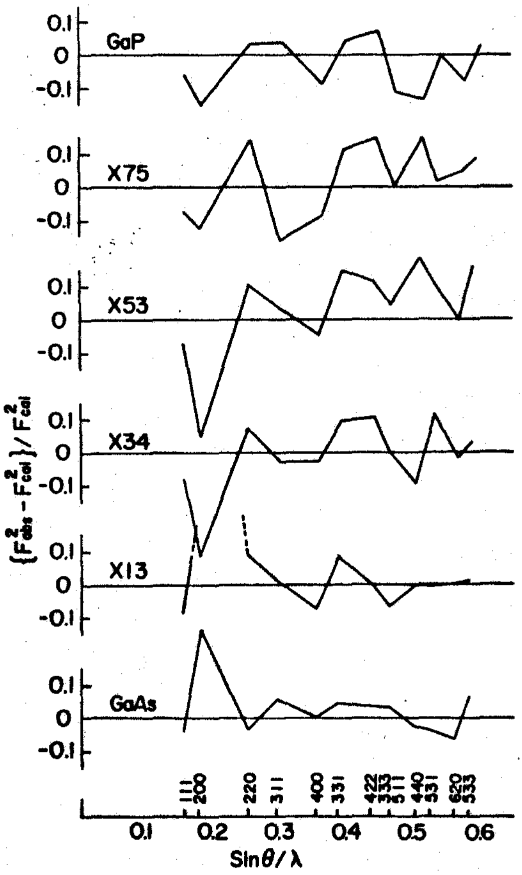

Fig. 5 The variation of r(h) factor as a function of sin θ /λ

(b) Effective charge

The values of the ionic charges can be determined from charts of electron distribution and directly from f curves. Here the values of structure factors would be discussed. The structure factor for the pair of atoms in the zinc blende lattice having even indices that can be divided by four is equal to the sum of atomic scattering factors of the component ions. On the other hand, the structure factors are equal to the difference of atomic scattering factors of the component ions for the planes with four indices which cannot be divided by four. The difference

Table 7 Observed and calculated structure factor of (200) reflection

	GaP	X75	X53	X34	X12	GaAs
$F_{obs}(200)$	47.16	32.60	18.85	11.70	6.58	8.08
$F_{cal}(200)$	51.06	34.75	23.05	13.85	0.74	6.94
ΔF	-3.88	-2.15	-4.20	-2.15	5.84	1.14
$F_{obs}(200)$	49.33*					5.27** 10.72*
e_{eff}	0.61	0.36	0.68	0.47		0.16

* Sirota; ** Uno et al

of atomic scattering factors is sensitive to the variation of ion charges. On using the apparent relation for the ratio of $F_{200}^{exp}/F_{200}^{neutral\ atom}$.

$$\frac{|f_A - f_B|_{200}^{neutral}}{F_{200}^{exp}} = \frac{Z_A - Z_B}{\Delta x} , \qquad (26)$$

where $Z_A - Z_B$ is the difference of atomic numbers of neutral atoms and Δx is the difference of actual number of the component ions in the crystal. Then the effective charge, is defined[9)] as follows.

$$e_{eff} = \frac{|(Z_A - Z_B) - \Delta x|}{Z} . \qquad (27)$$

The experimental and theoretical structure factors of (200) reflection line and the estimated effective charge are shown in Table 7. It is seen that both the possitive and negative value of ΔF for GaAs and GaP respectively give a same meaning, that is, negative charge is being passed from the III atom to the V atom and therefore the charges of ions A^{III} are positive and those of B^{V} are negative in conparison with the neutral states.

The apparent difference between the experimental and theoretical structure factor in the alloys seems to charge from negative value to possitive one and the structure factor arrives to be zero at an alloy composition. Fig. 6 shows the absolute structure factor of (200) line, where the solid line means the theoretical values and the dotted one is the connecting line of the experimental values in the GaP-rich side. When the experimental structure factor is zero at the composition, x*, the apparent relation is obtained,

$$F(200;x^*) = 4\{[f_{Ga}-(1-x^*)f_{As}-x^*f_P-2\Delta f]^2 + [f''_{Ga}-(1-x^*)f''_{As}-x^*f''_P]^2\}^{1/2} = 0\ , \qquad (28)$$

where f and f" is the real and imaginary part of each atomic scattering factor, and Δf is the variation from the neutral atomic scattering factor. x* being 0.15, Δf was estimated to be 0.11. The absolute values of structure factors measured in the alloys as shown in Fig. 6 would be thought to ensure the picture of the partial ionization of consutituent atoms in the III-V quasi-binary compounds.

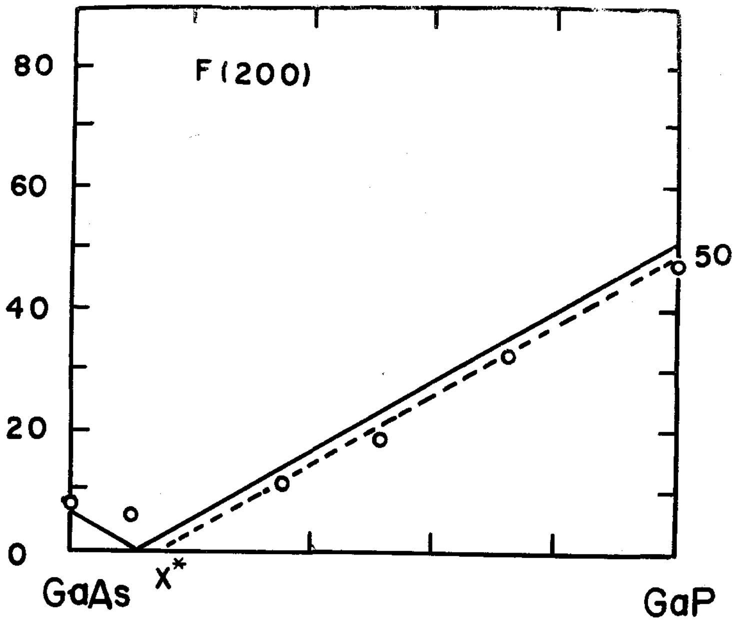

Fig. 6 Observed and calculated structure factors of (200) reflection

As above mentioned, the theoretical structure factors were calculated from the theoretical atomic scattering factors of Ga, As and P, where atoms are neutral, and on the other hand the observed values have been shown to deviate from the neutral states. The actual number of electrons around the nucleus of each atom could be estimated as following. According to V. Korhonen,$^{10)}$ the atomic scattering factors $F_{1,(h'k'l')}$ of an ion 1, belonging to this crystal, with the position coordinates (x_1, y_1, z_1) and the ionic radius R, can be represented by the series of the structure factors F(hkl),

$$F_{1,(h'k'l')} = \frac{4\pi R^3}{V}\left\{\frac{1}{3}F(h'k'l') + \sum_{hkl} F(hkl)\frac{1}{\alpha^2}\left(\frac{\sin\alpha}{\alpha} - \cos\alpha\right)\right\}, \tag{29}$$

$$\alpha = 2\pi R/d_{(h'-h,k'-k,l'-l)} , \tag{30}$$

where $d_{(h'-h,k'-k,l'-l)}$ denotes the distance of repetition of the lattice planes $(h'-h, k'-k, \ell'-\ell)$. Here the sphere with the center at (x_1, y_1, z_1) and the radius R is called the ionic sphere. In the case of $h'=0$, $k'=0$, and $\ell'=0$, the scattering factor, F_1,(000) in (29) means the total number of electrons within the sphere of ion 1. Assuming that $F^{obs}_{(000)}$ equals to $F^{cal}_{(000)}$, the difference of number of electrons between the actual and the nutral atom may be estimated by the equation,

$$\Delta Z = \frac{4\pi R^3}{V}\sum_{hkl}\Delta F(hkl)\cos\beta\,\frac{1}{\alpha^2}\left(\frac{\sin\alpha}{\alpha}-\cos\alpha\right), \qquad (31)$$

then $\alpha = 2\pi R\sqrt{h^2+k^2+\ell^2}/a$ and $\Delta F(hk\ell) = F_{obs}(hk\ell) - F_{cal}(hk\ell)$.

In the present work the series (31) has been applied to the calculation of the difference of electronic number of the Ga ion in GaAs, GaP and their alloys. The ionic radius of Ga has been assumed to be 1.26 Å as reported by Pauling.11) The result is shown in Table 8. The fact that the value of ΔZ is nearly equal over the quasi-binary system is very interesting and is reasonable in comparison with the result on the effective charge discussed in the previous paragraph. Here the minus sign of ΔZ denotes that the charge transfer occurs from the III atom to the V one.

Table 8 Experimental value of ΔZ

	GaAs	X13	X34	X53	X75	GaP
Z	-0.0735	-0.0627	-0.0738	-0.0624	-0.0544	-0.0695

1-7) Conclusion

In this work, the following contents have been performed;

(1) The precise measurements of X-ray intensity were carried out by the powder method, and the crystal structure factors of GaAs, GaP and their alloys have been determined.

(2) The temperature factors of Ga, As and P have been obtained in each samples, and the both Debye and Einstein model on the lattice vibration were concerned. Temperature factors of the III and the V atoms in GaP differ each other in magnitude. The difference could be explained using the Einstein model.

(3) The assumption that the atomic scattering factor of V atom in the alloy is represented by a linear combination of constituent V atoms might be thought to be valid in the present accuracy on the experimental analysis. However, the apparent temperature factors of each atom in the alloy seem to be systematically scattered. The experimental fact could be thought to be caused by the above assumption and the strain introduced by the alloying.

(4) The effective charge in III-V compounds has been estimated by three methods. Unfortunately the quantitative result could not be obtained, but the fact that negative charge is being passed from the III atom to the V atom has been concluded in GaAs, GaP and their alloys.

2. Crystal structures of α - and β -In_2Se_3 and their thermal properties

2-1) Introduction

This compound belongs to the group of semiconductor with general formula $A_2^{III}B_3^{VI}$, and there exist at least three different modifications[11] of In_2Se_3. Until recently, the results of some studies by X-ray powder method of Hahn et al.[12] and Sugaike et al.[13] or by the electrographic method of Semiletov,[14] led to the conclusion that the space group of α- and β-modification was C_6^6-$C6_3$ and C_6^3-$C6_1$, respectively.

We prepared the single crystal by the solution method (4) in which Se pressure was carefully controlled in 700 - 750 mmHg at the melting point of this compound.

In the present work, the crystal structure analysis on α- and β-In_2Se_3 has been performed by the Weissenberg method. The transition temperature from α- to β-In_2Se_3 was determined by the thermal analysis and the thermal expansion coefficients were measured.

2-2) Experimental procedure

a) Laue method

Laue patterns are usually indexed graphically by transforming the reflection spots to gnomonic poles, which are the intersections of the normals of the reflecting planes with the plane of projection, and plotting these poles to form a gnomonic projection. In the case of patterns taken with the incident beam parallel to a crystallographic axis and perpendicular to a flat film, the gnomonic net corresponds to a plane net of the reciprocal lattice and is indexed accordingly.

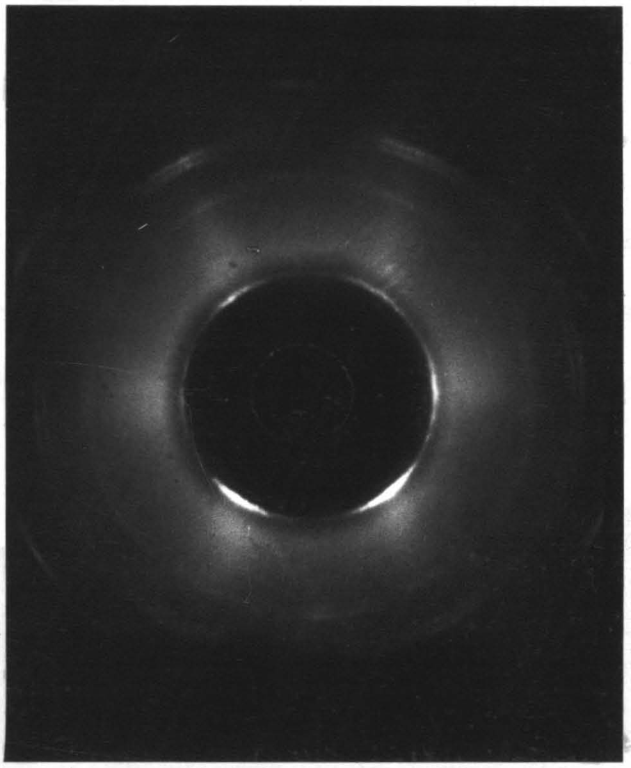

Photo. 1 Laue pattern of α-In_2Se_3

Photo. 1 showed the Laue pattern with the incident beam parallel to a c-axis of α-In_2Se_3. Intensity distribution over all spots has said that the c-axis has a three-hold symmetry.

b) Oscillation method

A crystal rotated in an x-ray beam around the normal to a set of reciprocal lattice-net planes will generate diffraction beams in the surface of a series of cones, corresponding to the circles in which the nets intersect the Ewald sphere. These cones are intercepted as straight-line rows of spots by a film rolled into a cylinder coaxial with the rotation axis. A typical pattern is shown in Photo. 2. If the rotation axis is the a-axis of the crystal, each row of spots will represent diffractions from the planes hkl for which the h index is constant. The reflections on the row through the trace of the direct beam will have a=0, the next will have a=1, then a=2, and so on. These rows are thus commonly referred to as the zero layer (or zero level), first layer, second layer, etc. This terminology is carried over from the rotation method to all the other single-crystal methods.

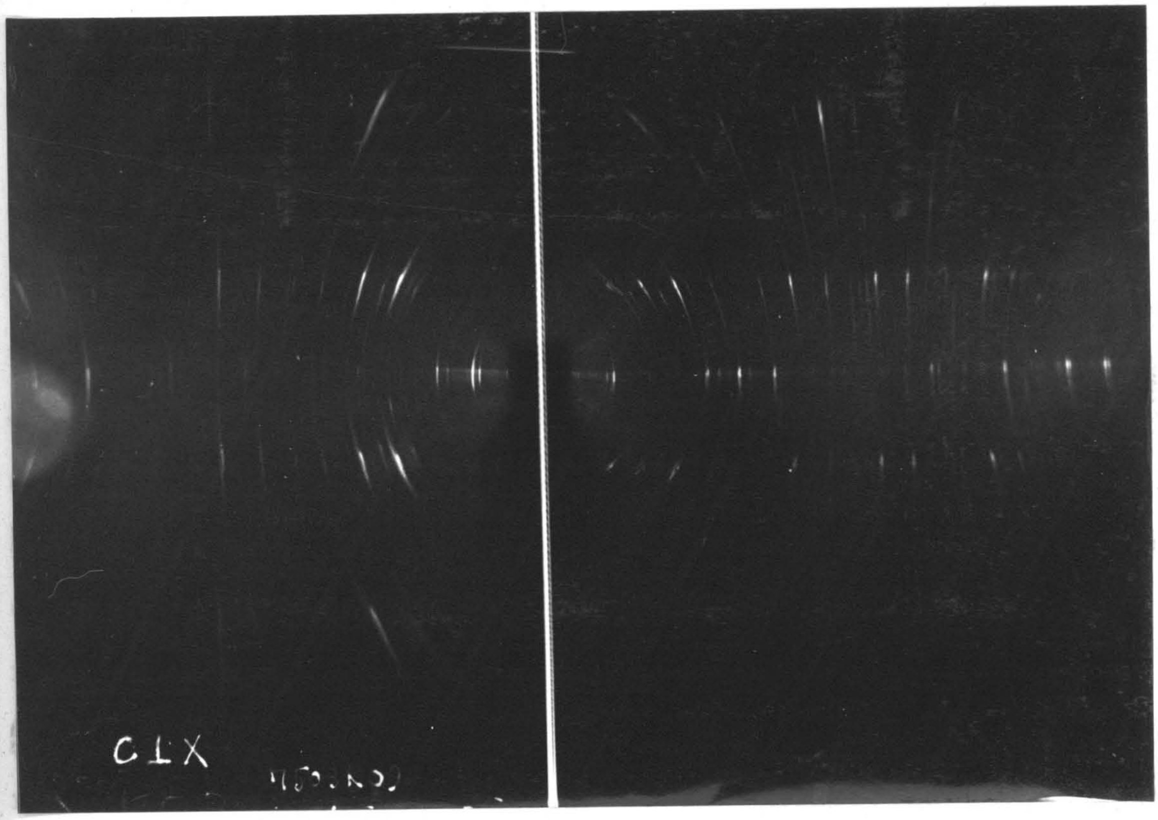

Photo. 2 Oscillation pattern of α-In_2Se_3

If the perpendicular distance from the zero layer row to an upper layer row is measured on the film as S_n, the corresponding distance between layers of the reciprocal lattice, ζ_n is given by

$$\zeta_n = \frac{S_n}{\sqrt{r^2 + S_n^2}} \qquad (32)$$

where r is the radius of the cylindrical film. The corresponding value of the a-axis is

$$a = n\lambda / \zeta_n \qquad (33)$$

where λ is the wavelength in Å and n the number of the layer. Thus the rotation photograph will give directly the dimension of the unit cell.

c) Weissenberg method

More widely used to resolve all the reflections of a single crystal is the Weissenberg camera, which produces patterns that are more easily conveniently interpreted. This apparatus is an adaptation of the rotation camera in which all but one layer line of reflections is stopped by a stationary slotted metal screen, and the cylindrical film holder is arranged to travel parallel to its axis a distance related to the degree of rotation of the crystal. The diffraction spots corresponding to one row on the rotation pattern thus become distributed over the whole film. The array of spots is actually a highly distorted image of the reciprocal-lattice net selected by the layer-line screen. In spite of the distortion, the fact that one whole net plane is registered on a single film, rather than scattered over a series of oscillation patterns, offers a tremendous advantage in studying the lattice, especially where intensity distributions are being considered in searching for symmetry. A typical Weissenberg pattern is shown in Photos. 3 and 4.

Upper layers are photographed by simply setting the layer-line screen opposite the appropriate rotation row line. If the X-ray beam is kept perpendicular to the rotation axis ("normal-beam" technique), the interesting circle in the Ewald sphere is displaced from the rotation axis and diminishes in size rapidly at higher layers, so that the range of the net plane recorded becomes greatly restricted. This effect is greatly ameliorated by tilting the X-ray beam to the rotation axis at an angle such that the beam lies in the surface of the cone of reflections for the layer being photographed. By this technique ("equi-inclination"), the reflecting circle always passes through the rotation axis and its radius is enlarged so that a much larger range of the reciprocal lattice may be recorded.

The setting is given for the equi-inclination method as follows. The angle of inclination ν_n of the X-ray collimator to the rotation axis is given by

$$\nu_n = \sin^{-1}\left(\frac{\zeta_n}{2}\right), \qquad (33)$$

where $\zeta_n = na^*$ and $a^* = \lambda/a$, and λ is the wavelength of X-ray and a the lattice constant. The position of layer-line screen, x_n translated from the zero-layer position opposite the X-ray beam collimator by an amount x_n.

$$x_n = \frac{\ell\sqrt{4-\zeta_n^2}}{\zeta_n} \qquad (34)$$

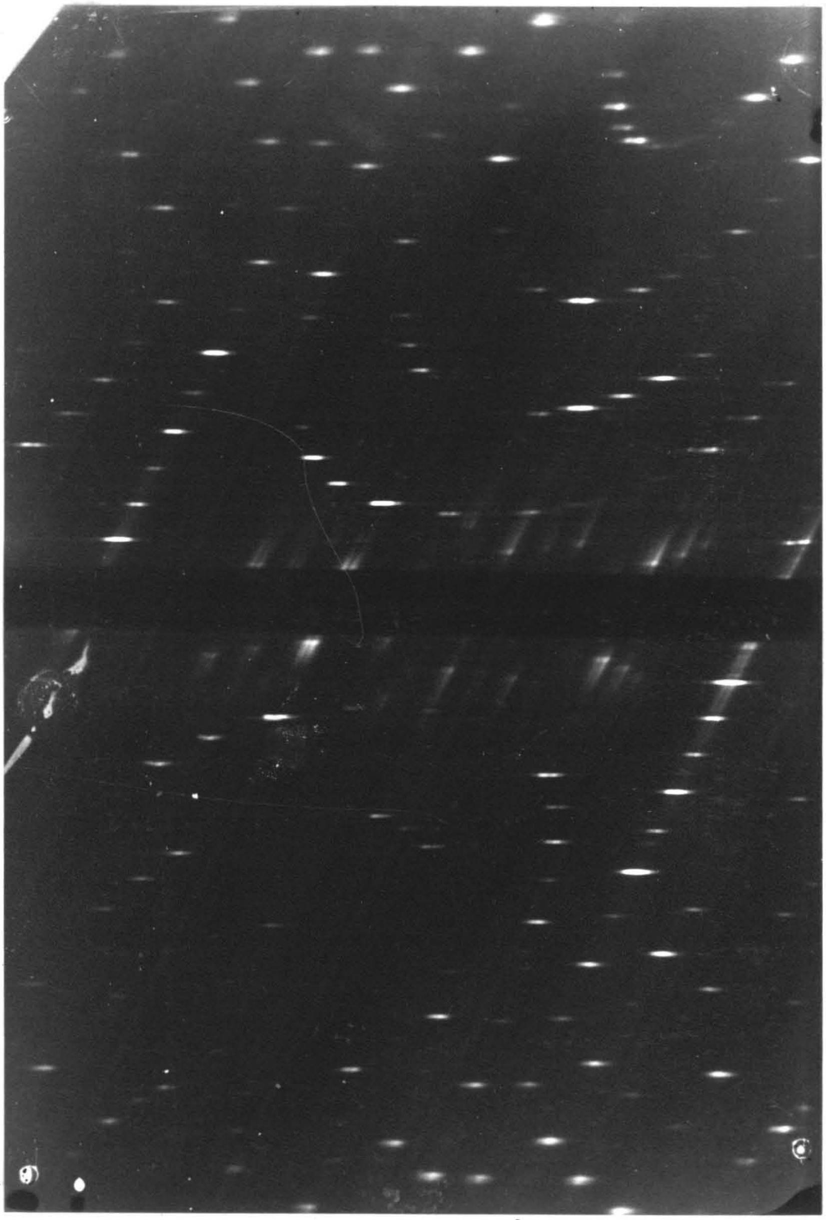

Fig. 3a Zero-layer Weissenberg photograph of α-In_2Se_3

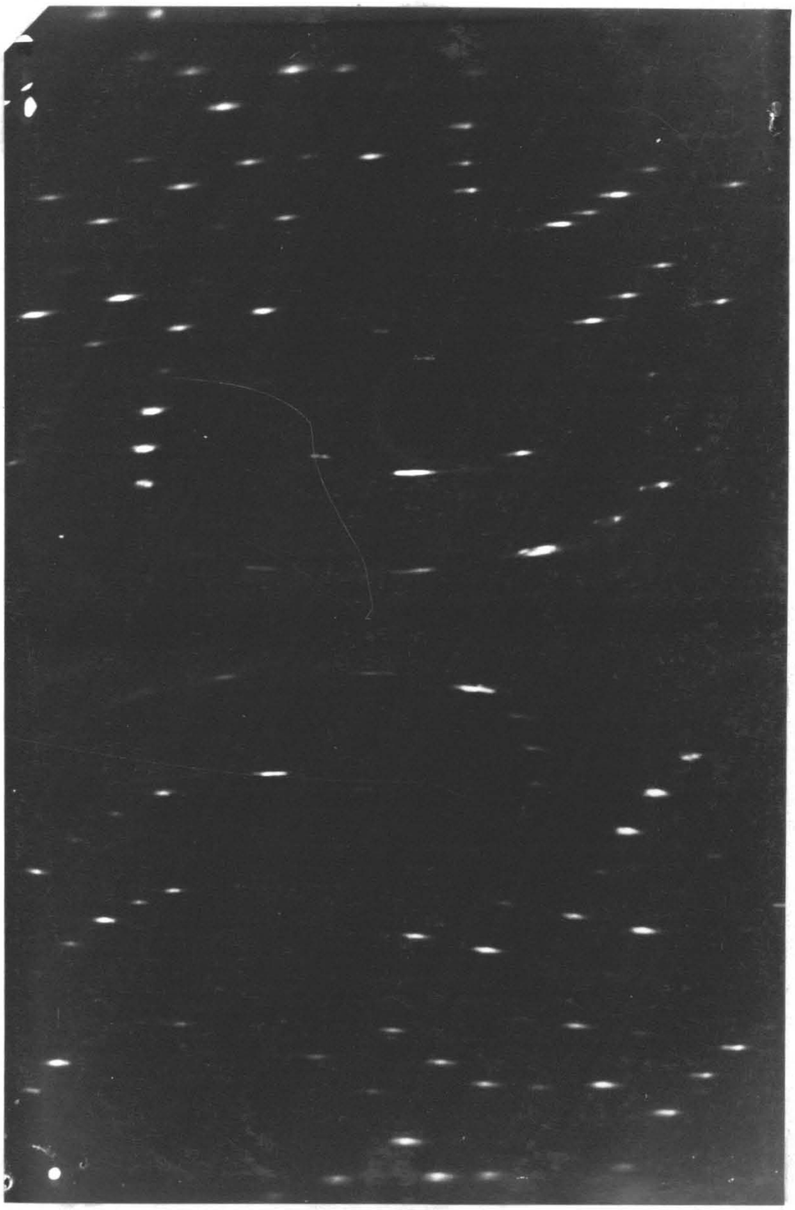

Fig. 3b First-layer Weissenberg photograph of α-In_2Se_3 by the equi-inclination method

Fig. 3c Second-layer Weissenberg photograph of α -In_2Se_3 by the equi-inclination method

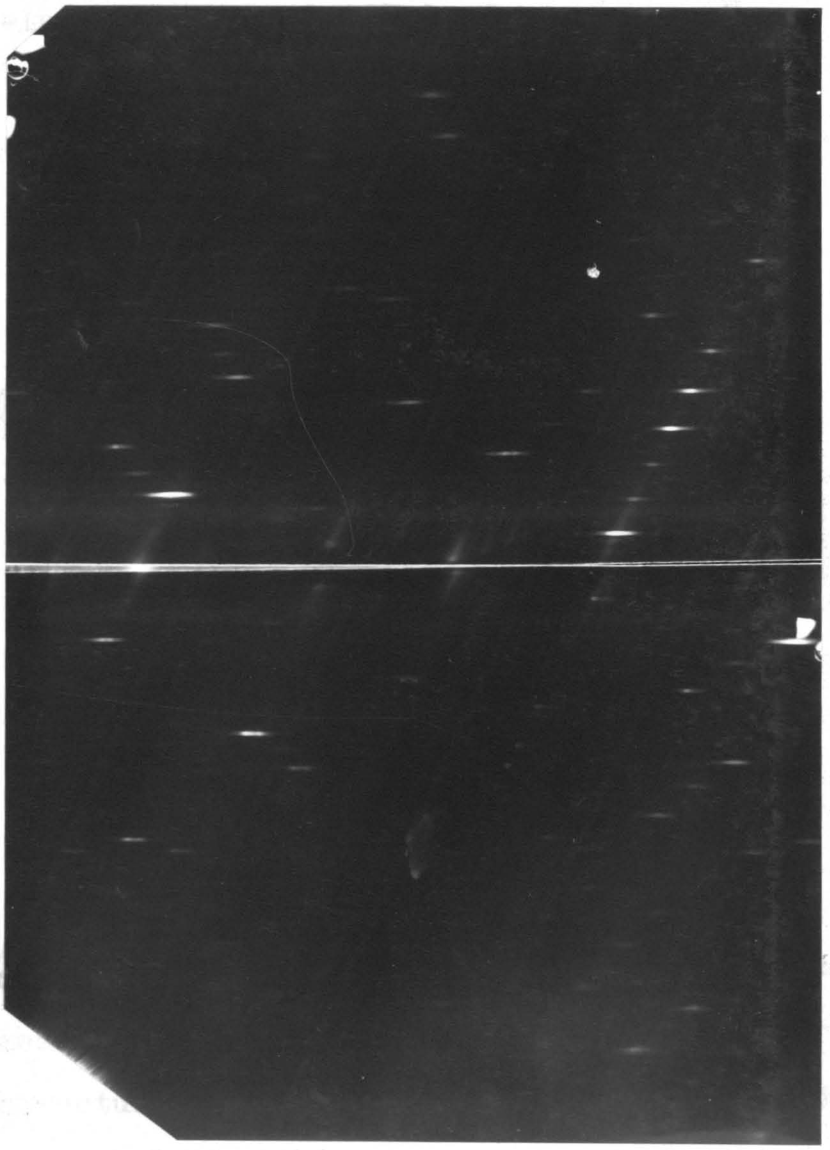

Fig. 4 Zero-layer Weissenberg photograph of β-In_2Se_3

where ℓ is the screen radius. The position of the beam trap, translated in a direction opposite to the layer-line screen on which it is mounted by the amount $2x_n$. These conditions for α- and β-In_2Se_3 are tabulated in Table 9.

Table 9 Some parameters necessary to the crystal structure analysis

		α-In_2Se_3	β-In_2Se_3
lattice parameter	a	4.05 A	4.05 A
First layer	ζ_1	0.380	0.380
	ν_1	11.00°	11.00°
	x_1	4.41 mm	4.41 mm
Second layer	ζ_2	0.760	0.760
	ν_2	22.35°	22.35°
	x_2	10.27 mm	10.27 mm

2-3) The measurement of diffraction intensities and indexing

a) The measurement of diffraction intensities

The structure factor is related to the intensity of diffraction I by the following expression:

$$|F|^2 = \frac{m^2c^4}{e^4}\,\frac{1}{\lambda^3 N^2 V}\,\frac{1}{ALp}\,\frac{I}{I_0} = \frac{K^2 I}{ALp} \qquad (36)$$

where e is the charge and m the mass of the electron, c is the velocity of light, λ the wavelength of the X-rays, N the number of unit cells per unit of volume, V the volume of the crystal, A an absorption factor, L the Lorentz factor, P the polarization factor, I_o the intensity of the primary beam, and K a scale factor.

The matter of primary interest in structure analysis is the relative values of F, so that I_o and N^2V assume secondary importance. In the photographic method, the whole diffraction pattern is exposed repeatedly over a relatively long time period so that variations in I_o are averaged out for the reflections on that pattern. In the present time, the experimental structure factor will be obtained from the collected relative K^2I/AL_p values.

The actual measurement of I was performed by the integrated intensity method, in which the crystal is rotated through the Bragg angle. An intensity strip of standard exposures was made and used to estimate the unknown spot intensities by direct comparison.

b) Intensity corrections

The measurements obtained by the Weissenberg method would now be transformed to the data needed for crystal-structure analysis, the structure amplitudes. Two strictly geometric factors which modify the relative intensities must be accounted for. The first, the polarization factor, is a function of the Bragg angle only and is the same for all methods of measurement. It is easily understood by considering the scattering by one electron in an atom in the crystal, which responds to an impinging X-ray beam. Its oscillations give rise to a secondary X-ray beam of two polarized components, vertical and horizontal, each of intensity one-half relative to the total forward-scattered intensity. At various angles in the horizontal plane, the intensity of the horizontal component as a transverse wave is a maximum at 0 and 180°, parallel to the primary beam, but decreases to zero at 90°, where the transverse electron oscillations have no contribution. The intensity of this wave, then, varies according to $\cos^2 2\theta$. The intensity of the vertical component, on the other hand, remains unchanged at all horizontal scattering angles.

A second important geometric factor, known as the Lorentz factor, arises from the fact that the manner in which the various diffracting planes in the crystal pass through the critical diffracting angle is different for different planes. This variation is best understood by considering the angle at which a reciprocal lattice point passes through the diffracting sphere.

If the lattice point were truly a geometric point, the idea of time opportunity that a diffracting plane has while its reciprocal lattice point passes through the geometric surface of the Ewald sphere would have no meaning; but as a matter of fact, because of the spread of wavelengths in the primary beam, the mosaic character of the crystal, and other factors, the reciprocal lattice point actually has a breadth as it is applied in the practical diffraction problem. Assuming that all the reciprocal lattice points have the same spread, it can be seen that a point which passes through the diffracting sphere at a grazing angle will have a longer time to diffract X-rays than one which passes through in a direction nearly normal to the surface. Moreover, the fact is taken into account that reciprocal lattice points of a rotating crystal which are farther from the origin more faster with respect to the sphere than those near the origin, and so have less time to diffract X-rays. Then the Lorentz factor is defined as a function of the projected component of the velocity of a reciprocal lattice point on the normal to the Ewald sphere at the point of contact. It is convenient to combine all these geometric factors into one algebric expression which is represented by L_p, the Lorentz polarization factor.

The formulas for the Lorentz polarization correction L_p for the equi-inclination Weissenberg method is given by

$$\frac{1}{L_p} = \frac{2\lambda \sqrt{(1/d)^2 - (\eta/b)^2}\ \cos\theta}{1 + \cos^2 2\theta}, \qquad (37)$$

where d is the distance between $(hk\ell)$ planes, 1/b the Z-component of the $(hk\ell)$ vector in the reciprocal lattice space.

Finally, the trouble some factor which must be accounted for in converting measured intensity values to structure amplitudes results from X-ray absorption in the crystal. A cylindrical or spherical crystal show absorption which is greatest at low diffraction angles and decreases monotonically with increasing angle. In the present analysis, as described before, the linear absorption coefficient is large and the specimen size is relatively gross, therefore the effect from X-ray absorption will cause much error. Assuming that the specimen shape is cylindrical and its radius is about 0.01 cm, the factor, μr is reduced to be about 9.0 and the absorption factor is simply given as a function of $\sin^2\theta$ by the author.15) The relative values of A are shown in Table 10.

Table 10 The relative value of absorption factor, A

$\mu r=9.0$

$\sin^2\theta$	0	0.1464	0.3290	0.5000	0.6710	0.8536	1.000
A	1.26	14.45	29.10	43.35	58.7	78.1	100

c) Indexing equi-inclination Weissenberg patterns

c-i) Geometrical construction of the reciprocal lattice

The hexagonal lattice is represented by two ways; one is referred to the hexagonal axis and then the components of the vector are taken as (a_2, b_2, c_2), and the another is referred to the orthogonal axis and the components are taken as (a_1, b_1, c_1). The relation between two axis is shown in Fig. 7.

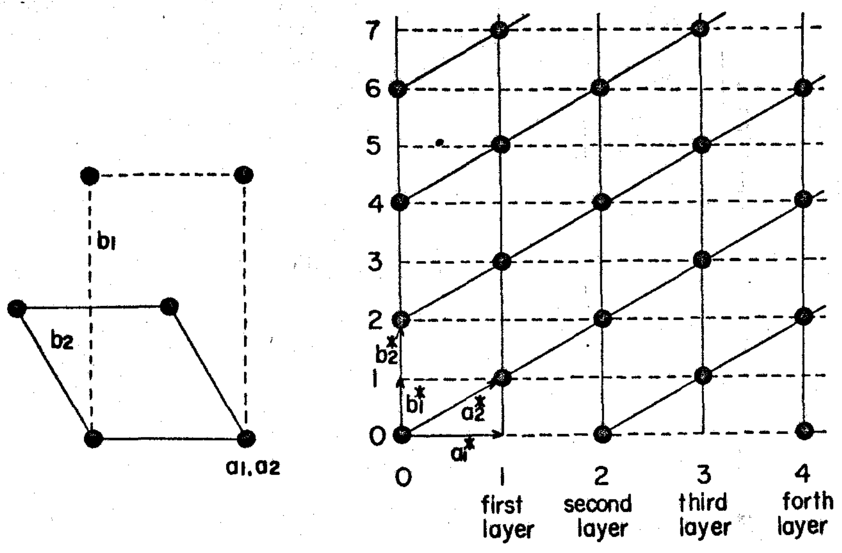

Direct Lattice

Reciprocal Lattice

Fig. 7 The representation of the hexagonal lattice

The corresponding reciprocal lattice is connected with the direct lattice in terms of a set of the above components of vector as shown in Fig. 7, and the magnitudes of the translations defining the reciprocal lattice are given by

$$|b_2^*|=2|b_1^*|=2\lambda/|b_1|$$
$$|a_2^*|=|b_1^*|/\cos 60=2\lambda/|b_1| \qquad (38)$$

and

$$b_2^*b_2=|b_2^*||b_2|\cos 30=1$$
$$a_2^*a_2=|a_2^*|\,|a_2|\cos 30=1 \qquad (39)$$

then

$$|b_2|=|a_2|=1/|a_2^*|\cos 30=|b_1|/2\lambda\ \cos 30 \qquad (40)$$

where the wavelength of X-ray, λ is assumed to be unity.

c-ii) Cylindrical coordinate system and indexing

In terms of the reciprocal lattice, the condition for reflection is that a point of the reciprocal lattice must lie on the surface of the sphere of reflection. Thus diffraction by a rotating crystal can be represented as the rotation of the reciprocal lattice about an axis or, conversely, as the rotation of the sphere through the reciprocal lattice. The origin of the reciprocal lattice is always placed at the point where the incident beam emerges from the sphere of reflection. As each reciprocal lattice point passes through the surface of the reflection sphere a diffracted beam is produced. The spots on a cylindrical film must be then identified with the corresponding reciprocal lattice points. To accomplish this it is convenient to define the position of the reciprocal lattice points using cylindrical coordinates, as in Fig. 8. ζ is the perpendicular distance of the reciprocal lattice point P from a plane normal to the rotation axis through the reciprocal lattice origin; ξ is the radius of a cylinder having the rotation axis as axis and passing through P, i.e., the perpendicular distance from the rotation axis of P; ϕ is the angular coordinate of P which acquires all values during a complete rotation and is indeterminate on a rotation photograph; and d^* is the reciprocal lattice point vector λ/d.

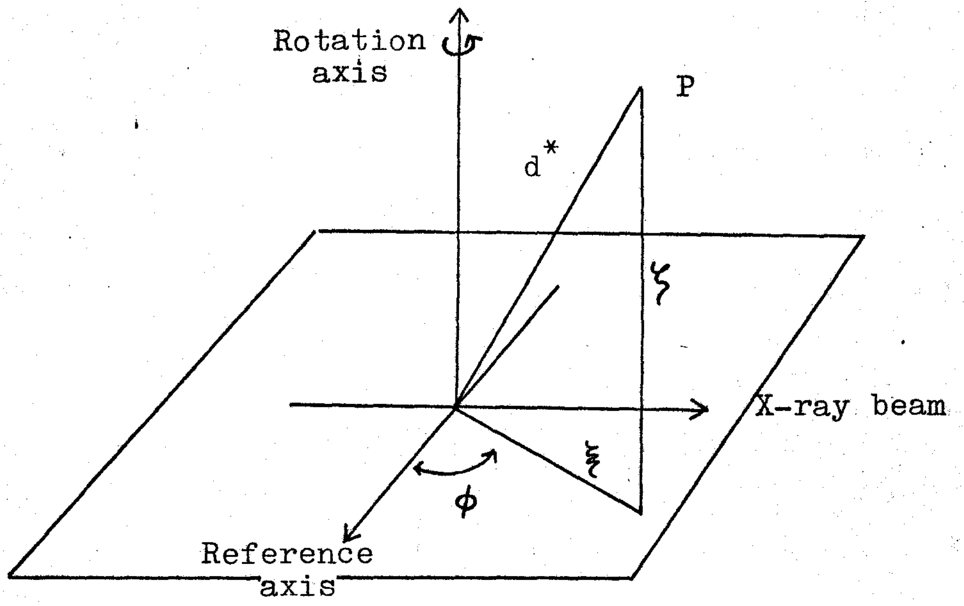

Fig. 8 Cylindrical coordinate system

Since Weissenberg patterns are photographed one level at a time, all spots on a given level have the same ζ value. The spots are spread over the two dimensions of the film, making it possible to fix uniquely the other two cylindrical coordinates ξ and ϕ. When x is the distance of a spot to the center line of the film, it is proportional to $2r \sin^{-1}(\xi/2)$. The distance Z of a spot to an arbitrary zero, measured parallel to the center line, is proportional to the angle the crystal has turned ϕ in going from the zero spot to the spot. Using a camera of 57.30 mm diameter, $\sin^{-1}(\xi/2)=x(\text{mm})^{\circ}$, $\phi=2Z(\text{mm})^{\circ}$.

Therefore the interplanar spacing d can then be computed using the Bragg relation

$$d/n = \frac{\lambda}{2 \sin \chi_n^m} \qquad (40)$$

Table 9 shows the lattice parameters determined by such a way and by the oscillation method.

To illustrate the procedure of indexing, the indexed dot copy of the (0hl) pattern of α-In_2Se_3 was shown in Fig. 9. The summarized results were shown in Table 11 for α- and β-In_2Se_3. We have determined that the condition for nonextinction is $-h+k+l=3n$ for both α- and β-In_2Se_3 as shown in Table 11.

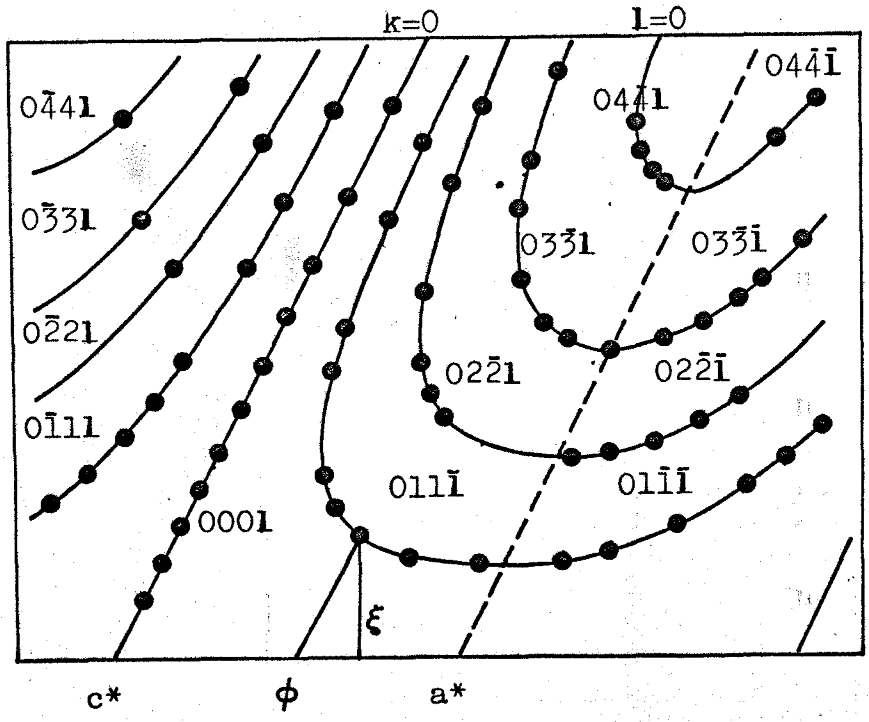

Fig. 9 The indexed dot copy of the (ohl) pattern of α-In_2Se_3

Table 11a List of intensities, lattice spacing and index in α-In_2Se_3

Observed Intensity	ξ	d_{obs}	d_{cal}	Indexing
Zero Layer No.7505 K35				
-	-	-	9.590	000 3
694.20	0.30	5.15	4.795	6
216.01	0.458	3.36	3.196	9
98.89	0.61	2.53	2.397	12
377.20	0.78	1.98	1.918	15
94.17	0.945	1.63	1.598	18
596.48	1.105	1.395	1.370	21
37.99	1.27	1.21	1.198	24
189.17	1.427	1.08	1.065	27
54.95	1.591	0.970	0.9590	30
72.32	1.755	0.880	0.8718	33
104.65	1.927	0.800	0.7991	36
117.51	0.45	3.43	3.481	$01\bar{1}$ 1
694.20	0.49	3.14	3.152	4
221.56	0.57	2.70	2.667	7
334.22	0.68	2.26	2.224	10
56.43	0.81	1.90	1.871	13
13.30	-	-	1.600	16
18.63	-	-	1.390	19
92.68	1.24	1.24	1.225	22
394.64	1.40	1.10	1.093	25
23.95	-	-	0.9860	28
227.46	1.70	0.908	0.8971	31
302.90	1.86	0.829	0.8225	34
89.38	0.435	3.54	3.407	$01\bar{1}$ $\bar{2}$
28.50	-	-	2.994	$\bar{5}$
29.38	-	-	2.510	$\bar{8}$
254.29	0.73	2.11	2.096	$\overline{11}$
121.80	0.88	1.75	1.773	$\overline{14}$
156.88	1.00	1.54	1.524	$\overline{17}$
74.22	1.16	1.33	1.330	$\overline{20}$
228.90	1.29	1.19	1.178	$\overline{23}$
24.41	-	-	1.055	$\overline{26}$
55.88	-	-	0.9546	$\overline{29}$

Observed Intensity	ξ	d_{obs}	d_{cal}	Indexing
192.43	1.75	0.880	0.8709	$\overline{32}$
215.85	1.92	0.802	0.8003	$\overline{35}$
60.09	0.89	1.73	1.750	$02\bar{2}\ \bar{1}$
540.61	0.93	1.66	1.703	$\bar{4}$
176.60	0.98	1.57	1.613	$\bar{7}$
391.48	1.02	1.51	1.497	$\overline{10}$
57.95	1.11	1.39	1.374	$\overline{13}$
12.60	-	-	1.255	$\overline{16}$
6.30	-	-	1.146	$\overline{19}$
40.96	-	-	1.048	$\overline{22}$
332.73	1.58	0.975	0.9621	$\overline{25}$
28.98	-	-	0.8865	$\overline{28}$
270.38	1.87	0.825	0.8202	$\overline{31}$
25.65	-	-	1.740	$02\bar{2}\ 2$
4.20	-	-	1.677	5
23.11	-	-	1.576	8
215.86	1.05	1.47	1.456	11
107.95	1.15	1.34	1.333	14
80.91	1.27	1.21	1.217	17
19.95	-	-	1.112	20
112.06	1.50	1.02	1.018	23
13.65	-	-	0.9358	26
38.89	-	-	0.8634	29
205.84	1.92	0.802	0.8000	32
454.70	1.32	1.17	1.169	$03\bar{3}\ 0$
14.12	-	-	1.160	3
102.48	1.36	1.13	1.135	6
21.97	-	-	1.098	9
12.44	0.525	1.01	1.050	12
66.22	1.60	0.965	0.9982	15
19.17	-	-	0.9436	18
252.33	1.73	0.890	0.8893	21
25.04	-	-	0.8369	24
209.13	1.94	0.795	0.7875	27

Table 11b List of intensities, lattice spacing and index in β-In_2Se_3

Observed Intensity	ξ	d_{obs}	d_{cal}	Indexing
Zero Layer No.7505 K56				
-	-	-	9.803	000 3
301.455	0.326	4.72	4.901	6
56.19	0.486	3.17	3.267	9
60.08	0.646	2.39	2.450	12
259.43	0.801	1.93	1.960	15
265.25	0.961	1.61	1.633	18
101.52	1.136	1.36	1.400	21
14.21	1.301	1.18	1.225	24
89.53	1.466	1.05	1.089	27
14.21	-	-	0.9803	30
-	-	-	0.8169	36
46.21	0.44	3.50	3.482	$0\bar{1}1$ 1
24.47	-	-	3.165	4
-	-	-	2.692	7
152.09	0.68	2.26	2.253	10
47.17	0.815	1.90	1.901	13
62.65	0.965	1.60	1.628	16
-	-	-	1.416	19
70.64	1.25	1.23	1.249	22
18.19	1.39	1.11	1.115	25
30.92	1.56	0.990	1.006	28
-	-	-	0.9158	31
-	-	-	0.8398	34
-	-	-	0.7752	37
-	-	-	3.411	$0\bar{1}1$ $\bar{2}$
435.18	0.50	3.08	3.012	$\bar{5}$
56.69	0.595	2.59	2.537	$\bar{8}$
111.18	0.71	2.17	2.126	$\bar{11}$
-	-	-	1.802	$\bar{14}$
27.29	0.995	1.55	1.551	$\bar{17}$
19.10	1.14	1.35	1.356	$\bar{20}$
33.64	1.295	1.19	1.201	$\bar{23}$
10.00	1.45	1.06	1.076	$\bar{26}$
4.55	-	-	0.9742	$\bar{29}$

Observed Intensity	ξ	d_{obs}	d_{cal}	Indexing
25.47	1.765	0.874	0.8890	$0\bar{1}1$ $\overline{32}$
-	-	-	0.8171	$\overline{35}$
-	-	-	1.741	$0\bar{2}2$ 2
251.61	0.92	1.68	1.680	5
25.05	0.99	1.56	1.582	8
78.66	1.065	1.45	1.466	11
-	-	-	1.346	14
-	-	-	1.231	17
17.48	-	-	1.126	20
58.66	1.51	1.02	1.033	23
32.30	-	-	0.9505	26
54.92	1.775	0.870	0.8779	29
64.61	1.915	0.805	0.8140	32
29.13	0.895	1.72	1.750	$0\bar{2}2$ $\bar{1}$
-	-	-	1.705	$\bar{4}$
29.13	0.92	1.67	1.618	$\bar{7}$
283.52	1.025	1.50	1.506	$\overline{10}$
97.54	1.12	1.38	1.386	$\overline{13}$
141.71	1.225	1.26	1.268	$\overline{16}$
-	-	-	1.160	$\overline{19}$
52.03	1.48	1.04	1.063	$\overline{22}$
-	-	-	0.976	$\overline{25}$
126.29	1.32	1.17	1.169	033 0
-	-	-	1.160	3
-	-	-	1.137	6
-	-	-	1.100	9
-	-	-	1.055	12
55.74	1.54	1.00	1.004	15
26.62	1.625	0.950	0.9507	18
29.45	1.725	0.894	0.8975	21
41.04	1.84	0.838	0.8459	24
27.83	-	-		27
24.47	1.76	0.875	0.8764	$0\bar{4}4$ 1
-	-	-	0.8706	4
-	-	-	0.8583	7

2-4) Patterson function

The first step in the structure analysis is to calculate the Patterson function, a Fourier series whose coefficients are the experimentally measured intensities. This function is

$$P(u,v,w) = \frac{1}{V}\sum_h\sum_k\sum_l |F(hkl)|^2\cos 2\pi(hu+kv+lw), \qquad (41)$$

where the next relation, that is Friedel's law, is used,

$$|F(h,\ k,\ l)|^2 = |F(\bar{h},\ \bar{k},\ \bar{l})|^2$$

It is important to appreciate that the Patterson function is calculated from the experimentally measured intensities and does not require any knowledge of the phases of F(h, k, l). The peaks contained in P(u, v, w) correspond to the interatomic vectors of the suructure, and the peak height is proportional to the peak weight only to the extent that the scattering factor of any given atom j can be represented as $Z_j\hat{f}$ where $\hat{f}$ is a factor dependent on the scattering angle and is independent of the atoms. In most cases,

$$\frac{\text{Height of a given peak } i\ j}{\text{Height of origin peak}} = \frac{Z_iZ_j}{\sum_{j=1}^{N} Z_j^2} \qquad (42)$$

In the present case, the space group for α - and β -In_2Se_3 is expected to be R3m, R32 or R$\bar{3}$m, accordingly the space group of Patterson function is given to be R3m. The two dimensional Patterson function is represented by

$$P(v,w) = \frac{1}{bc}\left\{\sum|F_{obs}(hkl)|^2\cos 2\pi(ky+lz)+\sum|F_{obs}(h\bar{k}l)|^2\cos 2\pi(-ky+lz)\right\} \qquad (43)$$

The projection on (o b_1 c) plane is shown in Fig. 10 (a) for α-In_2Se_3 and in Fig. 10 (b) for β-In_2Se_3.

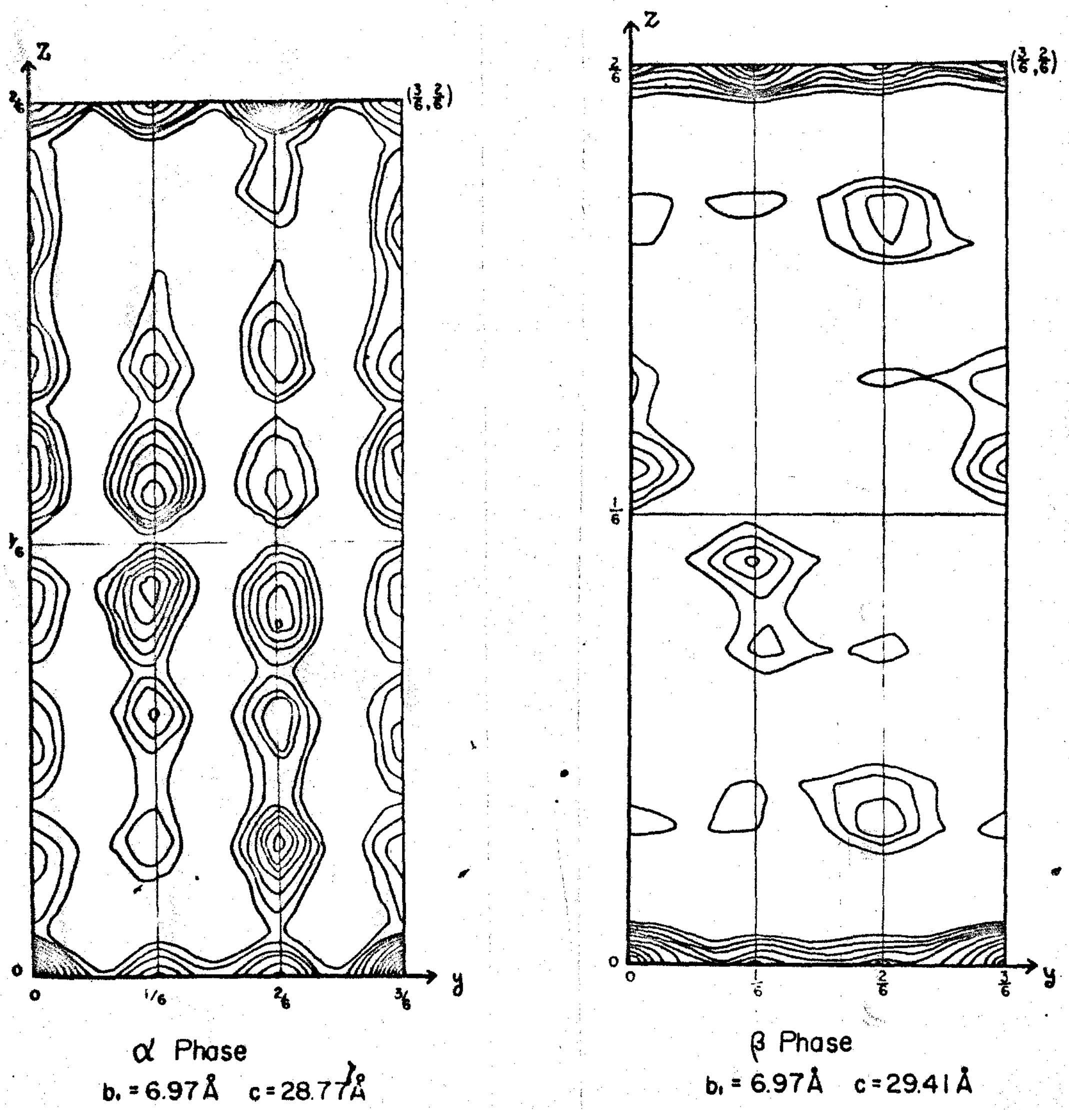

(a) α-In_2Se_3 (b) β-In_2Se_3

Fig. 10 Two dimensional Patterson diagrams

a) Determination of number of molecules per unit cell

The density of a crystal can be determined by the density equation

$$\rho = \text{mass/volume} = NM/V \qquad (44)$$

where M is the mass of the atomic ensemble constituting one unit of the chemical formula, N is the number of such chemical units in one unit cell of the crystal, and V is the volume of the crystalline unit cell as determined by X-ray diffraction methods. In the equation, the density was measured to be 5.91 (g/cm^3), the unit cell volume was determined from X-ray measurement to be $0.866a^2c$ (cm^3) and M is the 466.52 g for In_2Se_3. Thus the number of chemical unit, N was determined to be three, that is, the unit cell containes three molecules, $3In_2Se_3$.

b) Limitation of space group

As described above, the first step for the structure analysis is ready after maping the Patterson diagram, and the obtained knowledges are summarized as follows; (i) The symmetry of Laue photographs of α- and β-In_2Se_3 contained the three hold axis normal to the basal plane, (ii) the relation among intensities of the oscillating photographs is given by $I(hkl)=I(hk\bar{l})$, accordingly the Laue group of symmetry is limited to $\bar{3}m$, $3m$ or 32. Moreover, the condition for nonextinction determined from indexing the Weissenberg pattern is $-h+k+l=3n$, then the space group of these crystals belong to $R\bar{3}m$ or $R3m$. This alternative remains after determining z-parameters and after the Wilson statiscal approach.

c) Possible atomic arrangements for α- and β-In_2Se_3

When there are six indium atoms and nine selenium atoms per unit cell with R$\bar{3}$m or R3m symmetry, the symmetric positions are listed in Table 12.

Table 12 Symmetric positions of Se and In

	R3m	
	Number of positions, Wyckoff notation, and point symmetry	Coordinate of equivalent positions
Se	9 e 2/m	1/2,0,0; 0,1/2,0; 1/2,1/2,0.
	9 d 2/m	1/2,0,1/2; 0,1/2,1/2; 1/2,1/2,1/2.
	6 c 3m	0,0,Z; 0,0,Z.
	3 b 3m	0,0,1/2.
	3 a 3m	0,0,0,
In	6 c 3m	0,0,Z; 0,0,Z.
	3 b 3m	0,0,1/2.
	3 a 3m	0,0,0.

	R$\bar{3}$m	
	Number of positions, Wyckoff notation, and point symmetry	Coordinate of equivalent positions
Se	9 b m	x,x,z; x,2x,z; 2x,x,z.
	3 a 3m	0,0,Z.
In	3 a 3m	0,0,Z.

On the other hand, it was apparently understood from the Patterson diagram that the coordinates of x and y take a fixed value as 1/3, 1/2 and 2/3.

d) Determination of z-parameter

As discribed above, the unknown coordinate of equivalent positions was only the z component. The value could be determined with the aid of the Patterson diagram.

In β -In_2Se_3, the space group had been expected to be R3m. Assuming that six indium and nine selenium atoms occupy the following symmetric positions, respectively,

Se; 3a3m, 6c3m,
In; 6c3m,

then the coordinates of the maximum points in the Patterson diagram reduced from the assumed symmetric positions were all listed up in Table 13. As the atomic number, Z_{In} and Z_{Se} of In and Se is 49 and 34 respectively, the each peak height would be proportional to the magnitude of $Z_{In} \times Z_{Se}$, $(Z_{In})^2$ and $(Z_{Se})^2$ multiplied by the overlapping factor for the corresponding atoms pair.

Peak positions on the z axis are given as $\pm z_1$, $\pm 2z_1$, $\pm z_2$, $\pm 2z_2$, and $\pm z_2 \mp z_1$, where z_1 and z_2 is the z component of the coordinate of Se and In, respectively, occupying the positions with c3m symmetry. Trying that z_1=13.4/60, the expected peak positions were 10.7/60, 11.8/60, 13.4/60, 24.1/60 and 26.8/60. These values agreed with the experimental ones. In such a way, all maximum positions in two dimensional Patterson diagram should be satisfactorily interpreted in terms of two parameters, z_1 and z_2. The reduced coordinates of asymmetric units occupied by Se and In atoms was determined as follows.

3Se; 3a$\bar{3}$m (0, 0, 0)
6Se; 6c3m (0, 0, 13.38/60) (45)
6In; 6c3m (0, 0, 24.12/60)

Similarly, the asymmetric units for the proposed crystal structure of α-In_2Se_3 were represented by

3Se; 3a$\bar{3}$m (0, 0, 0)
3Se; 3a3m (0, 0, 14.5/60)
3Se; 3a$\bar{3}$m (0, 0, 48.0/60) (46)
3In; 3a3m (o, 0, 31.8/60)
3In; 3a3m (0, 0, 43.0/60)

Table 13 Maxima of Patterson Function of (a, c) plane

Peak for Se-Se		Peak for In-In		Peak for In-Se	
Position	Multip.	Position	Multip.	Position	Multip.
0,+Z_1	3	0,+$2Z_2$	3	0,+Z_2	6
0,+$2Z_1$	3	1/3,1/3	6	0,+Z_2+Z_1	6
1/3,1/3	9	1/3,1/3+$2Z_2$	3	1/3,1/3+Z_2	6
1/3,1/3+Z_1	6	2/3,2/3	6	1/3,1/3+Z_2+Z_1	6
1/3,1/3+$2Z_1$	3	2/3,2/3+$2Z_2$	3	2/3,2/3+Z_2	6
2/3,2/3	9			2/3,2/3+Z_2+Z_1	6
2/3,2/3+Z_1	6				
2/3,2/3+$2Z_1$	3				

2-5) Crystal structure factor

The sturnture factor F(hkl) may be expressed in exponential form by the formula

$$F(hkl) = \sum_r f_r(hkl)\, e^{2\pi i(hx_r + ky_r + lz_r)} \qquad (47)$$

where atomic scattering factor for is modified by thermal vibration to a value $f_r = f_{or} \exp(-B\sin^2\theta / \lambda^2)$. The structure factor is therefore a complex quantity, introducing both the absolute value and the phase of the scattered wave.

The electron density ρ at any point X, Y, Z in the unit cell can also be expressed as an exponential function.

$$\rho(X,Y,Z) = \frac{1}{V_c} \sum_h \sum_k \sum_l F(hkl)\, e^{-2\pi i(hX + kY + lZ)} \qquad (48)$$

where V_c is the volume of the unit cell. The coordinate X, Y, Z, which also represent fractions of the crystallographic axis, must not be confused with x_r, y_r, z_r, the coordinates of a scattering unit. The exponential terms in the expressions for F and ρ are opposite in sign, because these quantities are Fourier transforms of each other. It would have been equally correct to use the expressions $F = \sum f e^{-i\phi}$ and $\rho = \frac{1}{V}\sum F e^{i\theta}$. It simply means that the scattered wave has a phase-lag relative to the origin, instead of a phase-advance as in the equation(47).

The value of $|F(hkl)|$, which is the amplitude of the scattered wave, can be determined experimentally, by for the purpose of a Fourier analysis the value of the phase angle $\alpha(hkl)$, relative to the agreed origin, must also be known as accurately as possible. This quantity, $\alpha(hkl)$, which also depends on the nature and arrangment of the scattering material and on the direction of scattering, cannot be directly determined by experiment except in certain limited circumstance. It can, however, be calculated for any given structure, as follows: let $F(hkl)=A'+iB'$; $F(\bar{h}\bar{k}\bar{l})=A'-iB'$; $2\pi(hX+kY+lZ)=\theta$. Then

$$\rho(X,Y,Z) = \frac{1}{2V_c}\sum_h\sum_k\sum_l \{[A'+iB']e^{-i\theta}+[A'-iB']e^{i\theta}\}$$

$$= \frac{1}{V_c}\sum_h\sum_k\sum_l (A'\cos\theta + B'\sin\theta) \qquad (49)$$

Hence the electron density is everywhere real; and

$$\rho(-X,-Y,-Z) = \frac{1}{V_c}\sum_h\sum_k\sum_l (A'\cos\theta - B'\sin\theta) \qquad (50)$$

which means that the electron densities at (X, Y, Z) and at (-X, -Y, -Z) will differ unless B' is zero.

We can write $A'=|F(hkl)|\cos\alpha(hkl)$

$B'=|F(hkl)|\sin\alpha(hkl)$

then,

$$\rho(X,Y,Z) = \frac{1}{V_c}\sum_h\sum_k\sum_l |F(hkl)|\cos[\theta-\alpha(hkl)] \qquad (51)$$

where $|F(hkl)|^2=A'^2+B'^2$ and $\alpha(hkl)=\tan^{-1}(B'/A')$.

Summing over all the different kinds of atoms in a unit cell, we have

$$A'=\sum\sum f_r \cos 2\pi(hx_r+ky_r+lz_r)$$
$$B'=\sum\sum f_r \sin 2\pi(hx_r+ky_r+lz_r) \qquad (52)$$

the summations being taken over all the different kinds of atoms and all the different equivalent positions of those atoms in the unit cell. Here f_r is the atomic scattering factor, corrected for thermal vibration, appropriate to the set of planes (hkl), for any one of the scattering units in the unit cell, and x_r, y_r, z_r are the coordinates of any one of the equivalent positions at which that particular scattering unit is placed.

Now let

$$A=\sum\cos 2\pi(hx+by+lz)$$
$$B=\sum\sin 2\pi(hx+by+lz) \qquad (53)$$

the summation expending overall the equivalent positions in a unit cell. Then

$$|F(hk\ell)| = \{[\sum_r f_r A_r]^2+[\sum_r f_r B_r]^2\}^{1/2} \qquad (54)$$

$$\alpha(hk\ell) = \tan^{-1}\{[\sum_r f_r B_r]/[\sum_r f_r A_r]\} \qquad (55)$$

the summations in (24) and (25) being taken over all the different kinds of scattering units (atom or ions, or submultiples of these) in the unit cell. A and B are characteristic of the space group, being dependent entirely on the coordinates of equivalent positions.

Assuming that the space group for β-modification is $R\bar{3}m$, the summation expending overall the equivalent positions in a unit cell is represented as the terms,

$$\left\{\begin{array}{l} A=4\left(1+2\cos 2\pi\frac{-h+k+\ell}{3}\right)\{\cos\pi[(h-k)(x-y)+2\ell z]\cos\pi i(x+y) \\ \quad +\cos\pi[(k-i)(x-y)+2\ell z]\cos\pi h(x+y)+\cos\pi[(i-h)(x-y)+2\ell z]\cos 2\pi k(x+y)\} \\ \\ B=0 \end{array}\right. \qquad (56)$$

Table 14 Structure factor of β-In_2Se_3

(h k l)	$\|F_o\|$	$\|F_c\|$
0 0 3	-	2.30
0 0 6	6.61	6.33
0 0 9	1.55	1.72
0 0 12	3.71	2.40
0 0 15	5.30	6.07
0 0 18	5.60	6.65
0 0 21	4.16	4.62
0 0 24	3.52	3.49
0 0 27	8.05	6.36
0 0 30	3.64	3.97
0 0 33	-	0.52
0 0 36	-	0.14
0 1 $\bar{1}$	3.03	2.57
0 1 2	-	0.16
0 1 $\bar{4}$	1.65	0.43
0 1 5	10.72	12.78
0 1 $\bar{7}$	-	0.35
0 1 8	4.50	4.62
0 1 $\bar{10}$	7.54	9.24
0 1 11	5.85	7.05
0 1 $\bar{13}$	5.26	6.35
0 1 14	-	0.49
0 1 $\bar{16}$	6.10	6.46
0 1 17	4.74	4.56
0 1 $\bar{19}$	-	1.45
0 1 20	4.14	3.62
0 1 $\bar{22}$	8.74	6.03
0 1 23	5.92	4.73
0 1 $\bar{25}$	-	3.22
0 1 26	2.22	2.13
0 1 29	3.46	3.96
0 1 $\bar{31}$	-	0.46
0 2 1	2.64	2.11
0 2 $\bar{2}$	-	0.17
0 2 4	-	0.25
0 2 $\bar{5}$	8.95	12.05
0 2 7	-	0.32
0 2 $\bar{8}$	3.17	3.84
0 2 10	9.37	7.82
0 2 $\bar{11}$	6.30	6.01
0 2 13	6.41	5.41
0 2 $\bar{14}$	-	0.39
0 2 16	9.00	5.46
0 2 $\bar{17}$	2.93	3.99
0 2 19	-	1.32
0 2 $\bar{20}$	2.65	3.26
0 2 22	5.43	5.43
0 2 $\bar{23}$	3.79	4.27
0 2 25	1.70	2.89
0 2 $\bar{26}$	1.38	1.96
0 2 28	0.95	2.31
0 2 $\bar{29}$	1.22	3.66
0 2 31	-	0.44
0 3 0	8.38	7.67
0 3 3	-	1.36
0 3 6	3.71	3.82
0 3 9	-	0.88
0 3 12	-	1.66
0 3 15	4.56	4.24
0 3 18	4.16	4.70
0 3 21	3.88	3.48
0 3 24	2.65	2.70
0 4 $\bar{1}$	1.78	1.45
0 4 2	-	0.16
0 4 $\bar{4}$	-	0.54
0 4 5	7.10	6.85
0 4 $\bar{7}$	-	0.25
0 4 8	2.04	2.56

As the reduced coordinates of asymmetric units occupied by Se and In atoms have been determined as shown in the equation of (45), the summation over all the different kinds of atoms in a unit cell can be simplified in the following forms,

$$\begin{cases} A_{I}=3, & B_{I}=0 \\ A_{II}=6\cos 2\pi l\frac{13.38}{60}, & B_{II}=0 \\ A_{III}=6\cos 2\pi l\frac{24.12}{60}, & B_{III}=0 \end{cases} \qquad (57)$$

Accordingly the theoretical structure factor of β-In_2Se_3 is given by the equation,

$$F_c = f_{Se}\exp\left[-B_{Se}\frac{\sin^2\theta}{\lambda^2}\right]\left(3+6\cos 2\pi l\frac{13.38}{60}\right) + 6f_{In}\exp\left[-B_{In}\frac{\sin^2\theta}{\lambda^2}\right]\cos 2\pi l\frac{24.12}{60}\,. \qquad (58)$$

Assuming that $B_{Se}=B_{In}$, the structure factor without temperature factor is written as follows;

$$F_c^0 = f_{Se}\left(0.5+\cos 2\pi l\frac{13.38}{60}\right) + f_{In}\cos 2\pi l\frac{24.12}{60}\,. \qquad (59)$$

Using the least square mean method for the temperature factor, B and the scale factor, k, the theoretical structure factor, F_c^0 in (59) is connected with the observed structure factor given by the equation of (35). For the determination of the z parameters of In and Se atoms, a minimization of the R factor as defined below was carried out. The R factor is defined by the equation,

$$R = \frac{\sum_{lh}\{|F_{cal}(lh)| - |F_{obs}(lh)|\}}{\sum_{lh}|F_{obs}(lh)|} \qquad (60)$$

As a result it was established that the minimum of R(=0.18) is observed with z_{In}=0.401 (six In atoms located in the position of 6c3m), z_{Se}=0.222 (six Se atoms in 6c3m), z_{Se}=0.000 (three Se atoms in 3a$\bar{3}$m). The observed and calculated crystal structure factor are given in Table 14.

Similarly, the crystal structure factors have been determined for α-In_2Se_3, in which the lattice parameters are a=4.05 Å, c=28.77 Å and Z=3 at room temperature. When each atoms were located as z_{In}=0.385 (three In atoms in 3a3m), z_{In}=0.908 (three In atoms in 3a3m), z_{Se}=0.192 (three Se atoms in 3a3m), z_{Se}=0.475 (three Se atoms in 3a3m), and z_{Se}=0.667 (three Se atoms in 3a3m). R factor was calculated to be 0.18.

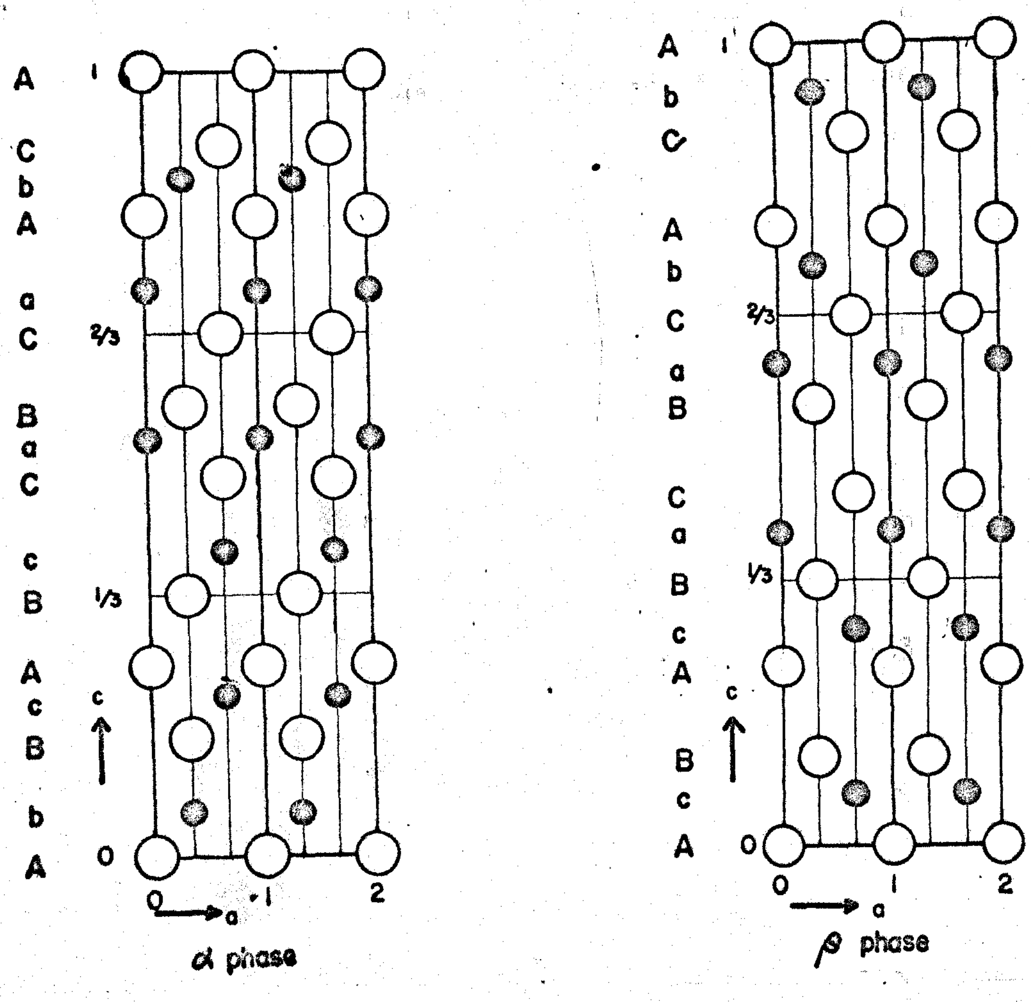

Fig. 11 Structure of In_2Se_3 (present work)

Double sandwich layers are found, in β-form, consisting of rhombohedral alternate of five sheets Se-In-Se-In-Se, and they are again packed rhombohedrally forming a repetition of of AbCaB·CaBcA·BcAbC stacking along the c-axis. (Fig. 11) Here the capital letters represent sellenium layers and small ones indium layers. In the α-form a different type double sandwich is found, and the repetition of layers is given as AaCbA· CcBaC·BbAcB. The basic difference between α- and β-modifications is, in the fact, that the indium atoms of β-form are situated in octahedral holes formed by selenium packing while indium atoms of former are situated in tetrahedral holes due, perhaps, to the predominance of the covalent bond nature at lower temperature.

The interatomic distances in the α- and β-forms turn out to be as follows; In-Se: 2.87 Å (In-situated in octahedral holes at 250 °C), and 2.69 Å (In-situated in tetrahedral holes at room temperature), and Se-Se: 4.01 Å (Se-between each layer).

2-6) Thermal properties

In this section, results of the differential thermal analysis and thermal expansion would be briefly described.

The thermogram of In_2Se_3 on the heating curve is indicated in Fig. 12. The transition temperature from α- to β-modification is recognized to be 205 °C. However the transition could not be measured on the cooling curve.

The measurements of thermal expansion coefficient were performed using the strain gauge. The results are shown in Fig. 13, where the expansion indicated by $C\perp$ and $C/\!/$ means the uniaxial expansion perpendicular and parallel to c axis respectively.

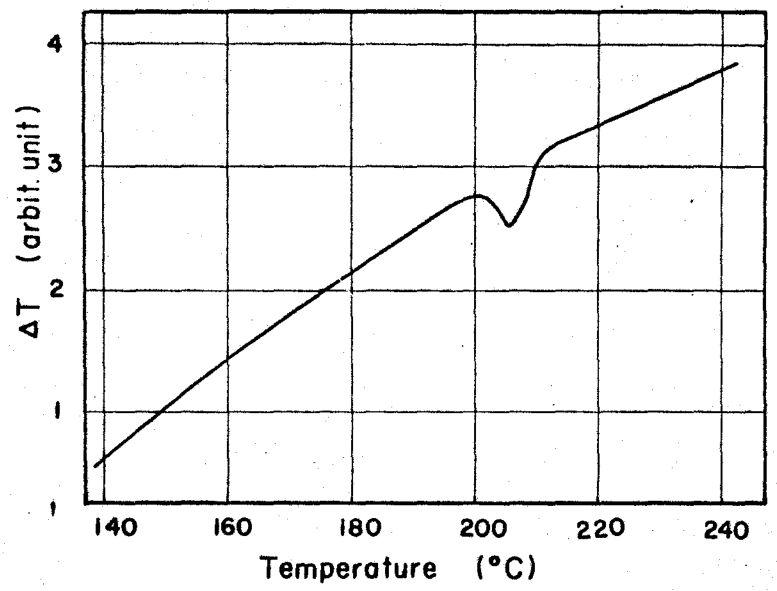

Fig. 12 Thermogram of In_2Se_3

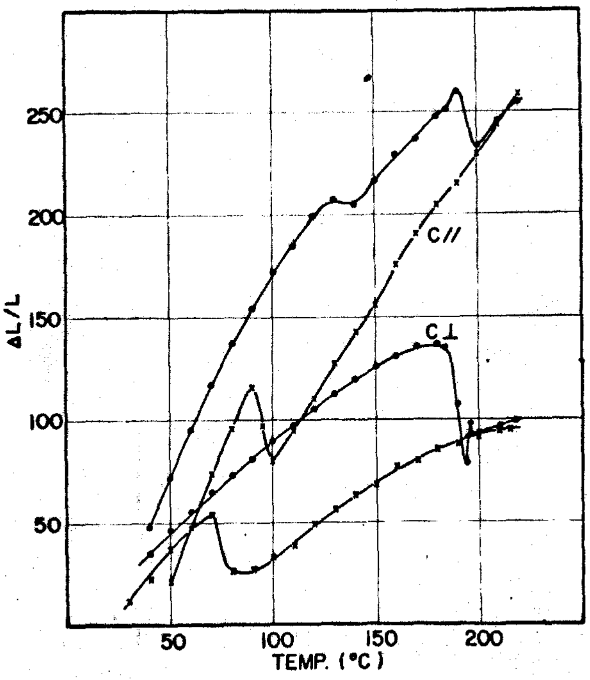

Fig. 13 Thermal expansion of In_2Se_3

The fact that α (C⊥) is layer than α (C//) seems to be closely related to the crystal structure with double sandwich layers towards c axis. The β -form has been observed to be greatly supercooled.

2-7) Conclusion

The following contents would be now concluded;

(1) The single crystal was prepared by a solution method in which vapour pressures of selenium were carefully controlled in the range of 700 - 750 mmHg just above the melting point of the compound. The crystal obtained shows remarkable cleavage parallel to the (001) plane.

(2) Since the β -phase is stable above 200 °C, the small specimen was sealed in a capillary and heated at about 250 °C to obtain X-ray photographs of the β -phase. The c axis Laue photographs show no six-hold symmetry as expected from the literatures but three-hold symmetry. High temperature photographs were taken with Ni filtered CuK$_\alpha$ radiation around the a axis. The a axis osillation photographs show that the layer lines are symmetrical with respect to the equatorial line. On the Weissenberg photographs the reflections are observed as -h+k+l=3n, the indices being based on the hexagonal system. The intensity statistics of the reflections indicate that the crystal should be of cectrosymmetric. Thus the space group of β -phase has been concluded to be rhombohedral D_{3d}^{5}-$R\bar{3}m$. The unit cell has the dimensions, a=4.05, c=29.41 Å at 250 °C, and Z=3. Observed intensities were corrected by ordinary way. There are sex indium and nine selenium atoms in a unit cell. Considering the equivalent positions of the space

group R$\bar{3}$m and the coordination of the atoms, it may be reasonable to locate the selenium atoms in 3(a) and 6(c), and the indium atoms in 6(c). There is no parameters in 3(a) and only z parameters in 6(c). The parameters were obtained from Patterson diagram, P(vw), and refined to minimize the discrepancy factor R. When the values are z_{In}=0.401, and z_{Se}=0.222, both in 6(c), the R factor is 0.18.

(3) The lattice parameters of α -phase were determined to be a=4.05, c=28.77 Å, and Z=3 at room temperature. The reflections are observed as -h+k+l=3n like β -phase. The α -phase crystal, however, seems to be of noncentro-symmetric from comparison of observed structure factors to those calculated. The α -phase space group is thus concluded to be C_{3v}^{5}-R3m. Some of intensities at low angles were corrected for the secondary extinction effect. All atoms are situated in the spacial position 3(a) of R3m. The final atomic parameters for indium are 0,0,0.242; 0,0,0.718, and for selenium atoms, 0,0,0,; 0,0,0.525; 0,0,0.818, respectively. The R factor is calculated to be 0.18.

(4) The transition temperature from α - to β -In_2Se_3 was determined to be 205 °C.

(5) It was observed that the thermal expansion toward c axis is than that perpendicular to c axis.

References

1) N. N. Sirota; Acta.Cryst. A25(1969)223

2) A. E. Attard and L. V. Azaroff; T. Appl. Phys. 34(1963)774

3) N. N. Sirota and N. M. Oleknovich; Dokl. Akad. Nauk. SSSR 136(1961)660

4) N. N. Sirota and N. M. Olekhnovich; Dokl. Akd. Nauk. SSSR 136(1961)879

5) D. T. Cromer; Acta. Crystall. 18(1965)17

6) G. Giesecke and H. Phister; Acta. Cryst. 11(1958)369

7) R. Uno, K. Yukino and T. Okano; J. Phys. Soc. Japan 25(1968) 911

8) M. E. Straumains et al.; J. Electrochem. Soc. 114(1967)640

9) N. N. Sirota; Semiconductors and Semimetals, Academic Press,

10) U. Korhonen; Acta. Meta. 2(1954)713

11) А.М. Чижиков, В.П. Счастливый; СЕЛЕН И СЕЛЕНИДЫ, ИЗДАТЕЛЬСТВО «НАУКА» Москва, 1964

12) H. Hahn and G. Frank; Z. anorg. allog. Chem. 278(1958)333

13) H. Miyazawa and S. Sugaike; J. Phys. Soc. Japan 12(1958)312

14) S. A. Semiletov; Soviet Phys. Solid State 3(1961)544

15) International Table for X-ray Crystallography, edited by K. Lonstale, Kynoch Pr. 1968

Chapter V

Optical Properties in the Infrared Region of III-V Compounds

Recently, studies on the optical properties of semiconductors have been developed, mainly in the region from visible rays to infrared ones, where it is possible to obtain much information about details of electronic energy band structure, impurity levels in the forbidden band, conduction electrons and lattice vibration of crystal. We shall deal mostly with gallium arsenide, gallium phosphide and their alloys to illustrate some optical properties of semiconductors.

The absorption of radiation by any medium occurs through the excitation of electrons and phonons, and phonon electron interactions. For semiconductors it is convenient to consider five separate types of absorption arising from: (1) electronic transitions between different energy bands, (2) lattice vibrations, (3) electronic transitions within an energy band, (4) electronic transitions to localized states of impurity atoms, and (5) vibrations of impurity atoms. In this chapter, the first absorption will be briefly described with our experimental results, and two main absorptions due to the interband and intraband transitions will be reported in the sections, 2 and 3 , and also the electronic transitions to localized states of impurity atoms will be mentioned in the section, 2 . The lattice vibration and vibrations of impurity atoms will be discussed in the section 4 .

1. Experimental methods

In the present work, both transmisivity and reflectivity have been studied by means of conventional spectrometers. Infrared transmission measurements have been made between 400 - 4,000 cm^{-1} with Hitachi EP1-G2 spectrometer. The data were obtained for three temperatures of 90, 297 and 423 ^{o}K. At low temperature the sample was mounted on a cold finger in vacuum. A cryostat vacuum lower than 10^{-4} mmHg was necessary to prevent a build up of ice on the surface of specimen. KBr crystals were used as the material for windows. The experimental arrangement is shown in Fig. 1.

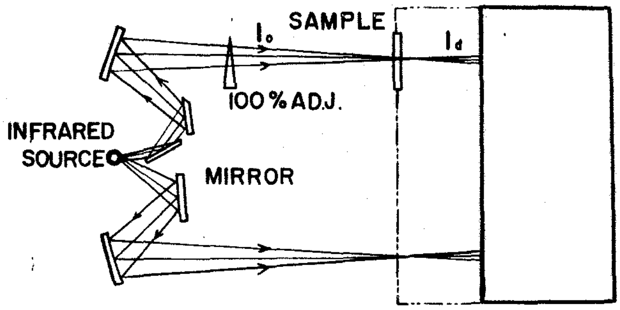

Fig. 1 Experimental arrangement

In the region of 2,000 to 20,000 cm^{-1}, the infrared transmission measurements have been qualitatively performed with other spectrometers. The absorption coefficient α was derived from

$$T = \frac{(1-R)^2 e^{-\alpha d}}{1 - R^2 e^{-2\alpha d}} \qquad (1)$$

where R is the bulk reflectance and d is the thickness of a specimen.

Fig. 2 shows the change of transmisivity as a function of sample thickness. However the transmisivity is greatly influenced by the flatness of the surface. The change of transmission at constant wave number is shown as a function of grain size of fine powder in Fig. 3. We have usually get the surface of specimen finished using fine powder with diameters less than 1 micron.

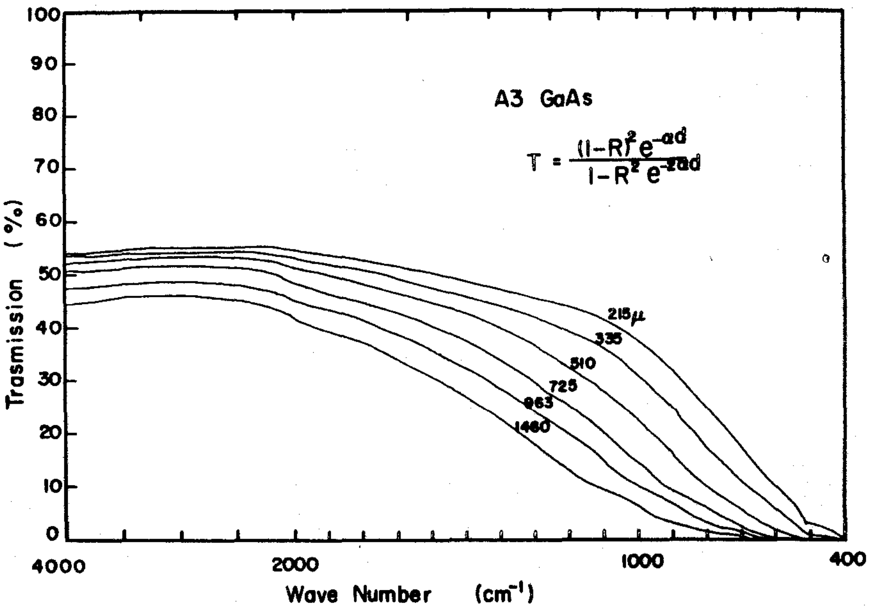

Fig. 2 Room temperature transmission as a function of sample thickness

Reflectivity is related to the refractive index, n, and extinction coefficient, κ , by

$$R = \frac{(n-1)^2 + \kappa^2}{(n+1)^2 + \kappa^2} \qquad (2)$$

is represented by

$$\alpha = 4\pi k \tilde{\nu}$$

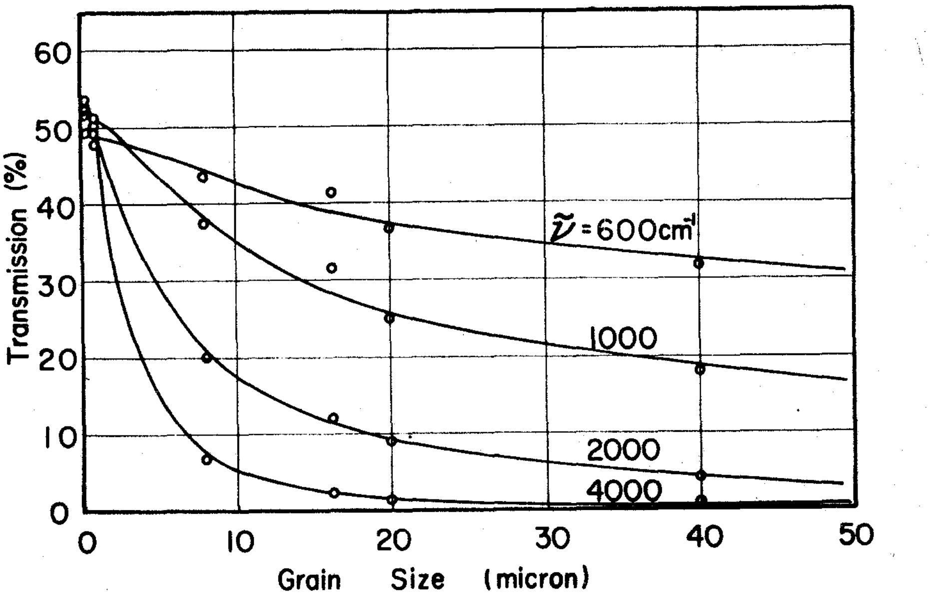

Fig. 3 Influence of the roughness of the surface for the transmisivity.

where $\tilde{\nu} = \nu/c$ is the wave number in cm^{-1}. Infrared reflectivity spectra for unpolarized light at normal incidence have been measured over the frequency range from 200 to 5,000 cm^{-1} by means of a conventional spectrometer.

Light of frequency $\nu < E_G/h$, where E_G is the thermal energy gap, suffers a reflection loss dependent on the refractive index of a semiconducting medium and is not absorbed by the pure material until the frequency nears values characteristic of the lattice vibrations. In the region where photon energies are approximately equal to E_G there is a rapid increase in the absorption coefficient.. Fig. 4 shows the absorption spectra of $GaAs_{1-x}P_x$ compounds at room temperature in the region of the absorption adge. The absorption edge of the compound changes continiously with composition.

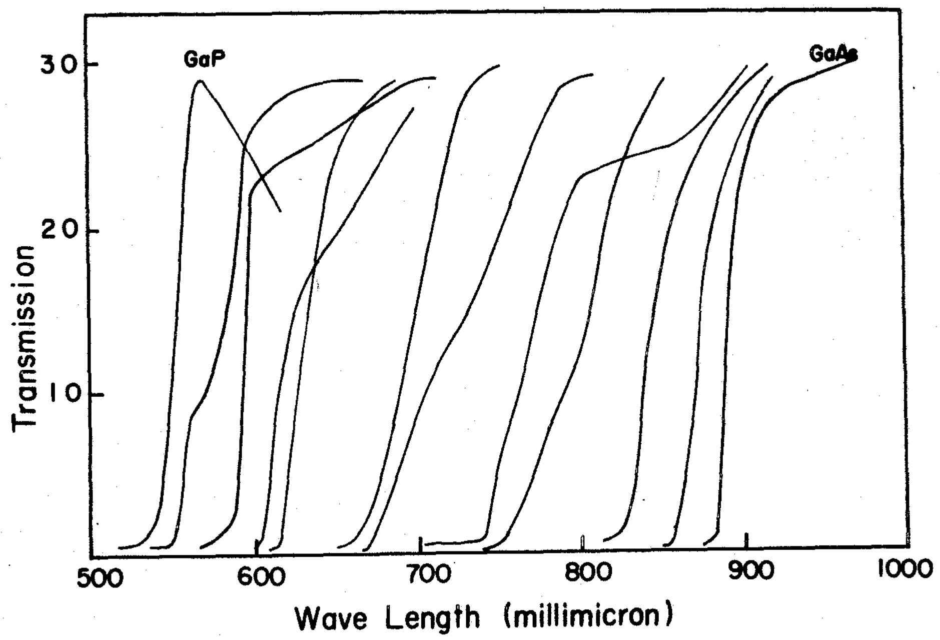

Fig. 4 The absorption spectra of $GaAs_{1-x}P_x$ compounds at room temperature in the region of the absorption edge.

Finally, the transmission interference fringes wolud be reported. When a ray of light is incident of a thin parallel sheet of transparent material, multiple reflections takes place inside the sheet, and at selected wavelengths constructive or distructive interference will occur in the reflected and transmitted beams. If a spectral measurement of transmission is carried out, a series of fringes will be obtained. Such a measurement is potentially the most accurate way of determining the refractive index.

The amplitude of the reflected beam relative to the incident beam of unit amplitude will be given by

$$r = -r_1 + r_1(1-r_1^2)e^{-2i\delta}(1-r_1^2 e^{-2i\delta})^{-1} \tag{3}$$

Similarly for transmission

$$t = (1-r_1^2)e^{-i\delta}(1-r_1^2e^{-2i\delta})^{-1} \qquad (4)$$

where r_1 is the amplitude of the directly reflected ray, and δ is the phase change on one traversal of the film as given by $\delta = (2\pi/\lambda)nd$. Maximum transmission occurs when the phase change is an integral number of half wavelengths per traversal, i.e. $\delta = n\pi$ and $e^{-2i\delta} = 1$. The energy transmission is given by the product of t and its complex conjugate, and hence

$$T = tt^* = \frac{(1-r_1^2)^2}{1-2r_1^2\cos 2\delta + r_1^4} \qquad (5)$$

Therefore the contrast between fringe maxima and minima is represented by, when there is absorption in the film,

$$T_{max}/T_{min} = \frac{(1+\tau^2R)^2}{(1-\tau^2R)^2} \qquad (6)$$

where τ is the parameter, suppose the transmission is τ for each traversal of the film.

For example, the data of the very thin specimen of GaAs was shown in Fig. 5. The relation between order number n and position of transmission interference fringe was plotted in Fig. 6. The dielectric constant of GaAs was shown in Fig. 7 as a function of wave number, where points were deduced from interference fringes and solid lines were calculated using the equation,

$$\epsilon = \epsilon_\infty + \frac{\epsilon_0-\epsilon_\infty}{1-(\tilde{\nu}/\tilde{\nu}_0)^2} - D/\tilde{\nu}^2 \qquad (7)$$

and, ϵ_0 and ϵ_∞ are the low and the high frequency dielectric constant, $\tilde{\nu}_0/c$ is the oscillator resonant frequency, and $D/\tilde{\nu}^2$ is the term related to the free carrier absorption.

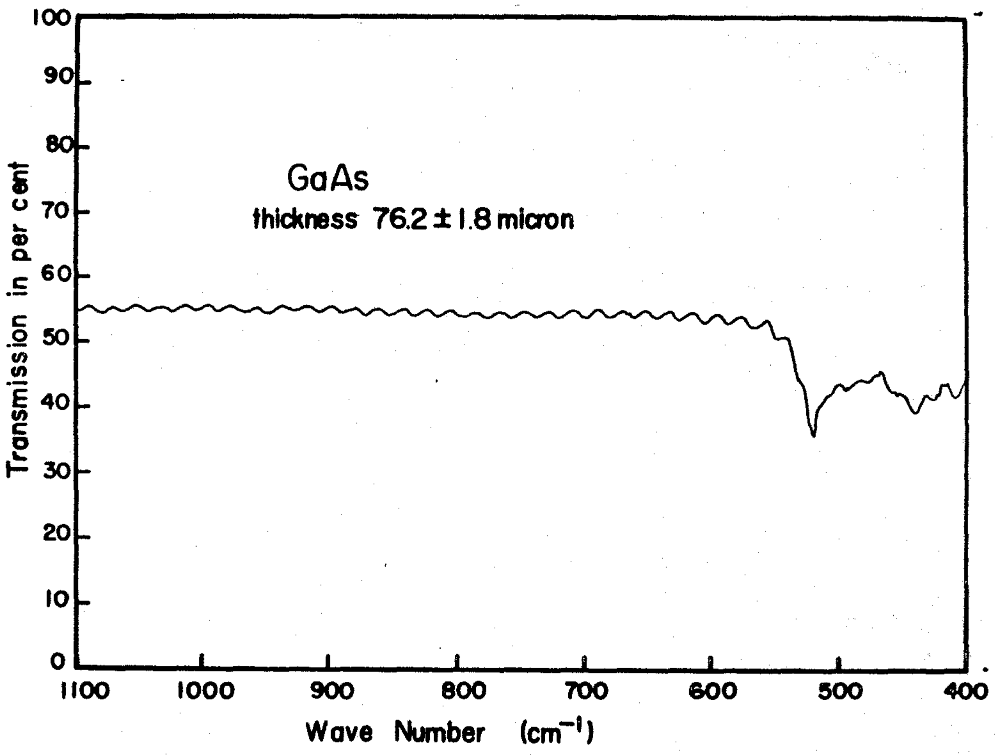

Fig. 5 Transmission interference fringes

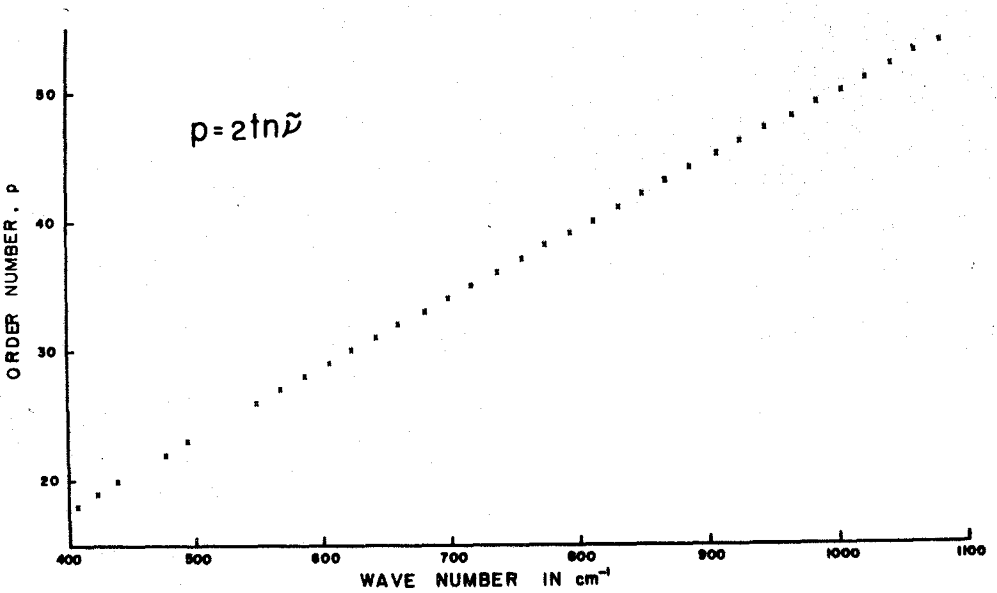

Fig.6 Relation between Order Number and Position of Transmision Interterenc Fringes

Fig. 6 Relation between order number and position of transmission interference fringes

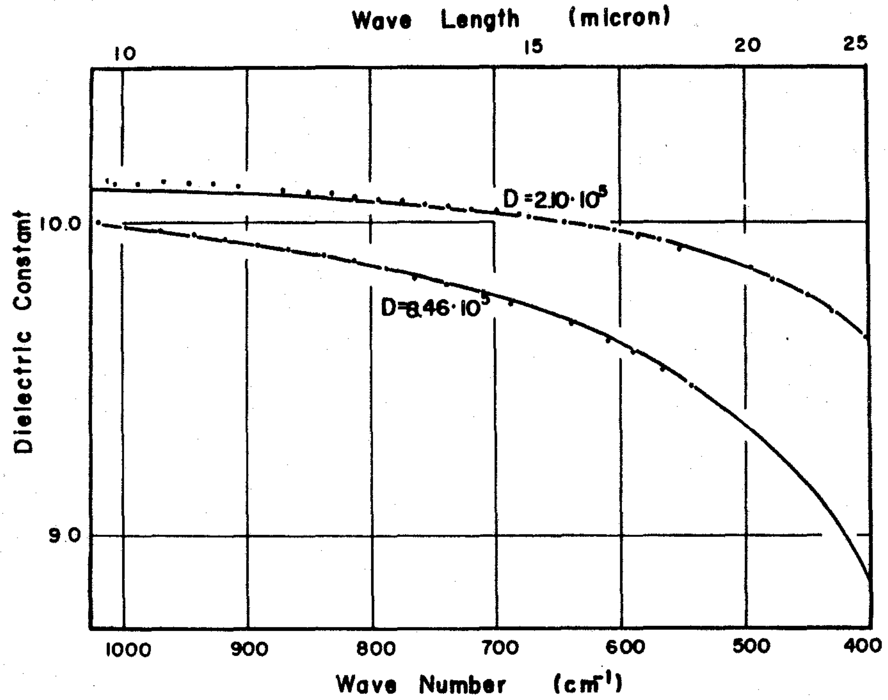

Fig. 7 Dielectric constant as a function of wave number for n type GaAs. Points show the experimental data and solid lines are theoretical values.

2. Transition from shallow donor to upper conduction band minimum and inter-conduction band transition

2-1) Introduction

In several III-V semiconductors, there is present such a band that has a subsidary minimum above a few tenth of eV from the bottom of the lowest conduction band$^{1)}$. The exploration of secondary conduction-band minima has attracted considerable interest for two reasons. Firstly such minima can be important for high-field transport properties, and secondly, an experimental determination of their position in energy and $\mathbf{k}$ space is valuable in comparison with band calculations. For example, the conduction band structures of GaAs and GaP are illustrated in Fig. 8. The conduction band in GaAs is characterized by a lowest minimum at $\mathbf{k} = 0$ and by sets of equivalent minimum at X and L of the zone boundary. Such a material is called as a direct type of semiconductors. Different types of band calculations2)-4) indicate that these secondary minima occur at 0.2 - 0.6 eV above the primary minimum. A separation of 0.36 to 0.38 eV between

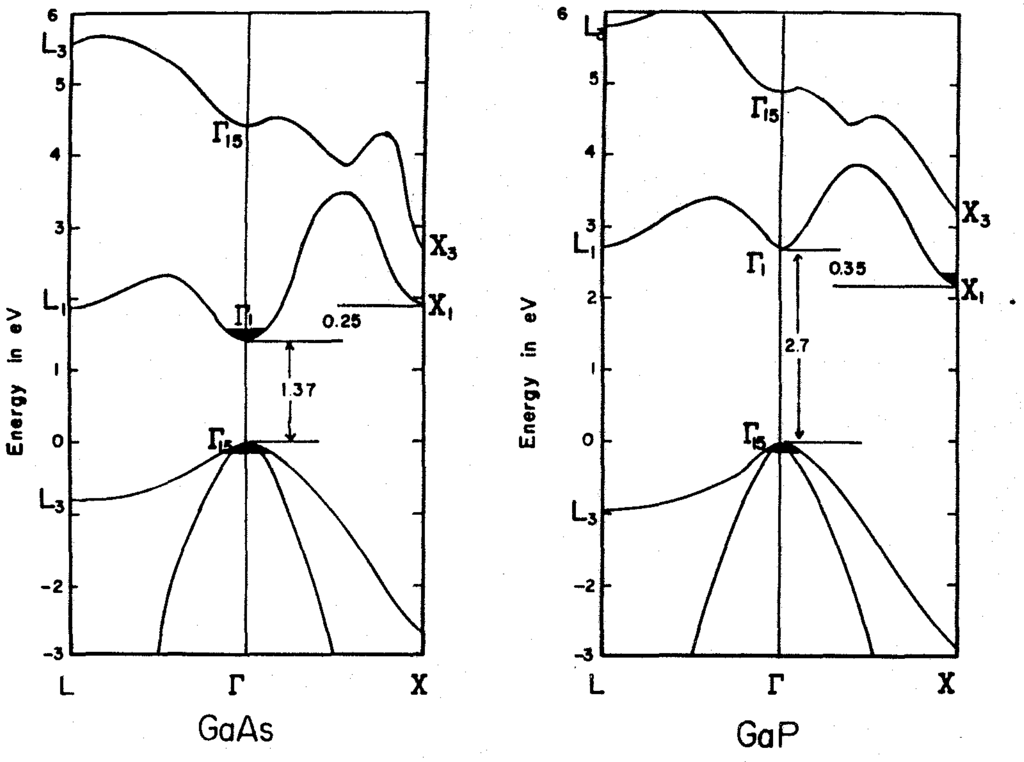

Fig. 8 Energy band structures of GaAs and GaP

primary and lowest secondary minimum has been drived from transport measurements,5)-7) whereas infrared measurements by Spitzer and Whelan8) were interpreted by Haga and Kimura9) to give a separation of 0.44 eV, and also Balslev12) reported that the secondary minimum is located at the Brillouin-zone edge along <001> direction, 0.43 eV above the k = 0 minimum at 80 °K. The influence of uniaxial stress on Gunn effect$^{10)}$ and some properties of GaAs-GaP alloys, e.g., Gunn effect and optical absorption edge,$^{11)}$ have established that the lowest secondary minimum is located at X, the optical studies indicating a separation of 0.4 eV. It is further known that a set of valleys with symmetry x_3 have extremum energies of 0.33 eV above the lower X_1 minima.$^{2)}$ On the other hand, the conduction band in GaP is characterized by a lowest minimum at X and by sets of equivalent minimum at Γ and L as shown in figure 1, where its material is called indirect type of semiconductor. The energy differences between Γ_1 and X_1 points are experimentally determined to be 0.35 - 0.4 eV. A set of valleys with symmetry X_3 have extremum energies of 0.3 eV above the lowest minimum X_1.$^{13)}$ Optical transitions.between these bands are allowed, and an additional absorption band has been experimentally observed in a short wavelength side of the curves of the intra-band free carrier absorption. It is reported that the bands observed in GaAs$^{8)}$ and GaSb$^{14)}$ are due to the inter-conduction band transition.

On the other hand, in such a range of photon energy, an additional absorption arises from the transitions of a donor-electron to the upper conduction band, in which the position of the minimum is same as that of the minimum of the lowest band. Allen and Hodby have proposed a model to interpret the temperature dependence of the additional absorption in n-GaP and n-GaAs-GaP alloys.$^{15)}$

The purpose of the present paper is to investigate quantitatively the shape, the temperature dependence and carrier concentration dependence of the absorption coefficient in n-type GaAs, GaP and GaAs-GaP alloys. A number of explanations have been proposed for this additional absorption. In the following section, some experimental results will be described which give a reasonably clear indication of the difference between the additional absorptions in n-GaAs-rich side alloys and ones in n-GaP-rich alloys.

2. Experimental

Specimens of n-GaAs-GaP alloys for the present work were prepared by the two temperatures mehtod. Polycrystalline ingots were grown from melts with various compositions. A slice of specimen was cut from the top portion of the ingot, where composition was found to be fairly uniform. As to GaAs, the large single crystals were obtained by the present method and, Cr, Se and Te doping in the melt was used for some ingots to have various electron concentrations. The homogeneity of specimens was tested by powder X-ray diffractometer and also by Hall measurements for the determination of conductivity type. The alloy compositions of the samples used in the infrared measurement are given in Table 1, where A1 is a nondoped GaAs crystal with carrier concentration of 1.8 x 10^{17} cm^{-3}, and A2, A3 are Te doped crystals, and A4 is Se doped one, whose carrier concentrations are 3.0 x 10^{17}, 7.4 x 10^{17} and 1.0 x 10^{18} cm^{-3}, respectively, and also P2 is the Cr doped one with high resistivity.

Infrared transmission measurements have been performed between 400 - 4,000 cm^{-1}. The data obtained was for three temperatures of 90, 297 and 423 °K.

Table 1 Alloy composition of the samples

Sample Number	A1	A2	A3	A4	M1	M2
Mol% GaP	0	0	0	0	4.0	5.0

Sample Number	M3	M4	M5	M6	M7
Mol% GaP	12.0	12.8	14.7	18.7	22.0

Sample Number	M10	M11	M12	M15	P1	P2
Mol% GaP	39.0	48.0	50.0	71.0	100	100

The reflectance for GaAs and GaP is taken from the table of optical constants by Serphin and Bennett17) as shown in Table 2, where the values for GaAs measured in the present work are in good agreement with their value. The reflectance for the alloy of GaAs-GaP is determined by the interpolation from the values of GaAs and GaP, assuming the linear relation of the dielectric constant.18) The difference in values is not large, for example, at 2,500 cm^{-1} the refractive index of GaAs is 3.30 and that of GaP is 2.95, and so this interpolation does not introduce much error.

The curves in Fig. 9 give the wave number-dependence of the room temperature absorption coefficient for n-type materials. The absorption at wave numbers $<$ 2,500 cm^{-1} increases with wave number and with the free-carrier concentration. The absorption at smaller wave numbers is typical of normal free carrier absorption observed in many semiconductors,21) and the absorption is represented by a symbol α_f, in the present paper. The detail of free-carrier absorption will be discussed in our next section. The 2,000 - 4,000 absorption band also increases with the electron concentration.

Table 2 Reflectance R of gallium phosphide and gallium arsenide as a function of wave number k

GaP*		GaAs*		GaAs**	
k(cm^{-1})	R	k(cm^{-1})	R	k(cm^{-1})	R
4840	0.244	5000	0.289	5000	0.285
3227	0.244	3333	0.289	4000	0.285
1613	0.243	2500	0.289	3000	0.285
759	0.228	2000	0.289	2000	0.285
714	0.226	1666	0.288	1800	0.285
625	0.220	1428	0.288	1600	0.285
555	0.207	1250	0.287	1400	0.284
500	0.188	1111	0.288	1200	0.284
431	0.107	1000	0.287	1000	0.283
		909	0.287	900	0.278
		833	0.286	800	0.274
		714	0.285	700	0.274
		600	0.283	600	0.264
		500	0.278	500	0.257
		400	0.266	400	0.230

* Seraphin and Bennett[15]
** present work

This phenomenon does not occur in p-type material, but in all n-type-GaAs, -GaP and -GaAs-GaP alloys. The latter absorption band is called as an additional absorption, which is represented as $\Delta\alpha$, in this paper. Then the additional absorption is defined by the following equation,

$$\Delta\alpha = \alpha_{obs.} - \alpha_f \qquad (8)$$

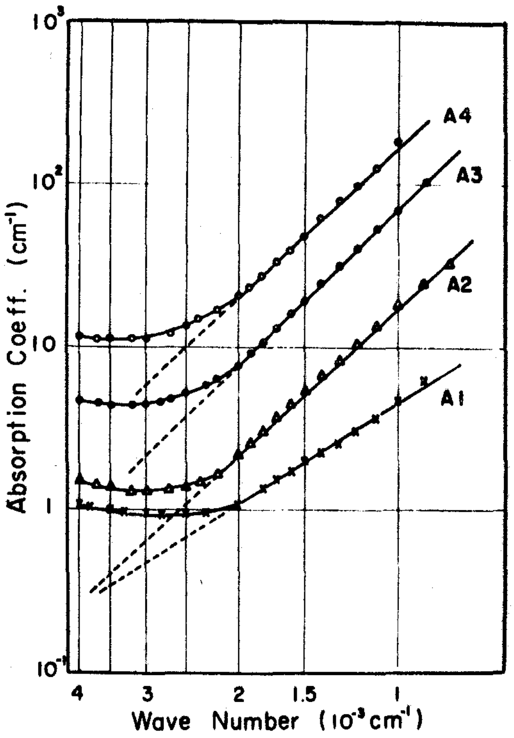

(a) GaAs

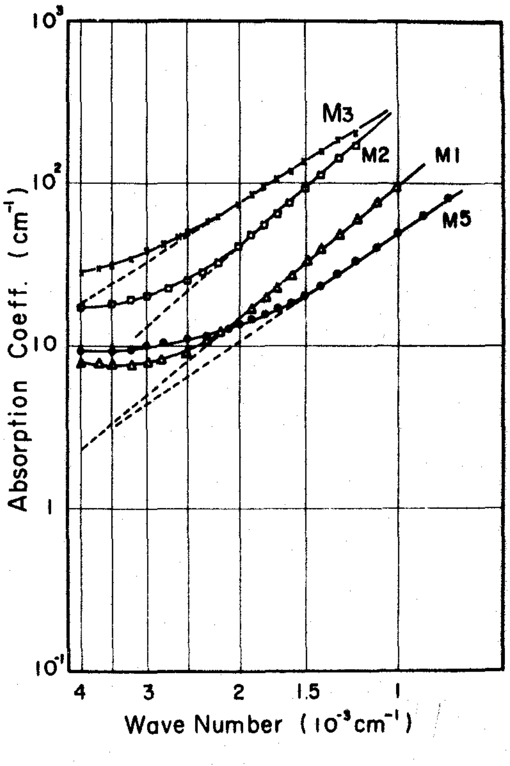

(b) GaAs-rich alloy

Fig. 9 Absorption coefficient as a function of wave number in n-type materials

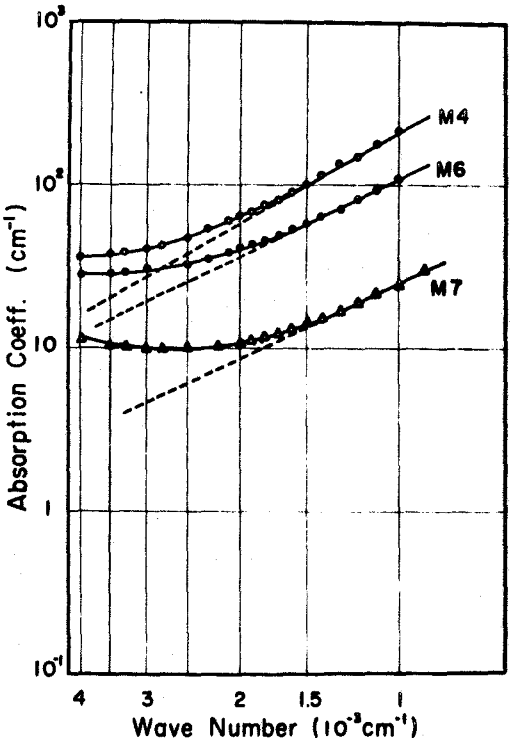

(c) GaAs-rich alloy

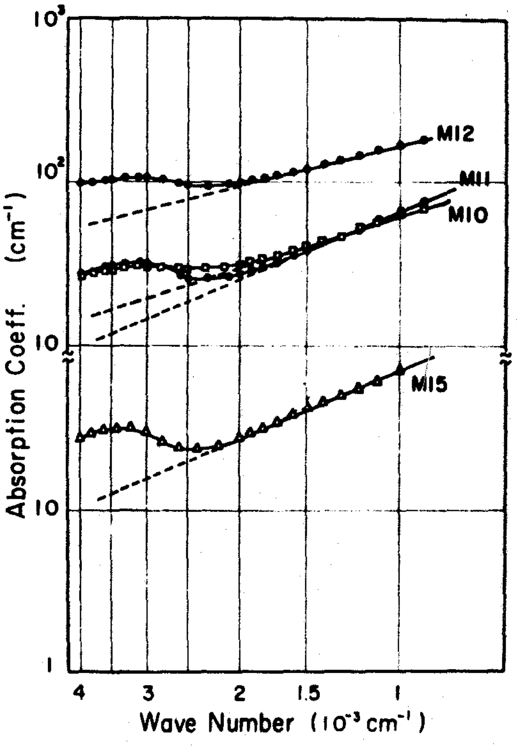

(d) GaP-rich alloy

Fig. 9 Absorption coefficient as a function of wave number in n-type materials

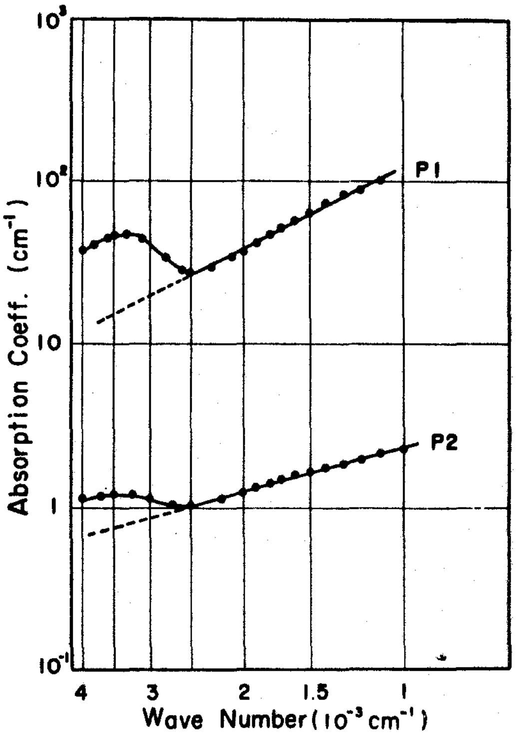

(e) GaP

Fig. 9 Absorption coefficient as a function of wave number in n-type materials.

When the absorption coefficient is plotted logarithmically as a function of wave number, the free carrier absorption in the smaller wave number region can be well represented by a straight line. The additional absorption could be obtained by extrapolation of the absorption coefficient to the large wave numbers. As to this point, the authors have paid much attention to the derivation of the additional absorption, although the previous workers derived ones from a simple background absorption. The free carrier absorption is proportional to the minus xth power of wave number k. It has been precisely determined that x is 3.0 in n-GaAs with high carrier concentration and is 2.5 in n-GaAs with low carrier concentration. In GaP, x is experimentally determined to be 1.5.

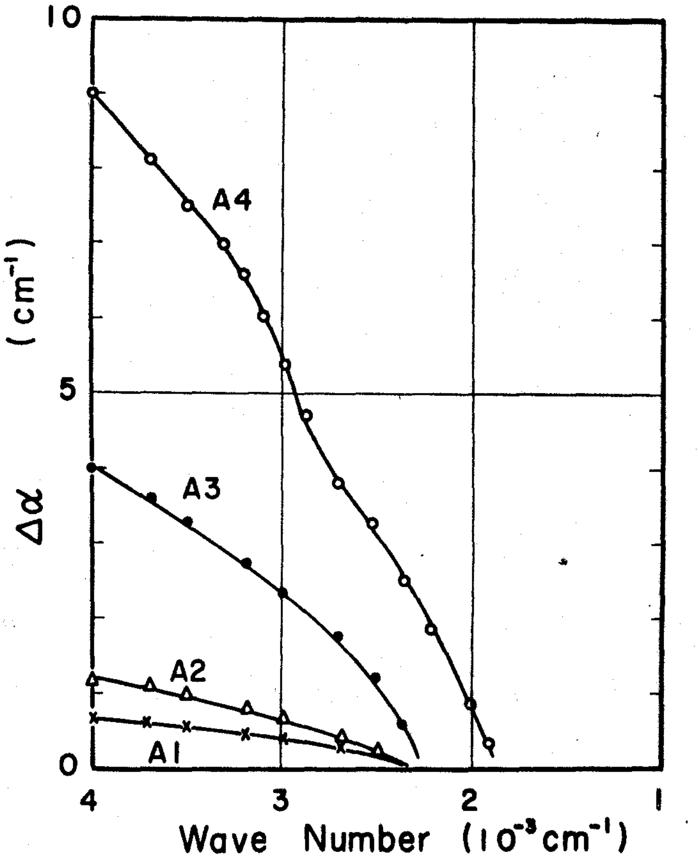

Fig. 10 Additional absorption as a function of wave number in n-GaAs

The measured additional absorption spectra between 1,000 and 4,000 cm^{-1} for n-GaAs samples with various carrier concentrations are shown in figure 10. It has been observed that the absorption increases with the carrier concentration, but the threshold energy remains unchanged. The spectra for n-GaAs rich alloys are shown in figure 11. Remarkable changes of the threshold energy have been observed to occur for the specimens with different compositions.

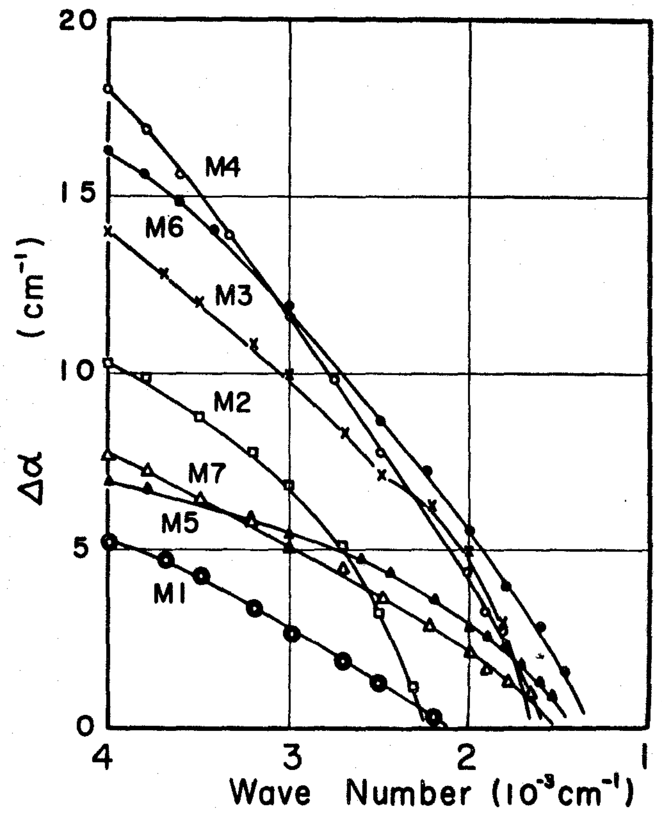

Fig. 11 Additional absorption as a function of wave. number in n-GaAs rich alloys

On the other hand, a typical spectrum for n-GaP sample and the spectra for n-GaP-rich alloys are shown respectively in figures 13 and 12, where these spectra are found to have relatively sharp peaks and not to have a composition dependence of the threshold energy. Moreover, the temperature dependence of the additional absorption bands are shown for some typical specimens in figures 14 - 17. The features in these alloys could be divided into the following two different groups. The one is the group of n-GaP and n-GaP-rich alloys, whose additional bands have the relatively sharp peak and similar shapes to Allen and Hodby's results. According to their model, the additional

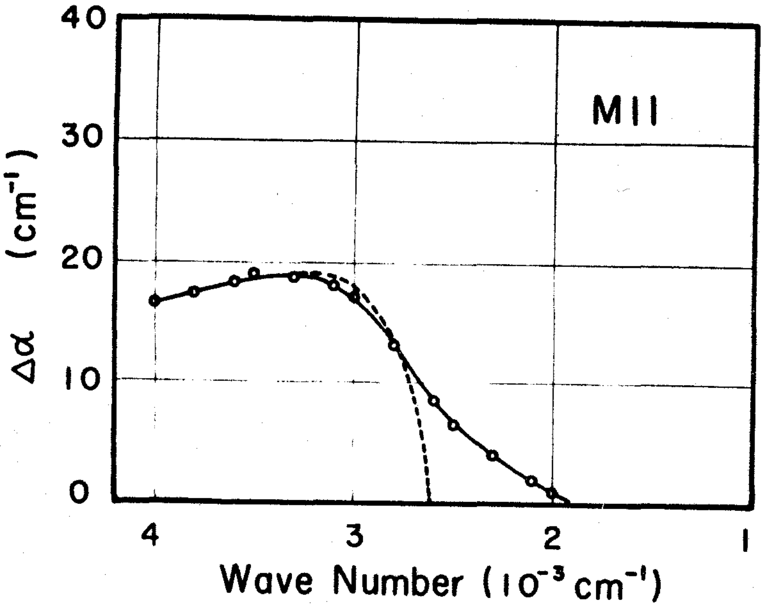

(a) $GaAs_{0.52}P_{0.48}$

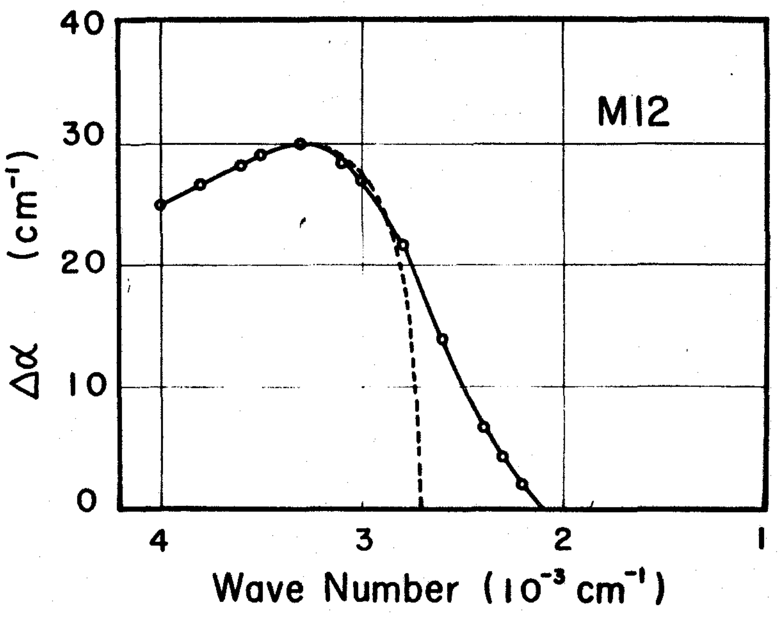

(b) $GaAs_{0.5}P_{0.5}$

Fig. 12 Additional absorption as a function of wave number in n-GaP-rich alloy. The dotted curve is calculated one.

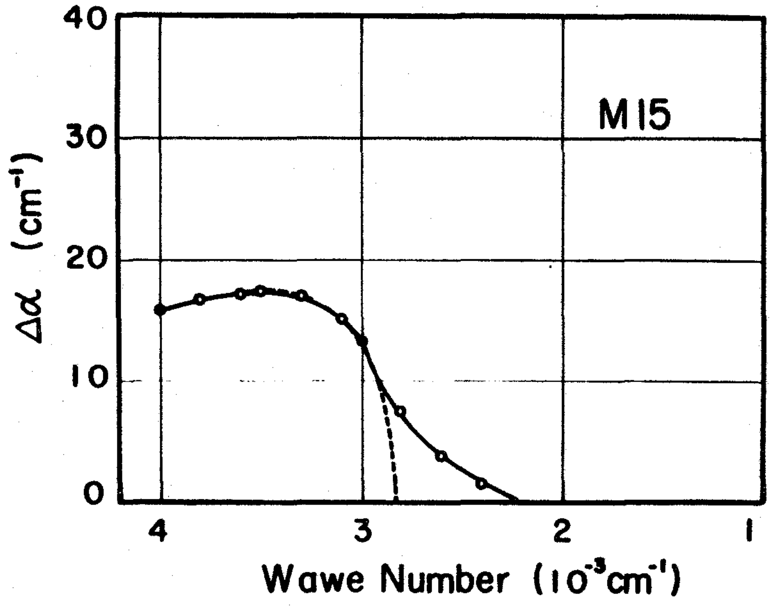

(c) $GaAs_{0.29}P_{0.71}$

Fig. 12 Additional absorption as a function of wave number in n-GaP-rich alloy. The dotted curve is calculated.

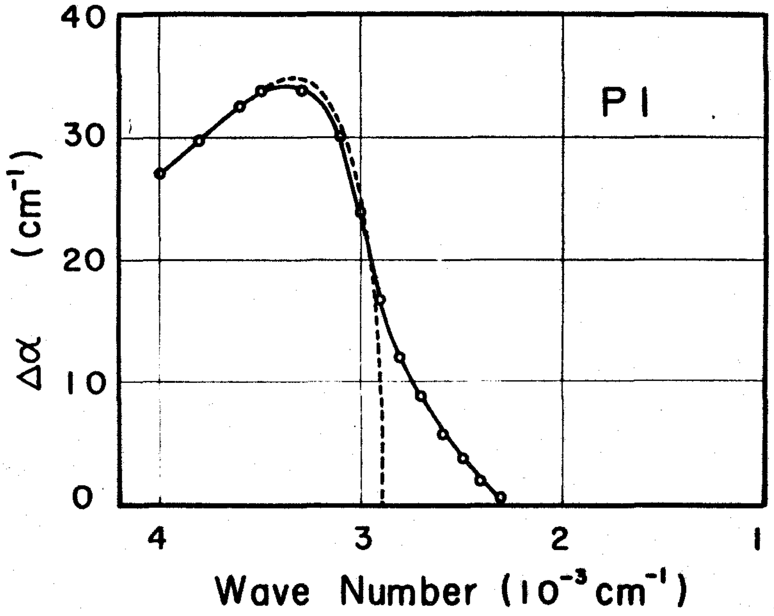

Fig. 13 Additional absorption as a function of wave number in n-GaP

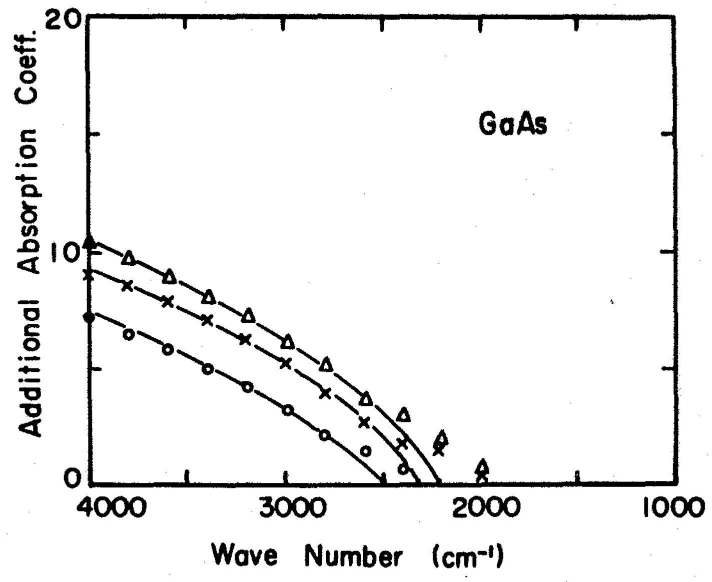

Fig. 14 Additional absorption coefficient at three temperatures, 90 °K; 297 °K; 423 °K.

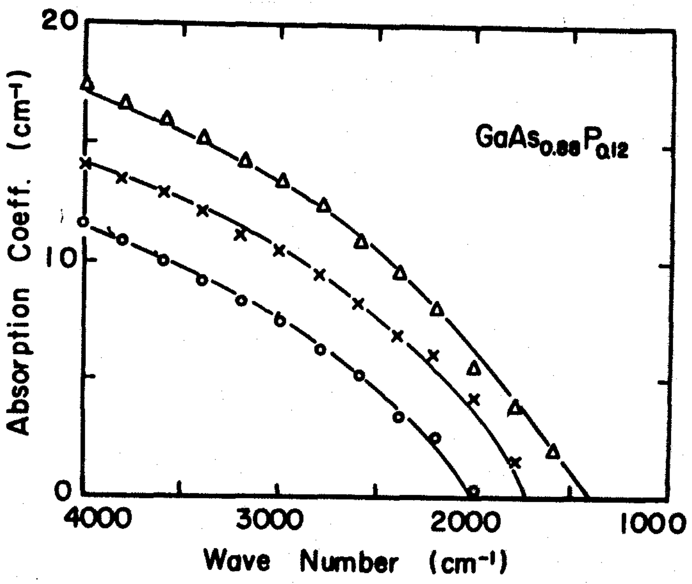

Fig. 15 Additional absorption coefficient at three temperatures, 90 °K; 297 °K; 423 °K

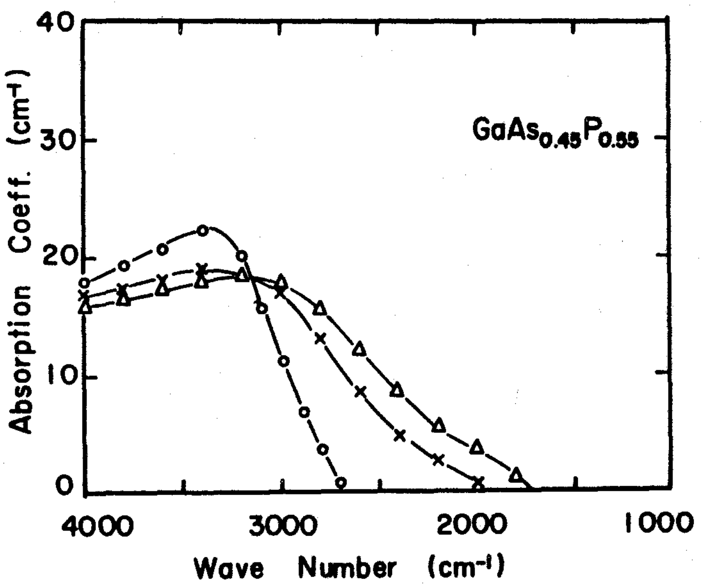

Fig. 16 Additional absorption coefficient at three temperatures, 90 °K; 297 °K; 423 °K.

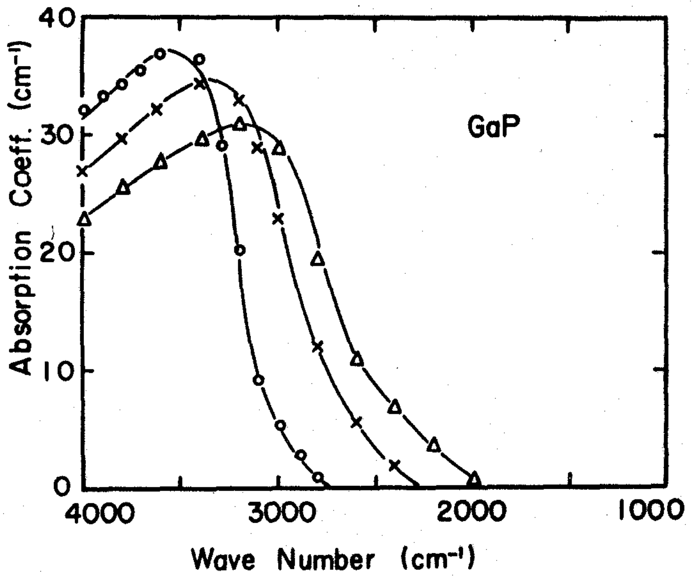

Fig. 17 Additional absorption coefficient at three temperatures, 90 °K; 297 °K; 423 °K.

absorption arises from the transition of a donor electron to the upper conduction band in n-GaP and n-GaP-rich alloys. However, the other group of absorption bands of n-GaAs and n-GaAs-rich alloys shows the rather broad band, which does not seem to have any remarkable peak. Recently, the additional absorption band in n-GaAs has been observed on the short wavelength side of the curves of the intra-band free carrier absorption by several workers 12), 9), 8).

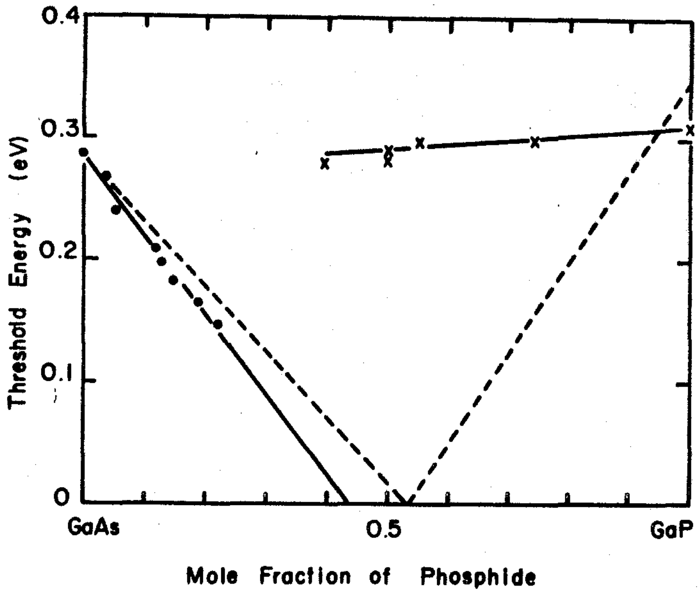

Fig. 18 Empirical threshold energy as a function of alloy composition

The absorption threshold energy was found by fitting the functions discussed below to the experimental curves. The variation with composition is shown in figure 18. The result for the composition dependence of the absorption threshold seems to give more definite evidence to the difference between the additional absorptions in GaAs-rich side and ones in GaP-rich side.

2-3) Results and Discussion

a) A transition from a shallow donor level to the upper conduction band minimum

As shown in Fig. 1, the lowest conduction band minimum of GaP is in the ⟨001⟩ direction of 𝕜 space and is split, there is a subsidiary minimum at 𝕜 = 0, and the material contains a variety of impurities of which the important ones for this discussion are hydrogen-like donors near the conduction band minimum and a deep level.

It is reasonable to consider the origin of the absorption for n-GaP and GaP-rich alloys as follows ; the wave function of a donor level can, to a good approximation, be expanded in terms of wave functions of the conduction band with 𝕜 values near the conduction band minimum, the spread of 𝕜 values being independent for temperature. A direct transition from such a level to an upper conduction band will therefore give an absorption whose width is independent of temperature and whose magnitude is not greatly influenced by temperature.

A simplified treatment of this transition is illustrated by Allen and Hodby.15) According to their treatment, the additional absorption coefficient due to this process is

$$\Delta\alpha = \frac{B n_I}{h\nu} \frac{y^{1/2}}{(1+y)^4} , \qquad (9)$$

$$y = \frac{m_2^*}{m_1^*} \frac{h\nu - E_o - E_I}{E_I} \quad , \tag{10}$$

B is a constant, n_I is the concentration of electrons in donor levels, m_1^* and m_2^* are scalar effective masses of two conduction band minima, E_o is the extremum energy from the lowest conduction band minima to the upper band minima, E_I is the donor ionization energy, and $h\nu$ is the photon energy.

The following method is very convenient for fitting the theoretical equation(9) to the experimental curve. The variable z, which is the additional absorption coefficient multiplied by photon energy, is a function of y as shown by the following equation

$$Z \equiv \Delta\alpha \cdot h\nu = Bn_I \frac{y^{1/2}}{(1+y)^4} \quad . \tag{11}$$

The maximum values of photon energy $h\nu_m$ and Z_m are represented as follows,

$$\frac{m_2^*}{m_1^*} \frac{h\nu_m - E_o - E_I}{E_I} = 1/7 \tag{12}$$

$$Z_m = 0.2216\ Bn_I \tag{13}$$

where subscript m refers to the maximum point. A plot of z/z_m vs. y shown in figure 19 is used in the present analysis. From a plot z vs. $h\nu$ for the experimental data, the values of $h\nu_m$, $h\nu_t$ and z_m are computed easily by using the above relation.

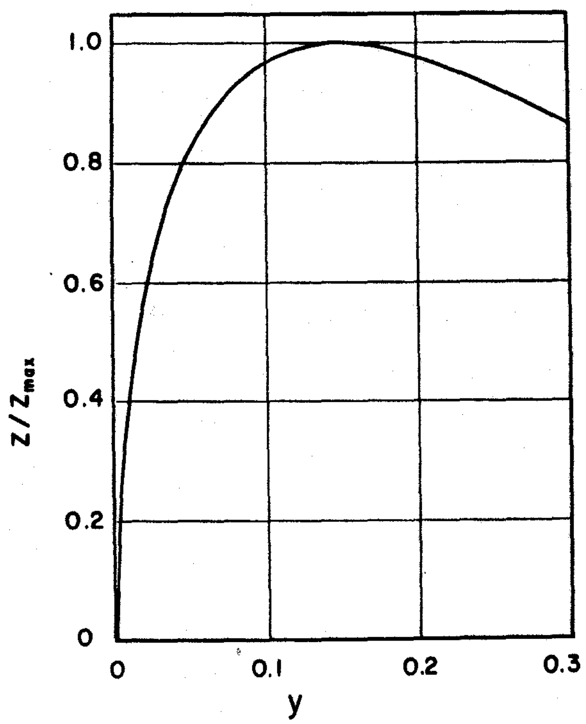

Fig. 19 z/z_{max} vs. y chart

Here, $h\nu_t$ is the threshold energy. Thereafter, a reasonable fit is obtained with equation(9), mainly in the large wave number region, where there is an exponential tail as shown by the solid curves in figures 12 and 13. Some parameters obtained from the curve fitting are also shown in Table 3. There appears to be a good agreement between experimental values and the calculated ones from the assumption that the additional absorption band in GaP and GaP-rich alloy is due to transitions from shallow donors to the upper <001> minima at room temperature and below. The composition dependence of the threshold energy $h\nu_t$ is shown in figure 18, where there is some uncertainty as to the exact position of the donor level involved. The results obtained in the present study may have some uncertainty to this extent,

Table 3 Experimentally determined parameters of the additional absorption bands in n-GaP and n-GaP-rich side alloys

Sample number	**Alloy composition**	k_o	k_{max}	a	Z_{max}	Bn_I	k'_o	x
P1	100	2900 cm^{-1}	3500 cm^{-1}	2.38 $x10^{-4}$	11.7 $x10^{4}$	5.3 $x10^{5}$	2300 cm^{-1}	1.30
P2	100	2900	5000	0.68	0.82	0.37	2400	1.26
M15	71.0	2830	3840	1.41	6.3	2.8	2200	1.30
M12	50.0	2720	3500	1.62	10.1	4.6	2100	1.30
M11	48.0	2700	3700	1.42	6.5	3.0	1800	1.30

that E_t corresponds to $E_o + E_I$ in equation(9). The threshold energy depends to a small extent on the composition. In general, it seems to be caused by the linear dependency on the energy difference between X_1 and X_3 points with the specimen composition. The other possibility, however, is proposed as follows. When assumed that the energy $E(X_1 - X_3)$ is the constant value of 0.30 eV in spite of the change in alloy compositions, a slight composition dependence of the threshold energy $h\nu_t$ should be caused by a change of donor ionization energy E_I. From figure 18, the composition dependence of E_t may be represented by a straight line. When the donor ionization energy in n-GaP is taken to be 0.06 eV, the change of E_I with compositions is experimentally obtained to be $0.060 - 0.041(1 - x)$, where x is the mole fraction of GaP in specimens. The donor ionization energy according to a simple hydrogen-like approximation is given by

$$E_I = -13.5 \frac{m^*}{m} \frac{1}{\epsilon^2} \qquad (14)$$

where ϵ is the dielectric constant. Then ϵ is to be 10.9 and 8.457 for GaAs and GaP, respectively. Therefore, the magnitude of the ionization energy for GaAs is deduced to be 0.036 eV. A slight dependence of E_t on composition could be practically explained in terms of an assumption of the linear relation of the dielectric constant with the composition of specimens.

The experimental data diverge at two points from the curve calculated from equation(9). First , the experimental absorption threshold, which is represented by $h\nu_t$ in Table 3, differs from the calculated one $h\nu_t$. Secondly , a reasonable fit for the higher temperature's data is difficult to be obtained with equatio (9). It seems that at temperatures well above room temperature most of the donors are ionized so that transitions from the lower to the upper <001> minima predominate with a consequent change in the magnitude and shape of the absorption.

One serious divergence between the experiment and the simple theory outlined above is that the threshold at low energies is not as sharp as expected. Near the absorption threshold the experimental results can be fitted by the empirical equation

$$\Delta\alpha \propto (h\nu - E_t')^x, \qquad (15)$$

where E_t' and x are empirical constants. A typical value obtained for x is 1.3. Several explanations for this absorption are

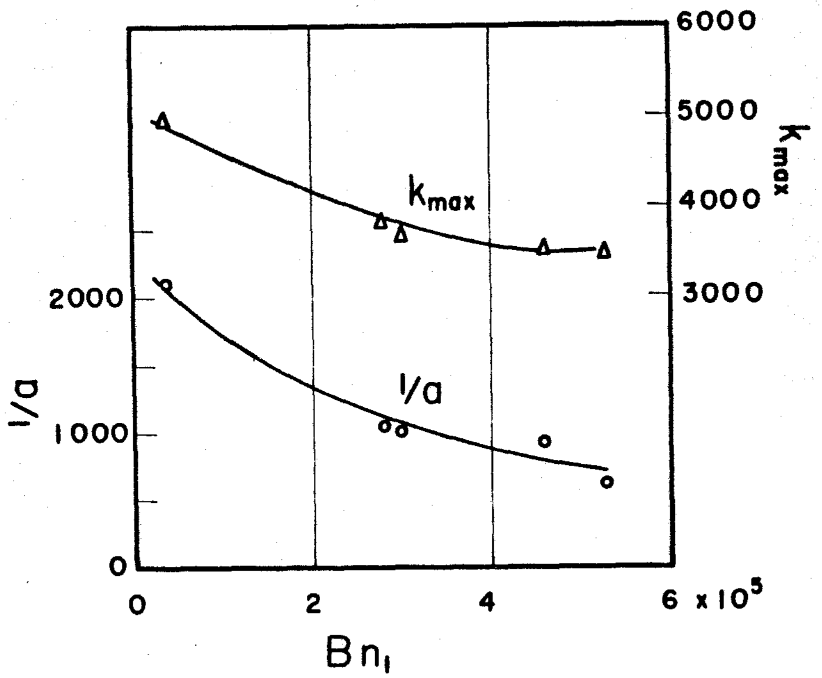

Fig. 20 Variation of k_{max} and $1/a$ as a function of B_{n_I}.

possible: (1) In the group IV elements, the conduction band is degenerate at the zone boundary in the <001> direction, i.e. at the point X, while in III-V compounds the degeneracy is removed and two bands with symmetries X_1 and X_3 occur. Optical transitions between bands are allowed.[19)] The absorption from such a transition should have a tail of exponential shape and vary exponentially with temperature. Experimentally it is found that at room temperature an exponential function is a poor approximation of the shape of the tail, but its transition may be possible at higher temperature. (2) Phonon-assisted transitions will occur at lower energies than direct ones and cause a smearing-out of the sharp threshold. The phonon energies in GaP seem to be about a few hundredth of eV, which is less than the divergent energy. (3) As to impurities, overlap between impurity atom wave functions is appreciable in our material and gives a spread of impurity ionization energies. Excited states of the impurity atoms are appreciably populated at the temperatures considered, and transitions from them will have a lower energy than transitions from the ground state. In this case, the absorption will be dependent on the impurity concentration n_I and vary exponentially with temperature. If the constant B in the 7th column of Table 3 does not change with composition, the term of B_n is only a function of n_I. The values of 1/a and $h\nu_{max}$ are plotted as a function of B_n as shown in figure 20, where 1/a is proportional to the donor ionization energy E_I and increases with decreasing of the impurity concentration. The result may be interpreted from the existence of excited states of the impurity atoms.

b) Inter-conduction band transitions

The absorption band of n-GaAs or GaAs-rich alloy is rather broad and does not seem to have any remarkable peak as shown in figures 10 - 11. In the first step of the analysis, the wave number dependence of z has been surveyed as similarly as that in the previous section. Some results are shown in figures 21 and 22 for n-GaAs and GaAs-rich specimens, respectively. Near the absorption threshold the experimental results can be fitted by the empirical equation

$$Z = \Delta\alpha \cdot h\nu = A\,(h\nu - E_t)^x, \qquad (16)$$

where E_t and x are empirical constants. A typical value found for x is 1.0 in n-GaAs and GaAs-rich specimens. The threshold

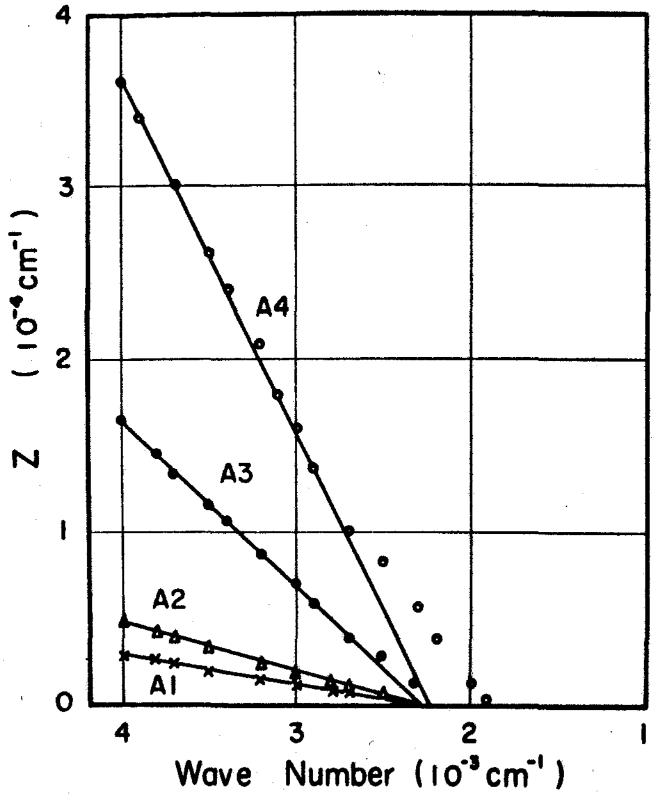

Fig. 21 Wave number dependence of Z in GaAs

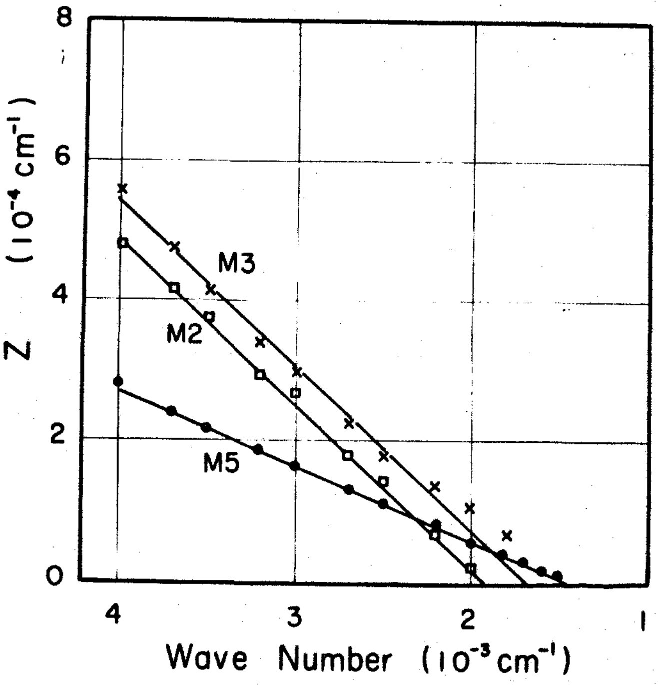

Fig. 22 Wave number dependence of Z in GaAs-rich alloy

energy for each specimen is reduced from a plot of z vs. hν. The threshold energy for n-GaAs with different carrier is the nearly same value at room temperature, but the lower carrier concentration specimens have a slightly higher energy than the higher one. The experimental absorption for the specimen A4 diverges from the equation(16) near the absorption threshold. The threshold energy for GaAs-rich specimens in observed to decrease to lower energy side with increasing of the concentration of GaP component. These empirical threshold energies are shown in Table 4 and figure 18.

Table 4 Empirical threshold energy due to inter-conduction band transition in n-GaAs and n-GaAs-rich alloys

Sample number	Alloy composition	Empirical threshold energy (eV)	
		at 90°K	at 297°K
A1	0	0.407	0.298
A4	0	0.310	0.288
M1	4.0		0.270
M2	5.0		0.240
M3	12.0	0.248	0.210
M4	12.8		0.198
M5	14.7		0.181
M6	18.7		0.166
M7	22.0		0.148

In the case that an electron with wave vector k, which is present near the lowest minimum of conduction band makes a transition, by the interaction with photons and crystal imperfections, into a state with wave vector $\mathbb{k}'$ in the conduction band of the subsidiary minimum which is present at the position different from the Γ-minimum, the transition probability should be calculated by use of the second order perturbation method. Haga and Kimura$^{9)}$ proposed that the absorption band calculated for the indirect type agrees well with the experimental one in n-GaAs at the points of the shape, the carrier concentration dependence and the temperature dependence reported by Spitzer and Whelan. According to their model, the absorption is characterized as following properties: (a) Acoustical phonon as the crystal imperfections contribute mainly for the absorption. Therefore, as the temperature decreases, the additional absorption band should change equally rapidly. (b) The absorption is proportional to carrier concentration. (c) The theoretical absorption coefficient contains an important ajustable parameter as $\Delta E_{10} = E(X_1 - \Gamma_1)$. The additional absorption coefficient is represented by the integral equation

$$\Delta\alpha = \frac{C}{\theta}\int_{u}^{\infty} x^{1/2}\{x-(\Delta-\theta)\}^{1/2}\,dx, \qquad (17)$$

$$x = \varepsilon/kT\,,\quad \Delta = \Delta E_{10}/kT\,,\quad \theta = h\nu/kT\,,$$

and $h\nu$ is the photon energy, ΔE_{10} is the energy difference between X_1 and Γ_1 points in $\mathbb{k}$ space. The integral values as a function of ΔE_{10} are shown in figure 23. ΔE_{10} is reported to be 0.44 eV for GaAs.$^{9)}$

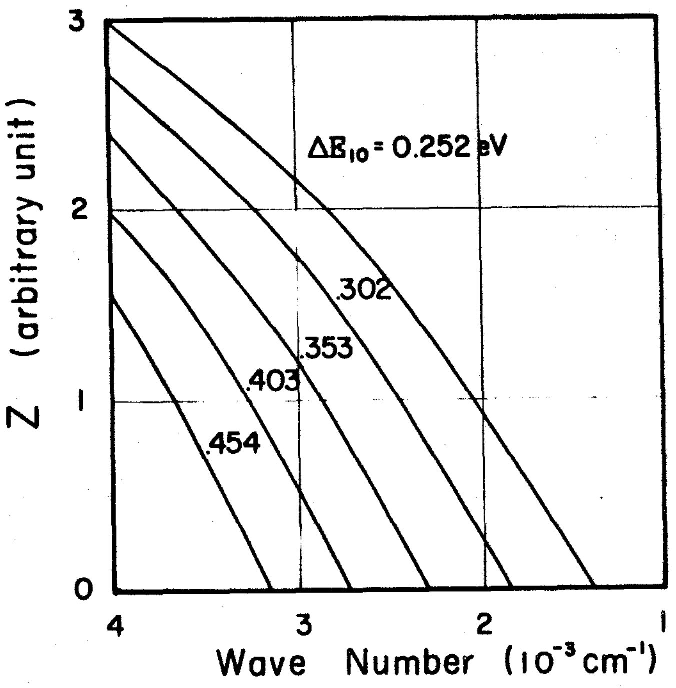

Fig. 23 Wave number dependence of theoretical Z parameter

The empirical threshold energy obtained previously from the equation(16) soes not represent the true energy difference between Γ_1 and X_1 points as understood from the theoretical consideration. The change of the threshold energy with composition is shown in figure 10, where the dotted curves express the difference between <000> and <001> minima and the cross-over point occurs at 53% GaP according to Ehrenreich.20) Then, according to the present experimental result, the threshold energy in GaAs-rich alloys has the dependence on composition x as $E_t = 0.29 - 0.67\ x$ (eV). The empirical cross-over point occurs at 43% GaP.

The other experimental interest in the treatment carried by Haga and Kimura is discussed as follows; at a constant photon energy well above acoustical phonon energies, the additional absorption coefficient may be given by the equation,

$$\Delta\alpha \propto N_e(D-\Delta)\left\{ \begin{matrix} n_q \\ n_q+1 \end{matrix} \right\} , \qquad (18)$$

assuming that the distribution function for conduction electrons is approximated by a Boltzman function, where N_e is the free carrier concentration, n_q is the acoustical phonon density and D is a constant. The absorption coefficients for n-GaAs samples at 3,500 cm^{-1} are shown in figure 41 as a function of free carrier concentration, where the absorption can be observed to change linearly with carrier concentration. The cross section due to this process is deduced to be 3.57×10^{-18} cm^2. Then, the cross sections were similarly determined for n-GaAs-rich specimens. The specimens of M5 and M6 compute to the values of 9.9×10^{-18} and 14.0×10^{-18} and 14.0×10^{-18} cm^2, respectively. These cross sections for alloys are three or four times larger than for n-GaAs as expected.

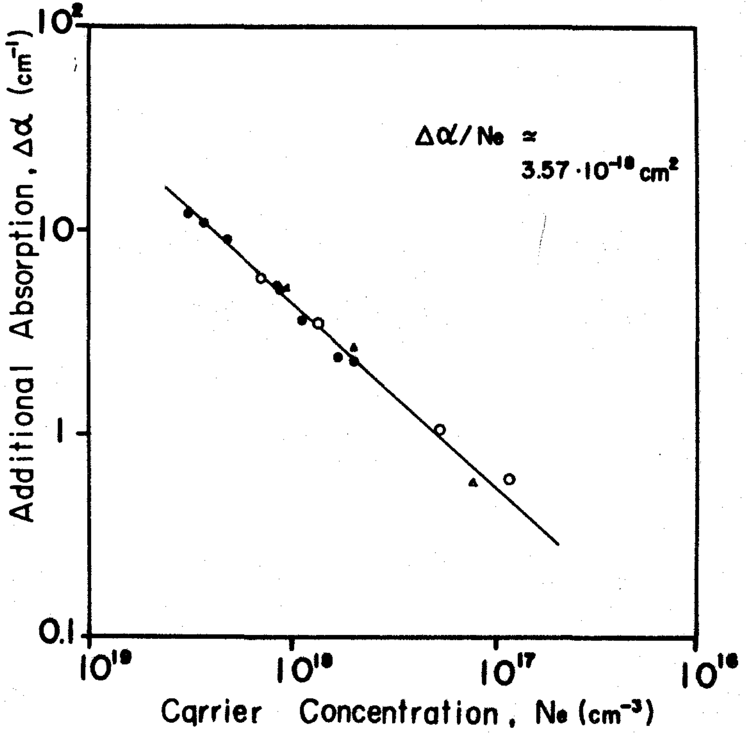

Fig. 41 Concentration dependence of $\Delta\alpha$ at 3,500 cm^{-1}

2-4) Conclusion

The present experimental results of the infrared absorption in the region from 1,000 to 4,000 cm^{-1} have given the following conclusions.

(a) The absorption bands in n-GaP and GaP-rich alloys have been illustrated to occur mainly by a transition from a shallow donor level to the upper conduction band minimum. The reasonable fit for the absorption profile have been obtained with the equation (9), especially in the large wave number region. Near the absorption threshold the experimental values diverge from the equation (9). The fact might be interpreted in terms of the existence of excited states of the impurity atoms. The threshold energy depends to a small extent on the composition. The dependence could be illustrated in terms of the composition dependence of the donor ionization energy.

(b) The absorption in n-GaAs and GaAs-rich alloys arises from the bottom of the lowest conduction band to a subsidiary minimum. The absorption is represented with the equation(16). The dependence of threshold energy on composition x is found to be expressed as $E_t = 0.29 - 0.67x$ (eV). The empirical cross over point occurs at 43 mol% GaP. At a constant photon energy well above acoustical phonon energies, it is concluded that the experimental absorption coefficient is proportional to the carrier concentration and the cross section for alloys are three or four times larger than for GaAs as expected from the theory.

3. Free carrier absorption in n-GaAs

3-1) Introduction

The main object of this work was to investigate the infrared absorption in gallium arsenide with relative low carrier densities. Absorption spectra for n-type samples with carrier concentration of 1.0×10^{16} to 3×10^{18} cm^{-3} were measured in the free carrier absorption region, 400 - 4,000 cm^{-1}, where its spectra include the contributions arising from the inter-conduction band transitions in the wave number range $\tilde{\nu} \geq 2,000$ cm^{-1} and from the multiphonon process in the range $\tilde{\nu} \leq 800$ cm^{-1}.

The study of the free carrier absorption is a powerful mean to understand the scattering mechanism of current carriers in semiconductors. The quantum mechanical theory of the infrared absorption by free carriers in nondegenerate semiconductors has been initially developed by Fan and Frohlich,22) and compared with the experiment on n-type Ge by Fan, Spitzer and Collins.23) Thereafter the more complete theories based on the band structure of Ge have been developed by some authors.24) They have taken into account the induced photon emission, which has been originally recognized by Smidt.25)

The infrared absorption due to the infrared transition of free carriers, which is treated here, arises only in the presence of crystal imperfections, because both the energy and the momentum must be conserved in the process of the absorption of a photon. Therefore the mechanism is closely related to the scattering mechanism in the conduction phenomena. Now, in such a partially polar semiconductor as GaAs, the electron scattering is caused by several sorts of imperfections, and hence to investigate the contribution of each sort of imperfections is an important subject on the line of the conduction phenomena. Here the following three scattering sources are considered to be very important, i.e. (i) acoustic phonons, (ii) optical phonons, and (iii) ionized impurities.

The free carrier absorptions in n-type gallium arsenide were investigated by W. G. Spitzer and J. M. Whelan,[26)] and E. P. Rashevskaya and V. I. Fistul.[27),28)] It is an interesting fact that the absorption coefficient is dependent on the type of additive for large carrier concentration, $N_e \geq 10^{18}$ cm^{-3}: it is largest for samples doped with sulfur and smallest for samples doped with tellurium. Haga and Kimura[29)] developed the quantum mechanical theory of free carrier absorption in III-V semiconductors and compared with the experiment on n-GaAs by W. G. Spitzer et al.[26)] They concluded that the free carrier absorption is mainly caused by the ionized impurity scattering for samples with high carrier concentration, $N_e \geq 10^{18}$, and the absorption due to the optical phonon scattering prevails in the region of relative lower carrier concentration.

In the present work, we have investigated the carrier dependence and the temperature dependence of free carrier absorption in the wide range of carrier concentration from 1×10^{16} to 3×10^{18} cm^{-3}. The degree of conpensation of impurity for each samples will be estimated by the adjusting parameter $C = (N_{imp}/N_e)$. The relation between the photon capture cross section (α/N_e) and ionized impurities (N_{imp}) is obtained and α/N_e vs N_{imp} chart is given at a constant photon energy, which seems to be very useful for the estimation of carrier concentration and for the correct calculation of the absorption due to other mechanisms, that is, inter-conduction band transition, and lattice absorption, in the corresponding region.

3-2) Experimental

A number of specimens of n-type GaAs doped with group IV elements, giving shallow donor levels, or nondoped, were used. Table 5 presents a list of the samples used with the data obtained from electrical measurements. The room temperature carrier concentrations (N_e) were determined from the measured values of Hall coefficient in which the Hall factor was taken to be unity. In n-type GaAs, there exist at least two type donor levels;36) one is the shallow donor of which the activation energy is 0.003 eV, and the another is the deep level. In each sample, the concentration is the same at three temperatures: 450 °K, 293 °K and 90 °K. At 450 °K, the intrinsic electron concentration (1.45×10^{10} cm^{-3}) is considerably smaller than the lowest value of N_e at room temperature as given in Table 5. At 90 °k, all samples are degenerate or nearly degenerate, and Hall coefficients give essentially the same values of N_e (within 10%) as obtained at room temperature.

Infrared transmission measurements have been made in the range from 400 to 4,000 cm^{-1}. The data were obtained for three temperatures of 90, 293 and 450 °K.

In Fig. 24 are shown the results of the room temperature optical measurements. For wave numbers, $\tilde{\nu} \leq$ 2,000 cm^{-1} the absorption curves rise smoothly with decreasing wave number,

Table 5 A list of samples used in the optical measurements at room temperature

Sample No.	N_e (cm^{-3})	μ_H (cm^2/volt sec)
H170	0.1×10^{17}	3700
N11C	0.45	4500 + 500
N16B	1.0	4500 + 500
SA802	1.85	
SA23	2.7	
A7	7.4	
A804Te	10.0	

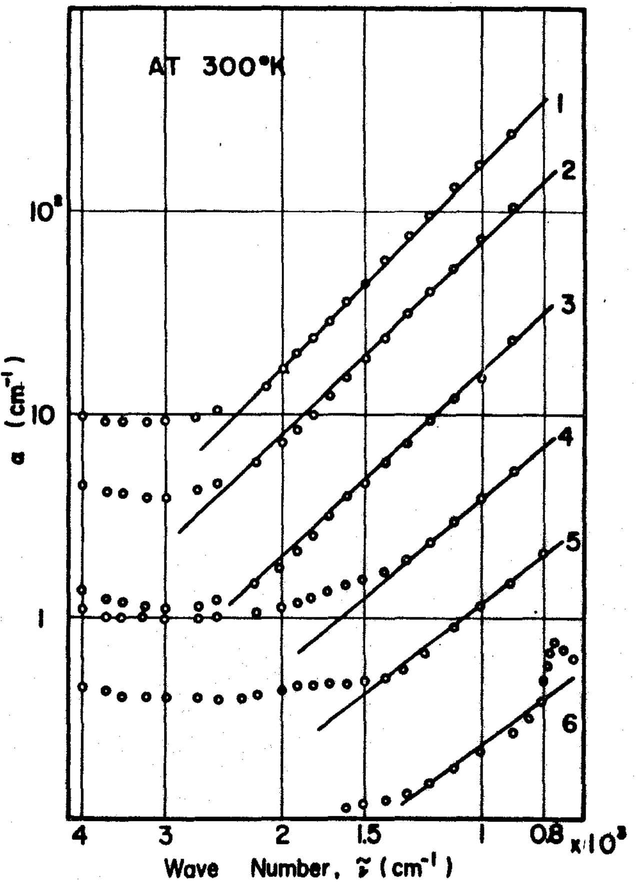

Fig. 24 Free carrier absorption as a function of wave number in n-GaAs, where the symbols of 1 to 6 represent the sample numbers, A804Te, A7, SA23, N16B, N11C and H170, respectively. The solid lines are theoretical ones.

which is characteristic of free carrier absorption. The bands observed in Fig. 24 for $\tilde{\nu} \leq 600$ cm^{-1} are due to absorption by the lattice vibration of which absolute absorption coefficient is lower than 60 cm^{-1}. In a fairly pure sample, relative weak absorptions are observed for $\tilde{\nu} \leq 800$ cm^{-1}, which may be interpreted to be caused by the three phonon processes. The magnitude of the absorption is lower than 6 cm^{-1}. Between 2,000 and 4,000 cm^{-1}, the curve is obtained as a result of the superposition of the normal free-carrier absorption at smaller wave numbers and some additional absorption due to another mechanism.

Thus, the normal free carrier absorption is observed only in the region from 800 to 2,000 cm^{-1}. The wave number dependence of the absorption coefficient is represented using some parameters as shown in Table 3. The free-carrier absorption is proportional to the minus r-th power of wave number, $(\tilde{\nu})^{-r}$. The magnitude of the power is experimentally obtained to be 3.4 for the specimens with high carrier concentration and to be about 2.5 for the fairly pure specimens.

At 450 ^{o}K, the spectral dependence is illustrated in Fig. 25 where the measured points are shown for three samples of widely different carrier concentrations. Due to the increasing absorption for lattice scattering with increasing temperature, this absorption mechanism should prevail at elevated temperatures. Indeed, the experimental results at 450 ^{o}K are consistent with the expected behavior of absorption; that is, the magnitude of the power of wave number decreases to 2.5 and the absolute absorption increases according to a function of phonon density.

At 90 ^{o}K, the dependence of α on $\tilde{\nu}$ is again the same for

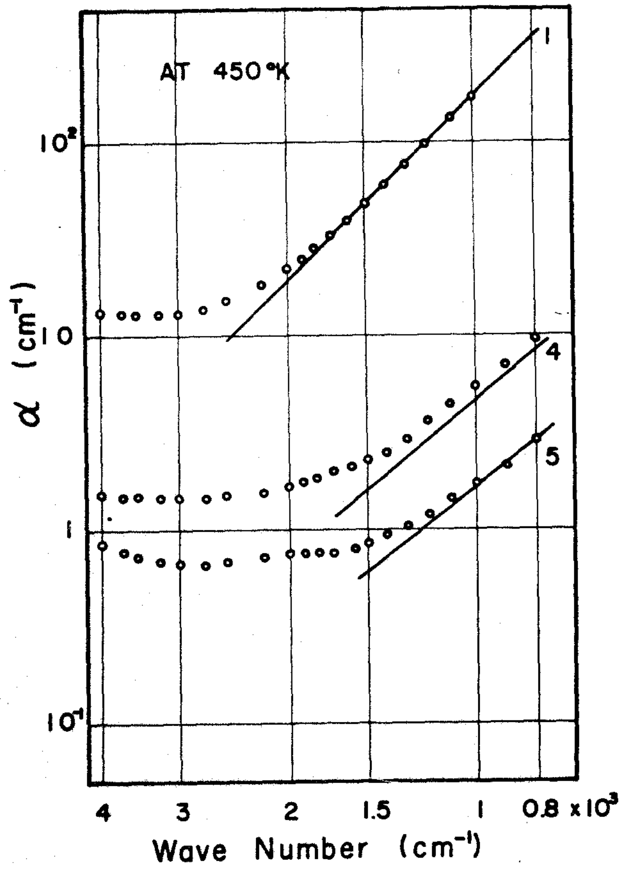

Fig. 25 Free carrier absorption at 450 $^{\mathrm{o}}$K, where the symboles have the same meanings in Fig. 24.

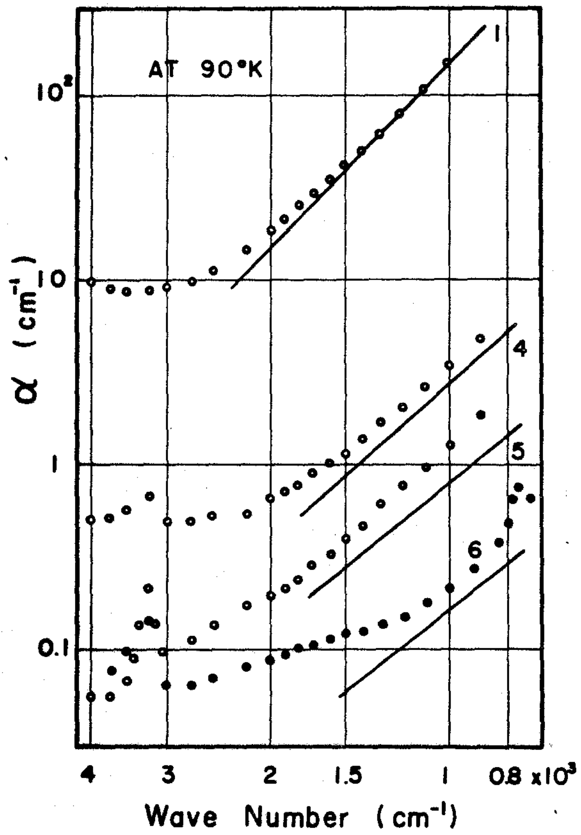

Fig. 26 Free carrier absorption at 90 $^{\mathrm{o}}$K

all samples measured at room temperature as indicated in Fig. 26. However, α decreases more rapidly with $\tilde{\nu}$ than at the room temperature, approximately proportional to $(\tilde{\nu})^{-3.5}$. The absorption for impurity scattering would be expected to be important because of the reduced absorption for lattice scattering. We would then expect the absorption coefficient to vary among the samples depending upon the impurity concentration. The experimental results obtained at 90 °K actually show such variations.

3-3) Results and Discussion

With $n = \sqrt{\epsilon_0}$, the carriers contribute an absorption coefficient that is additive to the absorption coefficient in the absence of carriers. Also we can consider separately free carrier and interband carrier absorption coefficients. It is convenient to express the free carrier absorption in terms of the ratio α/N, where N is the carrier concentration. The ratio is often referred to as the photon capture cross section of carriers.

Perfectly free carriers do not produce absorption. Absorption arises from the fact that there is scattering of carriers in motion. The treatment of the effect of acoustic mode scattering by the method of second-order perturbation, due originally to Fröhlich, was reported by Fan.23),30) For spherical energy bands, the photon capture cross section can be written30)

$$\alpha_{ac}/N = \frac{4\pi}{cn}\,\frac{1}{9\pi^{3/2}}\,\frac{e^3}{m^{*2}}\,\frac{1}{\nu^2}\left(\frac{h\nu}{k_0T}\right)^{1/2}\frac{1}{\mu_a}\,, \qquad (19)$$

where n is the refractive index, m* is the effective mass, $h\nu$ is the photon energy, and μ_a is the mobility corresponding to acoustic-mode scattering.

The effect of ionized impurity scattering can also be treated by the second-order perturbation method, using the Born approximation for the electron interaction with a Coulomb or screened Coulomb center.[23),31)] A preferable approach is to treat the absorption as the inverse process of bremsstrahlung, giving the result[23)]

$$\alpha_{imp}/N = \frac{4\pi}{cn} N_{imp} \frac{8\pi}{3} \left(\frac{Ze^2}{\epsilon}\right)^2 \frac{e^2\hbar^2}{m^*} \frac{1}{(2\pi m^* k_0 T)^{1/2}} \frac{1}{(h\nu)^3} (1-e^{-2X}) e^X K_0(X), \tag{20}$$

in the case of classical distribution of carriers, where K_0 is the modified Bessel function of order zero. N_{imp} is the impurity concentration, and Ze is the charge of an impurity center, and $X = h\nu/2k_0T$. The expression is an approximation valid[32),33),34)] when

$$E_0 \gg E_i$$

where E_0 is the thremal energy of the carriers and E_i is the impurity ionization energy.

The effect of polar mode scattering has been treated by Visvanathan.[35)] For classical distribution of carriers, the expression obtained in the form of an integral can be written

$$\alpha_{op}/N = \frac{4\pi}{cn} \frac{\sqrt{2}}{3} \frac{e^4(\epsilon_\infty^{-1} - \epsilon_0^{-1})}{m^*} \frac{\hbar\omega_\ell}{(h\nu)^{2.5}} \frac{e^{2Z}+1}{e^{2Z}-1} \left(1 + \frac{11}{8X} - \frac{4}{\sqrt{2\pi X}} \cdots\right), \tag{21}$$

under the limiting condition

$$2(X-Z) = (h\nu - \hbar\omega_\ell)/kT \gg 1.$$

The theoretical expression for the photon capture cross section (hereafter is called the cross section), (19), (20) and (21), can be written as

$$\alpha_{ac}/N = (m/m^*)^2 L_{ac}(\tilde{\nu}, T) \, , \tag{22}$$

$$\alpha_{op}/N = (m/m^*)^{1/2} L_{op}(\tilde{\nu}, T) \, , \tag{23}$$

$$\alpha_{imp}/N = N_{imp} (m/m^*)^{3/2} I(\tilde{\nu}, T) , \tag{24}$$

where $L_{ac}(\tilde{\nu}, T)$, $L_{op}(\tilde{\nu}, T)$ and $I(\tilde{\nu}, T)$ are functions of temperature and wavenumber. Fig. 27 shows the theoretical cross sections as a function of wave number at three different temperatures as calculated from equations(22) - (24). The parameter values given in Table 6 were used. The solid curves show α_{op}/N for three temperatures used in the absorption measurements. The dotted curve shows α_{ac}/N at 300 °K as a function of wave number. The factor μ_a is assumed to be 2×10^5 cm^2 Volt^{-1} sec^{-1}. Also the dashed curve is a similar graph for α_{imp}/N. The values calculated for 450 °K and 90 °K fall approximately on a common curve, showing the absorption to be insensitive to the temperature. It is seen that the cross section for both lattice scatterings decreases and has a less steep spectral dependence as the temperature is decreased. The cross section for the absorption due to acoustic phonon is smaller than the other cross sections, and therefore we neglected the contribution from the acoustic phonon-photon interaction.

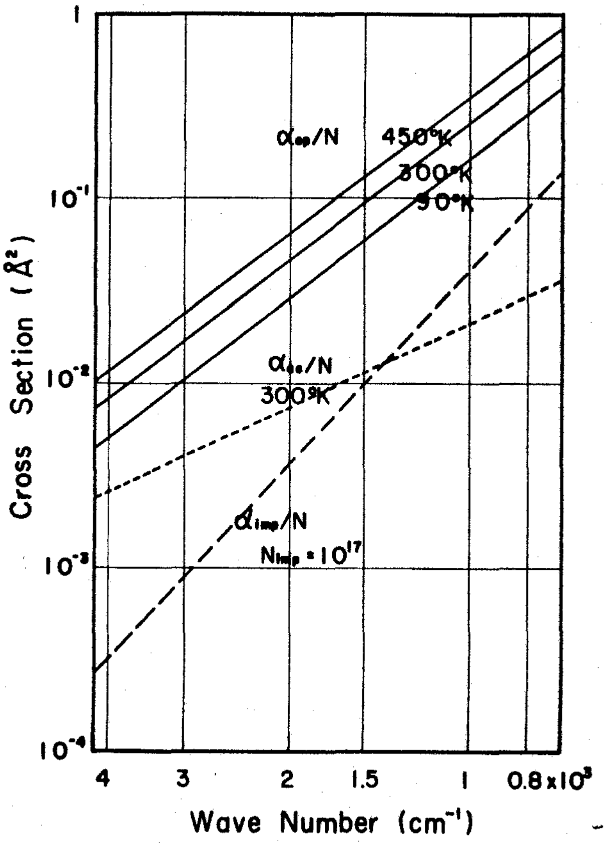

Fig. 27 Theoretical cross section

Table 6 Values for parameters for n-type gallium arsenide

m^*/m	ε_0	ε_∞	$h\omega_1$ (°K)	e^*/e	E_1(eV)
0.078	12.5	10.9	410	0.17	-6.3

ρ (g/cm^3)	V_a (cm^3)	M (g)	s (cm/sec)
5.31	4.52×10^{-23}	5.99×10^{-23}	5.22×10^5

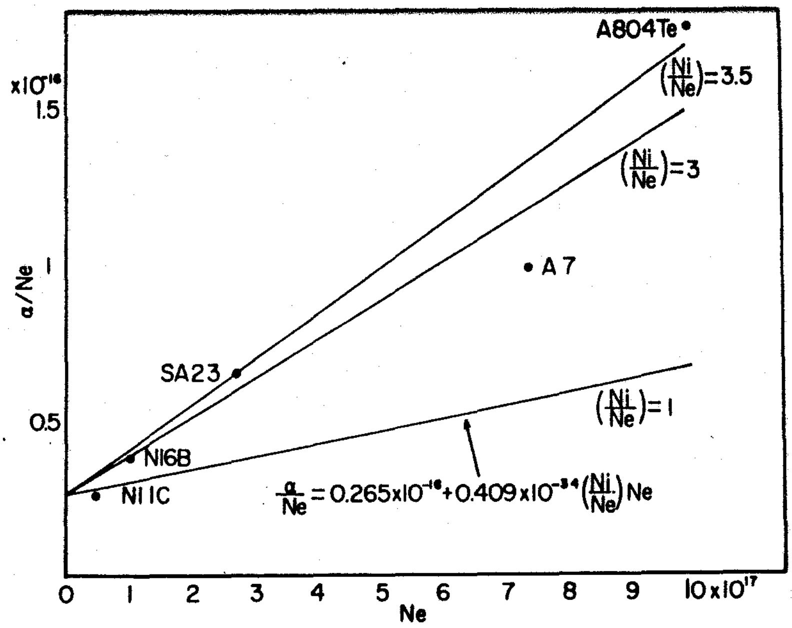

Fig. 28

Fig. 28 is a graph of the experimental values of cross section at $\tilde{\nu} = 10^3$ cm^{-1} as a function of carrier concentration, N_e. The solid curve shows the following relation.

$$\alpha/N_e = (m/m^*)^{1/2} L_{op}(\tilde{\nu}, T) + C(m/m^*)^{3/2} I(\tilde{\nu}, T) N_e \quad (25)$$

The term independent of N_e may be identified with the effect of lattice scattering while the term proportional to N_e should correspond to the effect of impurity scattering, where C is the degree of compensation, (N_{imp}/N_e). The experimental points are largely scattered, this indicates that the plotting as a function of carrier absorption is inadequate. Accordingly, the degree of compensation may be calculated from the equation(25) using the experimental total cross section. The results are shown in the fifth column of Table 7. The values of the degree of compensation indicate a lack of proportionality between α and N_e for different samples.

Table 7 Values of r, C and N_{imp} obtained in the present work

Sample No.	450°K		300°K		90°K		C	N_{imp}
	r_{exp}	r_{cal}	r_{exp}	r_{cal}	r_{exp}	r_{cal}		
H170		2.45	2.01	2.50		2.52	1.0	0.1×10^{17}
N11C	2.52	2.48	2.58	2.53	2.95	2.58	1.0	0.45
N16B	2.52	2.63	2.61	2.72	2.94	2.82	2.75	2.75
SA23		2.90	3.17	3.00		3.13	3.50	9.44
A7		3.04	3.32	3.14		3.25	2.25	16.7
A804Te		3.21	3.36	3.28		3.30	3.36	33.6

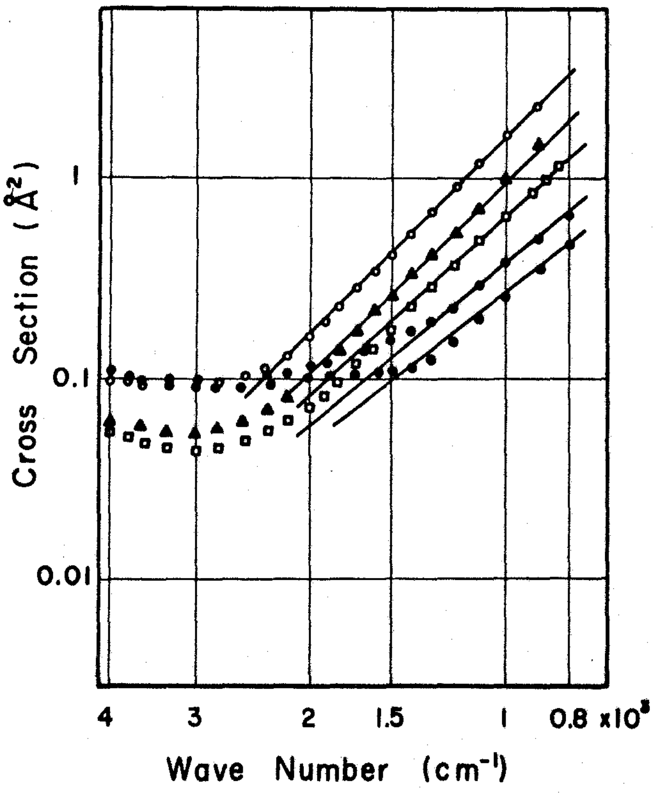

Fig. 29 Theoretical and experimental cross sections at room temperature

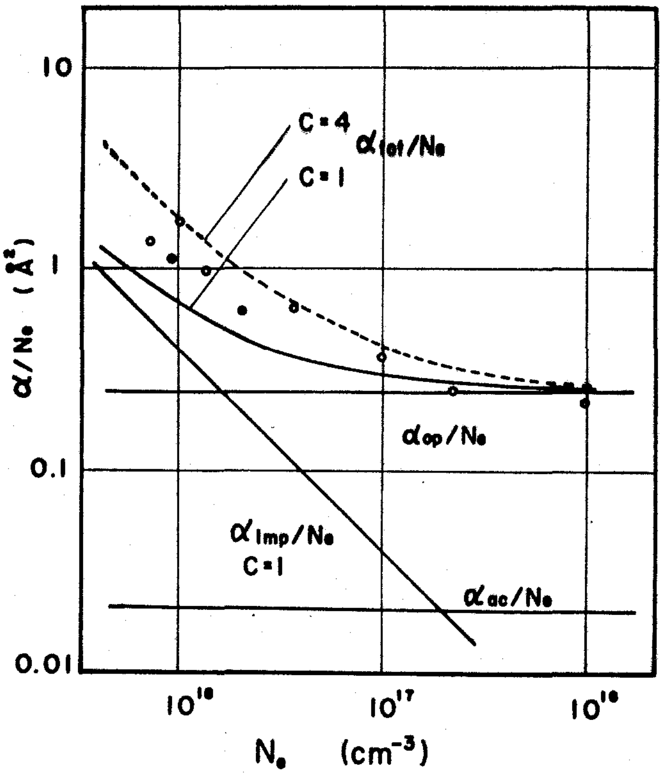

Fig. 30 α/N_e vs. N_e chart at $k = 10^3$ cm^{-1}

Now, the curve fitting of theoretical cross section can be made for the experimental data. Fig. 29 shows the cross sections at room temperature as a function of wave number. It is seen that the experimental curves are in agreements with the expected behavior of theoretical cross section.

3-4) Conclusion

1. The normal free carrier absorptions have been observed only in the region from 800 to 2,000 cm^{-1}. The absorption coefficient is proportional to the minus 3.5th of wave number for the specimens with high carrier concentration and to the minus 2.5th for the fairly pure specimens. The impurity scattering prevails at lower temperature. The contribution of various scattering

mechanisms for the free carrier absorption has been consistent with the theoretical behavior in the wide range of carrier concentration and at three temperatures as shown in Fig. 29.

2. The degree of compensation of impurity has been determined for all specimens using the theoretical equation (25). The values of the degree of compensation determined in the present method are reasonable because of the consideration for the electrical properties. In the present analysis, the effective mass ratio (m^*/m) has been assumed to be 0.078.

3. The α/N_e vs. N_{imp} and α vs N_e chart are obtained at constant wave number as shown in Figs. 29 and 30, where the data investigated by other authors26),27),28) are added in the present result.

4. Lattice absorption and anharmonic crystal interactions.

4-1) Introduction

In recent years there has been considerable activity concerned with the measurements of the infrared properties of crystals. Some of this effort has been directed towards utilizing the measurements of optical absorption by the lattice to gain information concerning the phonon spectrum of the material. Mainly, the infrared methods are an integral part of an over-all study in phonon spectroscopy. The semiconductors, including the III-V compounds, have proved to be very fruitful materials in many of these investigations, and it may be anticipated that optical studies will continue to provide basic information.

$GaAs_{1-x}P_x$ alloys are interesting for several reasons, one being their electronic band structure. GaAs is a direct gap material while GaP has an indirect gap. For the alloy, as x is decreased from unity, the band structure near the gap appears to change continuously, the central $\mathbb{k} = 0$ conduction band minimum falling relative to the other valleys until near $x = 0.4$ the $\mathbb{k} = 0$ minimum becomes the lowest valley changing the material from indirect to direct gap and drastically affecting the threshold for laser action and the luminescence properties.

The other interesting points are their phonon structure and infrared properties. Because these compounds are constituted from the unit cell with two kinds of atoms, the reflectivity shows the well-known residual ray behavior. Also the strong absorption bands due to the two phonon processes are observed in the region from 12 to 25 micron. These two phonon bands in the alloys are classified in two types; one is called the persistence type and the other called the amalgamation one.

Measurements have been made of the lattice absorption spectrum of GaAs, GaP and their alloys. The object of this work is to obtain as much information as possible about the vibrational spectrum of their materials and in part of a general study of the lattice spectrum of III-V semiconductors. Especially the investigation with the availability of the anharmonic force model[37)] is of primary interest in this paper.

4-2) Review of the basic theory

a) Phonon branch and selection rule

Firstly, consider a diatomic lattice in one dimension as given by two species of atoms, A and B, where the distance between nearest neighbours will be denoted by a. Then, assuming nearest neighbour interaction only, the equation of motion can be easily solved, and consequentially the following relation is reduced for the allowed vibrational modes in this system.

$$\omega_{\pm}^{2} = \frac{K}{M_r}\left[1 \pm \sqrt{1 - \frac{4M_r}{M}\sin^2 qa}\right] \qquad (26)$$

where $M = M_A + M_B$, and $M_r = M_A M_B/(M_A + M_B)$

and K is the force constant, and q is the wave vector of a particular mode of vibration.

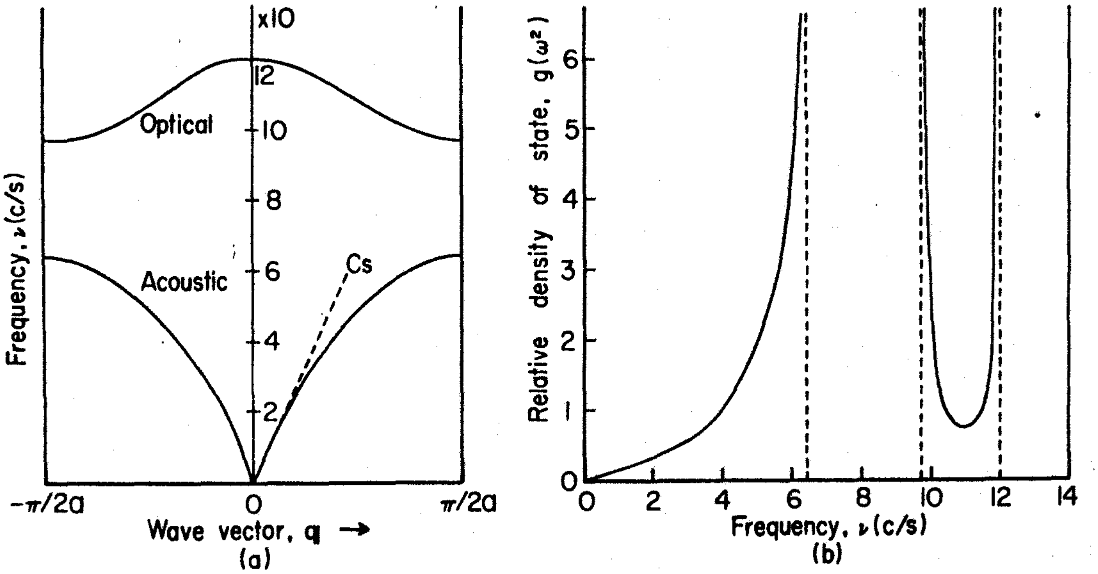

Fig. 31 Vibration frequencies (a) and relative density of states (b) of diatomic chain constituted from Ga and P atoms

Since ω should be positive, each value of ω^2 leads to a single value for ω. Thus in contrast to the monoatomic lattice, there are two angular frequencies ω_+ and ω_- corresponding to a single value of the wave vector q. In a plot of ω versus q (Fig. 31 (a)) this leads totwo branches; the one corresponding to ω_- is called the acoustical branch, the one associated with ω_+ is the optical branch. These two branches will now be discussed on the assumption that $M_A > M_B$. For q = 0 we obtain

$$\omega_+ = [2K/M_r]^{1/2}, \quad \text{and} \quad \omega_- = 0 \qquad \text{for } q = 0$$

From the form of (26) it is observed that the frequency is a periodic function of the wave vector. The first zone thus limits the values of q to the range between $-\pi/2a$ and $+\pi/2a$. For $q = \pm\pi/2a$, the two angular frequencies are evidently

$$\omega_+ = [2K/M_B]^{1/2}, \quad \text{and} \quad \omega_- = [2K/M_A]^{1/2} \qquad \text{for } q = \pm\pi/2a$$

The larger the mass ratio M_A/M_B, the wider the frequency gap between the two branches.

The density of states as a foundation of the square of the frequency is given by

$$g(\omega^2) = \kappa \frac{C_0}{C_+ C_-} \frac{1}{[(1 - \omega^2/\omega_1^2)(\omega^2/\omega_2^2 - 1)(\omega^2/\omega_3^2 - 1)]^{1/2}}, \qquad (27)$$

where $\omega_1 = [2K/M_A]^{1/2}$, $\omega_2 = [2K/M_B]^{1/2}$ and $\omega_3 = [2K/M_r]^{1/2}$.

The result is shown in Fig. 31 (b), where it is found that the density of states diverges to be infinite at the critical points of the frequencies $\omega = \omega_1$, ω_2 and ω_3. These critical points satisfy the condition of $\partial\omega/\partial q = 0$.

The diamond and zinc blende structures have two atoms per primitive cell, and therefore there are six branches in the vibrational spectrum. When the wave vector $q \to 0$, the acoustical modes reduce to rigid translations of the lattice, and hence the frequencies $\omega(q) \to 0$. Also the degeneracy of optical modes between the LO and the TO modes is lifted for the zinc blende crystal. If the longitudinal and transverse optical frequencies near $q = 0$ are ω_ℓ and ω_t, respectively, they are related by the Lyddane-Sachs-Teller expression[38)]

$$\omega_\ell/\omega_t = (\epsilon_0/\epsilon_\infty)^{1/2} \qquad (28)$$

where ϵ_∞ and ϵ_0 are the limiting values of the dielectric constant on the high- and low-frequency sides of the residual-ray band, respectively.

The relation that has been found to be valid for the materials studied here is the Brout sum rule,[39)] which states that the sum of the $\omega_b^2(q_i)$ for all b branches at a given q_i is a constant independent of q_i.

$$\sum_{b=1}^{6} \omega_b^2(q_i) = \frac{1}{\beta}\,\frac{18}{M}\,r_0 \qquad (29)$$

where β the compressibility, r_0 the interatomic distance and M is the reduced mass. This relation was originally derived for an ionic model employing Coulomb attractive forces and nearest-neighbour repulsion. More recently it has been shown[40)] that this relation should also hold for more generalized force models.

It is reasonable to inquire as to the origin of the peaks in the absorption spectrum. The two-phonon absorption is usually written as the product of a matrix element term, which is a function of q. times the density of states of phonons. For two phonon processes, this product must be summed over all states in the two branches. If the matrix element is not a strong function of q, then we might expect the absorption to be large at summation energies where the branches have large numbers of states within a small energy range. The density of states of q space is constant, and hence the number of states in a volume of q space of radius q is proportional to q^3. The states that will be most influential will be near the zone edges unless the dispersion is large in this region. Also the branches tend to become flat near the zone edges, giving rise to strong peaks in a curve of density of states $g(\omega)$ vs. ω . At the zone edge in certain symmetry directions - i.e., [100], [111], and [11/20] - the slope of ω vs. $\mathfrak{q}$ is zero for some branches. At these points of zero slope, which are called critical points and hereafter referred to as the X, L, and W points, respectively, it is anticipated that there will be critical points in the two-phonon densities of states and hence, at the corresponding summation energies, structure in the absorption.

Birman41) has recently deduced the selection rules for electric dipole-allowed two- and three-phonon processes for the diamond and zinc blende structures at the X, L, and W critical points and at the critical point $\mathfrak{q} = 0$. These rules modify the density of states discussion somewhat, then the two-phonon selection rules listed in Table 8 were determined from a space-group analysis for the zinc blende structures. The symbols TO(X), LO(X), etc., represent the frequency of energy of the branch at the indicated point in the zone. Therefore, TO(Γ) and LO(Γ) are what we have previously called ω_t and ω_ℓ. Thus it is found that except 2LO(X) and 2LA(X) in two phonon processes are infrared inactive, all overtones and combinations of two-phonons are infrared active and are active for Raman scattering.

Table 8 Infrared allowed processes in the zinc blende structure

Two-phonon processes
2LO(Γ), LO(Γ)+TO(Γ), 2TO(Γ)
2TO(X), TO(X)+LO(X), TO(X)+LA(X), TO(X)+TA(X)
LO(X)+LA(X), LO(X)+TA(X)
LA(X)+TA(X)
2TA(X)
2TO(L), TO(L)+LO(L), TO(L)+LA(L), TO(L)+TA(L)
2LO(L), LO(L)+LA(L), LO(L)+TA(L)
2LA(L), LA(L)+TA(L)
2TA(L)

b) Phonon-photon interaction

As discussed above, lattice absorption is a process in which there is absorption of energy from the radiation field by the lattice. If two phonons are involved the net probability of photon absorption is proportional to

$$[1 + n(q_1)][1 + n(q_2)] - n(q_1)n(q_2) ,$$

or

$$[1 + n(q_1)]n(q_2) - n(q_1)[1 + n(q_2)] , \qquad (30)$$

where $$n(q_i) = [\exp(\hbar\omega(q_i)/k_0T) - 1]^{-1}.$$

In addition to the above factors, the absorption will be proportional to a matrix element expressing the transition probability. If this term is assumed to be nearly temperature independent, then the dependence of the absorption of temperature will be controlled by the n(q) terms. As will be seen, this assumption appears to be in reasonably good agreement with experiment.

Table 9 Conservation law and temperature dependence

Energy dependence	Wave vector dependence	Temperature dependence
Single phonon interactions		
$\hbar\omega_1 = h\nu$	$q_1 = 0$	$n(q_1) = 0$
Two phonon interactions		
$\hbar\omega_1 + \hbar\omega_2 = h\nu$	$q_1 + q_2 = 0$	$(1 + n(q_1))(1 + n(q_2)) - n(q_1)\,n(q_2)$
$\hbar\omega_1 + \hbar\omega_2 = h$	$q_1 - q_2 = 0$	$(1 + n(q_1))\,n(q_2) - n(q_1)(1 + n(q_2))$
Three phonon interactions		
$\hbar\omega_1 + \hbar\omega_2 + \hbar\omega_3 = h\nu$	$q_1 + q_2 + q_3 = 0, \pm K$	$(1 + n(q_1))(1 + n(q_2))(1 + n(q_3)) - n(q_1)\,n(q_2)\,n(q_3)$
$\hbar\omega_1 + \hbar\omega_2 - \hbar\omega_3 = h\nu$	$q_1 + q_2 - q_3 = 0, \pm K$	$(1 + n(q_1))(1 + n(q_2))\,n(q_3) - n(q_2)\,n(q_2)(1 + n(q_3))$
$\hbar\omega_1 - \hbar\omega_2 - \hbar\omega_3 = h\nu$	$q_1 - q_2 - q_3 = 0, \pm K$	$(1 + n(q_1))\,n(q_2)\,n(q_3) - n(q_1)(1 + n(q_2))(1 + n(q_3))$

where $h\nu$ = photon energy; $\hbar\omega_1$, $\hbar\omega_2$, $\hbar\omega_3$ = phonon energies; q_1, q_2, q_3 = phonon wave vectors; K = reciprocal lattice vector; $n(q_i) = (\exp(\hbar\omega_i/kT) - 1)^{-1}$

Regardless of the coupling mechanism between the radiation field and the phonons, the absorption process is subject to the conservation laws of energy and wave vector. Therefore, if the photon has energy hν and wave vector k, then

$$h\nu = \sum_i (\pm 1)\hbar\omega(q_i) , \tag{31}$$

and $$\mathbb{K} = \sum_i (\pm) q_i + A\mathbb{K} , \tag{32}$$

where $\mathbb{K}$ is a reciprocal lattice vector, and A is a positive or negative integer or zero. If n = 1 or 2, A = 0; if n = 3, A = 1 or 0. The plus signs are used for phonon emission and the minus signs for absorption. These conditions for various phonon processes are concretely shown in Table 9.

For III-V compounds with mixed-covalent character, the part of Hamiltonian which is first order in the interaction of the crystal with the electromagnetic field is

$$\mathcal{H}_{phonon\text{-}photon} = \sum_{\sigma} (e_\sigma / m_\sigma c) \mathbb{A}(\mathbb{r}_\sigma) \mathbb{p}(\mathbb{r}_\sigma) \ . \qquad (33)$$

Where e_σ an effective charge so defined that the electric moment produced in the crystal by displacement of an ion is $e_\sigma \mathbb{u}(\mathbb{r}_\sigma)$, m_σ the mass of atom of type σ , c the light velocity, $A(\mathbb{r}_\sigma)$ the vector potential and $\mathbb{p}(\mathbb{r}_\sigma)$ is the momentum conjugate to the displacements of atoms.

Firstly consider the absorption due to one phonon process. The frequency dependence of the optical constants may be explained simply on the basis of the classical treatment which considers the solid as an assembly of oscillators which are set in forced vibration by the radiation. The results are

$$Re\, \epsilon^* = n^2 - k^2 = \epsilon_0 + \sum_i \frac{f_i e_i^2}{m_i} \frac{\omega_i^2 - \omega^2}{(\omega_i^2-\omega^2)^2 + (\gamma\omega)^2} , \qquad (34)$$

$$Im\, \epsilon^* = 2nk = \sum_i \frac{f_i e_i^2}{m_i} \frac{\gamma\omega}{(\omega_i^2-\omega^2)^2 + (\gamma\omega)^2} \qquad (35)$$

where ϵ^* the complex dielectric constant, f_i the oscillator strength, e_i the effective change of i-th atom, γ the damping factor, and ω_i is the resonant frequency. Then the absorption coefficient which equals to $2nk\omega/c$ is given by

$$\alpha = \sum_i \frac{f_i e_i^2}{m_i c} \frac{\gamma\omega^2}{(\omega_i^2-\omega^2)^2 + (\gamma\omega)^2} \qquad (36)$$

The more detailed quantum-mechanical treatment[42),43)] of dispersion gives results very similar in form to equation(34), and (35). This theory shows that the interaction of the field and absorbing atom may be represented by a set of linear oscillators each of which has a resonance frequency corresponding to an allowed transition. The magnitude of the contribution of each oscillator to the optical constants is determined by the oscillator strength f_i of each transition. For a material whose optical properties are represented by a single oscillator, the parameters in the above equations may be determined as follows: (a) ω_0 is ω at maximum $2nk\omega$, (b) $1/2\gamma$ is $(\omega_0 - \omega)/(1+\omega_0/\omega)$ at $2nk\omega = 1/2(2nk\omega)_{max}$, (c) $Ne^2/m\epsilon_0 = \gamma(2nk\omega)_{max}$ and (d) when $\omega \to 0$, $n_0^2 - k^2 - \epsilon_0 = f e_0^2/(m_0\omega_0^2)$. For III-V compounds with mixed ionic-covalent character the absorption constant becomes so high in the lattice absorption band that the reflectivity approaches 100 per cent. This selective reflection may be used to isolate narrow bands of long wavelength radiation -- the so-called "Reststrahlen bands", or "residual ray".

However the more important bands from our point of view are those that arise from the interaction of a photon with a pair of phonons. Two mechanisms are available for this type of coupling; one through anharmonic forces and the other through second order electric moments.

(1) The anharmonic mechanisms.

In the zinc blende crystals the mechanism of interaction for the phonons with the radiation field can be the anharmonic part of the crystal potential. The role of this mechanism in gallium phosphide has been considered in detail by Kleinman.37) The interaction is via the dipole moment of the fundamental resonance -- i.e., the transverse optical mode near $q = 0$. The absorption is a process in which a photon is absorbed and two phonons are created with fundamental as an intermediate state.

(2) Second-order electric moment mechanism

It has been pointed out by Born,44) Burnstein et al.45), Lax and Burnstein46) that combination bands can also be caused by second order and higher order terms in the electric dipole moment of the crystal as a function of the ionic displacements. Because of symmetry the fundamental resonance in the group IV semiconductors has no dipole moment and is infrared inactive. Therefore, the anharmonic mechanism will be inoperative in these cases. They have pointed out a mechanism that explains multiphonon absorption in these materials and may also have some importance in the zinc blende crystals. In this case the phonons interact directly with the radiation field through terms in the electric moment of second order in the atomic displacement.

In either case, energy and wave vector must be conserved between the initial photon and the two resulting phonons. Furthermore, both mechanisms predict the same temperature dependence for the absorption, and essentially the same shape for the absorption, which is determined primarily by the frequency distribution of the lattice vibrations. The equations for the conservation of energy and wave vector along with the expressions for the temperature dependence of the lattice bands are set out in Table 9. The temperature dependence is given by Bose-Einstein statistics, and is shown as the difference between the forward process in which a photon is absorbed and the reverse process in which the photon is emitted.

c) Localized modes of vibration

The presence of a point defect in an otherwise perfect crystal destroys the translational symmetry of the lattice and at the same time modifies its normal modes of vibration. There are two possibilities: (1) all the modified modes lie within the bands of perfect lattice frequencies (band modes) and any disturbance of the system involving the defect can be transmitted throughout the crystal, or (2) certain new modes occur at frequencies greater than the maximum perfect lattice (localized modes) or between bands of allowed frequencies (gap modes); disturbances at either of these two latter frequencies cannot be propagated and are highly localized spatially around the defect. Localized modes of vibration occur when the defect consists of an impurity atom which is somewhat lighter than the atoms of the host crystal, provided the force constants between this atom and its neighbours have a similar strength to those between pairs of host crystal atoms. In a cubic crystal47),48) (monoatomic with $s = 1$, or diamond structure with $s = 2$) where each atom in the unit cell has the same mass, the eigenfrequency associated with the defect becomes:

$$1 + \frac{\eta\,\omega^2}{3SN}\sum_{q,j}\frac{1}{\omega_j^2(q) - \omega^2} = 0 \qquad (37)$$

where q, the wavevector for the unperturbed lattice, has N values, j specifies the 3s branches and the mass defect is defined by $\eta = (M - M')/M$. As discussed above, it is shown that the presence in a crystal of a light impurity atom occupying a site of cubic symmetry leads to the formation of a localized mode of vibration which is triply degenerate because of the equivalence of displacements along the x, y, and z axes respectively. The energy levels of localized vibration can be firstly calculated by the approximation of the harmonic isotropic oscillator. The anharmonic terms, which must also reflect the local site symmetry, lead to energy shifts of the various states of a harmonic oscillator and admixing of wave functions; as a consequence of the latter effect, transitions are allowed between the ground state and various higher excited states. Here results for third harmonic transitions are discussed for the cubic symmetries.

A harmonic oscillator consists of a particle bound to the origin by a force whose component along the x, y, and z axes equals to K, where K is the force constant in the three dimensions and x, y, and z are the components of the displacement along the three axes. The potential energy is thus

$$V = \tfrac{1}{2} K^2 (x^2 + y^2 + z^2) . \qquad (38)$$

The expression in terms of the classical frequency ω becomes

$$V = \tfrac{1}{2} m \omega_0^2 (x^2 + y^2 + z^2) , \qquad (39)$$

since $K = m\omega_0^2$.

The three dimensional Hamiltonian assumes the form

$$\mathcal{H} = -\frac{\hbar^2}{2m}\nabla^2 + \frac{1}{2} m\omega_0^2 (x^2+y^2+z^2), \qquad (40)$$

and the complete wave function by the expression

$$\psi_{n_x n_y n_z}(x,y,z) = N_{n_x n_y n_z}\, e^{-\frac{1}{2}(\alpha_x x^2+\alpha_y y^2+\alpha_z z^2)} H_{n_x}(\sqrt{\alpha_x}\,x) H_{n_y}(\sqrt{\alpha_y}\,y) H_{n_z}(\sqrt{\alpha_z}\,z). \qquad (41)$$

The normalizing factor has the value

$$N_{n_x n_y n_z} = \left[\frac{(\alpha_x \alpha_y \alpha_z)^{1/2}}{\pi^{3/2}\, 2^{n_x+n_y+n_z}\, n_x!\, n_y!\, n_z!}\right]^{1/2}. \qquad (42)$$

The total energy is thus given by the equation

$$E = (n_x + n_y + n_z + 3/2)\hbar\omega_0 = (n + 3/2)\hbar\omega_0, \qquad (43)$$

and $n = n_x + n_y + n_z$ may be called the total quantum number, where $H_{n_i}(\sqrt{\alpha_i}\,x)$ is the Hermite polynomials and α equals to $2\pi m\omega_0/h$. Since the energy for this system depends only on the sum of the quantum numbers, all the energy levels for the isotropic oscillator, expect lowest one, are degenerate, with the quantum weight

$$(n+1)(n+2)/2 \qquad (44)$$

Figure 32 shows the first few energy levels, together with their quantum weights and quantum numbers.

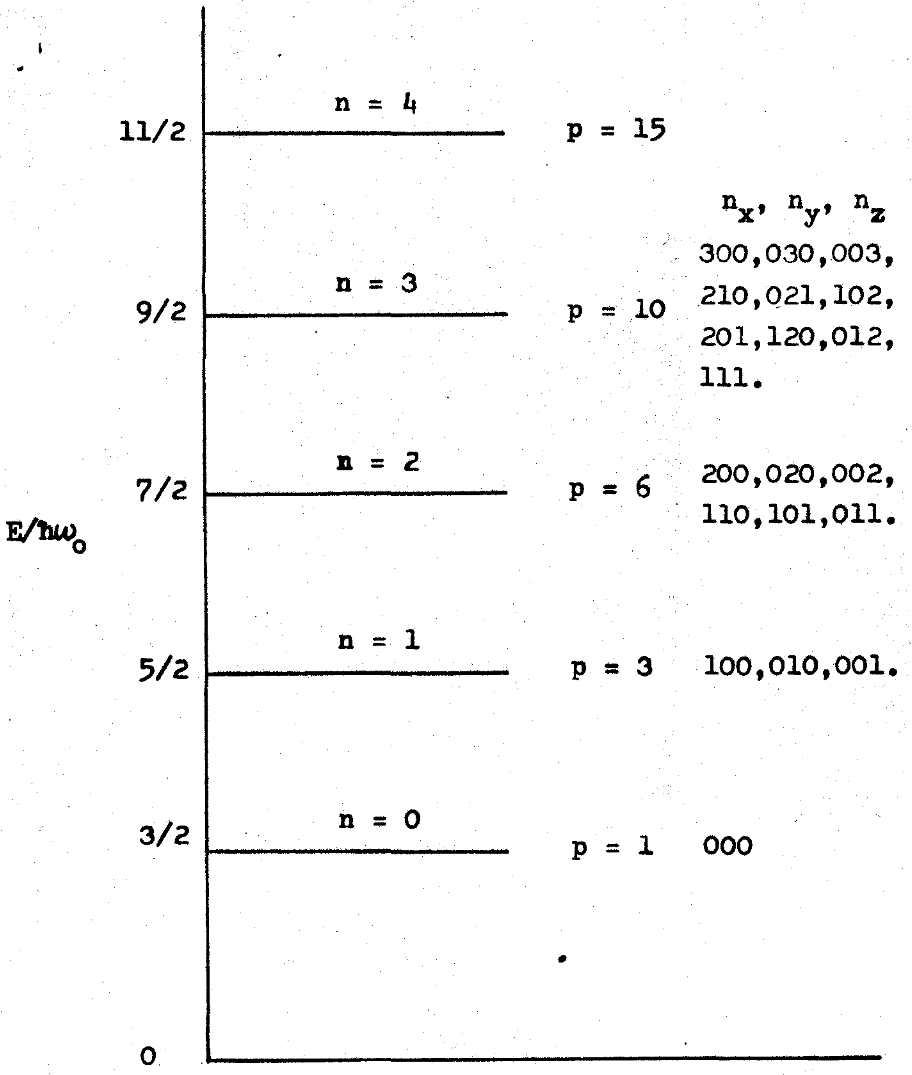

Fig. 32 Energy levels, degrees of degeneracy, and quantum numbers for the three dimensional isotropic harmonic oscillator

For a site of tetrahedral symmetry such that of the P impurity with 4 nearest Ga neighbours, the potential to terms of fourth order in displacement is

$$V = A(x^2+y^2+z^2) + Bxyz + C_1(x^4+y^4+z^4) + C_2(x^2y^2+y^2z^2+z^2x^2). \quad (45)$$

When B = 0 and $C_1 = C_2$, V is the potential for a spherical harmonic oscillator (R_3 symmetry). Also, being $C_1 \neq C_2$, and

B = 0 or B ≠ 0, V corresponds to the potential for the cubic oscillator with O_h or T_d symmetry, respectively. If B, C_1 and C_2 are small, we may treat these terms as perturbations, writing

$$\mathcal{H}' = Bxyz + C_1(x^4+y^4+z^4)+C_2(x^2y^2+y^2z^2+z^2x^2) \qquad (46)$$

we need then to evaluate the integrals, as to n = 0,

$$\begin{aligned} E_0^{(1)} &= (\psi_0|\mathcal{H}'|\psi_0) \qquad (47) \\ &= \int \psi_0^* Bxyz\,\psi_0\, d\tau + \int \psi_0^* C_1(x^4+y^4+z^4)\psi_0\, d\tau + \int \psi_0^* C_2(x^2y^2+y^2z^2+z^2x^2)\psi_0\, d\tau \end{aligned}$$

Since xyz is an odd function and ψ_0 an even function, the first of these integrals is zero, so that the first-order perturbation due to Bxyz is zero. To calculate the second and third integrals, on substituting for ψ_0 from above equation, we obtain the integral

$$\begin{aligned} I_B &= \int \psi_0^* Bxyz\,\psi_0\, d\tau = 0. \\ I_{C_1} &= \int \psi_0^* C_1(x^4+y^4+z^4)\psi_0\, d\tau = \frac{9}{4}\frac{C_1}{\alpha^4}, \\ I_{C_2} &= \int \psi_0^* C_2(x^2y^2+y^2z^2+z^2x^2)\psi_0\, d\tau = \frac{3}{4}\frac{C_2}{\alpha^4}. \end{aligned}$$

Thus the first-order perturbation energy for this system is therefore

$$E_0^{(1)} = \frac{9}{4}\frac{C_1\hbar^2}{m^2\omega_0^2} + \frac{3}{4}\frac{C_2\hbar^2}{m^2\omega_0^2}.$$

so that the total energy becomes

$$E_0 = E_0^{(0)} + E_0^{(1)} = \frac{3}{2}\hbar\omega + \frac{3\hbar^2}{4m^2\omega_0^2}(3C_1 + C_2). \qquad (48)$$

For the higher energy state in which n is the integer larger than zero, we need to use the treatment for degenerate systems. When n = 1, the three degenerate wave functions correspond to the states of n_x, n_y, n_z=100, 010 and 001. The result for the first order perturbed system shows that the degeneracy is unremoved and its perturbed energy is given by

$$E_1 = E_1^{(0)} + E_1^{(1)} = \frac{5}{2}\hbar\omega + \frac{7\hbar^2}{4m^2\omega_0^2}(3C_1 + C_2) \qquad (49)$$

Similarly, when n=2, the degree of degeneracy for the unperturbed system is six and their six linearly independent wave functions are ψ_{110}, ψ_{011}, ψ_{101}, ψ_{200}, ψ_{020} and ψ_{002}. Then the secular equation has the form

$$\begin{vmatrix} H_{11}-E_2^{(1)} & 0 & 0 & 0 & 0 & 0 \\ 0 & H_{22}-E_2^{(1)} & 0 & 0 & 0 & 0 \\ 0 & 0 & H_{33}-E_2^{(1)} & 0 & 0 & 0 \\ 0 & 0 & 0 & H_{44}-E_2^{(1)} & 0 & 0 \\ 0 & 0 & 0 & 0 & H_{55}-E_2^{(1)} & 0 \\ 0 & 0 & 0 & 0 & 0 & H_{66}-E_2^{(1)} \end{vmatrix} = 0 , \qquad (50)$$

where $$H_{11} = H_{22} = H_{33} = \frac{3}{4\alpha^2}(11C_1 + 5C_2),$$

and $$H_{44} = H_{55} = H_{66} = \frac{1}{4\alpha^2}(45C_1 + 11C_2).$$

The degenerate state with the quantum number n=2 is split into two triplets by the first order perturbation. The first state is the three-hold degenerate one represented by the zero-order wave function $1/\sqrt{3}(\psi_{110}+\psi_{101}+\psi_{011})$ and its energy is

$$E_z = E_z^{(0)} + E_z^{(1)} = \frac{7}{2}\hbar\omega + \frac{3\hbar^2}{4m^2\omega_0^2}(11C_1 + 5C_2). \qquad (51)$$

The other state is the three-hold degenerate one corresponding to $1/\sqrt{3}(\psi_{200}+\psi_{020}+\psi_{002})$ and its energy is

$$E_z = E_z^{(0)} + E_z^{(1)} = \frac{7}{2}\hbar\omega + \frac{\hbar^2}{4m^2\omega_0^2}(45C_1 + 11C_2) \qquad (52)$$

Thus the perturbed potential Bxyz does not influenced to the system in the first order perturbation theory and the second excited state is split by the perturbation in two levels. The complete representation for an anharmonic local oscillator with T_d(or O_h)symmetry[49),50)] is given in Fig. 33.

In the region with the lower impurity concentration where the interaction among impurities is negligible small, the above mentioned treatment is thought to be valid to consider the locarized vibration on an impurity.

However, at large impurity concentrations, the interaction among impurities should be considered to be sufficiently large for the local mode model for isolated impurities to be difficult to apply.

The investigation of the optical properties of mixed crystals has attracted many workers in the past several years. The most remarkable fact observed in optical measurements is that there exist two types of mixed crystal systems. To the first type, which will be called the persistence type, belong phonons in

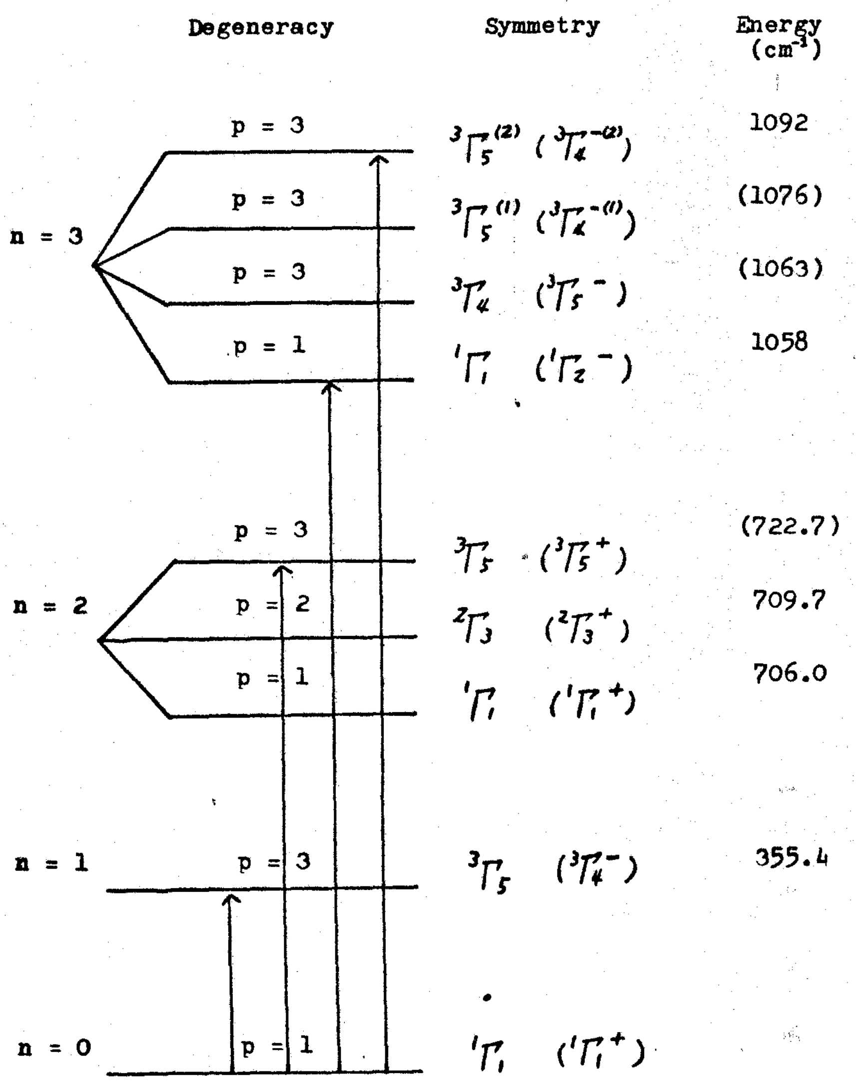

Fig. 33 Energy levels, degrees of degeneracy, and symmetries for the three dimensional anharmonic local oscillator with T_d (or O_h) symmetry, where energies show the values for the localized vibrations of P in GaAs at 80 °K; energies in branckets are calculated,49) and vertical arrows show the allowed electric dipole transitions.

halogen-substituted alkali halides, e.g., KBr-KCl.51) In this case, two phonon peaks which are due to the KBr-like vibration and KCl-like one respectively are observed. Their peak positions remain almost unchanged against the change in composition. Thus although the mixed crystal itself is homogeneous, two peaks corresponding to the consistuent substances persist.

To the second, which will be called the amalgamation type, belong a number of systems; phonons in alkali-substituted alkali halides,52) and interband transitions in alloys of semiconductors, say in Ge-Si. In these cases, only one structure is observed in the spectra. It shifts almost linearly as a function of the concentration between the absorptions of the two pure substances, with downward bending in some cases. It looks as though the two substance were completely amalgamated to yield another new crystal with perfect periodicity. The mixed crystal can then virtually be regarded as a perfect crystal.

Table 10 Classification of various alloys by a parameter r

System	r	type
KCl-NaCl	0.635	amalgamation
GaAs-GaSb	0.363	"
InAs-InSb	0.596	
GaAs-GaP	1.414	persistence
InAs-InP29)	2.170	"
GaSb-GaP	1.684	
InSb-InP	4.651	

The classification for the above two types is given in Table 10, where the semiempirical parameter r is defined by $r=|M_1^{-1}-M_2^{-1}|/M_A^{-1}$ in AX_1-AX_2 binary systems. The binary systems with r larger than unity belong to the persistence type. The quasi-binary compound of GaAs-GaP is this typical case. The other ones with r smaller than unity belong to the amalgamation type.

4-3) Experimental results and discussion

Specimens of GaAs-GaP alloys for the present work were prepared by the two temperature method. Ploycrystalline ingots were grown from melts with various compositions. A slice of specimen was cut from the top portion of the ingot, where composition was found to be fairly uniform. Cr doping in the melt was used for all ingots to have no influence for the free carrier absorption. The homogeneity of specimens were tested by a powder X-ray diffractometer. The alloy compositions of the samples used in the infrared measurement are given in Table 11.

Table 11 Alloy compositions used in the present work

Sample Number	GaAs	A16P	A17P	SA6PA
Alloy Composition	0	0.03	0.06	0.10

Sample Number	SA6PO	RF4	GaP	
Alloy Composition	0.20	0.70	1.0	

Infrared reflectivity spectra for unpolarized light at normal incidence have been measured over the frequency range

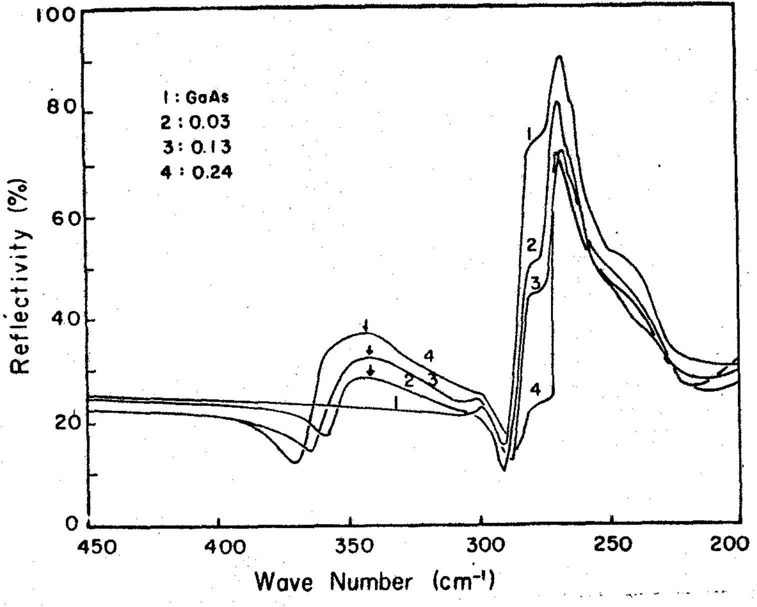

Fig. 34 Reststrahlen bands in $GaAs_{1-x}P_x$ alloys

from 200 to 5,000 cm^{-1} by means of a conventional spectrometer. The results are shown in Fig. 34 and Table 2. Also the reflectance for GaAs and GaP is taken from the table of optical constants by Serphin and Bennett17) as shown in Table 2, where the values for GaAs measured in the present work are in good agreement with their value. The reflectance for the alloy of GaAs-GaP is determined by the interpolation from the values of GaAs and GaP, assuming the linear relation of the dielectric constant.53) The difference in values is not large, for example, at 2,500 cm^{-1} the refractive index of GaAs is 3.30 and that of GaP is 2.95, and so this interpolation does not introduce much error. The major feature of these data is that two reflectivity maxima were observed to occur in the $GaAs_{1-x}P_x$ alloys: one closes to the reststrahlen band of pure GaP,54) and the other closes to that of pure GaAs. The values of these two resonant frequencies in the GaAs-rich side alloys are given in Table 12. As the mole fraction of P decreases, the GaP band shifts slightly fowards smaller wave number and decreases in strength. The shift with composition of the GaAs-like band is considerably smaller. In addition, the strength decreases much more rapidly with decreasing concentration.

Table 12 Measured reststrahlen energies and maximum reflectivities of $GaAs_{1-x}P_x$ alloys

	GaAs-like		GaP-like		Sum of ω_{TO}
Composition (%GaP)	ω_{TO} (cm^{-1})	R arb. unit	ω_{TO} (cm^{-1})	R arb. unit	(cm^{-1})
0	-	-	268	0.90	-
0.043	342	0.28	269	0.81	611
0.13	344.5	0.32	268	0.73	612.5
0.24	346	0.37	269	0.71	615

Infrared transmission measurements have been made in the range from 400 to 4,000 cm^{-1}. The data were obtained for three temperatures of 90, 297 and 423 $^{\circ}K$. Absorption spectra of GaAs, GaP and $GaAs_{1-x}P_x$ were obtained and are given in Figs. 35 to 37.

The data for pure GaAs and GaP are in good agreement with the results of Cochran et al.[55)] on GaAs and Kleinman and Spitzer[54)] on GaP respectively. These authors have given phonon-assignment

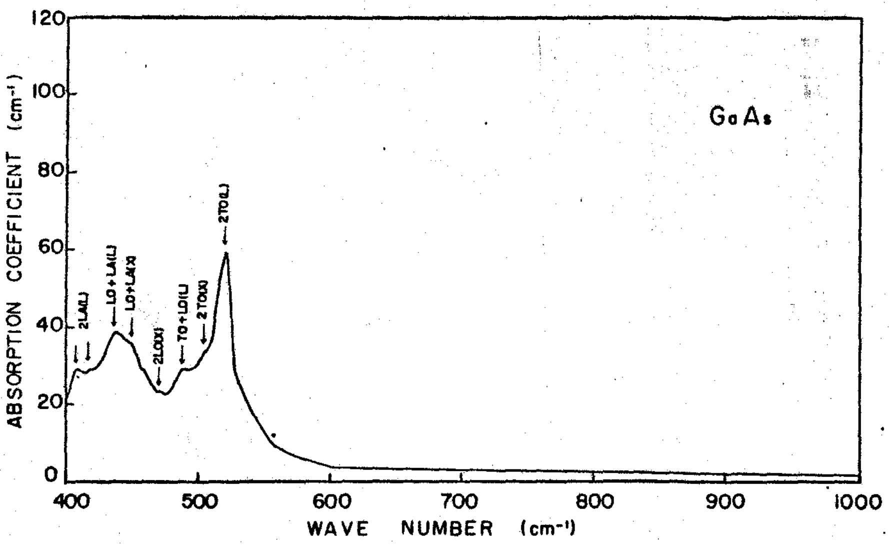

Fig. 35a Lattice absorption vs. wave number from 400 to 1,000 cm^{-1} in GaAs.

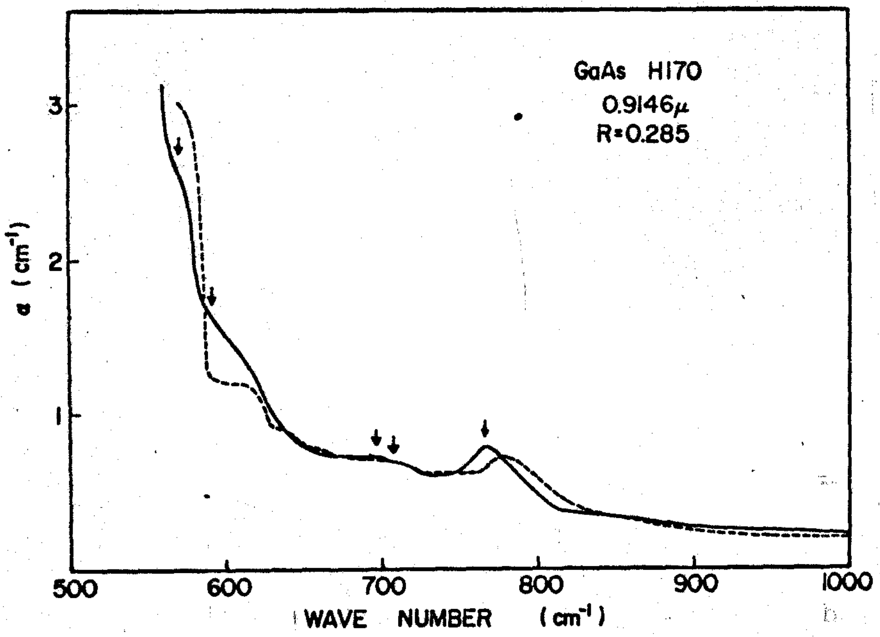

Fig. 35b Lattice absorption vs. wave number from 500 to 1,000 cm^{-1} in GaAs.

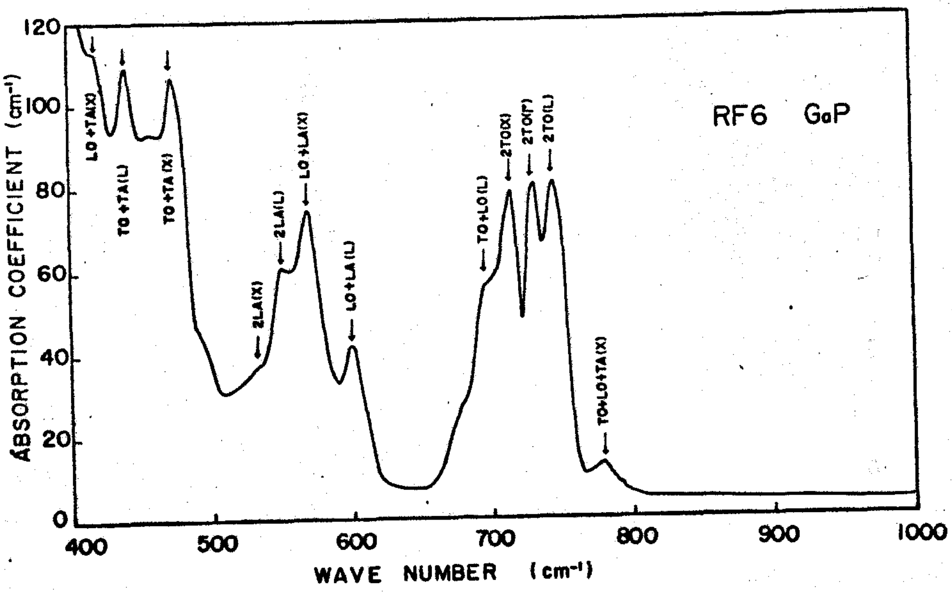

Fig. 36a Lattice absorption vs. wave number from 400 to 1,000 cm^{-1} in GaP.

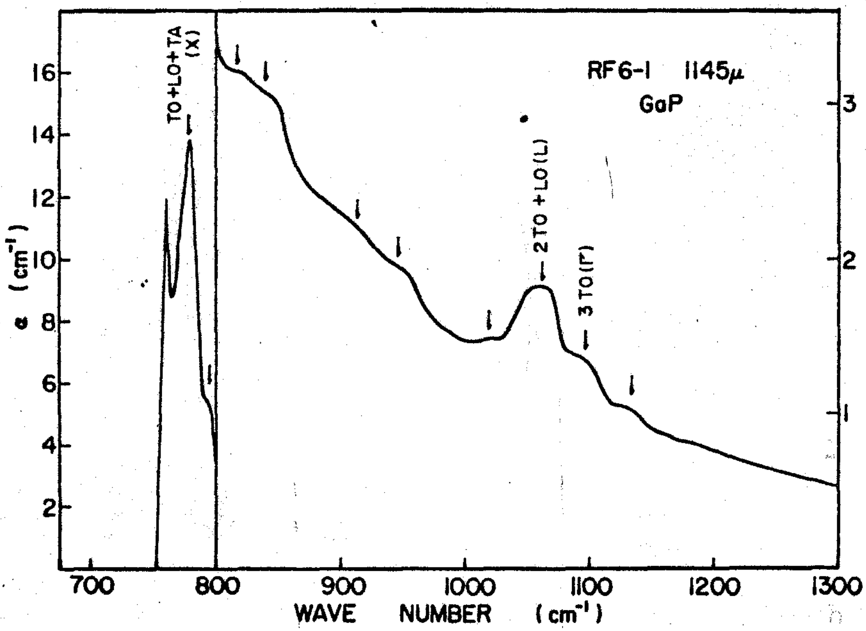

Fig. 36b Lattice absorption vs. wave number from 700 to 1,300 cm^{-1} in GaP.

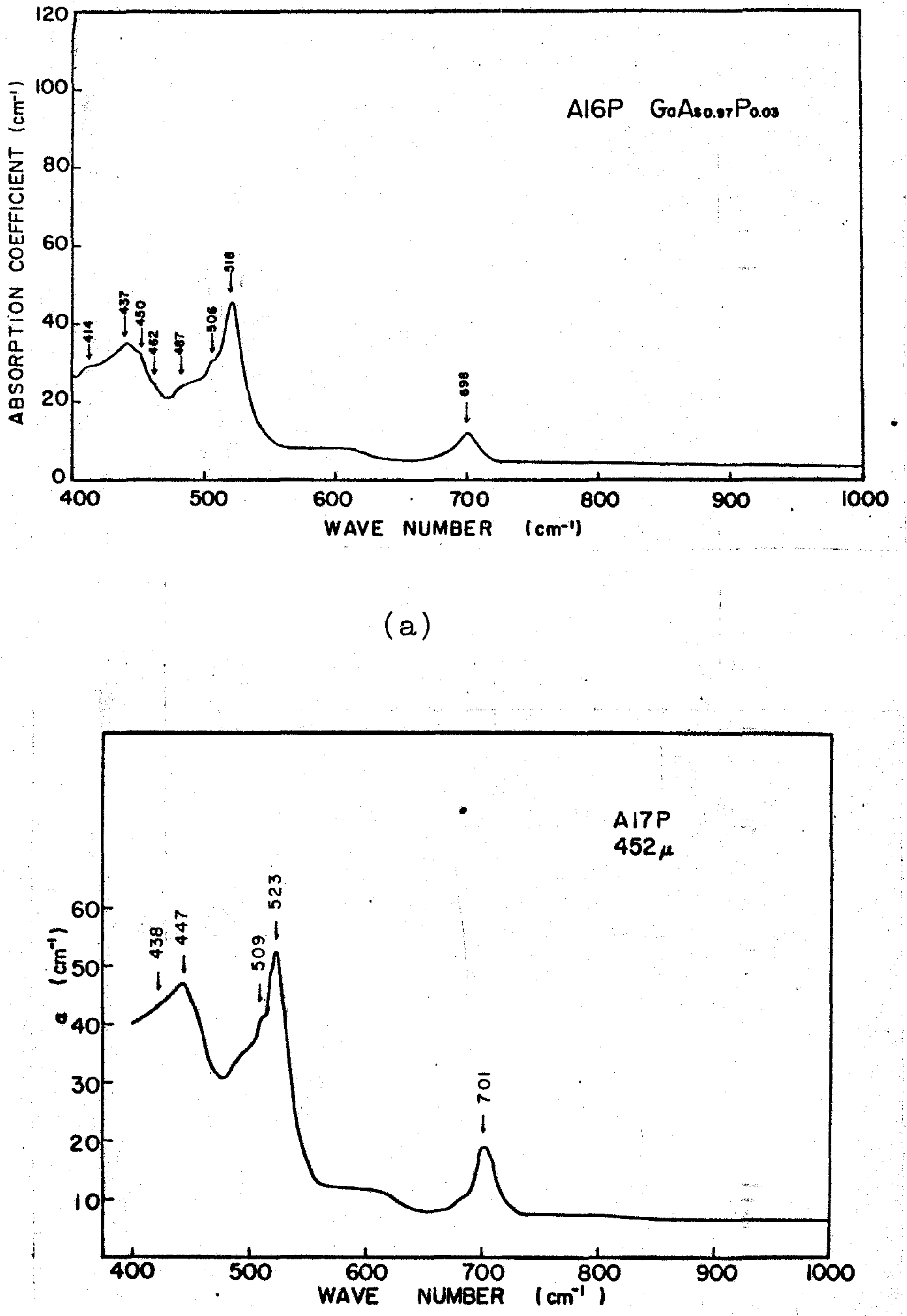

(a)

(b)

Fig. 37 Lattice absorption vs. wave number from 400 to 1,000 cm^{-1} in $GaAs_{1-x}P_x$ alloy.

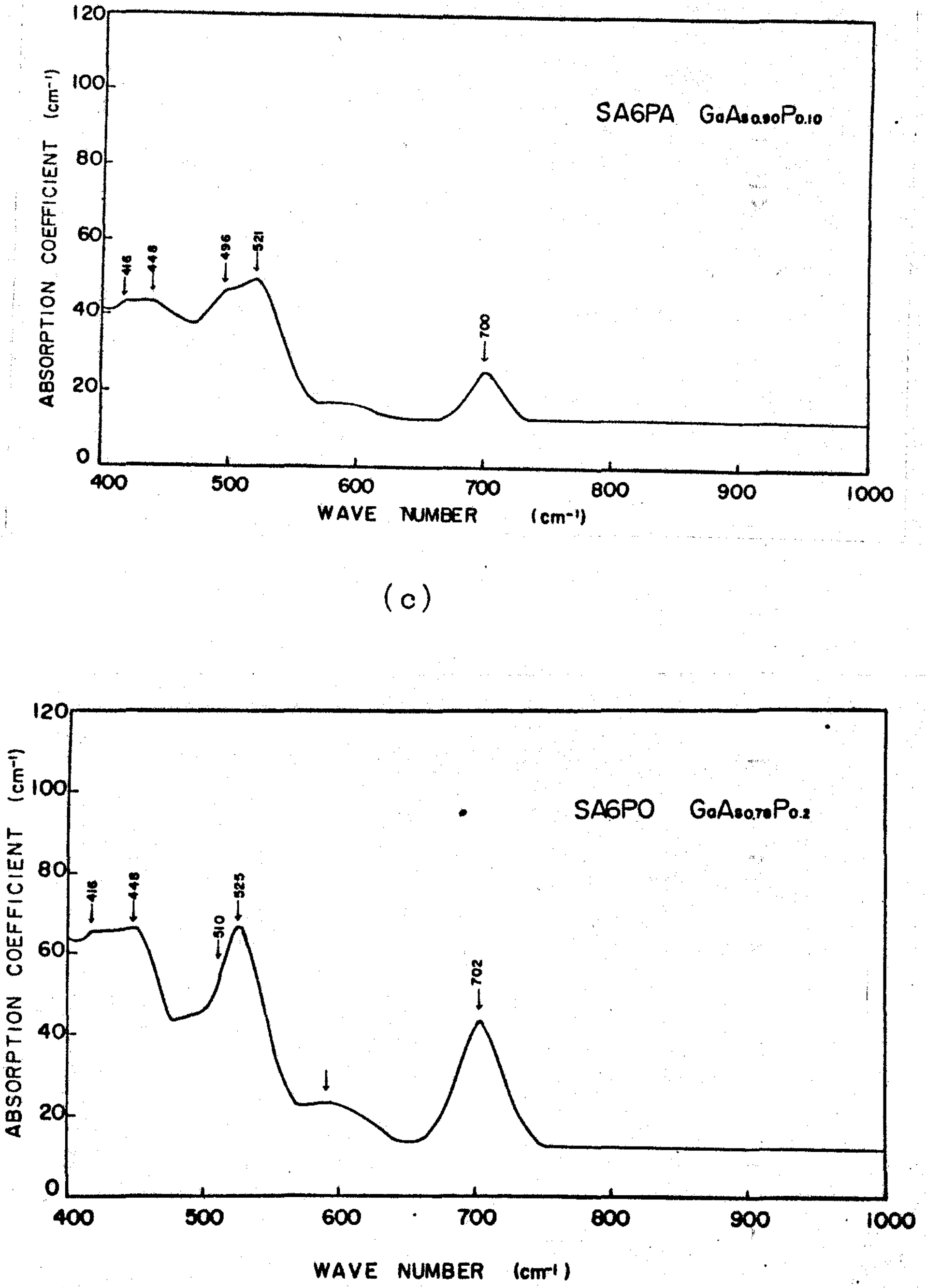

(c)

(d)

Fig. 37 Lattice absorption vs. wave number from 400 to 1,000 cm^{-1} in $GaAs_{1-x}P_x$ alloy.

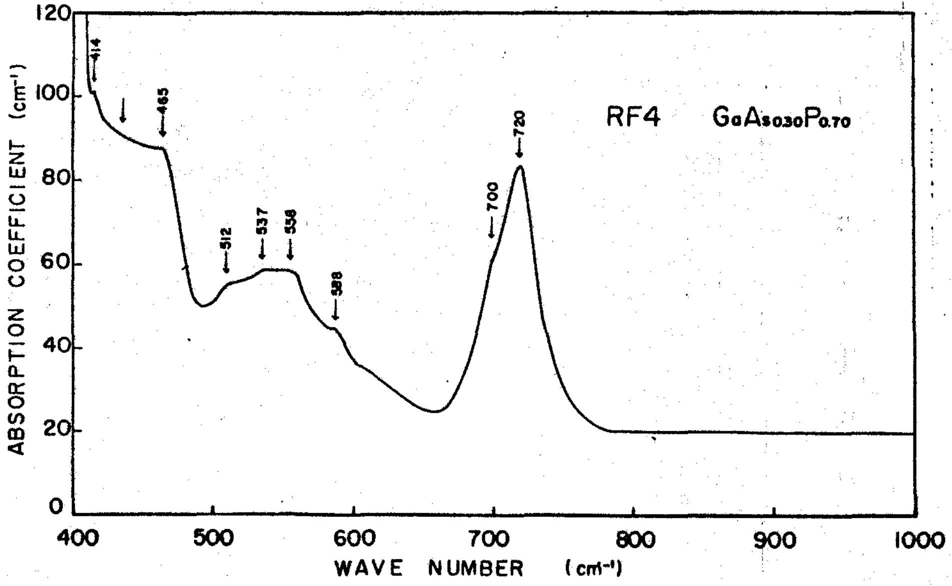

Fig. 37e Lattice absorption vs. wave number from 400 to 1,000 cm^{-1} in $GaAs_{1-x}P_x$ alloy.

schemes to the spectra with five phonon energies in each case. Johnson$^{56)}$ gave alternative assignment schemes to these spectra from a critical point analysis based on the space group symmetry. The assignment schemes of GaAs and GaP in the present work are indicated in Table 13, where TA and LA are the transverse- and longitudinal-acoustical phonons, TO and LO are the transverse- and longitudinal-optical phonons, and Γ , X, and L are the (0,0,0), (1,0,0), and (1/2,1/2,1/2) points in the Brillouin zone of zinc blende crystals. As can be seen, it should be believed that Johnson's assignments are sounder because of taking the physical properties of crystal symmetry into account.

The absorption coefficient for GaAs as a function of photon energy is given in Fig. 35, where twelve peaks observed were interpreted in terms of ten characteristic phonon energies indicated in Table 13. On the other hand, the absorption

Table 13-a Phonon assignments in GaAs

Peak energy cm^{-1}	Peak energy eV	Phonon assignment	Assignment energy cm^{-1}	Assignment energy eV
765	0.0948	2 TO + LO (L)	759	0.0940
707	0.0876	TO + LO + LA (X)	704	0.0872
696	0.0863	TO + LO + LA (L)	701	0.0869
591	0.0732	2 TO + TA (X)	590	0.0731
570	0.0706	TO + LO + TA (L)	569	0.0710
521	0.0645	2 TO (L)	522	0.0647
505	0.0626	2 TO (X)	508	0.0629
497	0.0616	TO + LO (L)	498	0.0617
484	0.0600	TO + LO (X)	484	0.0600
450	0.0557	LO + LA (X)	451	0.0559
437	0.0541	LO + LA (L)	440	0.0545
408	0.0505	2 LA (L)	406	0.0503

here, cutoff energies are 583 cm^{-1} (0.0722 eV) for two phonon process, and 874.5 cm^{-1} (0.1084 eV) for three phonon process.

Table 14-a Characteristic phonon energies in GaAs (cm^{-1})

	L	Γ	X
TO	261	268	252.5
LO	237	291.5	231.5
TA	71	-	85
LA	203	-	220

coefficient for GaP is shown in Fig. 36, where 21 two-phonon bands were explained in terms of 10 characteristic phonon energies. Because of the large energy difference between the four higher- and the seven-lower energy phonons, it was assumed that the four characteristic phonon energies were optical and the two acoustical.

Table 13-b Phonon assignments in GaP

Phonon assignments in GaP

Peak energy		**Phonon assignment**	**Assignment energy**	
cm^{-1}	**eV**		**cm^{-1}**	**eV**
1135	0.1407	2 TO + LO (Γ)	1132	0.1403
1097	0.1360	3 TO (Γ)	1096.5	0.1359
1065	0.1320	2 TO + LO (L)	1068	0.1324
1020	0.1264	2 TO + LO (X)	1019	0.1263
885	0.1097	2 LO + LA (X)	873	0.1082
793	0.0963			
778	0.0964	TO + LO + TA (X)	777	0.0963
746	0.0925	2 TO (L)	746	0.0925
731	0.0906	2 TO (Γ)	731	0.0906
716	0.0887	2 TO (X)	716	0.0887
695	0.0861	TO + LO (L)	695	0.0861
686	0.0850	LO + LA + TA (X)	686	0.0850
598	0.0741	LO +LA (L)	597	0.0740
570	0.0706	LO + LA (X)	570	0.0706
550	0.0682	2 LA (L)	550	0.0682
534	0.0662	2 LA (X), LO + 2 TA (X)	535	0.0663
490	0.0607	2 LO - TA (X)	490	0.0607
474	0.0587	TO + TA (X)	474	0.0587
456	0.0565	LO + 2 TA (L)	460	0.0570
442	0.0548	TO + TA (L)	442	0.0548
421	0.0522	LO + TA (X)	419	0.0519

Here, cutoff energies are 802 cm^{-1} (0.0994 eV) for two phonon process, and 1203 cm^{-1} (0.1491 eV) for three phonon process.

Table 14-b Characteristic phonon energies in GaP (cm^{-1})

	L	Γ	X
TO	373	365.5	358
LO	322	401	303
TA	69	-	116
LA	275	-	267

Table 14 shows the single phonon energies deduced from the frequencies of two phonon processed, and LO(Γ) calculated using the Lyddane-Sachs-Teller relation. Although LO(Γ) is larger than TO(Γ), it appears from the photon systematics that TO is larger than LO near zone edge. Also the results of the application of the Brout sum are summarized in Table 14. The data of compressibility obtained from the above relation are reasonable in comparison with that the values of Si and Ge are 1×10^{-12} and 1.3×10^{-12} cgs, respectively. One band, located at 793 cm^{-1}, did not fit into the assignment scheme and was assumed to be an impurity band. Attempts to identify the impurity as oxygen were unsuccessful.

The major feature of the absorption spectra of $GaAs_{1-x}P_x$ is that it is possible to trace the energies of the two phonon bands of both GaAs and GaP in the alloy as a function of composition. Two-phonon bands of GaAs and GaP are shown as a function of compositions in Fig. 38. Some of the two-phonon bands cannot be traced from the spectra of the alloy; this is particularly true for the bands of GaAs since the intensity of the GaP bands is inherently stronger than that of the GaAs bands. On the other hand, a number of the GaP bands appear in a spectral region in which GaAs is completely transparent and therefore are easily traced.

It is important, in this context, to note that the labels used to designate specific points in the Brillouin zone lose their meaning for the disordered alloy which lacks periodicity. Nevertheless, they remain a convenient means for characterizing the spectra and are retained in this paper.

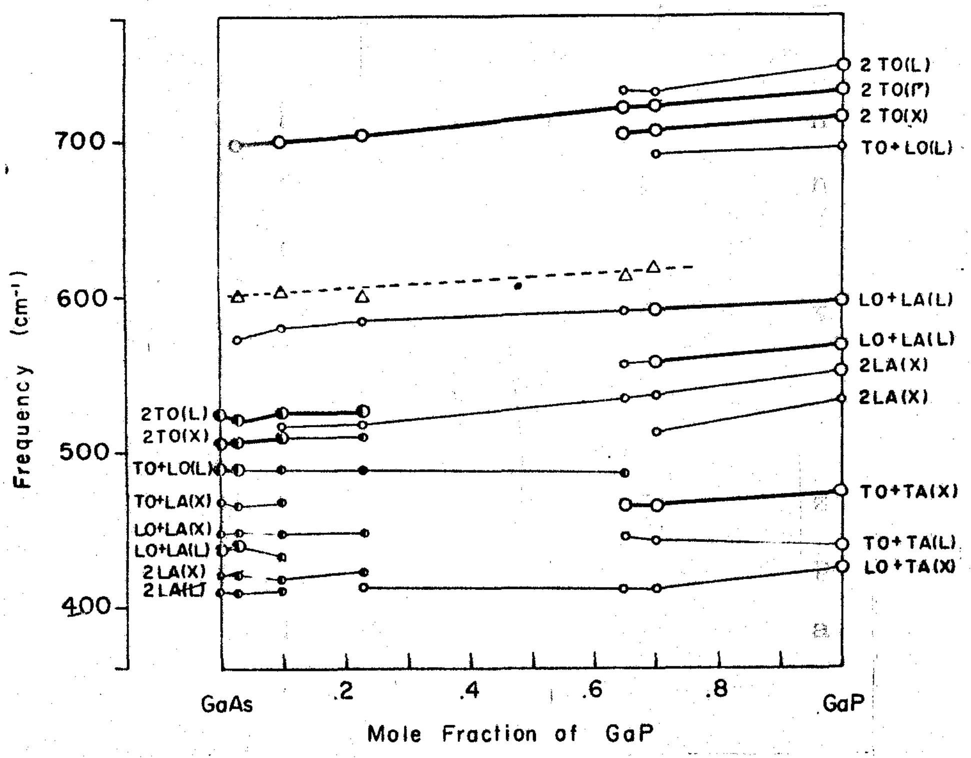

Fig. 38 Two-phonon bands of GaAs-GaP as a function of composition. Johnson's assignment schemes for GaAs and GaP are given.

a) Integrated absorption

It has been pointed out by D. A. Kleinman that combination bands can be caused by anharmonic forces. For cubic crystals with two kinds of atoms, the wave vector of the radiation is very small so that the acoustical branches do not contribute to the interaction of photon-phonon, and on the other hand, there are three optical branches which for very small wave vectors may be considered to be one longitudinal and two mutually perpendicular transverse branches. The longitudinal branch cannot interact with the transverse radiation field, and one of the transverse branches may be chosen perpendicular to the field. Then it is apparent that the interaction of the crystal with the electromagnetic field is caused through the transverse optical vibration of zero wave vector as the fundamental vibration designated by f.

For a crystal of the zinc blende structure the anharmonic forces can be introduced into an ideal harmonic model by connecting purely anharmonic springs between each atom and its four nearest neighbours of the opposite type. The potential energy of the purely anharmonic spring is $-Gx^3$, where x is the extension and G is a parameter whose value may be determined from a comparison of theory and experiment. It is concluded by Kleinman that the third order anharmonic potential produces only two-phonon processes in which the fundamental phonon is an intermediate state.

Under the approximation that the six possible optical-optical processes have equal integrated absorption, the quantity is of experimental interest in the present work, because the two-optical phonon combination bands of GaP-type are well separated from the optical-acoustical combination bands permitting their integrated absorption to be measured directly. According to Kleinman, the integrated absorption is given by

$$P_{op} \sim 24\pi^3 G^2 (N_0 \hbar \hat{e}^2 / m^4 \omega_f^7 \epsilon_0^{1/2})(1+2n(q)) \qquad (54)$$

where N_o is the number of unit cells per unit volume, $\hat{e}$ the effective charge, m is the reduced mass, ω_f is the fundamental phonon frequency, ϵ_o is the high frequency dielectric constant, and n is the phonon density. By equating the experimental value of P_{op} as given in Table 9 to the expression(54) we obtain the estimate

$$G \sim 3.2 \times 10^{12} \ (g\ cm^{-1}\ sec^{-2})$$

for the anharmonic parameter.

For the $GaAs_{1-x}P_x$ alloys, it may be considered that the As and P ions are randomly distributed on the anion sublattice and that anions of like species vibrate in phase and with identical amplitudes against the cations which also vibrate together as a rigid unit. Moreover, it could be thought that the alloy consists of two kinds of unit cell; one is a tetrahedron with the As ion at its center and four nearest neighbours of Ga ions and the another with the P ion at its center and four Ga ions at corners. The fundamental assumption for lattice has been called a random-element-isodisplacement model. The reststrahlen-like band spectra of these alloys have been explained well by the lattice model.57) On the other hand, the two phonon absorption bands due to the anharmonic mechanism have a process of the excitation of the fundamental phonon as an intermediate state, and then the probability of the interaction of phonons with the radiation may be proportional to the number of GaP-like unit cells per unit volume. Accordingly, the integrated absorption involving all optical-optical processes in the alloy with composition x corresponds to the quantity similar to the above

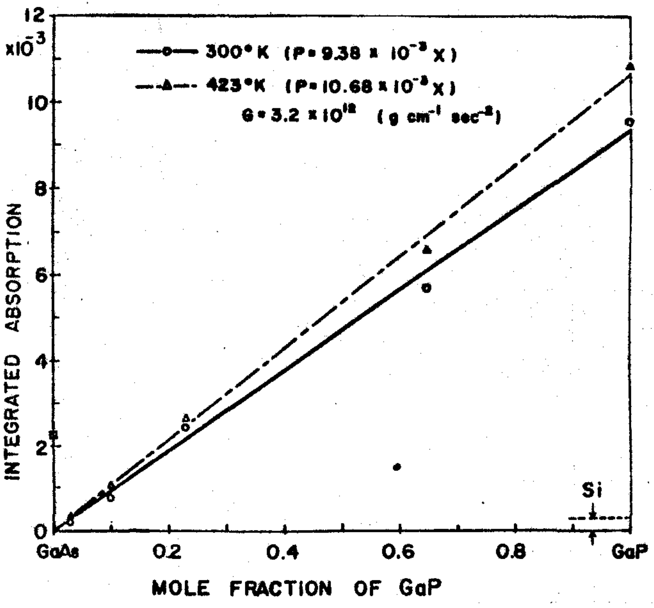

Fig. 39 Integrated absorption of 700 cm^{-1} band due to GaP-like two phonon process

expression(54) multiplied by x. As shown in Fig. 39, the observed values of 700 cm^{-1} bands have apparently a linear dependence with composition.

The same discussion may be applied to the optical-optical combination bands of GaAs crystal, unfortunately which overlap the optical-acoustical combination bands. Making a reasonable interporation in the region from 2TO(L) to TO+LO(L) bands, the integrated absorption P_{op} is $(2.2 \pm 0.4) \times 10^{-3}$ and the anharmonic parameter G for GaAs has been obtained to be $(3.1 \pm 0.3) \times 10^{12}$ g cm^{-1} sec^{-2} by use of some parameters as given in Table 15.

Table 15 Some values of 700 cm^{-1} band due to GaP-like two phonon process

Sample No.	X	Frequency (cm^{-1}) ω (peak)		$\frac{1}{\omega}\frac{\Delta\omega}{\Delta T}$	Absorp. Coeff. (cm^{-1}) α (Peak)		Integrated Intest. P		Half Width γ (cm)
		300°K	400°K		300°K	400°K	300°K	400°K	300°K
1	0.03	698	692	$5.5^{\times 10^{5}}$	6.3	7.0	$0.20^{\times 10^{-3}}$	$0.31^{\times 10^{-3}}$	$3.4^{\times 10^{-5}}$
2	0.10	700	692	-	16.3	17.5	0.76	1.04	6.3
3	0.23	702	698	-	31.1	32.0	2.44	2.61	7.9
4	0.65	720	-	-	-	-	-	-	-
5	0.70	721	714		62.7	94.2	5.66	6.57	9.0
6	1.00	731	728	4.4	77.0	85.0	9.49	10.87	12.2

here maximum frequency and integrated intensity as a function of alloy composition are,

at 300°K, **ω (peak) = 696 + 35X, P = 9.4X x 10^{-3}**

at 423°K, **ω (peak) = 689 + 38X, P = 10.7X x 10^{-3}**

b) Temperature and composition dependence

In the present treatment, both the temperature and the composition dependence of the combination bands should be explained in terms of the anharmonic potential. The Hamiltonian of the linear chain is useful of analyzing these dependences. If we now displace the equilibrium positions by adding δ to the interparticle spacing, the frequency shift resulting the modified spring constant is

$$\Delta\omega/\omega = -3G\delta/K \tag{55}$$

To relate δ to thermal expansion, the spring constant K may be eliminated by the relation $\omega_{max}=2(K/M)^{1/2}$ and ω_{max} identified with ω_{LA}, which gives the result

$$\frac{1}{\omega}\frac{\Delta\omega}{\Delta T} \sim -12\,\frac{Ga\alpha}{M\omega_{LA}^{2}} \qquad (56)$$

where a denotes the lattice constant and the coefficient of linear thermal expansion. Using some parameters given in Table 15, $-1/\omega\, \Delta\omega/\Delta T$ is calculated to be 1.4 for GaP, and $1.5\times10^{-5}(^{\circ}K^{-1})$ for $GaAs_{1-x}P_x$ with 0.03 mole fraction of GaP. These values are in agreement with the experimental values as shown in figure 40. Therefore the anharmonic mechanism for the infrared absorption seems to be in agreement with the temperature shift of the

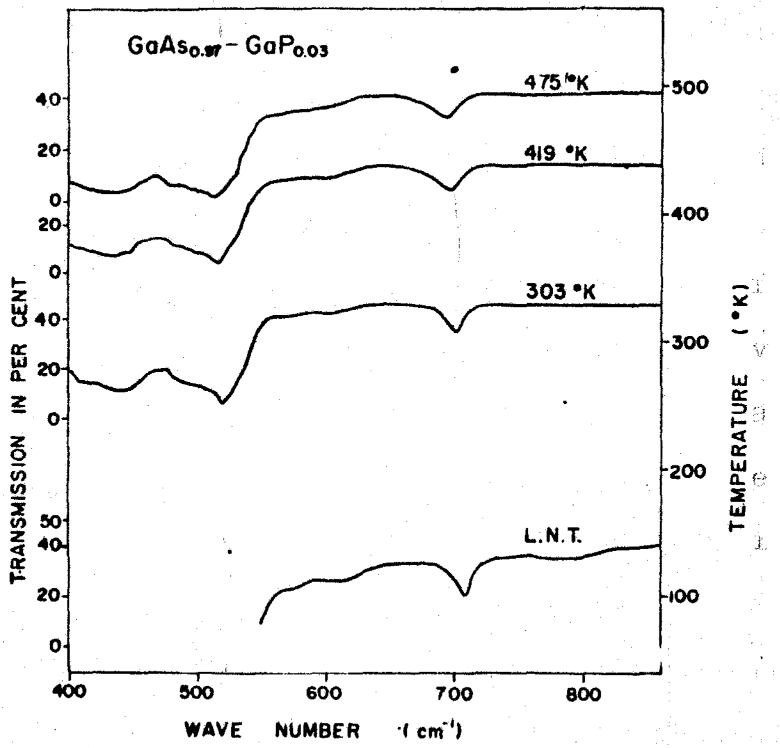

Fig. 40 Temperature dependence of multiphonon process

combination bands in the $GaAs_{1-x}P_x$ alloys over all composition. However, it should be understood that the linear chain model is applicable to well behaved cases in which the thermal expansion is positive, that is, normal in magnitude, and the Gruneisen parameter γ_{Gr} is approximately constant.

The relevance of γ_{Gr} to the composition dependence of frequency shift is that the Gruneisen theory is based on the approximation that with change in lattice constant all phonon frequencies depend on lattice constant as

$$\Delta\omega/\omega = 3\gamma_{Gr}\Delta a/a , \qquad (57)$$

Here, the Gruneisen's relations is represented by

$$\gamma_{Gr} = \frac{3\alpha V}{\beta C_v} . \qquad (58)$$

where β is the isothermal compressibility, and C_v is the specific heat of the crystal at constant volume. Using the values determined above for parameters represented in the equation(58), the Gruneisen constants of GaAs and GaP are obtained to be 0.97 and 1.15, respectively.

c) Half width of 700 cm^{-1} combination bands

In crystals of the III-V compounds which have zinc blende structure there is first order electric moment, and the transverse optical phonon branches near zero wave vector are infrared active in absorption. The two TO(Γ) branches are degenerate and a single reststrahlen band is observed. This phonon frequency in wave number is 366 for GaP$^{54)}$ and 268 cm^{-1} for GaAs$^{57),58)}$ at room temperature.

A number$^{57)-61)}$ of theoretical and experimental studies have emphasized the rôle played by an isolated substitutional impurity in the lattice dynamics and infrared absorption of crystals. The general conclusion is that the impurity can result in absorption bands not present in the pure crystal. In a monoatomic crystal, if the impurity is lighter than the host atom and the force constants are assumed to be unchanged, a locarized vibrational mode is obtained. The localization is spatial in the sense that the amplitude of vibration of the mode is exponentially attenuated with distance from the defect site. The attenuation length decreases and the frequency of the mode increases with decreasing impurity mass. Theory also indicates that the impurity slightly perturbed the lattice frequencies.

Line broadening of the absorption is caused by various processes. The line width theories usually assume one of two processes. The first is the decay of the local mode through the anharmonic potential into two or more lattice phonons.$^{59),62),63)}$ The second is the process due to an elastic scattering of band phonons. In addition to these processes which predict temperature dependent line widths, there are the inhomogeneous broadening processes. Isotopic line broadening is discussed by Dawber and Elliott.$^{60)}$ The presence of varying internal strain fields can split the triply degenerate P local mode and give the appearance of line broadening. If the internal strain is related to the presence of other P atoms in the crystal, we would expect this broadening to be concentration dependent. Also at large

P concentrations, P-P interactions could give line broadening particularly if the local mode extends out several lattice spacings. Once again this broadening would be expected to be concentration dependent if the P distribution is random in the host lattice. The $x \sim 0.03$ indicates that the attenuation length for the P local mode is of the order of the lattice constant and hence the mode frequency and the line width will be most sensitive to the influence of the immediate environment of the P. Therefore, the lowest P concentrations used in the present work are already sufficiently so large that the local mode model for isolated impurities might be difficult to apply. Several interesting effects were observed. A band was observed near 706 cm^{-1} for small x. As x increases the absorption shifts to higher frequency and shows structure at very large x and becomes indentifiable as GaP multiphonon bands involving combinations of optical mode frequencies.

d) Thermal expansion

Linear thermal expansion coefficients for some specimens of $GaAs_{1-x}P_x$ alloys have been measured by the method using a strain gauge from room temperature to 150 °C. These results are shown in Table 16. The observed coefficient for GaP agrees with Welker's data, but not with Straumanis data.

The thermal expansion calculated on the basis of the three dimensional GaP anharmonic model is

$$\alpha = \frac{3\sqrt{3}}{16} \frac{G a^3 k}{M^2 C_s^4} \qquad (59)$$

where C_s is the effective velocity of sound, and in order to obtain the linear thermal expansion the optical branches were entirely neglected and the acoustic branches put in the high-temperature approximation $n_{qt} \sim kT/h\omega_{qt}$. Using the values C_s=5.22x10^5 64) and 6.2x10^5 65) for GaAs and GaP, respectively, we obtain α =6.06x10^{-6} and 5.60x10^{-6} from the equation(59).

Table 16 Experimental and theoretical expansion coefficient, ($^oK^{-1}$)

	GaAs	0.2	0.4	0.6	0.65	0.8	GaP
present work	6.30 x 10^{-6}	5.70			5.45		5.40
(a)	6.07						
(b)							5.30
(c)	6.40	5.53	5.12	4.88		4.76	4.70
calculated	6.06						5.60

(a):**L.Bernstein et al**, (b):**H.Welker et al**, (c):**M.E.Straumanis et al**

4-4) Conclusion

The two phonon absorption in the partially polar materials is approximately an order of magnitude larger than that of silicon, germanium and diamond. It was shown that the integrated absorption for the optical-optical mode combination bands is $\int\alpha d\lambda$ =2x10^{-2} for SiC, and 6x10^{-4} for Si. The present work obtained for the integrated absorption to be 9.5x10^{-3} for GaP, and (2.2±0.4)x10^{-3} for GaAs. The value for Si already includes a factor of 2 to take into account the difference in selection rules between the diamond and zinc blende cases. This difference in integrated absorption is taken as evidince for the importance of the anharmonic mechanism in the cases for compounds with partially ionic character. Also the anharmonic parameter, G were obtained to be 3.2×10^{12} and $(3.1\pm0.3)\times10^{12}$ for GaP and GaAs, respectively.

The composition dependence of the integrated absorption is seems to support the random-element-isodisplacement model.

Various physical quantities could be estimated in terms of the anharmonicity considered by Kleinman. These theoretical values for GaAs, GaP and their alloys are reasonable in comparison with the experiments. The thermal expansion coefficients observed in the present work are in good agreements with the calculated ones.

References

1) H. Ehrenreich; J. Appl. Phys. Suppl. 32(1961)2155

2) M. Cardona, K.L. Shaklee and F. H. Pollak; Phys. Rev. 154 (1967)696

3) M. L. Cohen and T. K. Bergstresser; Phys. Rev. 141(1966)789

4) F. Herman, R. L. Kortum, C. D. Kuglin and J. L. Shay; in II-VI Semiconducting Compounds, edited by D. G. Thomas (W. A. Benjamin, Inc. New York, 1967), p503

5) A. R. Hutson, A. Jayaraman and A. S. Coriell; Phys Rev. 155(1967)786

6) J. M. Whelan and G. H. Wheatley; J. Phys. Chem. Solids 6(1958)169

7) L. W. Aukerman and R. K. Willardson; J. Appl. Phys. 31(1960) 293

8) W. G. Spitzer and J. M. Whelan; Phys. Rev. 114(1959)59

9) E. Haga and H. Kimura; J. Phys. Soc. Japan 19(1964)1596

10) M. Shyam, J. W. Allen and G. L. Pearson; IEEE Trans. Electron Devices 13(1966)63

11) D. Madelung; Physics of III-V Compounds (John Wiley & Sons, Inc., New York, 1964), 531

12) I. Valslev; Phys. Rev. 173(1968)762

13) R. Zallen and W. Paul; Phys. Rev. 134(1964)A1628

14) W. E. Becker, A. K. Ramdas and H. Y. Fan; J. Appl. Phys. Suppl. 10(1961)2094

15) J. W. Allen and J. W. Hodby; Proc. Phys. Soc. 182(1963)315

16) K. Osamura and Y. Murakami; Abstract2, Spring Meeting of Phys.Soc. of Japan, (1968)147

17) B. O. Seraphin and H. E. Bennett; Semiconductors and Semimetals, edited by R. K. Willardson and A. C. Beer (Academic Press, New York and London, 1967) vol.3, p499

18) H. W. Verleur and A. S. Barker,Jr.; Phys. Rev. 149(1966)715

19) G. Dresselhaus; Phys. Rev. 100(1955)582

20) H. Ehrenreich; Phys. Rev. 120(1960)1951

21) H. Y. Fan; Rep. Progr. Phys. 19(1956)107

22) H. Y. Fan; Semiconducting Materials (Reading Conference), edited H. K. Henisch 1951 p132

23) H. Y. Fan, W. Spitzer and R. J. Collins; Phys. Rev. 101 (1956)566

24) R. Rosenberg and M. Lax; Phys. Rev. 112(1958)843

25) H. Schmidt; Z. Physik. 139(1954)433

26) W. G. Spitzer and J. M. Whelan; Phys. Rev. 114(1959)59

27) E. P. Rashevskaya and V. I. Fistul'; Soviet Phys. Solid State 9(1967)1443

28) E. P. Rashevskaya and V. I. Fistul'; ibid 9(1968)2849

29) E. Haga and Kimura; J. Phys. Soc. Japan 19(1964)658

30) H. Y. Fan; Rept. Progr. Phys. 19(1956)107

31) R. Rosenberg and M. Lax; Phys. Rev. 112(1958)843

32) H. J. G. Meyer; Phys. Rev. 112(1958)298

33) S. Visvanathan; Phys. Rev. 120(1960)379

34) R. Wolfe; Proc. Phys. Soc. A67(1954)74

35) S. Visvanathan; Phys. Rev. 120(1960)376

36) T. Suzuki and S. Akai; Sumitomo Electric Technical Review No.13(1970)66

37) D. A. Kleinman; Phys. Rev. 118(1960)118

38) R. H. Lyddane, R.G.Sachs and E.Teller; Phys. Rev. 59(1941)673

39) R. Brout; Phys. Rev. 113(1959)43

40) H. B. Rosenstock; Phys. Rev. 129(1963)1959

41) J. L. Birman; Phys. Rev. 127(1962)1093: ibid 131(1963)1489

42) L. Rosenfeld; Theory of Electrons (North Holland, 1951)

43) N. F. Mott and H. Jones; Properties of Metals and Alloys,1936

44) M. Born; Revs. Modern Phys. 97(1955)39

45) E. Burstein, J. J. Oberly and E. K. Plyler; Proc. Indian. Acad. Sci. 28(1948)388

46) M. Lax and E. Burstein; Phys. Rev. 97(1955)39

47) P. G. Dawber and R. J. Elliott; Proc. Roy. Soc. A273(1963)222

48) P. G. Dawber and R. J. Elliott; Proc. Phys. Soc. 81(1963)453

49) S. D. Smith, R. E. V. Chaddock and A. R. Goodwin; J. Phys. Soc. Japan 21. Suppl. (1966)67

50) R. C. Newman; Advances in Physics 18(1969)545

51) G. Baldini et al.; J. Phys. Chem. Solids 27(1966)943

52) R. H. Parmenter; Phys. Rev. 97(1955)587

53) H. W. Verleur and A. S. Barker;Jr.;Phys. Rev. 149(1966)715

54) D. A. Kleinman and W. G. Spitzer; Phys. Rev. 118(1960)110

55) W. Cochran, S. J. Fray, F. A. Jhonson, J. E. Quarrington and N. Williams; J. Appl. Phys. 32(1961)2102

56) F. A. Jhonson; Progr. Semicond. 9(1965)179

57) Y. S. Chen, W. Schokley and G.L. Pearson; Phys. Rev. 151 (1966)648

58) M. Hass and B. W. Henvis; J. Phys. Chem. Solids 23(1962)1099

59) R. J. Elliott, W. Hayes, G.D. Jones, H. F. Macdonald and C. T. Sennett; Proc. Roy. Soc. 289(1965)1

60) P. G. Dawber and R. J. Elliott; Pro. Phys. Soc. 81(1963) 453: Pro. Roy. Soc. 273(1963)222

61) W. Hayes; Phys. Rev. 138(1965)1227: Pyhs. Rev. Lett. 13 (1964)275

62) P. G. Klemens; Phys. Rev. 122(1961)443

63) A. A. Maradudin; Ann. Phys. 30(1964)371

64) P. Aigrain et al.; Selcted Constants Relative to Semiconductors, Pergamon Press (1961)

65) R. W. Keyes; J. Appl. Phys. 33(1963)3371

66) F. von Oswald; Z. Naturforsch 14a(1959)374

Chapter VI

Summary

In this thesis, the study has been fulfilled on the preparation and properties of the compounds of gallium with the group V elements and an indium-selenide compound. The results are briefly reviewed as follows:

In the chapter II, the quasi-binary phase diagrams of GaAs-GaP and GaAs-GaSb system have been determined. The thermodynamic properties for III-V quasi-binary systems have been concerned and the molecular like model could be established to be applicable to these systems. The applicability of the MLP model to some quasi-binary systems could be tested by comparing the available experimental phase diagram data with the calculated results.

The computations of the binary phase diagram have been examined using the ideal, regular and athermal solutions.

In the chapter III, the methods of preparing the III-V compounds have been considered. The method of preparing $GaAs_{1-x}P_x$ solid solutions from the melt by controlling two volatile elements has been developed and the concept of pseudo-equilibrium in a heterogeneous system containing two different temperatures has been described.

In the chapter IV, the precise measurements of X-ray intensity were carried out by the powder method, and the crystal structure factors of GaAs, GaP and their alloys have been determined.

The temperature factors of Ga, As and P have been obtained in each samples, and the both Debye and Einstein model on the lattice vibration were concerned. Temperature factors of the III and the V atoms in GaP differ each other in magnitude. The difference could be explained using the Einstein model.

The assumption that the atomic scattering factor of V atom in the alloy is represented by a linear combination of constituent V atoms might be thought to be valid in the present accuracy of the experimental analysis. However, the apparent temperature factors of each atom in the alloy seem to be systimatically scattered. The experimental fact could be thought to be caused by the above assumption and the strain introduced by the alloying.

The effective charge in III-V compounds has been estimated by three methods. Unfortunately the quantitative result could not be obtained, but the fact that negative charge is being passed from the III atom to the V atom has been concluded in GaAs, GaP and their alloys.

The crystal structure factors of α- and β-In_2Se_3 have been established as follows; Since the β-phase is stable above 200 °C, the small specimen was sealed in a capillary and heated at about 250 °C to obtain X-ray photographs of the β-phase. The c axis Laue photographs show no six-hold symmetry as expected from the literatures but three-hold symmetry. High temperature photographs were taken with Ni filtered CuK_α radiation around the a axis. The a axis oscillation photographs show that the layer lines are symmetrical with respect to the equatorial line. On the Weissenberg photographs the reflections are ovserved as $-h+k+l=3n$, the indices being based on the hexagonal system. The intensity statistics of the reflections indicate that the crystal should be of cectro-symmetric. Thus the space group of β -phase has been concluded to be rhombohedral D_{3d}^5-$R\bar{3}m$. The unit cell has the dimensions, a=4.05, c=29.41 Å at 250 °C, and Z=3. Observed intensities were corrected by ordinary way. There are six indium and nine selenium atoms in a unit cell. Considering the equivalent positions of the space group R3m and the coordination of the atoms, it may be reasonable to locate the selenium atoms in 3(a) and 6(c), and the indium atoms in 6(c). There is no parameters in 3(a) and only z-parameters in 6(c). The parameters were obtained from Patterson diagram, P(vw), and refined to minimize the discrepancy factor R. When the values are Z_{In}=0.401, and Z_{Se}=0.222, both in 6(c), the R factor is 0.18.

The lattice parameters of α-phase were determined to be a=4.05, c=28.77 Å, and Z=3 at room temperature. The reflections are observed as -h+k+l=3n like β-phase. The α-phase crystal, however, seems to be of noncentro-symmetric from comparison of observed structure factors to those calculated. The α-phase space group is thus concluded to be C_{3v}^5-R3m. All atoms are situated in the spacial position 3(a) of R3m. The final atomic parameters for indium are 0,0,0.242; 0,0,0.718, and, for selenium atoms, 0,0,0; 0,0,0.525; 0,0,0.818, respectively. The R factor is calculated to be 0.18.

In the chapter V, the present experimental results of the infrared absorption in the region from 1,000 to 4,000 cm^{-1} have given the following conclusions.

(a) The absorption bands in n-GaP and GaP-rich alloys have been illustrated to occur mainly by a transition from a shallow donor level to the upper conduction band minimum. The reasonable fits for the absorption profile have been obtained with the equation(9), of the chapter V, especially in the large wave number region. Near the absorpiton threshold the experimental values diverge from the equation(9). The fact might be interpreted in terms of the existence of excited states of the impurity atoms. The threshold energy depends to a small extent on the composition. The dependence could be illustrated in terms of the composition dependence of the donor ionization energy.

(b) The absorption in n-GaAs and GaAs-rich alloys arises from the bottom of the lowest conduction band to a subsidiary minimum. The absorption is represented with the equation(16) of the chapter V. The dependence of threshold energy on composition x is found to be expressed as E_t=0.29-0.67x (eV). The empirical cross over point occurs at 43 mol% GaP. At a constant photon energy well above acoustical phonon energies, it is concluded that the experimental absorption coefficient is proportional to the carrier concentration and the cross section for alloys are three or four times larger than for GaAs as expected from the theory.

The normal free carrier absorptions have been observed only in the region from 800 to 2,000 cm^{-1}. The absorption coefficient is proportional to the minus 3.5th of wave number for the specimens with high carrier concentration and to the minus 2.5th for the fairly pure specimens. The impurity scattering prevails at lower temperature. The contribution of various scattering mechanisms for the free carrier absorption has been consistent with the theoretical behavior in the wide range of carrier concentration and at three temperatures as shown in Fig. 29 of the chapter V. The degree of compensation of impurity has been determined for all specimens using the theoretical equation(25) of the chapter V. The values of the degree of compensation determined in the present method are reasonable because of the consideration for the electrical properties. In the present analysis, the effective mass ratio (m*/m) has been assumed to be 0.078.

The two phonon absorption in the partially polar materials is approximately an order of magnitude larger than that of silicon, germanium and diamond. It was shown that the integrated absorption for the optical-optical mode combination bands is $\int \alpha d\lambda = 2\times10^{-2}$ for SiC, and 6×10^{-4} for Si. The present work provided for the integrated absorption to be 9.5×10^{-3} for GaP, and $(2.2 \pm 0.4)\times10^{-3}$ for GaAs. The value for Si already includes a factor of 2 to take into account the difference in selection rules between the diamond and zinc blende cases. This difference in integrated absorption is taken as evidence for the importance of the anharmonic mechanism in the cases for compounds with partially ionic character. Also the anharmonic parameter, G were obtained to be 3.2×10^{12} and $(3.1\pm0.3)\times10^{12}$ for GaP and GaAs, respectively.

The composition dependence of the integrated absorption seems to support the random-element-isodisplacement model.

Various physical quantities could be estimated in terms of the anharmonicity considered by Kleinman. These theoretical values for GaAs, GaP and their alloys are reasonable in comparison with the experiments. The thermal expansion coefficients observed in the present work are in good agreements with the calculated ones.

ACKNOWLEDGMENTS

The author is very grateful to his thesis supervisor, Professor Yotaro Murakami, for the encouragement and counsel given throughout the course of this work.

The author is also thankful to Mr. Kanehiko Imanishi (Nippon Steel Corporation), Mr. Jun Inoue (Graduate student, Kyoto University), Mr. Kazuo Nakajima and Mr. Yutaka Hiraoka (Under-graduate students), for their earnest assistance provided in the experimental works in this study.

The appreciation of the author extends to Assistant Professor Osamu Kawano for his thoughtful encouragement and help during this investigation.

The author wishes to express his hearty thanks to Mr. Shin-ichi Akai (Sumitomo Electric Industries, Ltd.) for useful discussion and comments.